D I S S E R T A T I O N

Simulation of Heterojunction Bipolar Transistors

ausgeführt zum Zwecke der Erlangung des akademischen Grades
eines Doktors der technischen Wissenschaften

eingereicht an der Technischen Universität Wien
Fakultät für Elektrotechnik und Informationstechnik
von

Vassil Palankovski

Wien, im Dezember 2000 . . . .

Abstract

HETEROJUNCTION Bipolar Transistors (HBTs) are among the most advanced semiconductor devices. They match well today's requirements for high-speed operation, low power consumption, high-integration, low cost in large quantities, and operation capabilities in the frequency range from 0.9 to 100 GHz. At present III-V HBT MMICs on six-inch wafers and SiGe HBT circuits as part of the CMOS technology on eight-inch wafers are in volume production. To cope with the explosive development costs of today's semiconductor industry Technology Computer-Aided Design (TCAD) methodologies are extensively used. Technology, device, and circuit simulation tools save expensive technological efforts while improving the device performance.

The thesis discusses the status of research regarding HBTs, including a review of state-of-the-art devices, a review of state-of-the-art device simulators, with emphasis on MINIMOS-NT, and a discussion on the materials and material systems on which HBTs are based on. MINIMOS-NT is a generic two-dimensional device/circuit simulator used in the VISTA TCAD framework. A large part of the work presented in this thesis is on the development and the practical application of MINIMOS-NT. A detailed discussion on the physical modeling in MINIMOS-NT is presented. It contains models for the lattice, thermal, and transport properties of various semiconductor materials, as well as models for several important effects taking place in HBTs. Critical issues concerning simulation of heterostructures are analyzed, such as interface modeling at heterojunctions and insulator surfaces, band structure and bandgap narrowing, the modeling of self-heating and high-field effects.

Simulation results for several different types of GaAs-based and Si-based HBTs demonstrating the extended capabilities of MINIMOS-NT are shown, most of them in comparison with experimental data. Special emphasis is put on the simulation of high-power AlGaAs/GaAs and InGaP/GaAs HBTs. Two-dimensional DC-simulations of different types of one-finger devices in very good agreement with measured data in a wide temperature range are demonstrated. Self-heating effects are accounted for the output device characteristics. The work is extended with transient simulation of small signal parameters to connect DC- and RF- device operation. A comparison of simulated and measured S-parameters and the dependence of f_T on some device parameters are presented. Device reliability investigations which confirm the usefulness of device simulation for practical applications are also offered. Examples of SiGe HBTs and polysilicon emitter BJT conclude the work presented in the thesis.

Kurzfassung

HETEROÜBERGANG-BIPOLAR-TRANSISTOREN (HBTs) gehören zu den modernsten Halbleiterbauelementen. Sie erfüllen alle Voraussetzungen, um im Frequenzbereich zwischen 0.9 und 100 GHz höchste Operationsgeschwindigkeiten, niedrigen Energieverbrauch und hohe Integrationsdichten mit niedrigen Grenzkosten zu erzielen. In großer Stückzahl werden zur Zeit III-V HBT MMICs auf sechs Zoll Scheiben, und SiGe HBT Schaltungen in CMOS Technologie auf acht Zoll Scheiben gefertigt. Um die exlodierenden Entwicklungskosten moderner Halbleiterbauelemente in den Griff zu bekommen, wird in großem Ausmaß Technology Computer-Aided Design (TCAD) eingesetzt. Technologie-, Bauelement- und Schaltungssimulatoren verbessern die Bauelementeigenschaften ohne teuren technischen Aufwand.

In der vorliegenden Dissertation wird der Status der HBT Forschung diskutiert. Ein Überblick über den Stand der Technik wird gebracht und die bei HBTs verwendete Materialien und Materialsysteme, unter besonderer Berücksichtigung von MINIMOS-NT, werden diskutiert. MINIMOS-NT ist ein generischer, zweidimensionaler Bauelementsimulator und Teil der VISTA TCAD Umgebung. Ein großer Teil der in dieser Arbeit ist der Weiterentwicklung und der praktischen Anwendung von MINIMOS-NT gewidmet. Die verwendeten physikalischen Modelle werden detailiert vorgestellt. Dies beinhaltet sowohl Modelle für die Gittereigenschaften, das Temperaturverhalten und die Transporteigenschaften verschiedener Halbleitermaterialien, genauso wie Modelle für wichtige HBT typische Effekte. Kritische, die Simulation von Heterostrukuren betreffende Punkte werden analysiert, zum Beispiel die Modellierung von Grenzflächen von Heteroübergängen und Isolatoroberflächen, von Bandstrukturen und der Abnahme der Bandkantenenergie bei Hochdotierung (bandap narrowing), von Selbsterwärmung und von Effekten die bei hohen Feldstärken auftreten.

Um die weiteren Fähigkeiten von MINIMOS-NT zu demonstrieren, werden Simulationsergebnisse für verschiedene Typen von GaAs- und Si-basierender HBTs, meist in Verbindung mit Messergebnissen, präsentiert. Hierbei wird spezielles Augenmerk auf die Simulation von Hochleistungs AlGaAs/GaAs und InGaP/GaAs HBTs gelegt. Weiters werden zweidimensionale Gleichstromsimulationen verschiedener Einfingerbauelemente, die in einem weiten Temperaturbereich mit den Messergebnissen übereinstimmen, vorgestellt, wobei bereits Selbsterwärmungseffekte in die Ausgangskennlinie eingehen. Die Arbeit wird noch durch transiente Simulation von Kleinsignalparametern ergänzt, wodurch das Gleich- und Hochfrequenzverhalten der Bauelemente gemeinsam analysiert werden kann. Ein Vergleich simulierter und gemessener S-Parameter und die Abhängigkeit von f_T von einigen Bauelementparametern wird präsentiert. Der praktische Nutzen von Baulementsimulationen wird durch Zuverlässigkeitsuntersuchungen unterstrichen. SiGe HBTs und Polisilizium Emitter BJT Beispiele bilden den Abschluss der in dieser Dissertation vorgestellten Studien.

Acknowledgment

FIRST I would like to thank Prof. Siegfried Selberherr who gave me the honor to work at the Institute for Microelectronics. What makes this place so special? Not only the perfect infrastructure, the nice working atmosphere, and the large experience and knowledge gathered there, which all serves as a stable basis for further scientific research. Also not only the long term relations to the semiconductor industry worldwide, which make the members of the institute face real industrial problems. These are the output standards set by Prof. Selberherr on world-level and often even higher. The harder it is to keep up with these high requirements on one hand, the sweeter the feeling to have them matched on the other hand. I highly appreciate the opportunity to present results of my work at various conferences at all five continents and at leading semiconductor companies, such as Siemens, LSI Logic, Intel, Sony, Hitachi, and AMS. Dear Prof. Selberherr, thank you so much for everything I learned from You!

I also thank Prof. Erich Gornik who agreed to participate in the examining committee.

Next, I would like to thank Prof. Philipp Philippov from TU Sofia for teaching me the basics of microelectronics and microelectronics technology. The work on my master's thesis on SiGe HBTs served as a good basis for my future work. In addition, Prof. Philippov gave me the first advices and recommendations for starting a doctoral study. I also thank Prof. Fritz Paschke and Prof. Wolfgang Fallmann for inviting me to visit TU Wien on the behalf of the Austrian Academy of Science and for supplying me with good recommendations.

I want to express my gratitude to Dr. Walter Kellner from Infineon Technologies AG (former Siemens AG) for giving me the opportunity to join his group as a free researcher. Thanks to him the III-V simulation was continuously supported by the corporate technology of Siemens over many years. The larger part of this thesis would not be possible without such valuable technical, theoretical, and financial support. I appreciate the opportunity to work in Münich in a 'brain-storming' fashion. During my several stays there I enjoyed discussions with Dr. Rüdiger Schultheis, Dr. Jan-Erik Müller, and Andrea Bonacina, in which many useful ideas both on the simulation and the technology side were born. It is a memorable feeling to see the work effort paid by the practical application of its results. I also enjoyed nice evenings out with my former colleague Dr. Rudolf Strasser who is now with Infineon.

I would also like to thank Dr. Sheldon Aronowitz from LSI Logic Corporation, Milpitas, California for inviting me to spend a summer-internship in his group. I enjoyed excellent working climate and many fruitful discussions, especially with him, Dr. Helmut Puchner,

and Dr. Nadya Belova. My stay was so nice that I included the possibility to work there in my future plans. I have to mention nice time out and discussions with my former colleague Dr. Claus Fischer, who is one of the creators of MINIMOS-NT and was with Intel at that time.

I am very grateful to all my colleagues at the Institute of Microelectronics. The atmosphere has always been a perfect source of motivation. It was great to be welcomed and introduced to MINIMOS-NT by Dr. Thomas Simlinger, now with IBM, and especially Dr. Martin Knaipp, now with AMS, with whom we still keep very good, also professional relations. It was pleasure to share office with Dr. Goran Kaiblinger who was the person "infecting" me to spend sometimes eighty, sometimes more, hours a week in working. Unfortunately, this style remained after he left. With his follower, Klaus Dragosits, we shared not only nice discussions during work, but also nice time in Puerto Rico and South Africa. I am very grateful to Prof. Hans Kosina who always took the time to answer my questions thoroughly sometimes even to the very depths of semiconductor physics. I would like to thank Dr. Tibor Grasser for his devotion to MINIMOS-NT which made the simulator so flexible and extendible. His programming expertise always served me as a good example when implementing a new code or reorganizing an old one. I thank him and Prof. Kosina for proofreading this thesis. My gratitude is also due to Christian Troger and Thomas Binder who made my life easy in the Linux environment. I thank also all others who were always willing to help, discuss some topic, or just go out for a beer.

I have to specially mention a long-standing co-worker and friend, Rüdiger Quay. Together we proved that long distance cannot be an obstacle for effective co-actions. He was always ready to enter discussions of new topics ideas, and results. For the several hundreds of mails we shared, the country we were working in, or sometimes the continent, did not matter. This was also proved in numerous common publications. I also enjoyed sharing few evenings out with him in Vienna, Freiburg, London, and Seattle.

Last, I want to thank my parents, without whom I would never have been able to achieve so much. I honor the memory of the three of my grandparents whom I lost during my first two years at the institute. I cordially thank my son for not forgetting me, even though he had so seldomly the opportunity to see me. I especially wish to express my love for Dessi who only knows the real price of this dissertation as we suffered and paid it together. I thank for her endless love, patience, and understanding.

Contents

List of Figures

List of Tables

List of Symbols

Δ	...	step, difference, change
Φ_{ms}	...	metal workfunction difference potential
α	...	exponent
β	...	exponent
$\beta_n,\ \beta_p,\ \beta_\nu$	...	electron, hole, and general exponents in mobility models
γ	...	exponent in mobility models
δE_ν	...	barrier height lowering
ε	...	dielectric constant
$\varepsilon_{\mathrm{s}},\ \varepsilon_{\mathrm{ins}}$	...	dielectric constant of semiconductor, insulator
ε_{r}	...	relative dielectric constant
κ_{L}	...	lattice thermal conductivity
$\kappa_n,\ \kappa_p$	...	thermal conductivity of electron and hole gas
μ_ν	...	mobility of carrier type ν
μ_ν^{L}	...	mobility due to lattice scattering
μ_ν^{LI}	...	mobility due to lattice and impurity scattering
μ_ν^{LIS}	...	mobility due to lattice, impurity, and surface scattering
μ_ν^{LISF}	...	mobility including lattice, impurity, surface scattering, and high-field reduction
μ_ν^{LIST}	...	mobility including lattice, impurity, surface scattering, and high-temperature reduction
$\mu_n,\ \mu_p$	...	electron and hole mobilities
ρ_{L}	...	mass density
σ_{s}	...	surface (interface) charge density
σ_{ox}	...	oxide conductivity
$\sigma_{\mathrm{T},n},\ \sigma_{\mathrm{T},p}$	...	trap capture cross sections for electrons and holes
$\tau_n,\ \tau_p$	...	recombination lifetimes for electrons and holes
$\tau_{\epsilon,n},\ \tau_{\epsilon,p},\ \tau_{\epsilon,\nu}$	...	energy relaxation times for electrons, holes, and general carrier type
φ_{s}	...	semiconductor contact potential
φ_{m}	...	metal quasi-*Fermi* level
$\varphi_n,\ \varphi_p$	...	quasi-*Fermi* potentials for electrons and holes
ψ	...	electrostatic potential
ψ_{bi}	...	built-in potential
C	...	net doping concentration
C_g	...	bandgap bowing parameter

C_μ	...	mobility bowing parameter
$C_{\mathrm{m},\nu}$	...	relative carrier mass bowing parameter
$\mathbf{D}$	...	dielectric flux
$\mathbf{E}$	...	local electric field
$\mathbf{E}_s$	...	local electric field in semiconductor
$\mathbf{E}_{ins}$	...	local electric field in insulator
$E_{\perp 2}$	...	electric field orthogonal to the interface
E_b	...	local band edge energy for electrons or holes
E_C	...	local band edge energy for electrons
E_{g}	...	bandgap energy
$E_{\mathrm{g},0}$, $E_{\mathrm{g},300}$	...	bandgap energy at 0 K, and at 300 K
E_{i}	...	intrinsic *Fermi* level
E_{off}	...	energy offset
E_V	...	valence band energy
$\mathbf{E}_{\mathrm{w}}$	...	workfunction energy difference
F_n, F_p	...	driving force for electrons and holes
H	...	heat generation
I_{E}, I_{B}, I_{C}	...	emitter, base, collector currents
$\mathbf{J}_n$, $\mathbf{J}_p$	...	electron and hole current densities
M_C	...	valley degeneracy factor of the conduction band
N	...	number of electrons of a given chemical element
N_{A}	...	acceptor doping concentration
N_C	...	effective density of states for electrons
$N_{C,0}$	...	effective density of states for electrons evaluated at reference temperature T_0
N_{D}	...	donor doping concentration
N_{T}	...	trap density
N_V	...	effective density of states for holes
$N_{V,0}$	...	effective density of states for holes evaluated at reference temperature T_0
Q_s	...	total charge in the device
R	...	net recombination rate
R^{AU}	...	*Auger* recombination rate
R^{BB}	...	band to band tunneling recombination rate
R^{II}	...	impact ionization recombination rate
R^{SRH}	...	SRH net recombination rate
R_g	...	global thermal resistance
R_{T}	...	thermal resistance
S_n, S_p	...	surface recombination velocities for electrons and holes
$\mathbf{S}_n$, $\mathbf{S}_p$	...	electron and hole heat flux density
$\mathbf{S}_{\mathrm{L}}$	...	lattice heat flux density
T_{C}	...	contact temperature
T_{L}	...	local lattice temperature
T_n, T_p	...	electron and hole temperatures
V_{ox}	...	voltage drop over the oxide at the polysilicon contact
V_{BE}, V_{CE}	...	base-to-emitter voltage, collector-to-emitter voltage

$V(r), V(k)$ ... *Coulomb* potential
Z ... atomic number of a given chemical element
c_L ... lattice heat capacity (specific heat)
c_n, c_p ... heat capacity of electron gas and hole gas
d ... thickness, length
d_tun ... effective tunneling length
d_ox ... oxide thickness
f_T ... current gain cutoff frequency
f_max ... maximum frequency of oscillation
g_m ... transconductance
h ... *Planck* constant
$\hbar$ ... reduced *Planck* constant
k_B ... *Boltzmann* constant
l_g ... gatelength
m_0 ... free electron mass
$m_{n,p}$ ... relative masses of electrons and holes
$\mathbf{n}$ ... a normal vector
n ... electron concentration
n_i ... intrinsic concentration
p ... hole concentration
q ... elementary charge
t ... time
$v_{n,300}, v_{p,300}$ ... thermal velocities at 300 K for electrons and holes
$v_{sat,n}, v_{sat,p}$ ... electron and hole saturation velocities
w ... average electron energy
y^ref ... surface reference distance

List of Acronyms

ASIC	...	Application-Specific Integrated Circuit
BB	...	Band-to-Band tunneling
BGN	...	Bandgap Narrowing
BICMOS	...	Bipolar CMOS
BJT	...	Bipolar Junction Transistor
BTE	...	*Boltzmann* Transport Equation
CAD	...	Computer Aided Design
CML	...	Current-Mode Logic
CMOS	...	Complementary MOS
CPU	...	Central Processing Unit
CQFL	...	Continuous Quasi-*Fermi* Level
CVD	...	Chemical Vapor Deposition
DD	...	Drift-Diffusion
DHBT	...	Double Heterojunction Bipolar Transistor
DOS	...	Density of States
ECAD	...	Electronic CAD
ECL	...	Emitter-Coupled Logic
ET	...	Energy Transport
GSH	...	Global Self Heating
HBT	...	Heterojunction Bipolar Transistor
HD	...	Hydrodynamic
HEMT	...	High-Electron-Mobility Transistor
HFET	...	Heterostructure Field Effect Transistor
IC	...	Integrated Circuit
II	...	Impact Ionization
MC	...	Monte-Carlo
MESFET	...	Metal Semiconductor Field Effect Transistor
MMIC	...	Monolithic Microwave Integrated Circuit
MOCVD	...	Metal Organic Chemical Vapor Deposition
MOS	...	Metal Oxide Semiconductor
MOSFET	...	MOS Field Effect Transistor
PAE	...	Power-Added Efficiency
PHEMT	...	Pseudomorphic High-Electron-Mobility Transistor
RF	...	Radio Frequency
SH	...	Self Heating

SHBT	...	Single Heterojunction Bipolar Transistor
SIMS	...	Secondary Ion Mass Spectroscopy
SRH	...	*Shockley-Read-Hall*
TBB	...	Trap-assisted Band-to-Band tunneling
TCAD	...	Technology CAD
TE	...	Thermionic Emission
TFE	...	Thermionic Field Emission
USD	...	United States Dollars
VISTA	...	Viennese Integrated System for TCAD Applications

Chapter 1

Introduction

THE industrial revolution started with the invention of the steam engine and the loom. Two hundred years later, the invention of the first transistor in 1947, marked the beginning of the so-called second industrial revolution. The device was smaller, faster, more powerful, and had a longer lifetime than the tubes. For the invention of the bipolar transistor three researchers of the Bell Laboratories, namely William Shockley, John Bardeen, and Walter Brattain, were awarded a Nobel Price in 1956.

After the transistor had been invented, it was still necessary to solder the different parts of electronic circuits together. Jack Kilby of Texas Instruments was the first person to realize that the different components in a circuit could be integrated on a single piece of silicon. The successful laboratory demonstration of that first simple microchip in 1958, made history. Microelectronics was born, one of the fastest developing industrial branches today, with an annual turnover of more than 120 billion USD and supporting electronic market of more than 1000 billion USD. Especially fast is the market growth in the communications area (cellular phones, personal communications systems, wireless local communications networks, electronic traffic management). This is a driving driving force for the development of ever faster ICs including super-fast transistors.

In 1957 Herbert Kroemer of RCA proposed the first heterostructure, device that contains thin layers of different semiconductors stacked on top of each other. His theoretical work showed that heterostructure devices could offer superior performance compared with conventional transistors. In 1963 Herbert Kroemer and Zhores Alferov of the Ioffe Institute in Russia independently proposed ideas to build semiconductor lasers from heterostructure devices. Alferov built the first semiconductor laser from gallium arsenide and aluminium arsenide in 1969.

This year's Nobel Prize in Physics has been awarded to Kilby "for his part in the invention of the integrated circuits", and to Kroemer and Alferov "for developing semiconductor heterostructures used in high-speed- and opto-electronics."

The Heterojunction Bipolar Transistors (HBTs) are among the most advanced semiconductor devices. They match well today's requirements for high-speed operation, low power consumption, high-integration, low cost in large quantities, and operation capabilities in the frequency

range from 0.9 to 100 GHz. For example, III-V semiconductor group devices and circuits were always known by their high speed, but also by their expensive production and lower integration, compared to the silicon-based ones. Today, with III-V heterojunction MMICs in mass production on six-inch wafers in quantities 10 million and above, this is no longer a concern for the gallium-arsenide based HBTs. The silicon bipolar junction transistors (BJTs) have the benefits of the silicon technology, e.g. the high integration and low-cost production, but are restricted to lower frequencies. Important steps forward to faster silicon-based devices were the invention of the polysilicon emitter transistor and the silicon-germanium HBT, which are competitive in terms of speed to the III-V devices.

To cope with the explosive development costs of today's semiconductor industry Computer-Aided Design (CAD) methodologies are extensively used. Electronic CAD (ECAD) is concerned with the design of ICs above the device level. Technology CAD (TCAD) is devoted to the simulation of the fabrication process and operation behavior of a single or a small number of devices. Technology, device, and circuit simulation tools save expensive experimental efforts to obtain significant improvements of the device performance.

MINIMOS-NT is a two-dimensional device/circuit simulator used in the VISTA TCAD framework. A large part of the work presented in this thesis is on the development and the practical application of MINIMOS-NT.

The status of research regarding HBTs will be presented in Chapter 2. It includes a review of state-of-the-art devices, a discussion on the materials and material systems on which HBTs are based on, and a review of state-of-the-art device simulators, including MINIMOS-NT.

In Chapter 3 the physical modeling in MINIMOS-NT is presented. It contains models for the lattice, thermal, and transport properties of various semiconductor materials, as well as models for several important effects taking place in HBTs.

Chapter 4 contains the simulation results for several different types of GaAs-based and Si-based HBTs demonstrating the extended capabilities of MINIMOS-NT. Most of the results are verified against experimental data. The chapter also includes investigations which confirm the usefulness of device simulation for practical applications.

A summary and outlook conclude this work in Chapter 5.

Chapter 2

Status of Research

THE following chapter offers a review of state-of-the-art devices, a discussion on materials and material systems on which HBTs are based on, and a review of state-of-the-art device simulators, including the two-dimensional device simulator MINIMOS-NT.

2.1 State-of-the-art Heterostructure Devices

HBTs and HEMTs (High Electron Mobility Transistors) are among the most advanced semiconductor devices. They both benefit from the use of heterojunctions formed by different materials. Among other different material parameters, the most important is the bandgap difference. This is in contrast to conventional homojunction devices, where junctions are utilized by p-type or n-type doping in the same material. The HBTs make use of wide bandgap emitter and narrow bandgap base. In an npn-transistor this favors the electron injection from the emitter to the base, and restricts hole injection from the base to the emitter. This advantage can be maintained even if the base is highly doped to get a low base resistance and the emitter is lightly doped. Microwave, millimeter-wave, and high-speed digital HBT ICs are used for microwave power and low power wireless communications applications between 0.9 GHz and 100 GHz.

2.1.1 Why and Where SiGe HBTs?

The SiGe HBTs are double heterojunction bipolar transistors (DHBTs) as the SiGe material is used as a narrow bandgap material in the p-type base. The emitter and the collector are silicon and have larger bandgap.

Since the first SiGe HBTs reported in the late eighties [1] many groups were involved in the development of these devices [2, 3, 4]. Transit frequencies of 116 GHz [5] and 130 GHz [6], and maximum oscillation frequencies of 160 GHz [7, 8] were reported. The devices are fully compatible with the existing state-of-the-art 0.18 μm CMOS technology [9, 10]. Digital application-specific integrated circuits (ASICs) are combined with SiGe HBT circuits in the so-called SiGe BICMOS technology and are in volume production [11]. The SiGe HBT is considered an essential technology for over 10 Gb/s optical communication systems [12, 13]. However, a shortcome of Si-based HBTs is their comparatively lower breakdown voltage.

2.1.2   Why and Where III-V HBTs?

The AlGaAs/GaAs and InGaP/GaAs HBTs benefit from a single heterojunction formed between the AlGaAs wide bandgap emitter and the GaAs p-type base. InP/InGaAs and InAlAs/InGaAs grown on InP substrate gives double heterojunction devices as both emitter and collector regions include wide bandgap materials.

In terms of speed the III-V HBTs are among the fastest devices. Transit frequencies f_T of about 150 GHz and maximum oscillation frequencies f_{max} of more than 250 GHz [14, 15] were reported for HBTs on GaAs. Transfer substrate InAlAs/InGaAs HBTs on GaAs with f_T >250 GHz [16] and record InP-based HBTs with f_{max} >800 GHz were demonstrated [17] but they are still lacking level of integration (<1000 transistors per chip) compared to the GaAs-based HBTs. Table 2.1 summarizes state-of-the-art HBTs from different technologies with their impressive cutoff frequencies.

Substrate	Emitter/Base	f_T [GHz]	f_{max} [GHz]	References
GaAs	AlGaAs/GaAs	83	253	Matsushita, 1995 [18]
GaAs	AlGaAs/InGaAs	140	250	NEC, 1998 [14]
GaAs	InGaP/GaAs	156	256	Hitachi, 1998 [15]
(GaAs)	InAlAs/InGaAs	251	233	UC Santa Barbara, 1998 [16]
InP	InAlAs/InGaAs	162	820	UC Santa Barbara, 1999 [17]
InP	InP/GaAsSb	216	240	SFU Burnaby, 2000 [19]
Si	Si/SiGe	154	48	Hitachi, 2000[20]
		122	163	Hitachi, 2000[21]

Table 2.1: High-frequency properties of state-of-the-art HBTs

Heterostructure field-effect transistors HFETs, and especially HEMTs, cover higher frequencies (see Table 2.2), have higher PAE than III-V HBTs and show comparable breakdown voltages. However, their low level of integration (<100 transistors per chip) and >10% larger chip size lead to higher cost of production. In addition, the breakdown voltages cannot be so easily controlled as in HBTs, due to the influence of surface effects. The III-V market tendency in the last two years shows the increasing importance of HBTs (see Table 2.3). GaAs

Substrate	Channel	f_T [GHz]	f_{max} [GHz]	l_g [nm]	References
InP	lattice-matched	350	350	30	NTT, 1998 [22]
InP	pseudomorphic	340	250	50	Hughes, 1992 [23]
InP	graded	305	340	100	TRW, 1994 [24]
GaAs	metamorphic	204	188	180	UI Urbana, 1999 [25]
GaAs	metamorphic	188	312	150	DaimlerChrysler, 2000 [26]

Table 2.2: High-frequency properties of state-of-the-art HFETs

	MESFET	HEMT	HBT
1998	75%	8%	17%
2000	60%	10%	30%

Table 2.3: Shares of HBTs, HEMTs, and MESFETs on the III-V market

MESFETs and MESFET-based monolithic microwave integrated circuits (MMICs) are still key parts of the existing cellular phones, as they offer acceptable performance at a reasonable cost [27]. However, drawbacks are the need of double voltage supply and the large chip size. High PAE is needed to increase the battery lifetimes. HBTs are devices which at higher material cost offer high performance.

The III-V HBTs are considered essential for high-power amplifiers at 3 V power supply, as they offer high current amplification and PAE at 0.9/1.8 GHz [28]. A small chip-size 2 W MMIC based on AlGaAs/GaAs HBTs with record performance for wireless applications (62% PAE at 1.8 GHz) was demonstrated in [27]. Considering higher frequencies for future wireless applications InP-based and even SiGe MMICs with excellent performance, 48% and 24 % PAE respectively, at 25 GHz were recently reported [29, 30] (see Table 2.4).

Substrate	Emitter/Base	f_T/f_{max} [GHz]	Advantage	References
GaAs	AlGaAs/GaAs	--	62% PAE at 2 W	Siemens, 1998 [27]
InP	InGaAs/InAlAs	70/120	48% PAE at 25 GHz	TRW, 1999 [29]
InP	InP/InGaAs	116/169	40 Gb/s at 72 GHz	NTT, 1999 [25]
Si	Si/SiGe	--/60	ECL gate delay 5.5 ps	Hitachi, 2000 [21]
Si	Si/SiGe	50/50	24% PAE at 25 GHz	Daimler, 2000 [30]

Table 2.4: HBT IC applications

A further advantage of III-V HBTs is the low phase noise figure making them attractive for digital applications. Digital ICs with AlGaAs/GaAs and InP/InGaAs HBTs are used for fiber-optic transmission of 40 Gb/s and 60 Gb/s, respectively.

2.1.3 Future

Today's GaAs RF components are an indispensable part of all major new applications in wireless communication. They are not intended as a substitute for Si RF devices, but instead represent a valuable supplement covering about 15-20% of RF applications. The GaAs technology contributes to major system innovations in mobile telephones, satellite communication, short-haul communication as well as traffic security. The vision of a universal wireless personal communication system, combining PC, telephone, fax, e-mail, and also TV, will become reality in the very near future. All such applications require high-grade RF components in Si and GaAs materials. GaAs will dominate in applications which require very low noise figure, high linearity, and most importantly, very good PAE at low supply voltages (3V and below).

RF CMOS technology, whose transistors have 80 GHz f_T's using 0.12-micron geometries, is currently seen as a better platform for integration than SiGe, whose f_T's are only 50-70 GHz. However, the recent advances of the SiGe technology are projecting its very promising future.

InP technology already starts to address not only military, but commercial applications showing an unprecedented performance [31]. Although the actual operating speeds of fiber-optic

data links can be satisfied using GaAs technology, InP HBTs are the preferred solution for future generations up to 100 Gb/s [32].

2.2 State-of-the-art Device Simulation

With the shrinking of device dimensions and the replacement of hybrid mounted transistors by MMICs, device simulations and circuit simulations with distributed devices need to be carried out by state-of-the-art tools, accounting for physical effects on a microscopic level. Several questions during device fabrication, such as device optimization and process control, can today be addressed by device simulation.

To enable predictive simulation of semiconductor devices proper models describing carrier transport are required. The drift-diffusion (DD) transport model [33] is by now the most popular model used for device simulation. However, with down-scaling the feature sizes, non-local effects become more pronounced and must be accounted for by using energy-transport (ET) or hydrodynamic (HD) model [34].

During the last decade Monte-Carlo (MC) methods for solving the time-dependent Boltzmann equation have been developed [35, 36] and applied for device simulation [37, 38, 39]. However, the MC algorithms encounter serious difficulties when applied to the extreme conditions occurring in the advanced semiconductor devices. The carrier distribution can vary by several orders of magnitude in the space and energy domain of interest. Since the MC simulation follows the natural carrier histories, the portion of the simulated trajectories in a given region is proportional to the carrier density in this region. As a consequence, the major part of the simulation time is spent by trajectory computation in densely populated regions, while the statistics in the low density regions remain insufficient. A simple increase of the total simulation time cannot solve the problem within reasonable CPU time, if statistics in the rarely visited regions needs to be increased by orders of magnitude. Thus, reduction of computation time is still an issue and, therefore, the MC device simulation is still not feasible for industrial application.

2.2.1 Device Simulators

Several commercial tools, e.g. [40, 41], and university-developed simulators, e.g. [42, 43], have been successfully employed for device engineering applications. However, most of them were focused on silicon-based devices.

In contrast to the silicon industry, where process-, device-, and interconnect- simulation tools form a continuous virtual workbench from material analysis to chip design, III-V simulation mainly is focused on device and circuit aspects. The latter is accompanied by few examples for MESFET technology simulation tools developed in parallel to SUPREM e.g. [44]. For heterojunction devices, inclusively SiGe HBTs, due to the extensive number of process steps, device simulation is focused on process control and inverse modeling e.g. of geometry.

A common feature is the lack of a rigorous approach to III-V group semiconductor materials modeling. As an example, modeling of AlGaAs, InGaAs, or even InAlAs and InGaP is

restricted to slight modifications of the GaAs material properties. Another common drawback is the limited feedback from technological state-of-the-art process development to simulator development. Critical issues concerning simulation of heterostructures are mostly not considered, such as interface modeling at heterojunctions and insulator surfaces, as well as hydrodynamic and high field effects modeling - carrier energy relaxation, impact ionization, gate current modeling, self-heating effects, etc.

The two-dimensional device simulator PISCES [42], developed at the Stanford University, incorporates modeling capabilities for GaAs and InP based devices. One of its many modifications G-PISCES from Gateway Modeling [44] has been extended by a full set of III-V models. Examples of MESFETs, HEMTs, and HBTs for several material systems, e.g. InAlAs/InGaAs, AlGaAs/InGaAs, AlGaAs/GaAs, and InGaP/GaAs HBTs are demonstrated. Disadvantage of this simulator is the lack ET or HD transport model, necessary to model high-field effects, in comparison to the original version of PISCES.

The device simulator MEDICI from Avant! [45], which is also based on PISCES, offers simulation capabilities for SiGe/Si HBTs and AlGaAs/InGaAs/GaAs HEMTs. Advantages of this simulator are HD simulation capabilities and the rigorous approach to generation/recombination processes. In addition, recently an option treating anisotropic properties was announced. Next to III-Vs materials modeling this simulator has drawbacks in the interface modeling and in the capabilities of mixed-mode device-circuit simulation. However, it has been successfully used for the simulation of AlGaAs/GaAs HBTs [46].

The two- and three-dimensional device simulator DESSIS from ISE [40] has demonstrated a rigorous approach to semiconductor physics modeling. Some critical issues, as the above stated extensive trap modeling, are solved. Recently, first steps in direction of interface and III-V modeling have been reported [47].

Using a simplified one-dimensional current equation quasi-two-dimensional approaches are demonstrated, formerly by the University of Leeds e.g. [48]. This approach has also been verified for a number of examples and for gate-lengths down to 50 nm [49]. It is available as a submodule of Agilents Advanced Design System (ADS) delivering an interface to a microwave circuit simulator. The emphasis is put on the extraction of compact large-signal models. Examples of S-parameter simulations of AlGaAs/GaAs HEMTs have been presented. This tool combines the advantages of a full HD transport model combined with *Schrödinger* solution, but has the drawback of the simplified one-dimensional current equations.

A similar quasi-two-dimensional tool is Fast Blaze from Silvaco, also based on code from Leeds, which together with the two-dimensional ATLAS [50] has claimed the simulation of AlGaAs/GaAs and pseudomorphic AlGaAs/InGaAs/GaAs HEMTs. In addition, simulations of SiGe HBTs were announced, based on simulator originally developed at the University of Illmenau, PROSA [51]. In the latter no materials interfaces are considered.

A drawback of most simulators, similarly to III-V modeling, is that the modeling of SiGe is performed by slight modifications of the properties of Silicon. However, several authors

made use of them e.g. [52, 53, 54]. A considerable advance in the SiGe HBT simulation was achieved with SCORPIO [55].

2.2.2 MINIMOS-NT

The two-dimensional device simulator MINIMOS-NT [56] is an ancestor of the well-known MOS device simulator MINIMOS 6 [57]. MINIMOS-NT is a generic simulator accounting for a variety of materials, including group IV semiconductors, III-V compound semiconductors and their alloys, and non-ideal dielectrics. A stable base of material parameters for semiconductors of interest is extracted and used for device modeling issues. MINIMOS-NT is applicable to devices with high complexity in respect to materials, geometries, etc. allowing state-of-the-art simulations of MOS devices [58], HEMTs [59, 60, 61], SiGe HBTs [62], and III-V HBTs [63, 64]. The models are verified against statistically analyzed measured data.

In MINIMOS-NT the simulation domain is partitioned into independent regions, so-called segments. This partitioning is done with respect to the material class, e.g., contacts, insulators, and semiconductors. For these segments different sets of parameters, models and algorithms can be independently defined. When the simulation domain is properly split into segments, there are no abrupt changes of the material parameters within the segments. Abrupt variations of the material parameters should only occur at the interface of two adjoining segments.

Various important physical effects, such as bandgap narrowing, surface recombination, and self heating, are taken into account. Heat generated at the heterojunctions cannot completely leave the device, especially in the case of III-V semiconductor materials. Therefore, significant self-heating occurs in the device and leads to a change of the electrical device characteristics.

Emphasis was also laid on bandgap narrowing as one of the crucial heavy-doping effects to be considered for bipolar devices [65]. A new physically-based analytical bandgap narrowing model was developed, applicable to compound semiconductors, which accounts for semiconductor material, dopant species, and lattice temperature. As the minority carrier mobility is of considerable importance for bipolar transistors, a new universal low field mobility model has been implemented in MINIMOS-NT [66]. It is based on Monte-Carlo simulation results and distinguishes between majority and minority electron mobilities.

Energy transport equations are necessary to account for non-local effects, such as velocity overshoot [67, 68]. A new model for the electron energy relaxation time has been presented [69] which is based on Monte-Carlo simulation results and is applicable to all relevant semiconductors with diamond and zinc-blende structure. The energy relaxation times are expressed as functions of the carrier and lattice temperatures and, in the case of semiconductor alloys, of the material composition.

Considering the nature of the simulated devices (including abrupt SiGe/Si, InGaP/GaAs and AlGaAs/InGaP heterointerfaces) and the high electron temperatures observed at maximum bias sophisticated thermionic-field emission interface models [70] in conjunction with the hydrodynamic transport model are used. At the other (homogeneous or graded) interfaces continuous quasi-*Fermi* levels are assumed.

2.3   Semiconductor Materials

Based on their electrical properties solids can be classified as conductors, insulators, and semiconductors. Amorphous solids have little or no regular geometric arrangement of their atoms in space, and therefore, cannot be easily studied. Crystalline solids have a perfect periodic arrangement of atoms, which allows them to be easily analyzed. Polycrystalline solids have atom arrangements between these two extremes. Semiconductor materials are nearly perfect crystalline solids with small amount of imperfections, such as impurity atoms, lattice vacancies, or dislocations, which are sometimes intentionally introduced to alter their electrical characteristics [71]. Fig. 2.1 is a summary of the chemical elements involved in the formation of semiconductors.

Group II	*Group III*	*Group IV*	*Group V*	*Group VI*
	B **Boron** 5	C **Carbon** 6	N **Nitrogen** 7	O **Oxygen** 8
Mg **Magnesium** 12	Al **Aluminium** 13	Si **Silicon** 14	P **Phosphorus** 15	S **Sulphur** 16
Zn **Zinc** 30	Ga **Gallium** 31	Ge **Germanium** 32	As **Arsenic** 33	Se **Selenium** 34
Cd **Cadmium** 48	In **Indium** 49	Sn **Tin** 50	Sb **Antimony** 51	Te **Tellurium** 52
Hg **Mercury** 80	Tl **Thallium** 81			

III–V
II–VI

Fig. 2.1: Part of the Periodic Table showing the elements involved in the formation of semiconductors: The elements considered in MINIMOS-NT are highlighted by red background.

The semiconductors can be elemental, such as Si, Ge, and other chemical elements from group IV. They can be also compound, a combination between elements from group III and group V, or respectively, from group II and group VI. Examples for such combinations are the binary compounds $Ga^{III}As^V$ and $Zn^{II}S^{VI}$. There are also several combinations of practical importance, which involve two or more elements from the same chemical group. Such alloy semiconductors can be binary (e.g. $Si^{IV}Ge^{IV}$), ternary (e.g. $Al^{III}Ga^{III}As^V$), quaternary (e.g. $In^{III}Ga^{III}As^VP^V$), and even pentanary ($Ga^{III}In^{III}P^VSb^VAs^V$) materials.

2.3.1   Semiconductor Materials in MINIMOS-NT

One of the strong features of MINIMOS-NT as a generic device simulator is its capability to consider various semiconductor materials, such as III-V binary and ternary compounds,

and SiGe. The past modeling experience from Si MOS structures [72] and $Al_{0.2}Ga_{0.8}As/$
$In_{0.2}Ga_{0.8}As/GaAs$ HEMTs is inherited and preserved.

A large number of published theoretical and experimental reports have been reviewed to
include the physical parameters for the Si, Ge from chemical group IV, and GaAs, AlAs,
InAs, InP, or GaP, which are III-V chemical group binary compounds. All these materials
are named *basic materials* later in this work. The combination between two III-V binary
materials results in a ternary or a quaternary material. SiGe as a combination of Si and
Ge, together with the ternary III-V materials as a combination of the respective binary
materials are named *alloy materials* later in this work. An attempt has been made to allow
the user choose arbitrary mole fractions for the *alloy materials*, although the majority of
the simulations performed in this work include III-V compounds lattice-matched to GaAs
substrate. This not only gives the designer a good degree of freedom as to the choice of
material, but also allows a direct comparison between various devices such as AlGaAs/GaAs,
InGaP/GaAs, InP/InGaAs, InAlAs/InGaAs, and SiGe/Si HBTs, AlGaAs/InGaAs/GaAs
and InAlAs/InGaAs HEMTs, or SiGe/Si MOSFETs. However, due to the very limited
experimental data on some compound materials such as InGaP, InAlAs, InAsP, and GaAsP,
one has to consider interpolation schemes as the only available option to model the variation
of some parameters in a continuous range of mole fraction. In these cases, variations of
interpolation schemes are studied to find the best fit to the sometimes limited reported data
in the literature.

2.3.2 Modeling Concept

For all models in MINIMOS-NT the general approach is to employ universal models, i.e. the
same functional form to be used for all materials, just with different parameter sets. In models
for *alloy materials* the respective models for the two *basic materials* are employed first and
then combined as a function of the material composition x. Additionally, full consistency
between the *alloy materials* and the *basic materials* is obtained by having all the models
for *alloy materials* inheriting their model parameters from the models for *basic materials*.
Although it is arbitrary which of the two *basic materials* will correspond to a mole fraction
$x = 0$ and which to a mole fraction $x = 1$, a choice has to be done, e.g. InGaAs is used
for $In_xGa_{1-x}As$ and not for $In_{1-x}Ga_xAs$. The *alloy materials* $(A_{1-x}B_x)$ formed by the *basic
materials* (A and B) are summarized in Table 2.5.

	A	B	$A_{1-x}B_x$
SiGe	Si	Ge	$Si_{1-x}Ge_x$
AlGaAs	GaAs	AlAs	$Al_xGa_{1-x}As$
InGaAs	GaAs	InAs	$In_xGa_{1-x}As$
InAlAs	AlAs	InAs	$In_xAl_{1-x}As$
InAsP	InP	InAs	$InAs_xP_{1-x}$
GaAsP	GaAs	GaP	$GaAs_{1-x}P_x$
InGaP	InP	GaP	$Ga_xIn_{1-x}P$

Table 2.5: Mole fraction x in *alloy materials*

2.3.3 Interpolation Schemes

Material parameters of Si, Ge, GaAs, InP, GaP, InAs, and InGaAs, as well as to some extent SiGe and AlGaAs, have received considerable attention in the past and many experimental data and theoretical studies for these parameters can be found in the literature. On the other hand, the band structure and transport related parameters of other III-V ternary and all quaternary materials has been the topic of few or no experimental/theoretical publications. These facts necessitate the use of some interpolation scheme, essentially based on known values of the physical parameters for the related *basic materials* and *alloy materials*. In the cases when experimental data scatters the most consistent or most recent published data has been adopted. In the cases when experimental data is inconsistent or missing Monte-Carlo (MC) simulation has been considered. Although the interpolation scheme is still open to experimental or MC verifications, it provides more useful and reliable material parameters for numerical device simulation over the entire range of alloy composition.

For many parameters, such as various lattice parameters, a linear interpolation is sufficient. Some parameters, like the electronic bandgap exhibit a strong non-linearity with respect to the alloy composition which arises from the effects of alloy disorder. In such cases, a quadratic interpolation is used and a so-called bowing parameter is introduced. For other parameters, such as carrier mobility, a linear interpolation of the inverse values - *Mathiessen* rule - is used. Finally, there are parameters, such as thermal conductivity, for which none of the interpolation schemes mentioned so far is sufficient, and a quadratic interpolation of the inverse values together with an inverse bowing factor is proposed.

The bandgap bowing parameters of InAsP and GaAsP are believed to be much smaller than those of InGaP and InGaAs [73, 74]. Similarly, for parameters where data are lacking no bowing factors are assumed.

In the following chapter, the choice of interpolation formula will largely depend on factors such as required accuracy, the physical nature of the parameter, and available experimental or MC data. For example, the bandgap energy is the most critical parameter in device modeling and a slight variation in this parameter can significantly affect the terminal characteristics of the semiconductor device.

2.3.4 The Effect of Strain

A general aim when growing a device is to avoid lattice mismatch between the substrate and the epitaxial layers. A main concern is that the strain originating from such mismatch can relax and lead to misfit dislocations and even to amorphous structures. Therefore, only materials which lattice constants match the ones of GaAs or InP, typical substrate materials, gained attention. Such materials are AlGaAs in the whole composition range and $Ga_{0.51}In_{0.49}P$ grown on GaAs, and $In_{0.53}Ga_{0.47}As$ and $In_{0.52}Al_{0.48}As$ grown on InP. The quaternary GaInAsP can also match either GaAs or InP for certain mole fractions. However, if x is sufficiently low or the layer is sufficiently thin, it can preserve the substrate lattice constant, respectively, the strain. The result can be alteration of the bandgap, which can be beneficial sometimes, e.g. for SiGe grown on Si.

Chapter 3

Physical Models

3.1 Sets of Partial Differential Equations

IN MINIMOS-NT carrier transport can be treated either by the drift-diffusion (DD) or by the hydrodynamic (HD) transport models. For both carrier types the transport model can be chosen independently, or transport can even be neglected by assuming a constant quasi-*Fermi* level for one carrier type. In addition, the lattice temperature can be treated either as a constant or as an unknown governed by the lattice heat flow equation.

3.1.1 The Basic Semiconductor Equations

The basic equations solved in a device simulator are the *Poisson* equation and the continuity equations for electrons and holes.

$$\mathrm{div}(\varepsilon \cdot \mathrm{grad}\ \psi) = \mathrm{q} \cdot (n - p - C) \tag{3.1}$$

$$\mathrm{div}\ \mathbf{J}_n = \mathrm{q} \cdot \left(R + \frac{\partial n}{\partial t} \right) \tag{3.2}$$

$$\mathrm{div}\ \mathbf{J}_p = -\mathrm{q} \cdot \left(R + \frac{\partial p}{\partial t} \right) \tag{3.3}$$

The unknown quantities of this equation system are the electrostatic potential, ψ, and the electron and hole concentrations, n and p, respectively. C denotes the net concentration of the ionized dopants and other charged defects, ε is the dielectric permittivity of the semiconductor, and R is the net recombination rate.

3.1.2 The Drift-Diffusion Transport Model

The drift-diffusion current relations can, amongst others, be derived from the *Boltzmann* transport equation by the method of moments [33] or from basic principles of irreversible thermodynamics [75]. The electron and hole current densities are given by

$$\mathbf{J}_n = \mathrm{q} \cdot \mu_n \cdot n \cdot \left(\mathrm{grad}\left(\frac{E_C}{\mathrm{q}} - \psi \right) + \frac{\mathrm{k_B}}{\mathrm{q}} \cdot \frac{N_{C,0}}{n} \cdot \mathrm{grad}\left(\frac{n \cdot T_\mathrm{L}}{N_{C,0}} \right) \right), \tag{3.4}$$

$$\mathbf{J}_p = \mathrm{q} \cdot \mu_p \cdot p \cdot \left(\mathrm{grad}\left(\frac{E_V}{\mathrm{q}} - \psi \right) - \frac{\mathrm{k_B}}{\mathrm{q}} \cdot \frac{N_{V,0}}{p} \cdot \mathrm{grad}\left(\frac{p \cdot T_\mathrm{L}}{N_{V,0}} \right) \right). \tag{3.5}$$

These current relations account for position-dependent band edge energies, E_C and E_V, and for position-dependent effective masses, which are included in the effective density of states, $N_{C,0}$ and $N_{V,0}$. The index 0 indicates that $N_{C,0}$ and $N_{V,0}$ are evaluated at some (arbitrary) reference temperature, T_0, which is constant in real space regardless of what the local values of the lattice and carrier temperatures are.

3.1.3 The Hydrodynamic Transport Model

In the hydrodynamic transport model, carrier temperatures are allowed to be different from the lattice temperature. The basic equations (3.1) through (3.3) are augmented by energy balance equations which determine the carrier temperatures. The current relations take the form

$$\mathbf{J}_n = q \cdot \mu_n \cdot n \cdot \left(\operatorname{grad} \left(\frac{E_C}{q} - \psi \right) + \frac{k_B}{q} \cdot \frac{N_{C,0}}{n} \cdot \operatorname{grad} \left(\frac{n \cdot T_n}{N_{C,0}} \right) \right), \tag{3.6}$$

$$\mathbf{J}_p = q \cdot \mu_p \cdot p \cdot \left(\operatorname{grad} \left(\frac{E_V}{q} - \psi \right) - \frac{k_B}{q} \cdot \frac{N_{V,0}}{p} \cdot \operatorname{grad} \left(\frac{p \cdot T_p}{N_{V,0}} \right) \right). \tag{3.7}$$

The energy balance equations state conservation of the average carrier energies. In terms of the carrier temperatures T_n and T_p they can be written as

$$\operatorname{div} \mathbf{S}_n = \operatorname{grad} \left(\frac{E_C}{q} - \psi \right) \cdot \mathbf{J}_n - \frac{3 \cdot k_B}{2} \cdot \left(\frac{\partial (n \cdot T_n)}{\partial t} + R \cdot T_n + n \cdot \frac{T_n - T_L}{\tau_{\epsilon,n}} \right), \tag{3.8}$$

$$\operatorname{div} \mathbf{S}_p = \operatorname{grad} \left(\frac{E_V}{q} - \psi \right) \cdot \mathbf{J}_p - \frac{3 \cdot k_B}{2} \cdot \left(\frac{\partial (p \cdot T_p)}{\partial t} + R \cdot T_p + p \cdot \frac{T_p - T_L}{\tau_{\epsilon,p}} \right). \tag{3.9}$$

Here, $\tau_{\epsilon,n}$ and $\tau_{\epsilon,p}$ denote the energy relaxation times, while $\mathbf{S}_n$ and $\mathbf{S}_p$ are the energy fluxes.

$$\mathbf{S}_n = -\kappa_n \cdot \operatorname{grad} T_n - \frac{5}{2} \cdot \frac{k_B \cdot T_n}{q} \cdot \mathbf{J}_n \tag{3.10}$$

$$\mathbf{S}_p = -\kappa_p \cdot \operatorname{grad} T_p + \frac{5}{2} \cdot \frac{k_B \cdot T_p}{q} \cdot \mathbf{J}_p \tag{3.11}$$

The carrier thermal conductivities, κ_n and κ_p, are assumed to obey a generalized *Wiedemann-Franz* law.

$$\kappa_n = \left(\frac{5}{2} + c_n \right) \cdot \frac{k_B^2}{q} \cdot T_n \cdot \mu_n \cdot n \tag{3.12}$$

$$\kappa_p = \left(\frac{5}{2} + c_p \right) \cdot \frac{k_B^2}{q} \cdot T_p \cdot \mu_p \cdot p \tag{3.13}$$

The heat capacities c_n and c_p are usually neglected ($c_n = c_p = 0$).

Strictly speaking, the model described above in this subsection represents an energy transport (ET) model. Such a model is obtained when in the course of deriving the moment equations the average kinetic energy is consequently neglected against the thermal energy, assuming that $\frac{1}{2} \cdot m_\nu \cdot v_\nu^2 \ll k_B \cdot T_\nu$. Since in the literature the terms *energy transport* and *hydrodynamic transport* are often used synonymously, and since during the development of MINIMOS-NT the term *hydrodynamic transport* was used, this notation is retained throughout this work.

3.1.4 The Lattice Heat Flow Equation

MINIMOS-NT accounts for self-heating effects in semiconductor devices by solving the lattice heat flow equation self-consistently with the DD or HD transport equations, forming together a system of four, or respectively six, partial differential equations.

$$\text{div } \mathbf{S}_{L} = -\rho_{L} \cdot c_{L} \cdot \frac{\partial T_{L}}{\partial t} + H \tag{3.14}$$

$$\mathbf{S}_{L} = -\kappa_{L} \cdot \text{grad } T_{L} \tag{3.15}$$

In (3.14) T_{L} denotes the lattice temperature, t is the time variable, and H is the heat generation term. The coefficients ρ_{L}, c_{L}, and κ_{L} are the mass density, specific heat, and thermal conductivity of the respective materials.

The model for the heat generation, H, depends on the transport model used. In the drift-diffusion case H equals the *Joule* heat,

$$H = \text{grad}\left(\frac{E_{C}}{q} - \psi\right) \cdot \mathbf{J}_{n} + \text{grad}\left(\frac{E_{V}}{q} - \psi\right) \cdot \mathbf{J}_{p} + R \cdot (E_{C} - E_{V}), \tag{3.16}$$

whereas in the hydrodynamic case the relaxation terms are used

$$H = \frac{3 \cdot k_{B}}{2} \cdot \left(n \cdot \frac{T_{n} - T_{L}}{\tau_{\epsilon,n}} + p \cdot \frac{T_{p} - T_{L}}{\tau_{\epsilon,p}}\right) + R \cdot (E_{C} - E_{V}). \tag{3.17}$$

3.1.5 The Insulator Equations

In insulating materials only the *Poisson* equation (3.1) and the lattice heat flow equation (3.14) are solved. The presence of doping and mobile carriers is neglected ($n = p = C = 0$), therefore the carrier continuity equations are not solved. This assumption leads to the reduction of (3.1) to the *Laplace* equation (3.18) and the neglecting of the heat generation term of (3.14), which is invoked for semiconductor segments only.

$$\text{div}(\varepsilon \cdot \text{grad } \psi) = 0 \tag{3.18}$$

$$\text{div}(\kappa_{L} \cdot \text{grad } T_{L}) = \rho_{L} \cdot c_{L} \cdot \frac{\partial T_{L}}{\partial t} \tag{3.19}$$

Thus, as a result no currents flow through insulators and the influence of the charges inside the insulators is neglected. This assumptions can be neglected, in case of the insulator is treated as a semiconductor material. This approach was successfully applied to $Si_{3}N_{4}$ and shall be illustrated later in this work. Another approach is the consideration of charges at the semiconductor/insulator interface, which is discussed in the next subsection.

3.1.6 Boundary Conditions

The basic semiconductor equations are posed in a bounded domain. At the boundaries of this domain appropriate boundary conditions need to be specified for the unknowns ψ, n, p, T_{n}, T_{p}, and T_{L}.

Artificial Boundaries

In order to separate the simulated device from neighboring devices, artificial boundaries must be specified which are not boundaries in a physical sense. The *Neumann* boundary condition guarantees that the simulation domain is self-contained and there are no fluxes across the boundary.

$$\mathbf{n} \cdot \mathbf{E} = 0, \quad \mathbf{n} \cdot \mathbf{J}_{n,p} = 0, \quad \mathbf{n} \cdot \mathbf{S}_{n,p} = 0, \quad \mathbf{n} \cdot \mathbf{S}_{\mathrm{L}} = 0 \tag{3.20}$$

$$\mathbf{n} \cdot \mathbf{E} = 0, \quad \mathbf{n} \cdot \mathbf{S}_{\mathrm{L}} = 0 \tag{3.21}$$

Here, $\mathbf{n}$ denotes an outward oriented vector normal to the boundary. (3.20) and (3.21) give the boundary conditions at the artificial boundaries for semiconductor and insulator segments, respectively.

Semiconductor-Metal Boundaries

Ohmic Contact
At Ohmic contacts simple *Dirichlet* boundary conditions apply. The contact potential φ_{s}, the carrier contact concentrations n_s and p_s, and in the HD simulation case, the contact carrier temperatures T_n and T_p are fixed. The metal quasi-*Fermi* level (which is specified by the contact voltage φ_{m}) is equal to the semiconductor quasi-*Fermi* level. The contact potential at the semiconductor boundary reads

$$\varphi_{\mathrm{s}} = \varphi_{\mathrm{m}} + \psi_{\mathrm{bi}}. \tag{3.22}$$

The built-in potential ψ_{bi} is calculated after [76]

$$
\begin{aligned}
\psi_{\mathrm{bi}} &= \frac{\mathrm{k_B} \cdot T_{\mathrm{L}}}{\mathrm{q}} \cdot \ln\left(\frac{1}{2 \cdot C_1} \cdot \left(C + \sqrt{C^2 + 4 \cdot C_1 \cdot C_2} \right) \right) \\
&= -\frac{\mathrm{k_B} \cdot T_{\mathrm{L}}}{\mathrm{q}} \cdot \ln\left(\frac{1}{2 \cdot C_2} \cdot \left(-C + \sqrt{C^2 + 4 \cdot C_1 \cdot C_2} \right) \right),
\end{aligned}
\tag{3.23}
$$

Here, C is the net concentration of dopants and other charged defects at the contact boundary. The auxiliary variables C_1 and C_2 are defined by

$$C_1 = N_C \cdot \exp\left(\frac{-E_C}{\mathrm{k_B} \cdot T_{\mathrm{L}}} \right), \quad C_2 = N_V \cdot \exp\left(\frac{E_V}{\mathrm{k_B} \cdot T_{\mathrm{L}}} \right) \tag{3.24}$$

The carrier concentrations in the semiconductor are pinned to the equilibrium carrier concentrations at the contact. They are expressed as

$$n_s = N_C \cdot \exp\left(\frac{-E_C + \mathrm{q} \cdot \psi_{\mathrm{bi}}}{\mathrm{k_B} \cdot T_{\mathrm{L}}} \right) \tag{3.25}$$

$$p_s = N_V \cdot \exp\left(\frac{E_V - \mathrm{q} \cdot \psi_{\mathrm{bi}}}{\mathrm{k_B} \cdot T_{\mathrm{L}}} \right) \tag{3.26}$$

The carrier temperatures T_n and T_p are set equal to the lattice temperature T_{L}.

$$T_n = T_{\mathrm{L}}, \quad T_p = T_{\mathrm{L}} \tag{3.27}$$

In the case of a thermal contact the lattice temperature T_L is calculated using a specified contact temperature T_C and thermal resistance R_T. The thermal heat flow density $\mathbf{S}_L$ at the contact boundary reads:

$$\mathbf{n} \cdot \mathbf{S}_L = \frac{T_L - T_C}{R_T} \tag{3.28}$$

In case no thermal resistance is specified an isothermal boundary condition is assumed and the lattice temperature T_L is set equal to the contact temperature T_C.

$$T_L = T_C \tag{3.29}$$

In the case of DD simulation with self-heating an additional thermal energy is accounted for. This thermal energy is produced when the carriers have to surmount the potential difference between the conduction or valence band and the metal quasi-*Fermi* level. The energy equation reads:

$$\mathbf{J}_n \cdot \left(\frac{E_C}{q} + \varphi_m \right) + \mathbf{J}_p \cdot \left(\frac{E_V}{q} + \varphi_m \right) = \mathrm{div}_A\ \mathbf{S}_L \tag{3.30}$$

The expression $\mathrm{div}_A(\mathbf{S}_L)$ denotes the surface divergence of the thermal heat flux at the considered boundary. In the case of HD simulation with self-heating the thermal heat flow across the boundary is accounted for self-consistently.

Schottky Contact

At the Schottky contact mixed boundary conditions apply. The contact potential φ_s, the carrier contact concentrations n_s and p_s, and in the HD simulation case, the contact carrier temperatures T_n and T_p are fixed. The semiconductor contact potential is the difference of the metal quasi-*Fermi* level (which is specified by the contact voltage φ_m) and the metal workfunction difference potential φ_w.

$$\varphi_s = \varphi_m - \varphi_w, \quad \text{where} \quad \varphi_w = -\frac{E_w}{q} \tag{3.31}$$

The difference between the conduction band energy E_C and the metal workfunction energy gives the workfunction difference energy E_w which is the so-called barrier height of the Schottky contact. The applied boundary conditions are

$$\mathbf{n} \cdot \mathbf{J}_n = -q \cdot v_n \cdot (n - n_s) \qquad\qquad \mathbf{n} \cdot \mathbf{J}_p = q \cdot v_p \cdot (p - p_s) \tag{3.32}$$

Here v_n and v_p are the thermionic recombination velocities. The carrier concentrations are expressed as

$$n_s = N_C \cdot \exp\left(\frac{-E_C - E_w}{k_B \cdot T_L} \right) \qquad\qquad p_s = N_V \cdot \exp\left(\frac{E_V - E_w}{k_B \cdot T_L} \right) \tag{3.33}$$

The default values for v_n and v_p are set to 0 (see Table 3.1) which suppresses current flow through the Schottky contact ($\mathbf{n} \cdot \mathbf{J}_{n,p} = 0$).

The Schottky contact boundary conditions for the carrier temperatures T_n and T_p and the lattice temperature T_L are similar to the ones which apply for the Ohmic contact, i.e. (3.27) and (3.28), or respectively (3.29).

Material	E_w [eV]	v_n [m/s]	v_p [m/s]
n-Si/Au	-0.55	0.0	0.0
p-Si/Au	0.55	0.0	0.0
others	0.0	0.0	0.0

Table 3.1: Parameter values for Schottky contact model

Polysilicon Contact

In MINIMOS-NT the polysilicon contact model after [77] is implemented. The dielectric flux D through the oxide reads

$$\mathbf{n} \cdot \mathbf{D} = -\frac{\varepsilon_{\mathrm{ox}}}{d_{\mathrm{ox}}} \cdot V_{\mathrm{ox}} \tag{3.34}$$

where V_{ox} is the voltage drop over the thin oxide layer which is introduced between polysilicon and silicon, $\varepsilon_{\mathrm{ox}}$ and d_{ox} denote respectively the permittivity and thickness of this layer. The electron and hole current densities across the contact interface read

$$\mathbf{n} \cdot \mathbf{J}_n = \sigma_{\mathrm{ox}} \cdot V_{ox} \qquad\qquad \mathbf{n} \cdot \mathbf{J}_p = \mathrm{q} \cdot p \cdot S_p \tag{3.35}$$

where σ_{ox} is the oxide conductivity, p is the hole concentration in the semiconductor, and S_p is the hole surface recombination velocity. V_{ox} depends on the quasi-*Fermi* level in the metal (which is specified by the contact voltage φ_{m}), the potential in the semiconductor φ_{s}, and the built-in potential ψ_{bi}.

$$V_{\mathrm{ox}} = \varphi_{\mathrm{s}} - \varphi_{\mathrm{m}} - \psi_{\mathrm{bi}}. \tag{3.36}$$

The polysilicon contact boundary conditions for the carrier temperatures T_n and T_p and the lattice temperature T_{L} are similar to the ones which apply for the Ohmic contact, i.e. (3.27) and (3.28), or respectively (3.29).

Insulator-Metal Boundaries

In the case of insulator-metal boundaries a model similar to the Schottky contact model is used to calculate the insulator contact potential. The semiconductor contact potential is the difference of the metal quasi-*Fermi* level (which is specified by the contact voltage φ_{m}) and the metal workfunction difference potential Φ_{ms}.

$$\varphi_{\mathrm{s}} = \varphi_{\mathrm{m}} - \Phi_{\mathrm{ms}}, \quad \text{where} \quad \Phi_{\mathrm{ms}} = -\frac{E_{\mathrm{w}}}{\mathrm{q}} \tag{3.37}$$

Again, E_{w} is the workfunction difference energy. The lattice temperature is set equal to the contact temperature (3.29).

Semiconductor-Insulator Interface

In the absence of surface charges at the semiconductor-insulator interface the normal component of the dielectric displacement is continuous, and so is the potential.

$$\mathbf{n} \cdot \varepsilon_{\mathrm{s}} \cdot \mathbf{E}_{\mathrm{s}} - \mathbf{n} \cdot \varepsilon_{\mathrm{ins}} \cdot \mathbf{E}_{\mathrm{ins}} = 0, \qquad \varphi_{\mathrm{s}} = \varphi_{\mathrm{ins}} \tag{3.38}$$

In the presence of surface charges along the interface the dielectric displacement obeys the law of *Gauß*

$$\mathbf{n} \cdot \varepsilon_{\mathrm{s}} \cdot \mathbf{E}_{\mathrm{s}} - \mathbf{n} \cdot \varepsilon_{\mathrm{ins}} \cdot \mathbf{E}_{\mathrm{ins}} = \sigma_{\mathrm{s}}. \tag{3.39}$$

At the semiconductor-insulator interface the carrier current densities (or driving forces) and the carrier heat fluxes normal to the interface vanish.

$$\mathbf{n} \cdot \mathbf{J}_{n,p} = 0, \quad \text{i.e.} \quad \mathbf{n} \cdot \mathbf{F}_{n,p} = 0 \tag{3.40}$$

$$\mathbf{n} \cdot \mathbf{S}_{n,p} = 0 \tag{3.41}$$

The lattice temperature at the interface is continuous.

Insulator-Insulator Interface

Similarly to the semiconductor-insulator interface (3.38) or (3.39) apply depending on the presence of surface charges. The lattice temperature must be continuous.

Semiconductor-Semiconductor Interface

The calculation of the electrostatic potential at interfaces between two semiconductor segments is similar to the one at semiconductor-insulator interfaces.

$$\varphi_{\mathrm{s1}} = \varphi_{\mathrm{s2}} \tag{3.42}$$

$$\mathbf{n} \cdot \varepsilon_{\mathrm{s1}} \cdot \mathbf{E}_{\mathrm{s1}} - \mathbf{n} \cdot \varepsilon_{\mathrm{s2}} \cdot \mathbf{E}_{\mathrm{s2}} = \sigma_{\mathrm{s}}. \tag{3.43}$$

Here σ_{s} is the interface charge density which can be zero or non-zero. The subscripts are used to distinguish between the two semiconductor segments on both sides of the interface.

To calculate the carrier concentrations and the carrier temperatures at the interface of two semiconductor segments three different models are considered These are a model with continuous quasi-*Fermi* level across the interface (CQFL), a thermionic emission model (TE), and a thermionic field emission model (TFE). The derivation of these models is given in [78]. Each model can be specified separately for electrons and holes for each semiconductor-semiconductor interface.

In the following J denotes the current density, S the energy flux density, and ΔE_ν the difference in the conduction or valence band edges, respectively. The carrier concentration is denoted by ν. The subscripts denote the semiconductor segment and the carrier type.

Continuous Quasi-*Fermi* Level Model

$$\nu_2 = \nu_1 \cdot \left(\frac{m_{\nu 2}}{m_{\nu 1}}\right)^{3/2} \cdot \exp\left(-\frac{\Delta E_\nu}{k_{\mathrm{B}} \cdot T_{\nu 1}}\right) \tag{3.44}$$

$$T_{\nu 2} = T_{\nu 1} \tag{3.45}$$

Thermionic Field Emission Model

$$J_{\nu 2} = J_{\nu 1} \tag{3.46}$$

$$J_{\nu 2} = q \cdot \left(v_{\nu 2} \cdot \nu_2 - \frac{m_{\nu 2}}{m_{\nu 1}} \cdot v_{\nu 1} \cdot \nu_1 \cdot \exp\left(-\frac{\Delta E_\nu - \delta E_\nu}{k_B \cdot T_{\nu 1}} \right) \right) \tag{3.47}$$

$$S_{\nu 2} = S_{\nu 1} - \frac{1}{q} \cdot (\Delta E_\nu - \delta E_\nu) \cdot J_{\nu 2} \tag{3.48}$$

$$S_{\nu 2} = -\left(k_B \cdot T_{\nu 2} \cdot v_{\nu 2} \cdot \nu_2 - \frac{m_{\nu 2}}{m_{\nu 1}} \cdot k_B \cdot T_{\nu 1} \cdot v_{\nu 1} \cdot \nu_1 \cdot \exp\left(-\frac{\Delta E_\nu - \delta E_\nu}{k_B \cdot T_{\nu 1}} \right) \right) \tag{3.49}$$

with the thermionic emission velocity (3.50) and the barrier height lowering (3.51).

$$v_{\nu i} = \sqrt{\frac{2 \cdot k_B \cdot T_{\nu i}}{\pi \cdot m_{\nu i}}} \tag{3.50}$$

$$\delta E_\nu = \begin{cases} q \cdot E_{\perp 2} \cdot d_{tun}, & E_{\perp 2} > 0 \\ 0, & E_{\perp 2} \le 0 \end{cases} \tag{3.51}$$

The barrier height lowering depends on the electric field orthogonal to the interface $E_{\perp 2}$ and the effective tunneling length d_{tun}. For $\delta E_\nu = 0$ the TFE model reduces to the TE model.

By using the CQFL model a *Dirichlet* interface condition is applied. The carrier concentrations are directly determined in a way that the quasi-*Fermi* level across the interface remains continuous. The model is suitable for use at homojunctions. However, it is erroneous to assume continuous quasi-*Fermi* levels at abrupt heterojunctions. Also the bandgap alignment of the adjustent semiconductors is ignored when such continuous condition is enforced. Therefore, models using a *Neumann* interface condition, like the TFE model or the TE model, which determine the current flux across the interface, must be used. Modeling the electron and hole current as well as the energy flux across heterointerfaces is a complex task. Several models for different types of interfaces have been proposed [79, 80, 81, 82]. The TE model is commonly used to model the current across heterojunctions of compound semiconductors. The TFE model extends the TE model by accounting for tunneling effects through the heterojunction barrier by introducing a field dependent barrier height lowering. In [83] a method for unified treatment of interface models was presented. It allows a change of the interface condition from *Neumann* to *Dirichlet* type in the limit case of very strong barrier reduction due to tunneling.

Semiconductor-Semiconductor Thermal Interface
The lattice temperature is assumed to be continuous across semiconductor-semiconductor interfaces. In the case of DD simulation with self-heating an additional thermal energy is accounted for at heterojunction interfaces. This thermal energy is produced when the carriers have to surmount the energy difference in the conduction and valence bands, ΔE_C and ΔE_V, respectively. The energy equation reads:

$$\frac{\mathbf{J}_n}{q} \cdot \Delta E_C + \frac{\mathbf{J}_p}{q} \cdot \Delta E_V = \mathrm{div}_A (\mathbf{S}_L) \tag{3.52}$$

The expression $\mathrm{div}_A (\mathbf{S}_L)$ denotes the surface divergence of the thermal heat flux at the considered boundary. In the case of HD simulation with self-heating the thermal heat flow across the boundary is accounted for self-consistently.

3.2 Lattice and Thermal Properties

The semiconductor equations discussed in the previous section contain several important physical parameters. Accurate models for these parameters are crucial for successful device simulation. Lattice properties, such as the lattice constant, relative permittivity ε_r, and mass density ρ are already well determined for important semiconductors. Others, such as thermal conductivity and heat capacity, have been studied at room temperature. Due to the importance of these parameters for device simulation they are discussed in the following section. These are parameters of the *Poisson* equation (3.1) and the lattice heat flow equation (3.14), which are solved not only in the semiconductor, but also in the insulating materials. Therefore, models for important insulating materials, such as SiO_2 and Si_3N_4, are also presented.

3.2.1 Permittivity

The dielectric constant or relative permittivity ε_r is one of the basic properties of semiconductor and insulating materials. The data reported in literature shows minor discrepancies about the values of this parameter (see Table 3.2). The temperature dependence, if any at all, can be neglected. Recently, insulating materials with high dielectric constants (high-k materials) attract much interest as possible replacement of the gate oxide (SiO_2) in MOSFETs in order to avoid tunneling gate leakage currents. Table 3.2 includes in addition some of these materials.

Material	Default ε_r	Reported Range	References
Si	11.9	11.7 - 11.9	[84, 85, 86]
Ge	16.0	16.0 - 16.2	[85, 86]
GaAs	13.1	12.9 - 13.18	[87, 88, 73, 89]
AlAs	10.1	10.06 - 10.1	[90, 91, 89, 92, 93]
InAs	14.6	14.55 - 15.15	[88, 73, 93, 94]
InP	12.4	12.35 - 12.61	[95, 96, 93, 94]
GaP	11.1	11.1	[73, 90, 91]
SiO_2	3.9	3.75 - 3.9	[97, 86]
Si_3N_4	7.4	6.0 - 8.0	[98, 86]
$BaSrTiO_3$	200.0	60.0 - 300.0	[99, 100, 101]
Ta_2O_5	30.0	20.0 - 75.0	[99, 100]
TiO_2	20.0	4.0 - 100.0	[99, 100]
Al_2O_3	9.8	8.5 - 13.0	[100, 101]

Table 3.2: Parameter values for the relative permittivity

The permittivities of *alloy materials* $A_{1-x}B_x$ are interpolated from the values of the *basic materials* as a quadratic function of x [73].

$$\varepsilon_r^{AB} = (1-x) \cdot \varepsilon_r^A + x \cdot \varepsilon_r^B + x \cdot (1-x) \cdot C_\varepsilon \tag{3.53}$$

C_ε is referred to as a nonlinear or bowing parameter. Setting $C_\varepsilon = 0$ yields a linear interpolation. The parameters used in this model are summarized in Table 3.3.

Material	C_ε	Reported Range	References
SiGe	0.0		
AlGaAs	0.0		
InGaAs	-1.0	13.1-14.1	[102, 93] x=0.53
InAlAs	-1.0	12.46	[102] x=0.52
InAsP	0.0		
GaAsP	0.0		
InGaP	0.0	11.75	[103] x=0.51

Table 3.3: Parameter values for the permittivity bowing factor

3.2.2 Mass Density

The values of the mass densities of the *basic materials* are well-known, and are used to model the values for *alloy materials*. A linear change between the values of *basic materials* is used.

$$\rho_{\mathrm{L}}^{\mathrm{AB}} = (1 - x) \cdot \rho^{\mathrm{A}} + x \cdot \rho^{\mathrm{B}} \tag{3.54}$$

The parameter values used are summarized in Table 3.4.

Material	ρ [g/cm^3]	Reported Range	References
Si	2.33	2.238 - 2.239	[90, 85, 86]
Ge	5.327	5.3234- 5.3267	[90, 85]
GaAs	5.32	5.307 - 5.36	[87, 84, 104]
AlAs	3.76	3.76	[84, 104]
InAs	5.667	5.667	[88, 84, 73]
InP	4.81	4.79-4.81	[96, 84, 73]
GaP	4.138	4.13-4.14	[84, 73]
SiO$_2$	2.203	2.2 - 2.207	[85, 86]
Si$_3$N$_4$	3.1	3.1	[85, 86]

Table 3.4: Parameter values for mass density

3.2.3 Thermal Conductivity

The temperature dependence of κ_{L} of the *basic materials* and insulators is modeled by a simple power law

$$\kappa_{\mathrm{L}}(T_{\mathrm{L}}) = \kappa_{300} \cdot \left(\frac{T_{\mathrm{L}}}{300 \ \mathrm{K}}\right)^{\alpha} \tag{3.55}$$

where κ_{300} is the value for the thermal conductivity at 300 K. This approximation is in good agreement with experimental data [105, 106, 107, 108], as presented in Fig. 3.1 and Fig. 3.2 where comparisons in the temperature range from 300 K to 800 K. The parameter values used are summarized in Table 3.5.

In the case of *alloy materials* $\mathrm{A}_{1-x}\mathrm{B}_x$, κ_{L} varies between the values of the basic materials (A and B). A harmonic mean is used to model κ_{300}. An additional bowing factor C_κ is introduced in order to account for the drastic reduction of the thermal conductivity with the

Material	κ_{300} [W/K m]	α	Reported κ_{300} [W/K m]	References
Si	148	-1.65	150	[85, 86]
Ge	60	-1.25	60	[85, 86]
GaAs	46	-1.25	45.5-46	[108, 92, 85, 86]
AlAs	80	-1.37	80	[108]
InAs	27.3	-1.1	27.3-48	[108, 92]
InP	68	-1.4	68	[108, 92]
GaP	77	-1.4	77	[108, 92]
SiO$_2$	1.38	0.33	1.4	[85, 86]
Si$_3$N$_4$	18.5	0.33	15-27	[98]

Table 3.5: Parameter values for thermal conductivity

increase of material composition x. The exponent α is linearly interpolated because of lack of experimental data at temperatures other than 300 K.

$$\kappa_{300}^{AB} = \frac{1}{\left(\dfrac{1-x}{\kappa_{300}^{A}} + \dfrac{x}{\kappa_{300}^{B}} + \dfrac{(1-x) \cdot x}{C_\kappa}\right)} \tag{3.56}$$

$$\alpha^{AB} = (1-x) \cdot \alpha^A + x \cdot \alpha^B \tag{3.57}$$

The parameter values used are summarized in Table 3.6.

Material	C_κ [W/K m]
SiGe	2.8
AlGaAs	3.3
InGaAs	1.4
InAlAs	3.3
InAsP	3.3
GaAsP	1.4
InGaP	1.4

Table 3.6: Parameter values for thermal conductivity bowing factor

In Fig. 3.3 and Fig. 3.4 comparisons between data from [106, 107, 108, 109, 110, 111] and the results obtained with our model are shown for the thermal conductivity in *alloy materials* at 300 K.

3.2.4 Specific heat

The specific heat capacity c_L is modeled by

$$c_L(T_L) = c_{300} + c_1 \cdot \frac{\left(\dfrac{T_L}{300 \text{ K}}\right)^\beta - 1}{\left(\dfrac{T_L}{300 \text{ K}}\right)^\beta + \dfrac{c_1}{c_{300}}}. \tag{3.58}$$

c_{300} is the value for the specific heat at 300 K [92]. The model is used for the *basic materials* and for insulators. In Fig. 3.5, Fig. 3.6, and Fig. 3.7 we present comparisons between experimental data and the results obtained with our model for the specific heat. Note the excellent
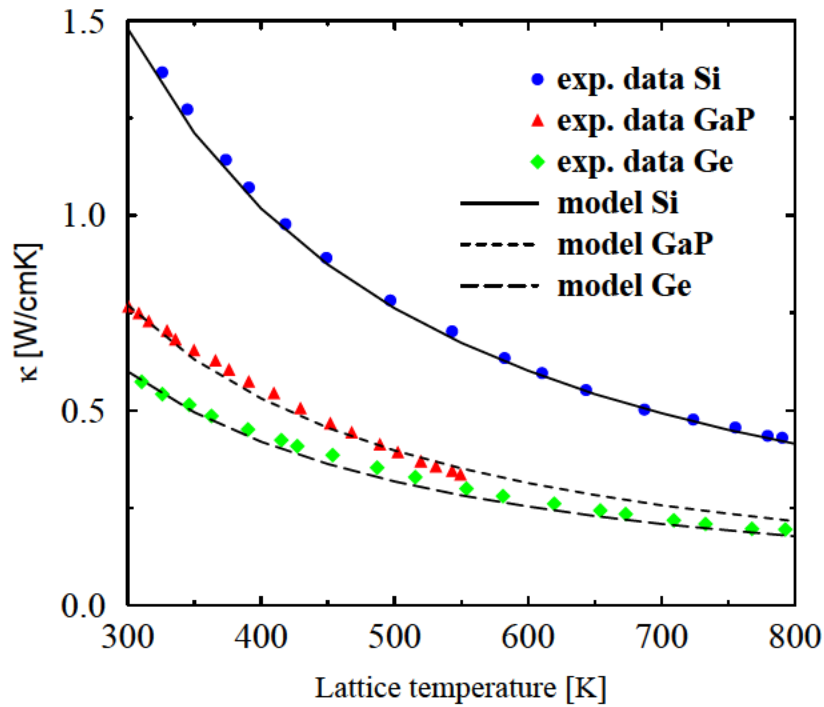
Fig. 3.1: Temperature dependence of the thermal conductivity: Comparison between experimental data and the model for Si, Ge, and GaP

agreement it gives in a wide temperature range (50 K – 800 K). The parameter values used are summarized in Table 3.7.

Material	c_{300} [J/K kg]	c_1 [J/K kg]	β	Reported c_{300} [J/K kg]	References
Si	711	255	1.85	700	[85]
Ge	360	130	1.3	310	[85]
GaAs	322	50	1.6	350	[85, 92]
AlAs	441	50	1.2	490	[92]
InAs	394	50	1.95	394	[92]
InP	410	50	2.05	410	[92]
GaP	519	50	2.6	519	[92]
SiO_2	709	696	1.5	1000	[85]
Si_3N_4	709	820	1.5	800	[98]

Table 3.7: Parameter values for the specific heat

The specific heat capacity coefficients for *alloy materials* are expressed by a linear interpolation between the values of the *basic materials* (A and B).

$$c_L^{AB} = (1 - x) \cdot c_L^A + x \cdot c_L^B \qquad (3.59)$$

The specific heat capacity is then expressed by (3.58).
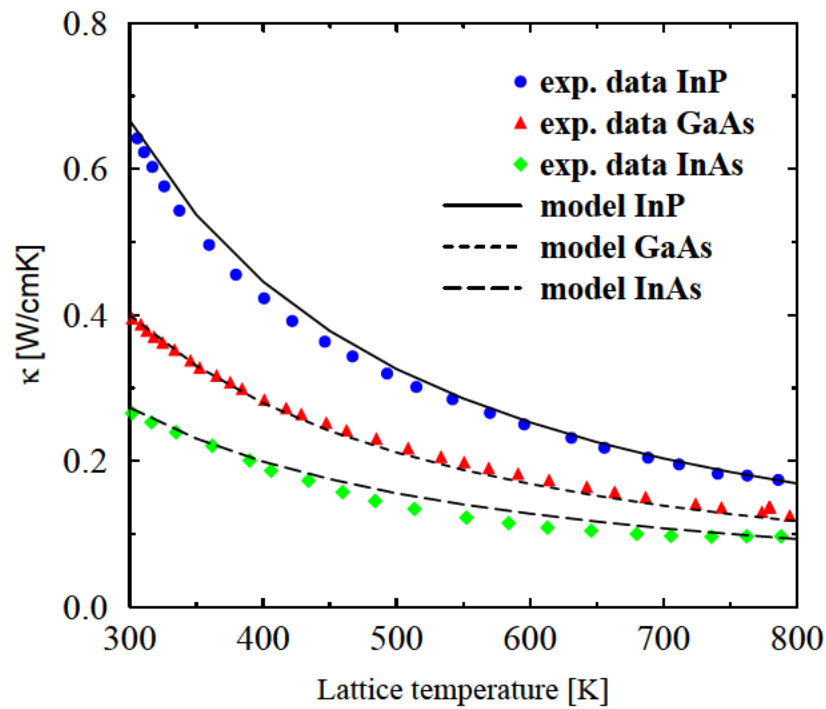
Fig. 3.2: Temperature dependence of the thermal conductivity: Comparison between experimental data and the model for InP, GaAs, and InAs
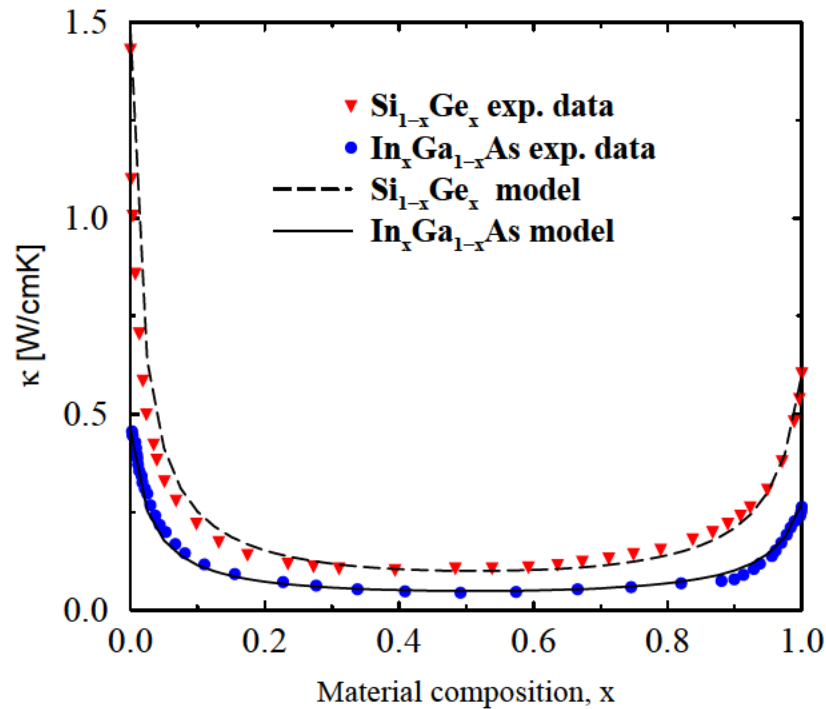
Fig. 3.3: Material composition dependence of the thermal conductivity: Comparison between experimental data and the model for SiGe and InGaAs
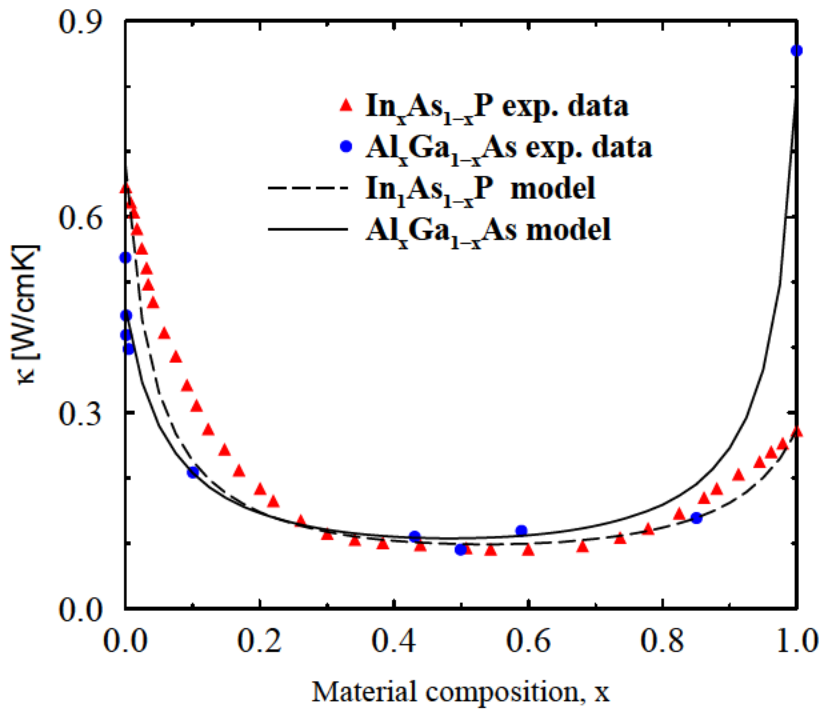
Fig. 3.4: Material composition dependence of the thermal conductivity: Comparison between experimental data and the model for InAsP and AlGaAs
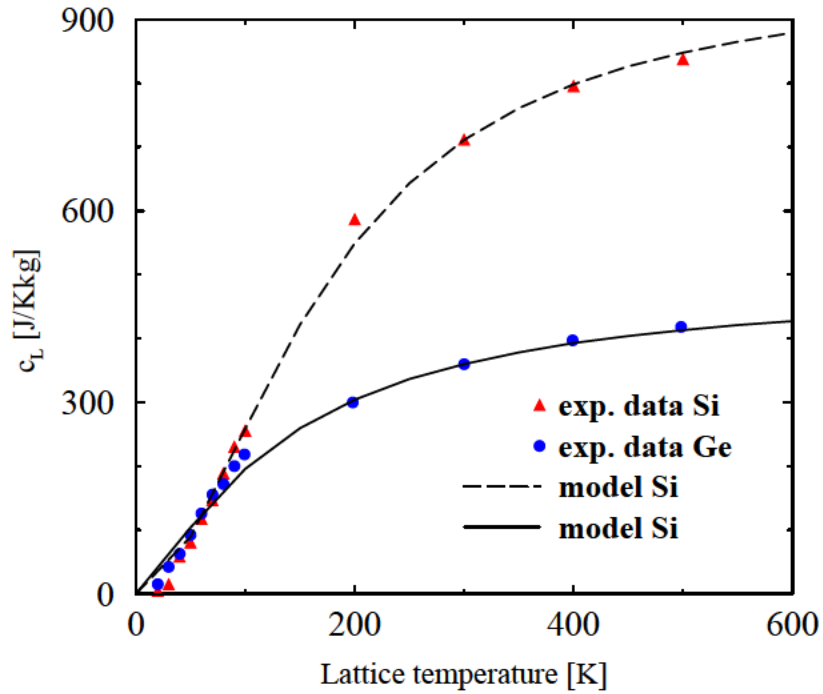
Fig. 3.5: Temperature dependence of the specific heat: Comparison between experimental data and the model for Si and Ge
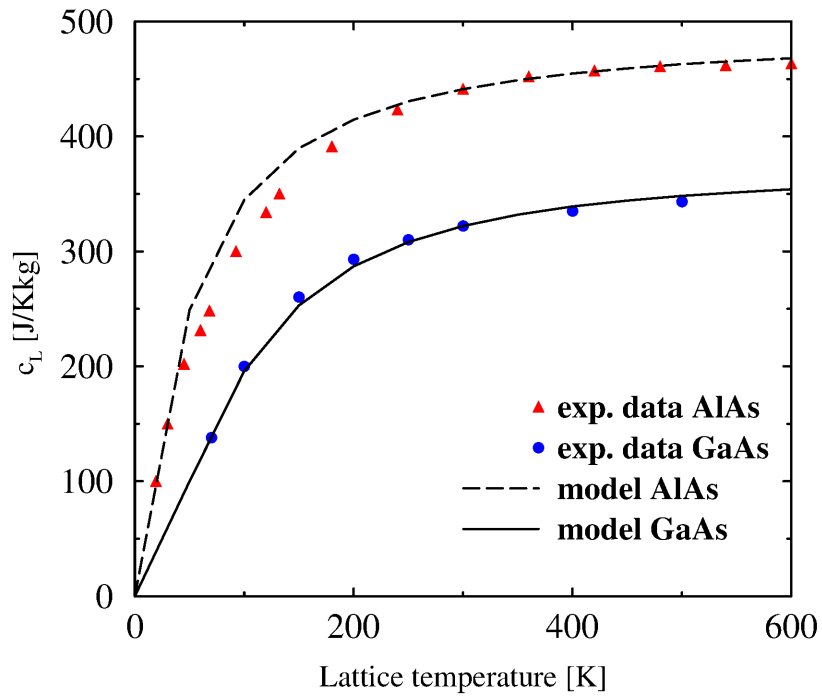
Fig. 3.6: Temperature dependence of the specific heat: Comparison between experimental data and the model for GaAs and AlAs
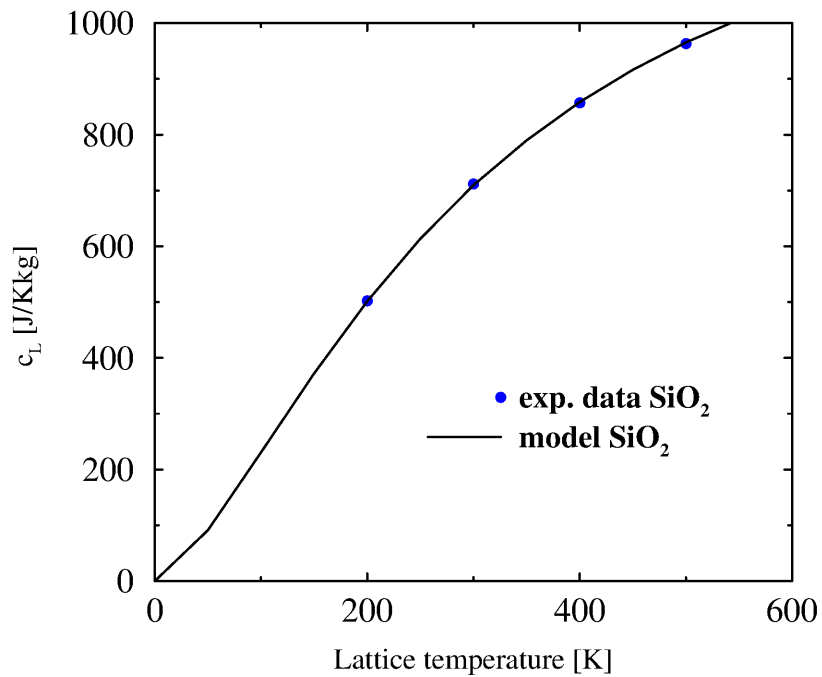
Fig. 3.7: Temperature dependence of the specific heat: Comparison between experimental data and the model for SiO_2

3.3 Band-Structure

In this section the models for the effective masses of electrons and holes, bandgap energy and effective density of states in Si, Ge, SiGe, and III-V materials are presented.

3.3.1 Bandgap Energy

The bandgap (or forbidden energy zone) is one of the most important semiconductor parameters. Various models define the temperature dependence of the bandgap energy in semiconductors (e.g. [112]). For an alloy $A_{1-x}B_x$, the temperature-dependent bandgaps of the constituents (A and B) are calculated first. The bandgap and the energy offset are then calculated depending on the material composition. This is important to assure consistency between the values for *alloy materials* at $x = 0$ and $x = 1$ and the values for the respective *basic materials*. For materials where the bandgap changes between direct and indirect the multiple valley conduction bands are considered.

Temperature dependence of the bandgap

In MINIMOS-NT the model of Varshni [112] is used for *basic materials*. The temperature dependence is calculated by (3.60), where $E_{g,0}$ is the bandgap at 0 K.

$$E_g = E_{g,0} - \frac{\alpha \cdot T_L^2}{\beta + T_L} \tag{3.60}$$

The parameter values are summarized in Table 3.8. Note, for these materials always the lowest conduction band valley minimum is taken into account. In addition, the resulting bandgaps at 300 K, $E_{g,300}$, are included in Table 3.9.

Material	Minimum	$E_{g,0}$ [eV]	α [eV/K]	β [K]	Reported $E_{g,0}$ [eV]	References
Si	X	1.1695	$4.73 \cdot 10^{-4}$	636	1.17	[90, 86]
Ge	L	0.7437	$4.774 \cdot 10^{-4}$	235	0.74	[86]
GaAs	G	1.521	$5.58 \cdot 10^{-4}$	220	1.51-1.55	[113, 114, 115]
AlAs	X	2.239	$6.0 \cdot 10^{-4}$	408	2.22-2.239	[94, 90, 108]
InAs	G	0.420	$2.5 \cdot 10^{-4}$	75	0.414-0.43	[92, 113]
InP	G	1.421	$3.63 \cdot 10^{-4}$	162	1.42-1.432	[108, 86, 114]
GaP	X	2.338	$5.771 \cdot 10^{-4}$	372	2.338-2.346	[108, 86, 90]

Table 3.8: Parameter values for modeling the bandgap energies

Material	Minimum	$E_{g,300}$ [eV]	Reported $E_{g,300}$ [eV]	References
Si	X	1.124	1.12-1.1242	[85, 86, 90]
Ge	L	0.663	0.66-0.67	[90, 85, 86]
GaAs	G	1.424	1.42-1.43	[116, 95, 104, 85]
AlAs	X	2.163	2.14-2.168	[94, 116, 104, 90]
InAs	G	0.360	0.354-0.37	[93, 92, 115, 117]
InP	G	1.350	1.34-1.351	[90, 115, 92]
GaP	X	2.261	2.26-2.272	[85, 92, 90]

Table 3.9: Bandgap energies at room temperature compared to reported data

For Si two additional models can be chosen which are based on polynomial fits of second and third order. The first one after *Gaensslen* [118, 119] was also used in MINIMOS 6. The second model is based on data from *Green* [120].

$$E_\mathrm{g} = E_0 + E_1 \cdot \left(\frac{T_\mathrm{L}}{300\ \mathrm{K}}\right) + E_2 \cdot \left(\frac{T_\mathrm{L}}{300\ \mathrm{K}}\right)^2 + E_3 \cdot \left(\frac{T_\mathrm{L}}{300\ \mathrm{K}}\right)^3 \tag{3.61}$$

The parameter values for these models are summarized in Table 3.10. In Fig. 3.8 the results

Model	E_0 [eV]	E_1 [eV]	E_2 [eV]	E_3 [eV]	$E_{\mathrm{g},300}$ [eV]
Gaensslen	1.1785	-0.02708	-0.02745	0.0	1.124
Green	1.17	0.00572	-0.06948	0.018	1.124

Table 3.10: Parameter values for modeling the bandgap energies

obtained with the three different models for Si are compared to data from [120]. In Fig. 3.9 and Fig. 3.10 the temperature dependence of the direct gap in GaAs and InP, respectively, are compared to other models.

Semiconductor Alloys

In the case of *alloy materials* the temperature-dependent bandgaps of the constituents, E_g^A and E_g^B, are calculated by (3.60). However, for materials where the bandgap changes between direct and indirect the multiple valley conduction bands are considered. For that purpose, additional model parameters are needed for the higher energy valleys in the respective III-V binary materials (Table 3.11). In addition, the resulting bandgaps at 300 K, $E_{\mathrm{g},300}$, are included in Table 3.12.

Material	Minimum	$E_{\mathrm{g},0}$ [eV]	α [eV/K]	β [K]	Reported $E_{\mathrm{g},0}$ [eV]	References
GaAs	X	1.981	$4.6 \cdot 10^{-4}$	204	1.9-1.91	[116, 104]
AlAs	G	2.891	$8.78 \cdot 10^{-4}$	332	2.907-3.02	[59, 95, 94, 104]
InAs	X	2.278	$5.78 \cdot 10^{-4}$	83		
InP	X	2.32	$7.66 \cdot 10^{-4}$	327	2.32-2.38	[109, 84, 121]
GaP	G	2.88	$8.0 \cdot 10^{-4}$	300	2.869-2.895	[91, 84, 122]

Table 3.11: Parameter values for modeling the bandgap energies

Material	Minimum	$E_{\mathrm{g},300}$ [eV]	Reported $E_{\mathrm{g},300}$ [eV]	References
GaAs	X	1.899	1.9-1.91	[116, 104]
AlAs	G	2.766	2.671-2.766	[93, 59]
InAs	X	2.142	1.37-2.14	[116, 108, 123]
InP	X	2.21	2.21-2.30	[116, 123, 121]
GaP	G	2.76	2.73-2.85	[84]

Table 3.12: Bandgap energies at room temperature compared to reported data

The bandgap and the energy offset of an alloy $\mathrm{A}_{1-x}\mathrm{B}_x$ are calculated by

$$E_{\mathrm{g,X}}^{\mathrm{AB}} = E_{\mathrm{g,X}}^{\mathrm{A}} \cdot (1-x) + E_{\mathrm{g,X}}^{\mathrm{B}} \cdot x + C_{\mathrm{g,X}} \cdot (1-x) \cdot x \tag{3.62}$$

$$E_{g,\Gamma}^{AB} = E_{g,\Gamma}^{A} \cdot (1-x) + E_{g,\Gamma}^{B} \cdot x + C_{g,\Gamma} \cdot (1-x) \cdot x \qquad (3.63)$$

$$E_g^{AB} = \min\left(E_{g,X}^{AB}; E_{g,\Gamma}^{AB}\right) \qquad (3.64)$$

The bowing parameters $C_{g,X}$ and $C_{g,\Gamma}$ are summarized in Table 3.13. Additional bowing parameters C_g are given as a reference for the case when a one-valley bandgap fit is used.

$$E_g^{AB} = E_g^A \cdot (1-x) + E_g^B \cdot x + C_g \cdot (1-x) \cdot x \qquad (3.65)$$

Material	$C_{g,\Gamma}$ [eV]	$C_{g,X}$ [eV]	C_g [eV]	Reported	References
SiGe			-0.4	-0.4	[124]
AlGaAs	0.0	-0.143	0.7	0^Γ, -0.143^X	[93, 125]
InGaAs			-0.475	-0.4, -0.475, -0.555	[108, 90, 71]
InAlAs	-0.3	-0.713	1.2	-0.689^Γ,-0.24^Γ	[108, 90]
InAsP			-0.32	-0.101, -0.32	[108, 90]
GaAsP	-0.21	-0.21	0.5	-0.176^Γ,-0.23^Γ	[108, 126]
InGaP	-0.67	-0.17	0.6	-0.786^Γ,-0.6^Γ,-0.18^X	[108, 90, 109]

Table 3.13: Parameter values for the bandgap of alloy materials

For example, such a one-valley bandgap fit is used in the case of the technologically important strained $Si_{1-x}Ge_x$ grown on Si (see Fig. 3.11). In certain cases for $x > 0.6$ the bandgap can become smaller than the one of pure Ge [127] depending on the strain. In the unstrained case, however, an X-to-L gap transition is observed at about $x = 0.85$.

The material composition dependence of the Γ, L, and X-band gaps in $Al_xGa_{1-x}As$ at 300 K is shown in Fig. 3.12. A direct-to-indirect gap transition is observed at about $x = 0.45$. The one-valley bandgap fit which is included for comparison gives a good agreement only for $x < 0.28$. In Fig. 3.13 the temperature dependence of the bandgap in $Al_xGa_{1-x}As$ with Al content as a parameter is shown. In Fig. 3.14 the material composition dependence of the Γ, L, and X-band gaps in $In_xGa_{1-x}As$ at 300 K is shown. As can be seen this material has a direct bandgap for the entire composition range. Therefore, only the energy of the Γ valley is taken into account. However, in the case of strain the bandgap can significantly differ [128]. For example, a good fit to the strained bandgap values of $In_xGa_{1-x}As$ grown on GaAs can be achieved by changing the $E_{g,0}$ of InAs from 0.42 eV to 0.58 eV. In Fig. 3.15 the temperature dependence of the bandgap in $In_xGa_{1-x}As$ with In content as a parameter is shown. In the case of $In_xAl_{1-x}As$ there is direct-to-indirect gap transition at about $x = 0.3$ and the use of one valley fit is nearly impossible. It gives comparatively accurate values for the lattice matched case of $x = 0.52$ and above (see Fig. 3.16). $InAs_xP_{1-x}$ has a direct gap for the complete material composition range so only the Γ valley energy is calculated. The bowing parameter value suggested in [108] is used. $GaAs_{1-x}P_x$ has a direct-to-indirect gap transition at about $x = 0.5$. As can be seen in Fig. 3.17 a one valley model can be successfully used for this material. In Fig. 3.18 the material composition dependence of the Γ, L, and X-bandgaps in $Ga_xIn_{1-x}P$ at 300 K is shown. The direct-to-indirect gap transition is at about $x = 0.7$. Only at the technologically important value of $x = 0.51$, when $Ga_xIn_{1-x}P$ lattice matches the one of GaAs the one-valley model gives a good fit for the bandgap. The temperature dependence of the bandgap in $Ga_xIn_{1-x}P$ with Ga content as a parameter is shown in Fig. 3.19.
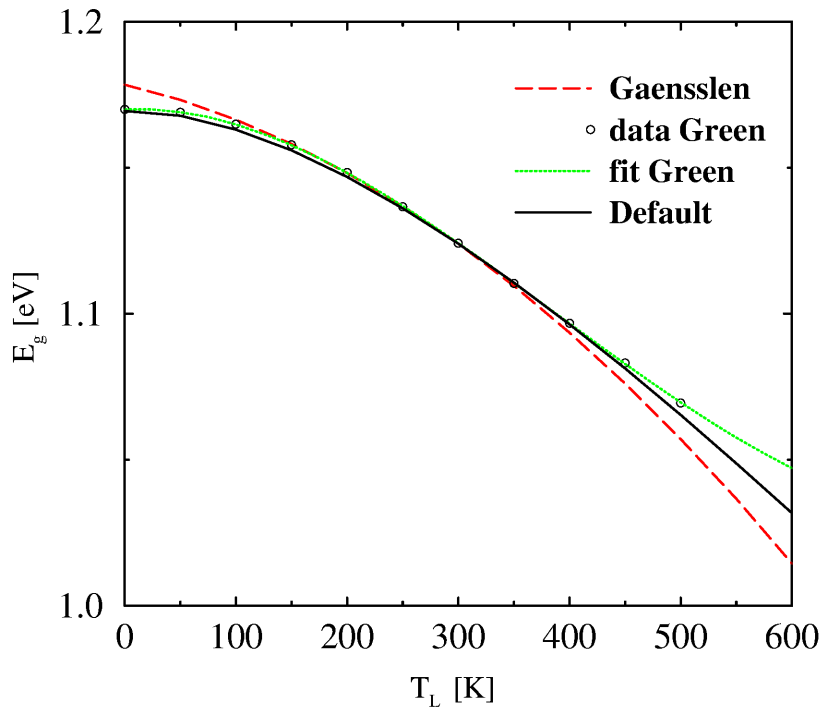
Fig. 3.8: Comparison of different models for the temperature dependence of the bandgap in Si
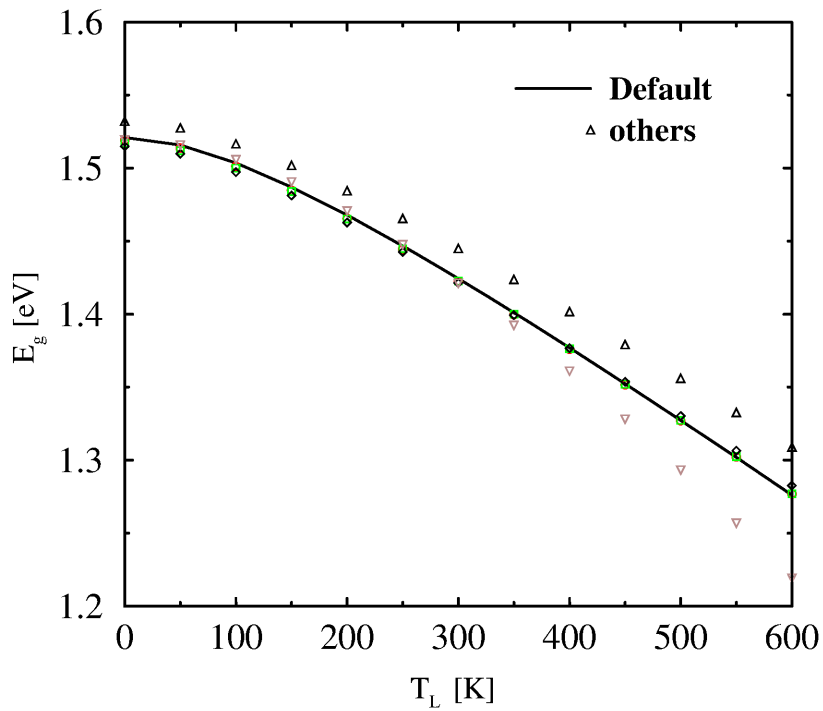
Fig. 3.9: Comparison of different models for the temperature dependence of the bandgap in GaAs
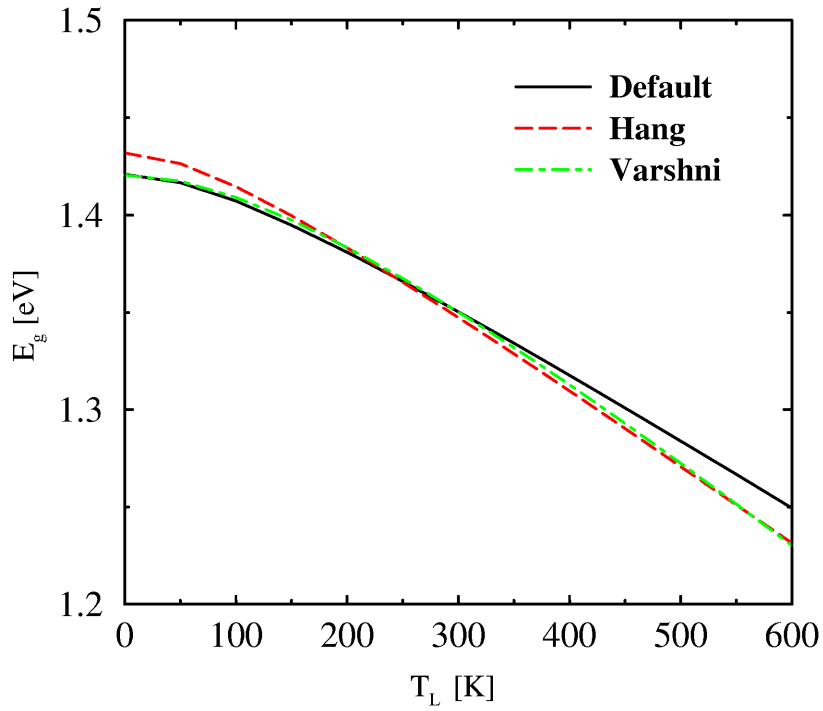
Fig. 3.10: Comparison of different models for the temperature dependence of the bandgap in InP
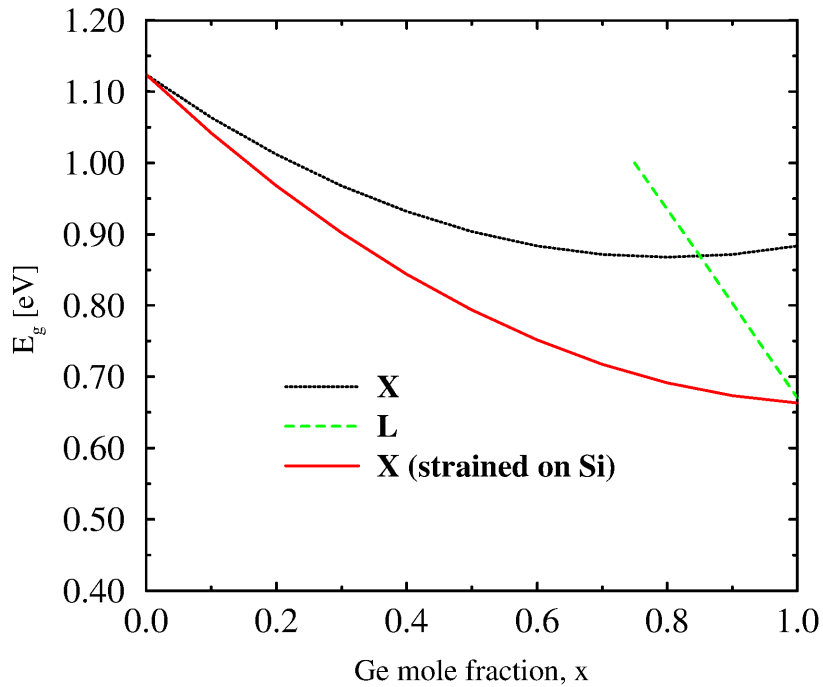
Fig. 3.11: Material composition dependence of the Γ, L, and X-bandgaps in $Si_{1-x}Ge_x$ at 300 K
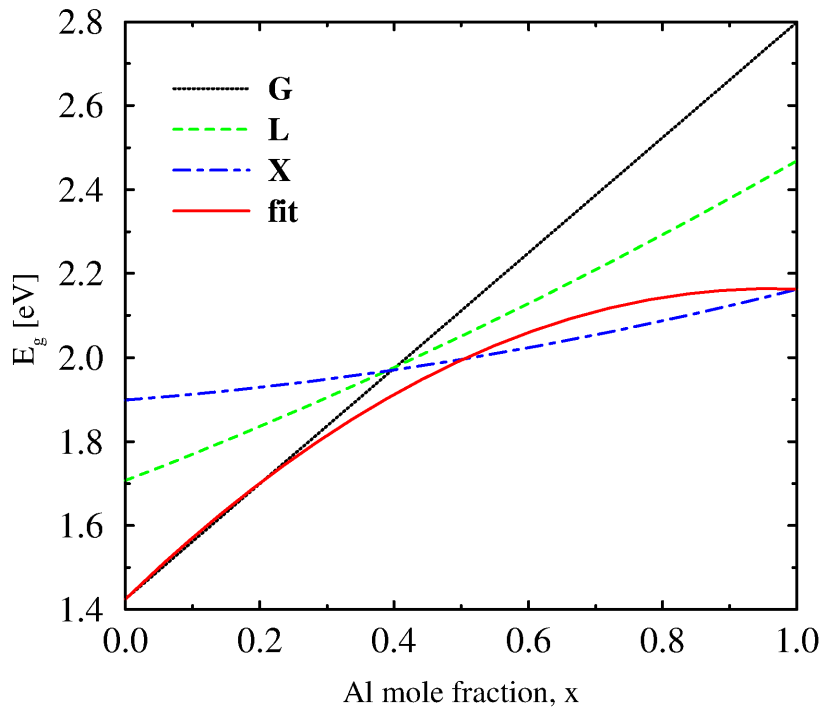
Fig. 3.12: Material composition dependence of the Γ, L, and X-bandgaps in $Al_xGa_{1-x}As$ at 300 K
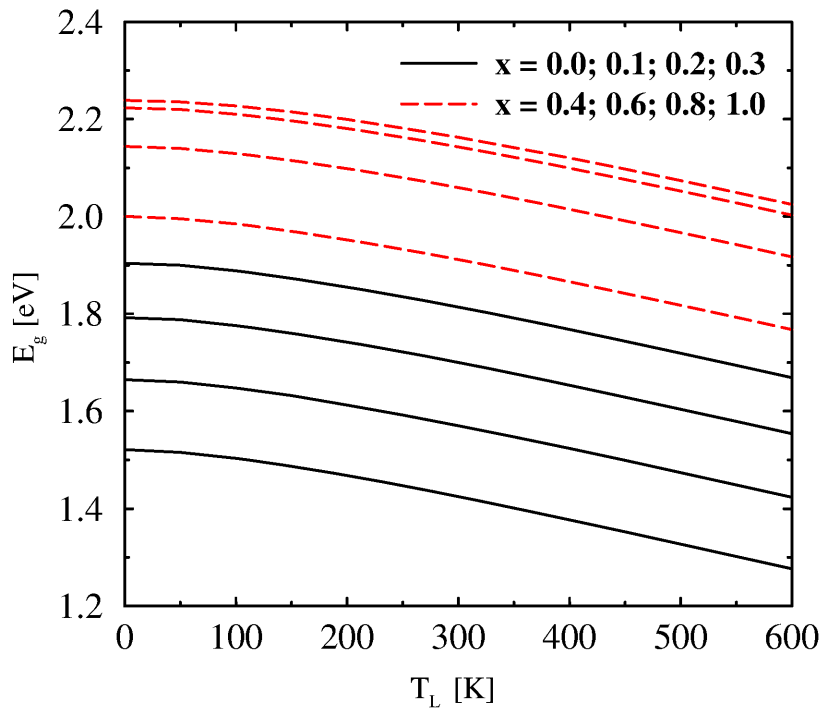
Fig. 3.13: Temperature dependence of the bandgap in $Al_xGa_{1-x}As$ with Al content as a parameter
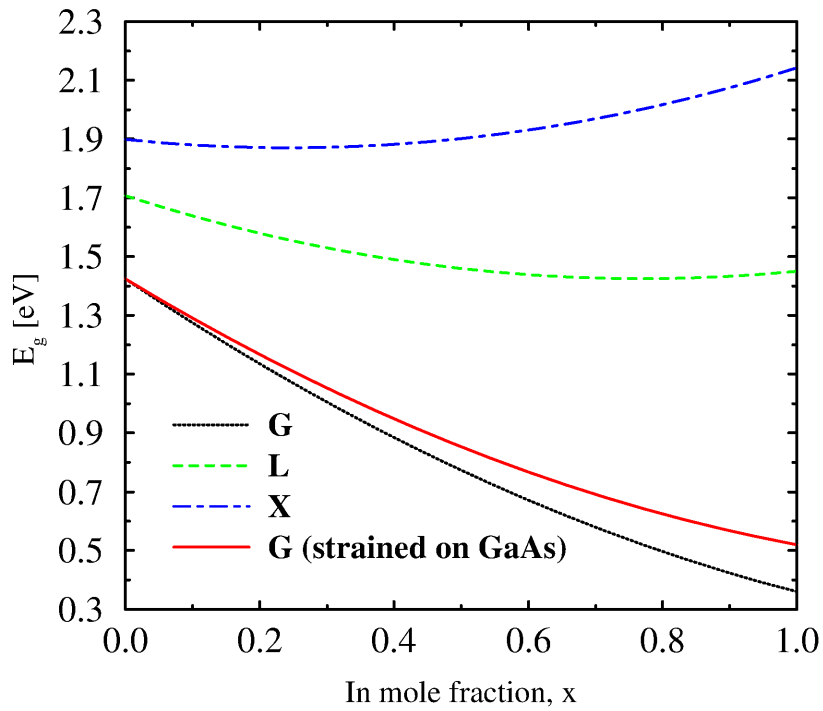
Fig. 3.14: Material composition dependence of the Γ, L, and X-bandgaps in $In_x Ga_{1-x} As$ at 300 K
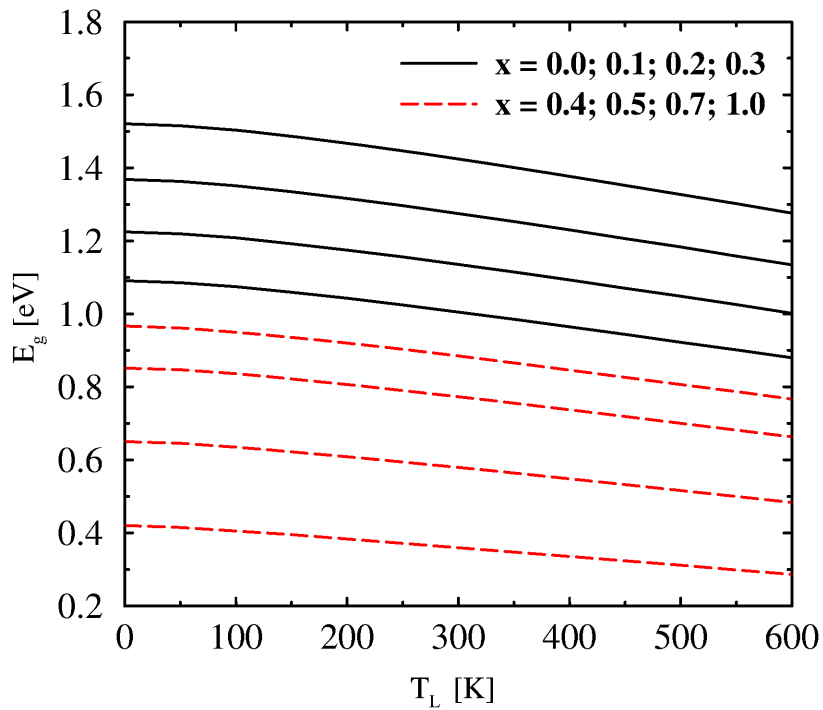
Fig. 3.15: Temperature dependence of the bandgap in $In_x Ga_{1-x} As$ with In content as a parameter
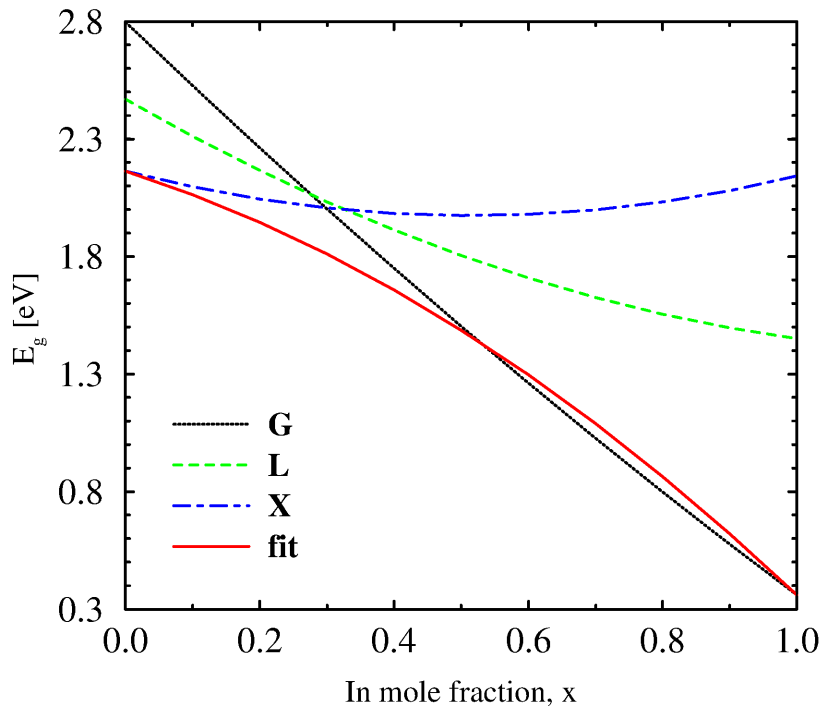
Fig. 3.16: Material composition dependence of the Γ, L, and X-bandgaps in $In_x Al_{1-x} As$ at 300 K
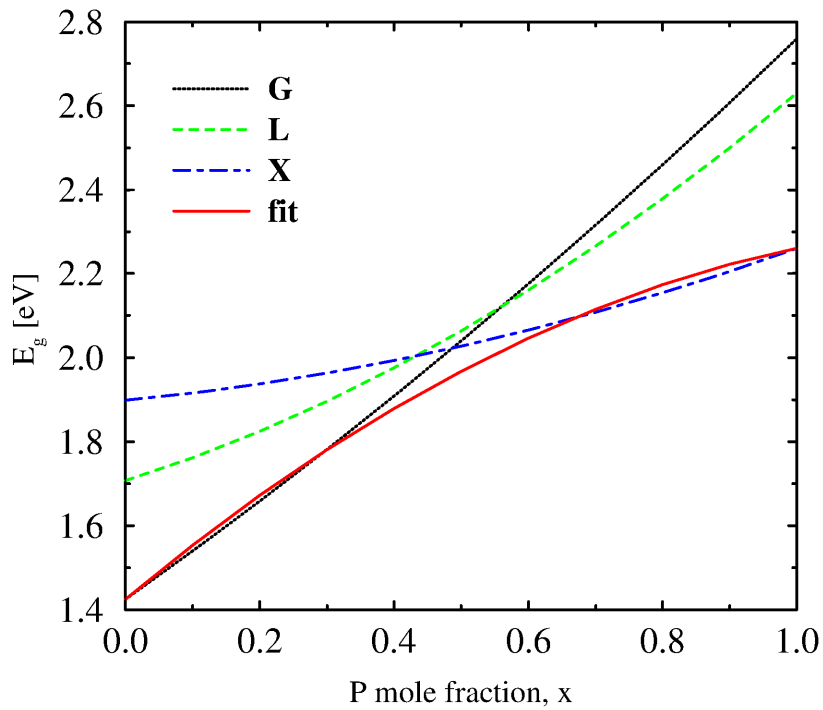
Fig. 3.17: Material composition dependence of the Γ, L, and X-bandgaps in $GaAs_{1-x} P_x$ at 300 K
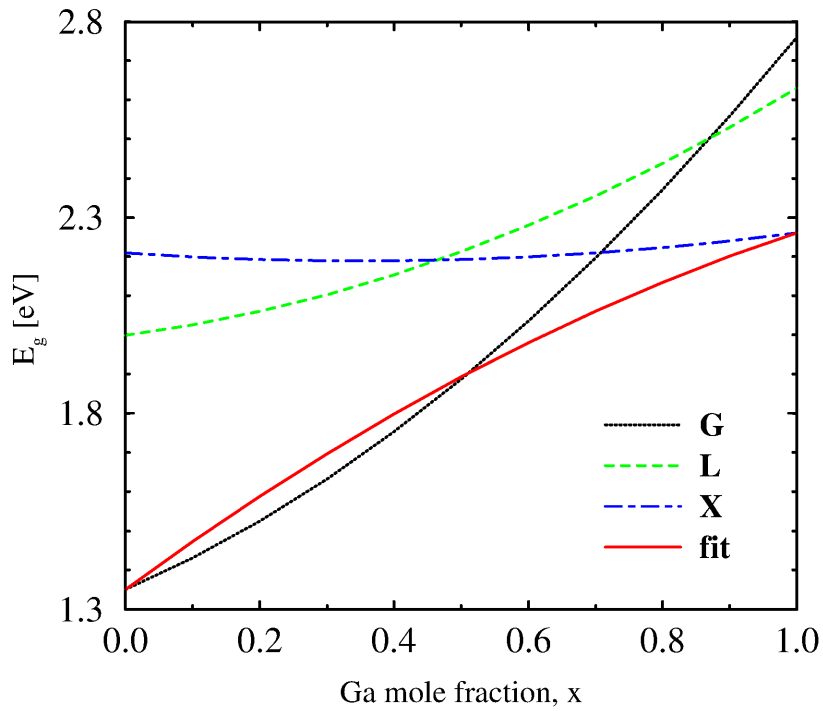
Fig. 3.18: Material composition dependence of the Γ, L, and X-bandgaps in $Ga_xIn_{1-x}P$ at 300 K
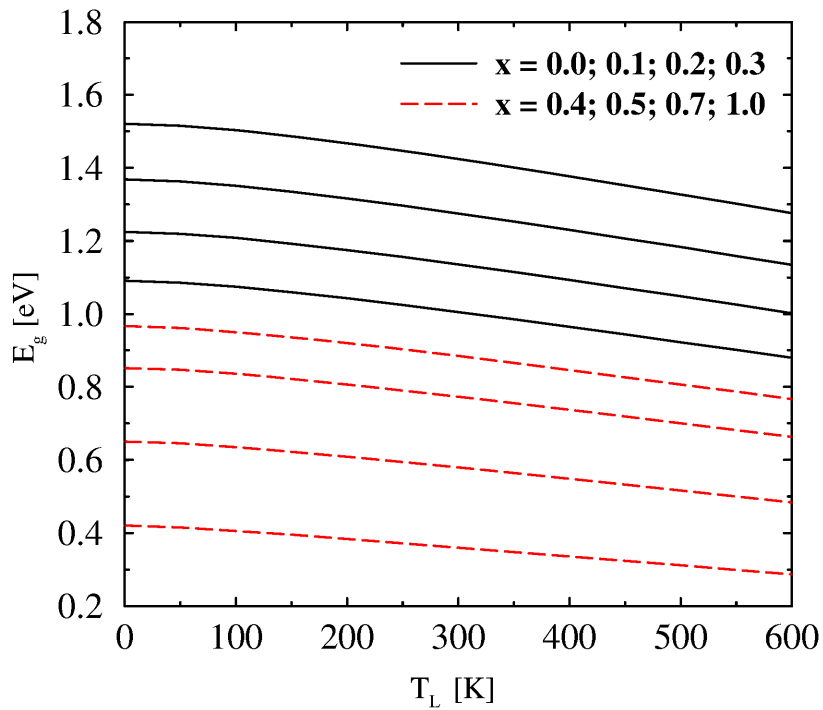
Fig. 3.19: Temperature dependence of the bandgap in $Ga_xIn_{1-x}P$ with Ga content as a parameter

3.3.2 Bandgap Offsets

The problem to align the bandgaps of two or more different materials is old and not completely solved [129, 130, 131] due to the dependence on the growth conditions. The many suggested approaches mainly differ in whether to use the electron affinity to align the conduction bands, whether to align the midgaps, or whether to align the valence band edges. In MINIMOS-NT the last approach is used.

An energy offset, E_{off}, is used to align the band edge energies of different materials. E_{off} is an arbitrary value and by changing it consistently for all materials at the same time the same results are obtained. As a default in MINIMOS-NT for the group IV materials the reference material is Si. The origin of the energy axis is assumed to be in the middle of the Si bandgap at 300 K. This corresponds to a fixed value for Si of $E_{\text{off}} = -E_{\text{g}}/2 = -0.562$ eV. For the III-V material system GaAs is chosen as the reference material. Therefore, the offset for GaAs is $E_{\text{off}} = -E_{\text{g}}/2 = -0.712$ eV. The default offsets for other materials, summarized in Table 3.14, are chosen to give good agreement with reported data from [108, 111, 129, 130, 131].

Material	E_{off} [eV]	Material	E_{off} [eV]
Si	-0.562	InAs	-0.286
Ge	-0.157	InP	-0.724
GaAs	-0.712	GaP	-1.062
AlAs	-1.008		

Table 3.14: Parameter values for modeling the bandgap energies

The energies of the conduction and valence band edges are calculated by

$$E_V = E_{\text{off}} \tag{3.66}$$
$$E_C = E_V + E_{\text{g}} \tag{3.67}$$

For *alloy materials*, the following expressions for the conduction and valence band energies are often used.

$$E_C = E_{\text{off}}^{\text{A}} + E_{\text{g}}^{\text{A}} + \left(\frac{\Delta E_C}{\Delta E_{\text{g}}}\right) \cdot \left(E_{\text{g}}^{\text{AB}} - E_{\text{g}}^{\text{A}}\right) \tag{3.68}$$

$$E_V = E_C - E_{\text{g}}^{\text{AB}} \tag{3.69}$$

The change of the bandgap with the material composition is defined by the ratio $\Delta E_C/\Delta E_{\text{g}}$, starting from one of the materials. For example, for $\text{Al}_x\text{Ga}_{1-x}\text{As}/\text{GaAs}$ interface it is known that this ratio equals 60%. This means that, with increasing x, 60% of the increase of the bandgap ($\Delta E_{\text{g}} = \Delta E_C + \Delta E_V$) is contributed to the conduction band (ΔE_C) and 40% to the valence band (ΔE_V). The model, being so formulated, is not symmetric and general enough. However, assuming $\Delta E_C/\Delta E_{\text{g}}$ is constant for the whole composition range one obtains:

$$E_C = E_{\text{off}}^{\text{B}} + E_{\text{g}}^{\text{B}} + \left(\frac{\Delta E_C}{\Delta E_{\text{g}}}\right) \cdot \left(E_{\text{g}}^{\text{AB}} - E_{\text{g}}^{\text{B}}\right) \tag{3.70}$$

Thus, from (3.68) and (3.70) the ratio $\Delta E_C/\Delta E_{\text{g}}$ can be expressed as:

$$\Delta E_C/\Delta E_{\text{g}} = 1 + \frac{E_{\text{off}}^{\text{A}} - E_{\text{off}}^{\text{B}}}{E_{\text{g}}^{\text{A}} - E_{\text{g}}^{\text{B}}} \tag{3.71}$$

Replacing it in (3.68) or (3.70) the offset of alloy material is obtained:

$$E_{\text{off}}^{\text{AB}} = \frac{E_{\text{off}}^{\text{A}} \cdot \left(E_{\text{g}}^{\text{AB}} - E_{\text{g}}^{\text{B}}\right) - E_{\text{off}}^{\text{B}} \cdot \left(E_{\text{g}}^{\text{AB}} - E_{\text{g}}^{\text{A}}\right)}{E_{\text{g}}^{\text{A}} - E_{\text{g}}^{\text{B}}} \tag{3.72}$$

The valence and the conduction band energies are calculated by (3.66) and (3.67), respectively. Using the default model parameters in MINIMOS-NT ratios $\Delta E_C/\Delta E_{\text{g}}$ of 0.12 for SiGe, 0.6 for AlGaAs, 0.5 for InAlAs, 0.6 for InGaAs, InAsP, GaAsP, and 0.3 for InGaP are obtained, which are in fairly good agreement with experimental data [110, 89, 111, 108, 132].

The complete bandgap alignment of all semiconductor materials presented in MINIMOS-NT is shown in Fig. 3.20.

Special attention is paid to the band offsets at the heterointerfaces and thermionic emission or thermionic-field emission model must be used in the case of abrupt heterojunctions (see Section 3.1.6).

3.3.3   Bandgap Narrowing

Bandgap narrowing (BGN) is one of the crucial heavy-doping effects to be considered for bipolar devices. In MINIMOS-NT the use of BGN model is optional. The model of *Slotboom* [133] is widely used in case of silicon.

$$\Delta E_{\text{g}} = E_{\text{ref}} \cdot \left(\ln\left(\frac{C_I}{C_{\text{ref}}}\right) + \sqrt{\ln^2\left(\frac{C_I}{C_{\text{ref}}}\right) + \frac{1}{2}} \right) \tag{3.73}$$

The shifts of the conduction and valence band edges are calculated by

$$\Delta E_C = \left(\frac{\Delta E_C}{\Delta E_{\text{g}}}\right) \cdot \Delta E_{\text{g}} \tag{3.74}$$

$$\Delta E_V = \Delta E_{\text{g}} - \Delta E_C \tag{3.75}$$

$\Delta E_C/\Delta E_{\text{g}}$ gives the part of the total BGN ΔE_{g} which is contributed to the conduction band. The default parameter values are summarized in the following table.

Material	E_{ref} [eV]	C_{ref} [cm^{-3}]	$\Delta E_C/\Delta E_{\text{g}}$
Si	0.009	1e17	0.5

Table 3.15: Parameter values for modeling the bandgap narrowing

Using the physically-based approach from [93], a new analytical BGN model was developed. It is applicable to compound semiconductors [134] and considers the semiconductor material and the dopant species for arbitrary finite temperatures. In this section a comparison with experimental data and other existing models is presented and study of BGN in III-V group semiconductors is performed.
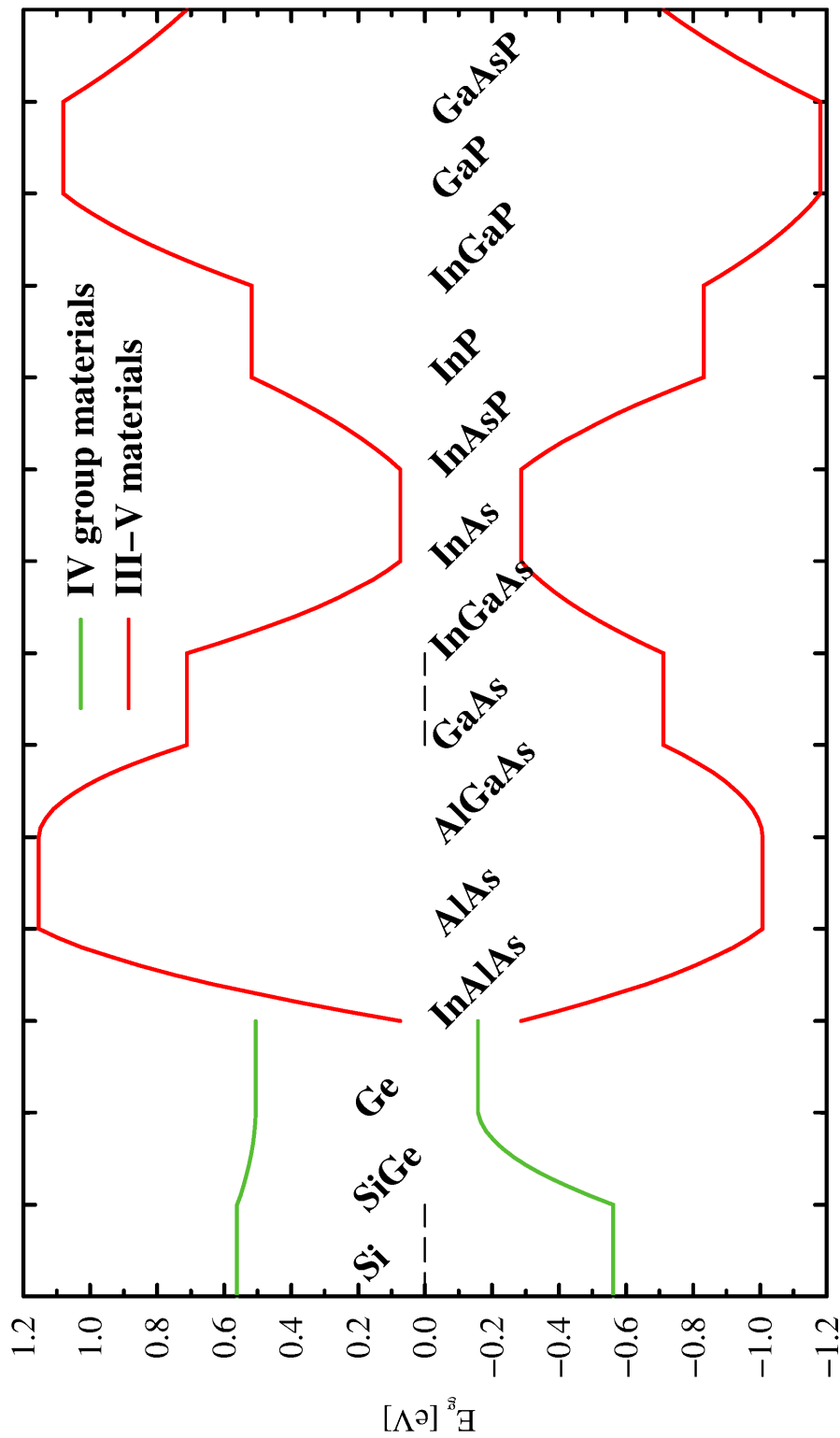
Fig. 3.20: Bandgaps of all semiconductor materials modeled in MINIMOS-NT: Reference energies for IV group and III-V group materials are the mid gaps of Si and GaAs, respectively, placed at 0 eV.

Dopant-Dependent Bandgap Narrowing

Despite of many papers dedicated on BGN in semiconductors, the optimal balance between accuracy of the results and simplicity of model implementation seems had not been achieved. Commercial device simulators, such as ATLAS [50] , DESSIS [40], and MEDICI [41], use the logarithmic fit models for BGN in Si from [133, 135, 136, 137] which are simple to implement, but deliver non-physical values below and above definite doping levels. Furthermore, the functional form of models for Si is used for models for other materials (e.g. III-V compounds [138]) or the BGN effect is left completely ignored. Comparisons of these models are shown in Fig. 3.21. The physical limit our model offers (0 meV for undoped materials), the physically sound explanation of some existing effects it gives, the ability to treat various semiconductor materials and dopants, and the simplicity of the model, make it very applicable for device simulation purposes.

Physical background of the new model

The basic assumption in our model is that BGN is a result of five types of many-body interactions (electron-electron, electron-impurity, hole-hole, hole-impurity, and electron-hole). The electron-impurity contribution is assumed to be dominant at high doping concentrations. Though BGN is very difficult to model rigorously due to multiple carrier interactions one can approximate the energy shift to first order by the classical self-energy of the electron in the field of an ionized impurity [93]. Thus one obtains

$$\Delta E_{\mathrm{g}} \quad = \quad \mathrm{q} \cdot \lim_{r \to 0} \left(V_s\left(r\right) - V(r) \right) \tag{3.76}$$

$$V(r) \quad = \quad \frac{1}{(2 \cdot \pi)^3} \int V(k) \cdot \exp\left(i \cdot \mathbf{k} \cdot \mathbf{r}\right) \, \mathrm{d}\mathbf{k}, \quad k = |\mathbf{k}| \tag{3.77}$$

Here $V_s\left(r\right)$ and $V(r)$ denote the screened and unscreened *Coulomb* potentials of the impurity, respectively. (3.76) represents the change in the electrostatic energy of the impurity before and after the electron gas redistribution. If the potential of a point-like impurity is assumed, the Fourier transform of the scattering potential is expressed by (3.78), where Z and N are the atomic number and the number of electrons of a given material, β denotes the inverse *Thomas-Fermi* length, and $\mathcal{F}_j(x)$ is the *Fermi* integral of order j [139]. This approach leads to a simple BGN model [93] given by (3.80).

$$V(k) \quad = \quad \frac{\mathrm{q}^2}{\varepsilon_0 \cdot \varepsilon_{\mathrm{r}}} \cdot \left(\frac{Z - N}{k^2 + \beta^2} \right) \tag{3.78}$$

$$\beta^2 \quad = \quad \frac{n \cdot \mathrm{q}^2}{\varepsilon_0 \cdot \varepsilon_{\mathrm{r}} \cdot \mathrm{k_B} \cdot T_{\mathrm{L}}} \cdot \frac{\mathcal{F}_{-1/2}(\eta)}{\mathcal{F}_{1/2}(\eta)} \tag{3.79}$$

$$\Delta E_{\mathrm{g}} \quad = \quad -\frac{\mathrm{q}^2 \cdot \beta}{4 \cdot \pi \cdot \varepsilon_0 \cdot \varepsilon_{\mathrm{r}}} \tag{3.80}$$

Removing the point-charge approximation yields a refined model. The charge density of the impurity can be accounted for by an atomic form factor F. Following the work [140] the impurity potential takes the form

$$V(k) \quad = \quad \frac{\mathrm{q}^2}{\varepsilon_0 \cdot \varepsilon_{\mathrm{r}}} \cdot \left(\frac{Z - F(k, \alpha)}{k^2 + \beta^2} \right) \tag{3.81}$$

$$F(k, \alpha) \quad = \quad \frac{N \cdot \alpha^2}{k^2 + \alpha^2} \tag{3.82}$$

Solving (3.77) using (3.81) and (3.82), and then replacing V(r) in (3.76), leads to the final expression for the energy shift

$$\Delta E_g \quad = \quad -\frac{q^2 \cdot \beta}{4 \cdot \pi \cdot \varepsilon_0 \cdot \varepsilon_r} \cdot \left(\frac{\beta \cdot N_I}{\beta + \alpha_I} - \frac{\beta \cdot N_{SC}}{\beta + \alpha_{SC}} + Z_I - N_I \right). \tag{3.83}$$

The subscripts SC and I refer to a semiconductor and impurity, respectively. Z and N are the atomic number and the number of electrons of a given material. α can be interpreted as size parameters of the electron charge density and α_0 is the Bohr radius. They are expressed as

$$\alpha \quad = \quad \frac{Z^{1/3}}{c_k \cdot \alpha_0 \cdot \epsilon_r} \cdot \frac{1 - 2 \cdot \left(\dfrac{Z}{N} \right)}{\dfrac{5}{3} - 4 \cdot \left(\dfrac{Z}{N} \right)^{1/3}} \tag{3.84}$$

$$c_k \quad = \quad \frac{\Gamma(4/3)}{2} \cdot \left(\frac{3 \cdot \pi}{4} \right)^{2/3} \cdot \left(\frac{3}{5} \right)^{7/3} \approx 0,24. \tag{3.85}$$

The size parameter α uses $\varepsilon_r = 1$, which is the most pessimistic estimation, since it is still not clarified which value for $\varepsilon_r = 1$ in the range between 1 and ε_{SC} is valid at microscopic level. Even though the influence of the dopant type is reduced to minimum this way, our model still delivers appropriate results at 300 K in agreement with experiment [141] (see Fig. 3.22). The temperature dependence of the BGN in Si is shown in Fig. 3.23. Neglecting of the stronger BGN at low temperatures, especially for doping levels of about 10^{19} cm^{-3}, may result in an error of about 50%. Thereby, even larger errors might be introduced into the simulation results, with respect to the electrical device characteristics. In the case of III-V semiconductors our model delivers a comparatively weaker BGN temperature dependence (see Fig. 3.24). Similar observations were reported in the case of p-GaAs in [142], [143]. Thus, according to our knowledge, our BGN model is the first theoretically derived model predicting different shifts for various dopant species and taking temperature into account.

Extending the new model to semiconductor alloys

The model extends its validity also for alloy semiconductors by material composition dependent relative effective masses for electrons and holes, on the one hand, and permittivity, on the other hand. In Fig. 3.25 the results for boron and gallium doped $Si_{1-x}Ge_x$ for different Ge contents are presented. This is even better illustrated in Fig. 3.26 where the BGN versus material composition in $Si_{1-x}Ge_x$ is compared to another model proposed by *Jain* and *Roulston* [144] suggesting increased BGN. The decrease of the BGN with increase of the Ge fraction was already experimentally observed in [145], [146]. Our theoretical approach explains this effect by the decreased valence band density of states and increase of the relative permittivity in the SiGe alloy.

In the case of p-type GaAs good agreement with experimental data [142], [143] is obtained. The few available experimental data for n-type GaAs suggest sometimes lower [147] (open triangles in Fig. 3.27) values for BGN and more often higher [148] (filled triangles) than
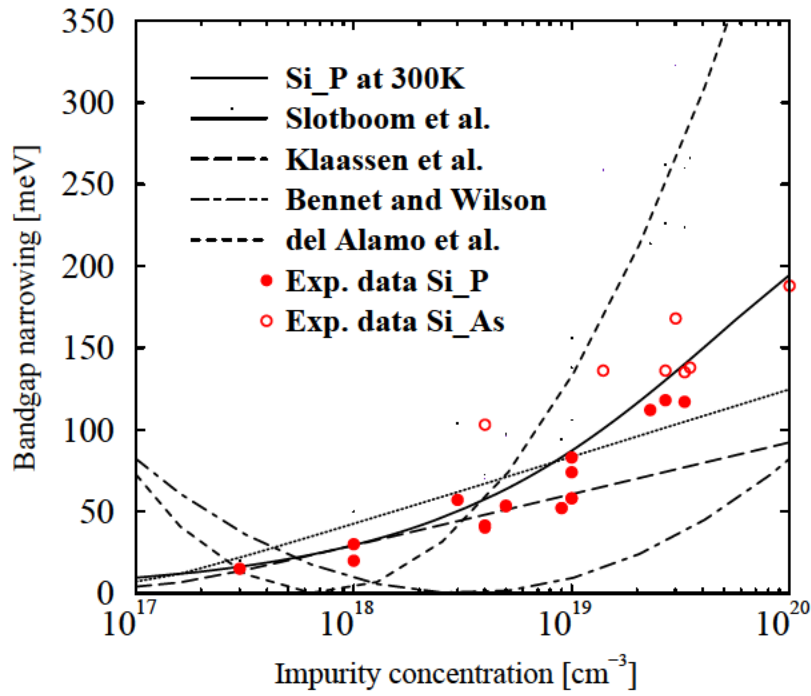
Fig. 3.21: Comparison with models used in other device simulators
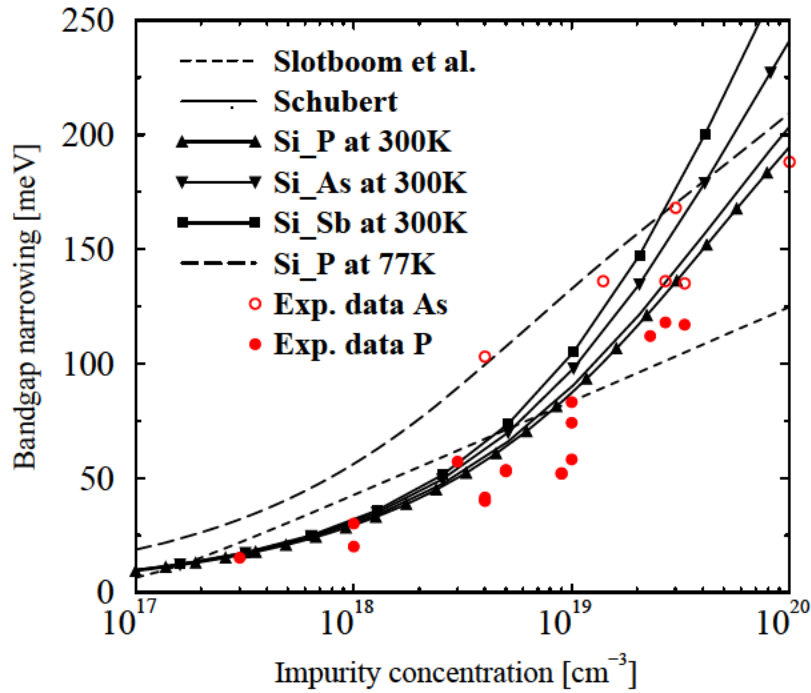
Fig. 3.22: Influence of the dopant material on BGN in n-Si
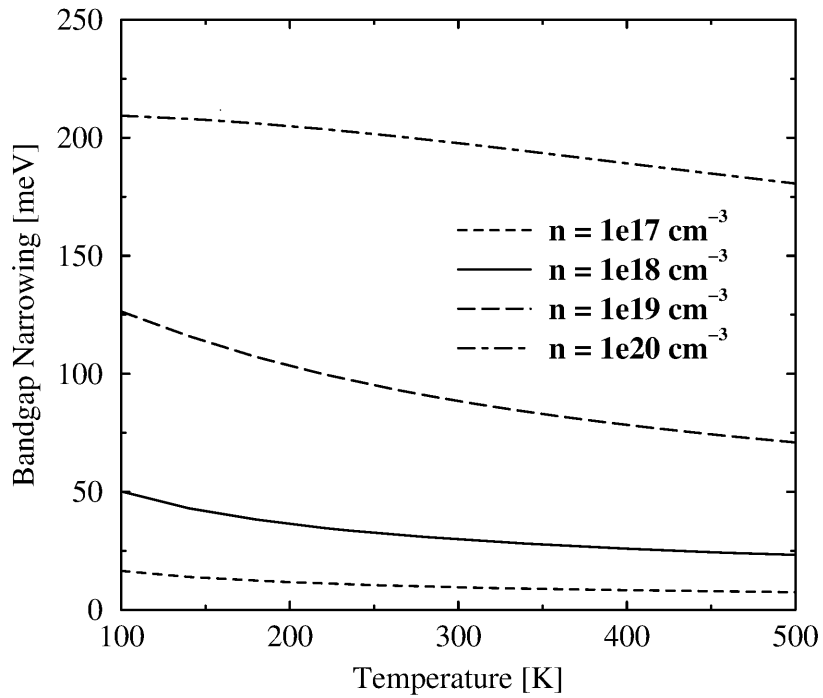
Fig. 3.23: Temperature dependence of the bandgap narrowing in n-Si
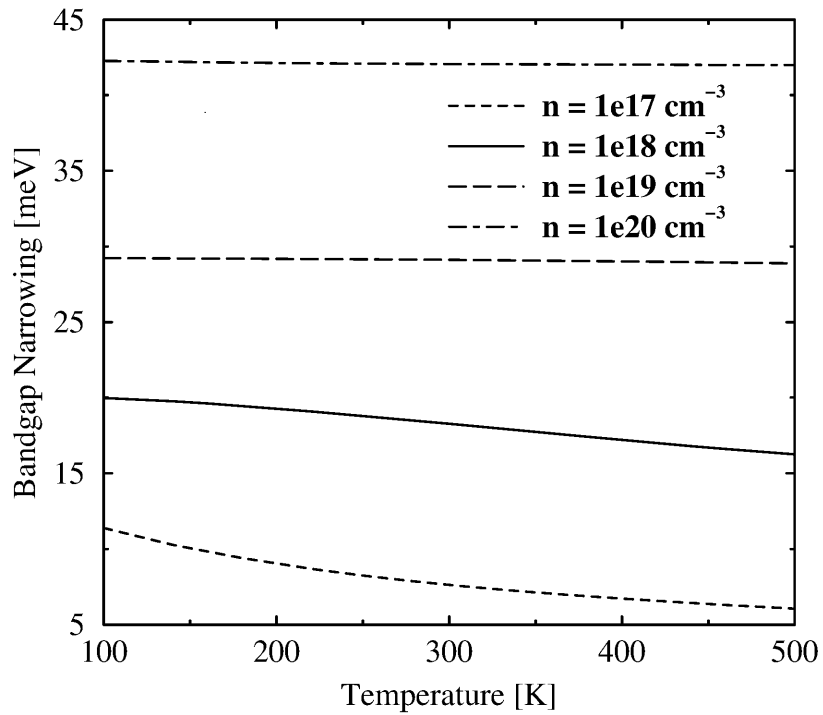
Fig. 3.24: Temperature dependence of the bandgap narrowing in n-GaAs
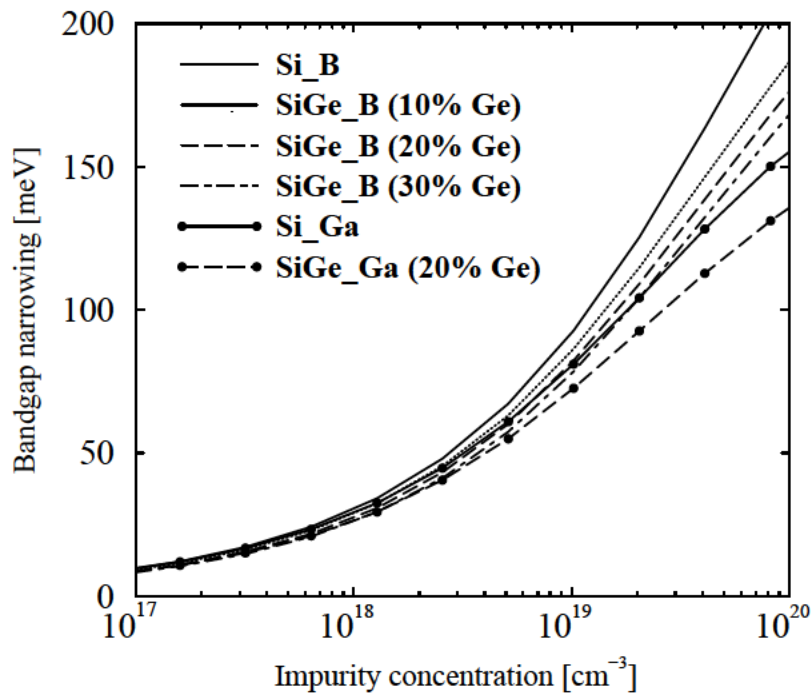
Fig. 3.25: Influence of the dopant material and material composition in p-Si and p-SiGe
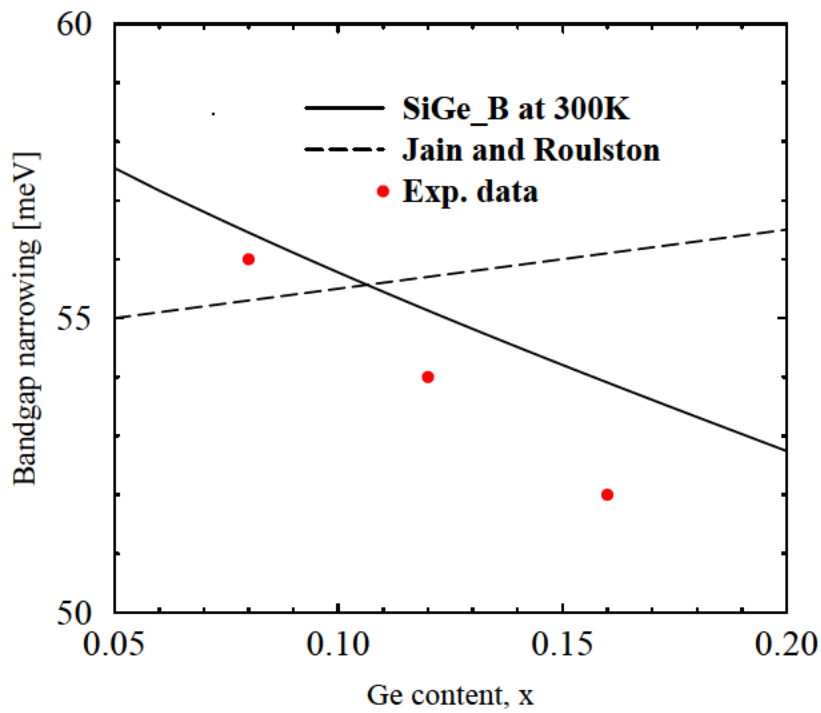
Fig. 3.26: Ge-content dependence in p-SiGe compared to experimental data
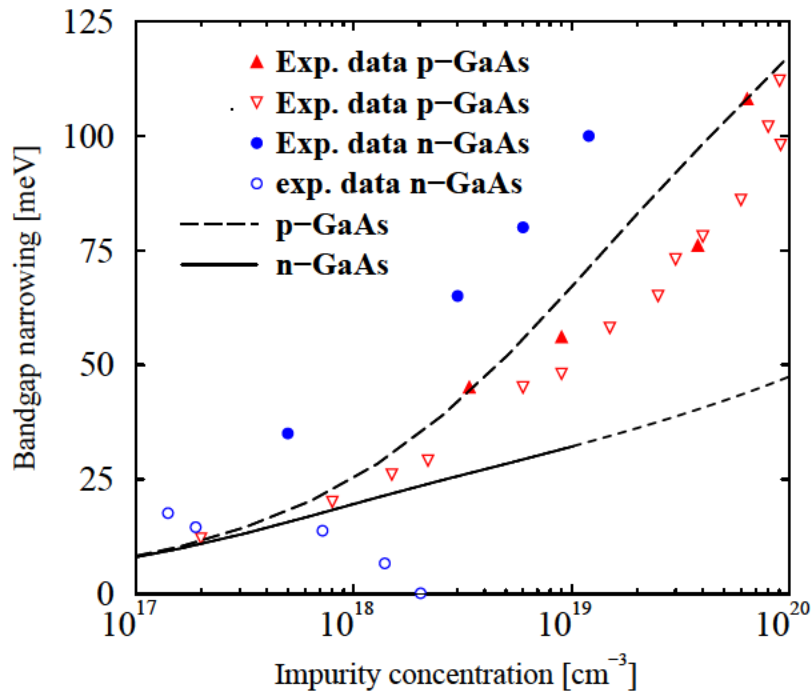
Fig. 3.27: BGN in GaAs compared to experimental data
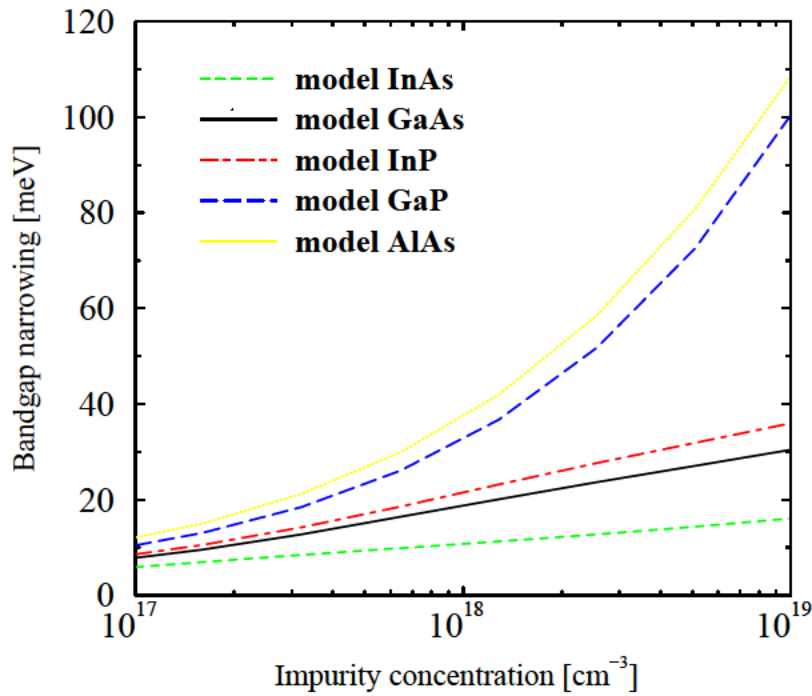
Fig. 3.28: BGN for various n-type binary compounds

our model delivers. This confirms the importance of modeling BGN in III-V semiconductors, instead of leaving this effect unconsidered, which is the case with most device simulators.

Experiments showed higher BGN in n-InP than in n-GaAs [149]. Higher conduction band density of states and lower relative permittivity explain the expected higher values for BGN in AlAs and GaP (Fig. 3.28) than in InP, GaAs, and InAs. The parameter values are taken from [108]. The model is physics-based and contains no free parameters except the ratio $\Delta E_C/\Delta E_g$ used in (3.74).

3.3.4 Effective Carrier Mass

In this work, parabolic conduction and valence bands are assumed, and the effects of band non-parabolicity are assumed to be negligible. Therefore, effective masses for each of the three conduction band minima (Γ, X, and L) can be defined and used to calculate the density of states (DOS). The DOS in the valence band can be characterized by the effective masses of three sub-bands, all in the center of the *Brillouin* zone: two degenerate sub-bands of light and heavy holes, and the split-off sub-band. The contribution of the split-off band, which is depressed in energy and is much less populated, is neglected in this work.

The effective DOS masses scaled by the free electron mass give relative carrier masses. In materials with direct bandgap the value of the relative mass for electrons from the Γ valley is considered. In the case of materials with indirect bandgaps namely Si, Ge, AlAs, and GaP the transverse and the longitude electron masses (m_{nt} and m_{nl}) from the X valley (respectively L valley for Ge) are taken into account by (3.86). For all materials the hole masses are calculated by (3.87) accounting for the heavy and the light hole masses (m_{pl} and m_{ph}) [86].

$$
m_{0,n} = \begin{cases} m_\Gamma & \text{for GaAs, InAs, and InP} \\ m_X = \left(m_{nt}^2 \cdot m_{nl}\right)^{1/3} & \text{for Si, AlAs, and GaP} \\ m_L = \left(m_{nt}^2 \cdot m_{nl}\right)^{1/3} & \text{for Ge} \end{cases}
\tag{3.86}
$$

$$
m_{0,p} = \left(m_{pl}^{3/2} + m_{ph}^{3/2}\right)^{2/3}
\tag{3.87}
$$

The model parameters m_Γ, m_{nt}, m_{nl}, m_{ph}, and m_{pl} are summarized in Table 3.16. In addition, the calculated values for m_X and $m_{0,p}$ are included, after comparison to calculated values reported in literature.

| Material	m_Γ	m_L	m_X	m_{nt}	m_{nl}	$m_{0,p}$	m_{ph}	m_{pl}	References
Si			0.328	0.19	0.98	0.55	0.49	0.16	[90, 86, 85]
Ge		0.222	0.42	0.082	1.64	0.28	0.29	0.04	[90, 86, 85, 94]
GaAs	0.067		0.471	0.229	1.987	0.49	0.49	0.08	[117, 86, 115, 150]
AlAs	0.15		0.38	0.19	1.5	0.81	0.76	0.16	[108, 71]
InAs	0.023		0.64	0.271	3.619	0.41	0.41	0.025	[86, 85, 88, 94]
InP	0.077		0.462	0.273	1.321	0.64	0.6	0.12	[108, 71, 92, 94]
GaP	0.15		0.5	0.25	1.993	0.6	0.79	0.14	[85, 94, 73, 91]

Table 3.16: Parameter values for modeling the effective carrier masses

The temperature dependence of the relative carrier masses is well studied in the case of Si (see [120] and references therein). However, for III-V materials such data are scattering or missing and the effect is often neglected. A linear temperature dependence (3.88) is sufficient to model the relative electron masses for all materials [151]. A quadratic temperature dependence model (3.89) is introduced for the relative hole masses, as the simplest expression sufficient to fit well the data for Si. Table 3.17 summarizes the values of the model parameters. The values of $m_{0,n}$ shown in brackets are not taken into account for *basic materials*. They are used in the calculation of the relative electron masses in *alloy materials*.

Material	Minimum	$m_{0,n}$	$m_{1,n}$	$m_{0,p}$	$m_{1,p}$	$m_{2,p}$
Si	X	0.321	0.009	0.55	0.6	-0.1
Ge	L (X)	0.2158 (0.42)	0.0068	0.2915	0.1	
GaAs	Γ (X)	0.067 (0.471)	-0.0036	0.49		
AlAs	X (Γ)	0.38 (0.15)	-0.0036	0.8		
InAs	Γ (X)	0.0237 (0.64)	-0.0027	0.41		
InP	Γ (X)	0.077 (0.462)	-0.004	0.64		
GaP	X (Γ)	0.5 (0.15)		0.6		

Table 3.17: Parameter values for modeling the effective carrier masses

$$m_n = m_{0,n} + m_{1,n} \cdot \left(\frac{T_L}{300 \text{ K}} \right) \tag{3.88}$$

$$m_p = m_{0,p} + m_{1,p} \cdot \left(\frac{T_L}{300 \text{ K}} \right) + m_{2,p} \cdot \left(\frac{T_L}{300 \text{ K}} \right)^2 \tag{3.89}$$

For *alloy materials* a temperature dependence is introduced first. Then a quadratic interpolation of the masses is used as a function of the material composition of an alloy $A_{1-x}B_x$.

$$m_\nu^{AB} = m_\nu^A \cdot (1 - x) + m_\nu^B \cdot x + C_{m,\nu} \cdot (1 - x) \cdot x \tag{3.90}$$

$C_{m,\nu}$ are bowing parameters summarized in Table 3.18.

Material	$C_{m,n}$	$C_{m,p}$	Reported Range	References
SiGe	-0.183	-0.096		
AlGaAs	0.0	0.0		[110, 93]
InGaAs	-0.012	-0.03	0.038-0.044	[152, 93, 153] x=0.53
InAlAs	0.0	0.0	0.070-0.083	[102, 93, 111, 153] x=0.52
InAsP	0.0	0.0		
GaAsP	0.0	0.0		
InGaP	0.0	0.0	0.092-0.118	[103, 154, 155, 156] x=0.5

Table 3.18: Bowing parameter values for modeling the effective carrier masses

For materials where the bandgap changes between direct and indirect the relative electron mass of the lowest band is considered. Such examples are AlGaAs (Fig. 3.29), InAlAs (Fig. 3.30), InGaP (Fig. 3.31), and GaAsP. For other materials, such as InGaAs (Fig. 3.32) and InAsP only the Γ valley masses are considered. For SiGe a strained bandgap without X-to-L transition is assumed and only the X-valley masses are used in the interpolation.
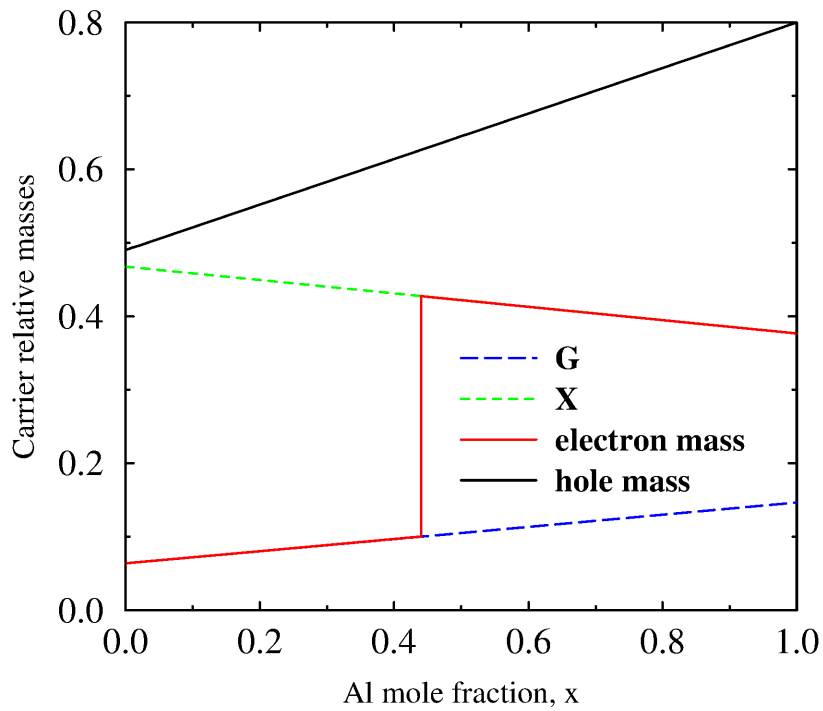
Fig. 3.29: Relative masses of electrons and holes in AlGaAs as a function of the material composition
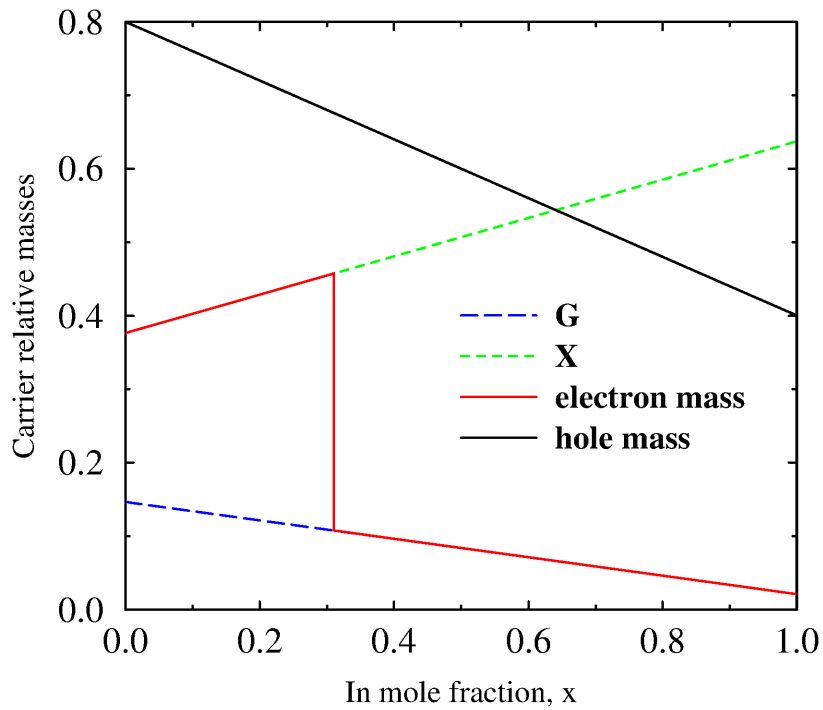
Fig. 3.30: Relative masses of electrons and holes in InAlAs as a function of the material composition
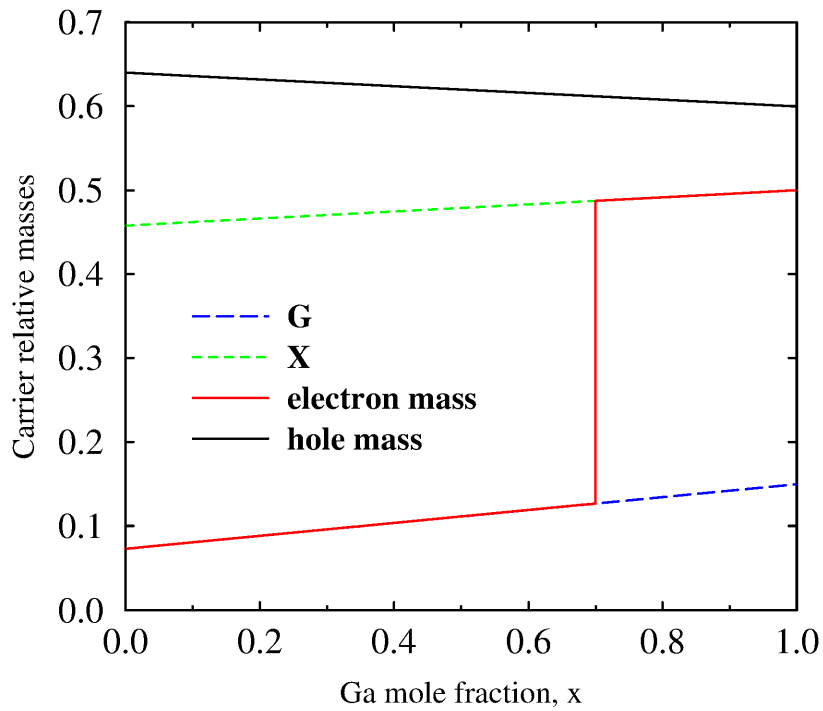
Fig. 3.31: Relative masses of electrons and holes in InGaP as a function of the material composition
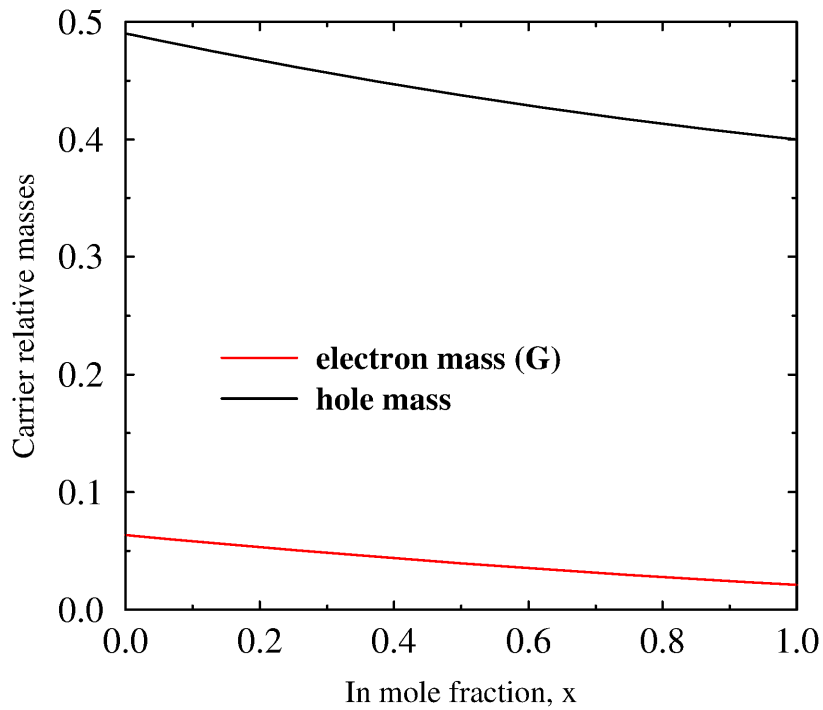
Fig. 3.32: Relative masses of electrons and holes in InGaAs as a function of the material composition

3.3.5 Effective Density of States

The effective density of states (DOS) in the conduction and the valence bands are expressed by the following theoretical expressions [86]:

$$N_C = 2 \cdot M_C \cdot \left(\frac{2 \cdot \pi \cdot m_n \cdot k_B \cdot T_{\mathrm{L}}}{h^2} \right)^{3/2} \tag{3.91}$$

$$N_V = 2 \cdot \left(\frac{2 \cdot \pi \cdot m_p \cdot k_B \cdot T_{\mathrm{L}}}{h^2} \right)^{3/2} \tag{3.92}$$

M_C represents the number of equivalent energy minima in the conduction band.

Material	M_C	Material	M_C
Si	6	InAs	1
Ge	4	InP	1
GaAs	1	GaP	3
AlAs	3		

Table 3.19: Parameter values for energy minima in the DOS model

For Si an alternative model based on data after *Green* [120] is implemented, which is based on a second order polynomial fit.

$$N_{C,V} = N_{0,\nu} + N_{1,\nu} \cdot \left(\frac{T_{\mathrm{L}}}{300 \ \mathrm{K}} \right) + N_{2,\nu} \cdot \left(\frac{T_{\mathrm{L}}}{300 \ \mathrm{K}} \right)^2 \tag{3.93}$$

Material	$N_{0,n}[\mathrm{cm}^{-3}]$	$N_{1,n}[\mathrm{cm}^{-3}]$	$N_{2,n}[\mathrm{cm}^{-3}]$	$N_{0,p}[\mathrm{cm}^{-3}]$	$N_{1,p}[\mathrm{cm}^{-3}]$	$N_{2,p}[\mathrm{cm}^{-3}]$
Si	-0.14e19	1.56e19	1.44e19	-0.17e19	0.93e19	2.34e19

Table 3.20: Parameter values for modeling the effective carrier masses

In the model for *alloy materials* effective carrier masses of the constituents are used in the expressions (3.91) and (3.92).

In the case of a transition between a direct and an indirect bandgap in III-V ternary compounds the valley degeneracy factor M_C is modeled by an expression equivalent to the one proposed in [157].

$$M_C = M_C^{\mathrm{d}} \cdot \exp \left(\frac{E_{\mathrm{g}} - E_{\mathrm{g,\Gamma}}}{k_{\mathrm{B}} \cdot T_L} \right) + M_C^{\mathrm{i}} \cdot \exp \left(\frac{E_{\mathrm{g}} - E_{\mathrm{g,X}}}{k_{\mathrm{B}} \cdot T_L} \right) \tag{3.94}$$

The superscripts d and i denote direct and indirect, respectively.
In the case of SiGe the splitting of the valley degeneracy due to strain is modeled accordingly as in [158].

$$M_C = M_C^{\mathrm{Si}} \cdot \exp \left(-\frac{\delta E_C}{k_{\mathrm{B}} \cdot T_L} \cdot x \right) + M_C^{\mathrm{Ge}} \cdot \left(1 - \exp \left(-\frac{\delta E_C}{k_{\mathrm{B}} \cdot T_L} \cdot x \right) \right) \tag{3.95}$$

Here, δE_C denotes the energy difference between the valleys shifted down and up in energy, respectively. It is set equal to 0.6 eV as given in [158].

3.4 Carrier Mobility

Electron and hole mobilities, μ_n and μ_p, are among the most important carrier transport parameters. They are basic inputs for expressing the current in the semiconductor.

Carrier mobilities are influenced by several physical mechanisms, such as scattering by interaction with thermal lattice vibrations, charged or neutral impurities, lattice defects, and surfaces. For *alloy materials* also alloy scattering mechanism has to be accounted for.

For Si the established mobility model of MINIMOS 6 [43] is used. For a more detailed discussion see [159, 160]. The approach is extended for all other semiconductor materials. The mobility models have to support both the DD and the HD transport models. While the low-field mobility is independent of the transport model used, the high-field mobility is modeled in a different way. Thus, the various effects affecting the mobility are grouped into low-field effects, including the impact of lattice scattering, ionized impurities scattering, and surface scattering, and high-field effects, respectively.

3.4.1 Lattice Mobility

At finite temperature the lattice atoms oscillate about their equilibrium sites. The carriers are scattered and this results in a temperature dependent mobility μ^{L}. The superscript L stands for lattice scattering. The temperature dependence of the lattice mobility is modeled by a power law for all semiconductors.

$$\mu_\nu^{\mathrm{L}} = \mu_{\nu,300}^{\mathrm{L}} \cdot \left(\frac{T_{\mathrm{L}}}{300 \ \mathrm{K}} \right)^{\gamma_{0,\nu}}, \qquad \nu = n, p \tag{3.96}$$

The parameter values used in this model for electrons and holes, respectively, are summarized in Table 3.21.

Material	ν	$\mu_{\nu,300}^{\mathrm{L}}$ [cm^2/Vs]	$\gamma_{0,\nu}$	Range	References
Si	n	1430	-2	1500	[86, 90, 85]
	p	460	-2.18	450-500	[86, 90, 85]
Ge	n	3800	-1.66	3900	[86, 90, 85, 161]
	p	1800	-2.33	1900	[86, 90, 85, 161]
GaAs	n	8500	-2.2	8500-9400	[86, 117, 85, 162]
	p	800	-0.9	400-492	[86, 117, 85, 162]
AlAs	n	410	-2.1	400-1200	[162, 117, 85]
	p	130	-2.2	130-420	[93, 117, 85]
InAs	n	32500	-1.7	22600-34000	[117, 86, 92, 162]
	p	510	-2.3	200 - 530	[117, 86, 92, 162]
InP	n	5300	-1.9	4200-5400	[117, 86, 91]
	p	200	-1.2	130-180	[117, 86, 85]
GaP	n	210	-1.94	110-300	[86, 92, 91, 85]
	p	160	-2.0	75-150	[86, 117]

Table 3.21: Parameter values for the lattice mobility

3.4.2 Ionized Impurity Scattering

In semiconductor devices mobility reduction due to ionized impurity scattering is a dominant effect. The influence of lattice and impurity scattering must be combined to obtain an effective mobility μ^{LI}. In MINIMOS-NT the following models are available.

Mobility Model of MINIMOS 6
To account for mobility reduction due to ionized impurity scattering, the formula of *Caughey* and *Thomas* [163] is used in conjunction with temperature dependent coefficients. C_{I} denotes the concentration of ionized impurities. The model is well applicable for Si.

$$\mu_\nu^{\mathrm{LI}} = \mu_\nu^{\min} + \frac{\mu_\nu^{\mathrm{L}} - \mu_\nu^{\min}}{1 + \left(\dfrac{C_{\mathrm{I}}}{C_\nu^{\mathrm{ref}}}\right)^{\alpha_\nu}} \tag{3.97}$$

$$\mu_\nu^{\min} = \begin{cases} \mu_{\nu,300}^{\min} \cdot \left(\dfrac{T_{\mathrm{L}}}{300\ \mathrm{K}}\right)^{\gamma_{1,\nu}} & T \geq 200\ \mathrm{K} \\[3ex] \mu_{\nu,300}^{\min} \cdot \left(\dfrac{2}{3}\right)^{\gamma_{1,\nu}} \cdot \left(\dfrac{T_{\mathrm{L}}}{200\ \mathrm{K}}\right)^{\gamma_{2,\nu}} & T < 200\ \mathrm{K} \end{cases} \tag{3.98}$$

$$C_\nu^{\mathrm{ref}} = C_{\nu,300}^{\mathrm{ref}} \cdot \left(\frac{T_{\mathrm{L}}}{300\ \mathrm{K}}\right)^{\gamma_{3,\nu}} \tag{3.99}$$

$$\alpha_\nu = \alpha_{\nu,300} \cdot \left(\frac{T_{\mathrm{L}}}{300\ \mathrm{K}}\right)^{\gamma_{4,\nu}} \tag{3.100}$$

Simpler expressions are applied to other *basic materials*. By setting $\gamma_{1,\nu} = \gamma_{2,\nu}$ and $\gamma_{4,\nu} = 0$, (3.98) and (3.100), respectively, reduce to

$$\mu_\nu^{\min} = \mu_{\nu,300}^{\min} \cdot \left(\frac{T_{\mathrm{L}}}{300\ \mathrm{K}}\right)^{\gamma_{1,\nu}} \tag{3.101}$$

$$\alpha_\nu = \alpha_{\nu,300} \tag{3.102}$$

The model parameter values are summarized in Table 3.22. The results delivered by the model for the hole mobility as a function of the doping concentration for various III-V group binary semiconductors compared to measured data are shown in Fig. 3.33.

Model for Majority and Minority Electrons
Though numerous theoretical and experimental papers [164, 165, 166] on electron mobility in semiconductors have been published there are still some issues under discussion, particularly in the very high doping regime. The difference between majority and minority electron mobility is a well-known phenomenon caused by effects such as degeneracy and the different screening behavior of electrons and holes in semiconductors. However, the mobility models usually employed in device modeling do not reflect these facts.

One of the basic assumptions in the models for ionized-impurity scattering is that the charge of an impurity center is treated as a point charge. In the approach from [140] it was shown that considering the spatial extent of the charge density one can explain various doping effects due to the chemical nature of the dopant at high doping concentrations. In [140] Monte-Carlo

Material	ν	$\mu_{\nu,300}^{min}$ [cm^2/Vs]	$\gamma_{1,\nu}$	$\gamma_{2,\nu}$	$C_{\nu,300}^{ref}$ [cm^{-3}]	$\gamma_{3,\nu}$	$\alpha_{\nu,300}$	$\gamma_{4,\nu}$
Si	n	80	-0.45	-0.15	1.12e17	3.2	0.72	0.065
	p	45	-0.45	-0.15	2.23e17	3.2	0.72	0.065
Ge	n	850			2.6e17		0.56	0.0
	p	300			1.0e17		1.0	0.0
GaAs	n	800	-0.9	-0.9	1.0e17	6.2	0.5	0.0
	p	40			1.0e17	0.5	1.0	0.0
AlAs	n	10			1.0e17		0.5	0.0
	p	5			2.9e17	0.5	1.0	0.0
InAs	n	11700	-0.33	-0.33	4.4e16	3.6	0.5	0.0
	p	48			2.55e17	0.5	1.0	0.0
InP	n	1520	2.0	2.0	6.4e16	3.7	0.5	0.0
	p	24	1.2	1.2	2.5e17	0.47	1.0	0.0
GaP	n	76	-1.07	-1.07	2.85e17	1.8	0.5	0.0
	p	27			2.33e17		1.0	0.0

Table 3.22: Parameter values for the impurity mobility

(MC) simulation results for the low-field mobility in silicon, covering arbitrary finite concentrations, temperatures and dopants are presented (see Fig. 3.34 and Fig. 3.35). The minority mobility at doping levels above 10^{19} cm^{-3} exceeds the majority mobility more than three times at 300 K. The difference gets even stronger at low temperatures (up to sixteen times).

A model which distinguishes between the majority and minority electrons in Si, as well as between dopant species is described in [167, 168, 66]. Although initially proposed for the majority electron mobility in Si

$$\mu_n^{LI} = \frac{\mu_n^L - \mu_1 - \mu_2}{1 + \left(\frac{C_I}{C_1}\right)^\alpha} + \frac{\mu_1}{1 + \left(\frac{C_I}{C_2}\right)^\beta} + \mu_2 \tag{3.103}$$

offers enough flexibility to model also the minority electron mobility in Si (see Fig. 3.36). In general, it can be applied also for any other material of interest (Fig. 3.37, Fig. 3.38). (3.103) is similar to (3.97), a function with two extreme values (μ^L as a maximum and μ_1 as a minimum mobility). (3.103) is a mathematical function which can deliver a second maximum or minimum at very high impurity concentrations depending on the sign of μ_1. Thus, it allows both majority and minority carrier mobilities to be properly modeled.

In [169] an automated parameter extraction using an optimizer [170] for the mobility models was presented. Most of the existing experimental data on the low-field mobility together with accurate MC simulations for Si [140] and for III-V semiconductor compounds [128, 171, 172] are used as input. The temperature dependence of the lattice mobility μ_n^L preserves the expression (3.96). The majority electron mobility μ_n^{maj} is modeled as a function of the donor concentration N_D and the lattice temperature. The temperature dependence of the
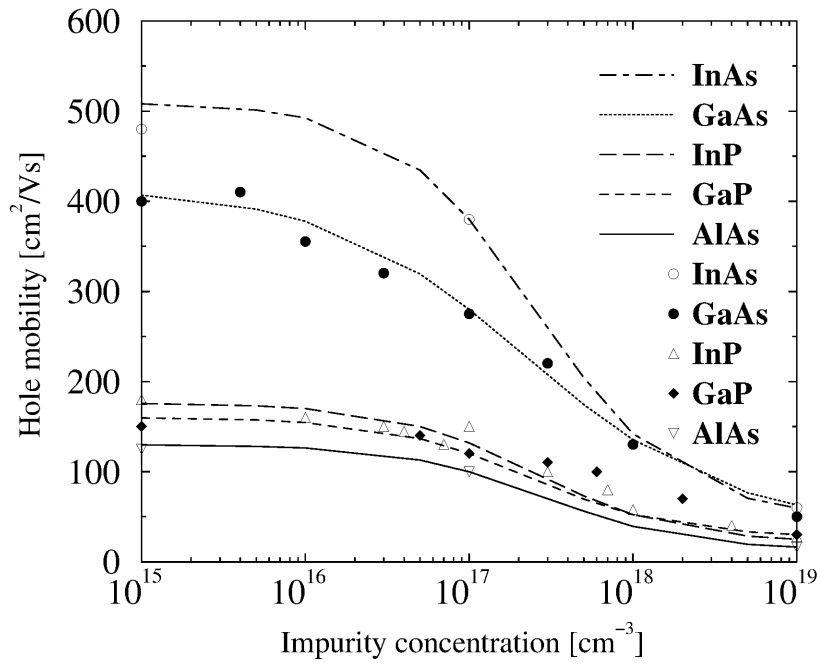
Fig. 3.33: Hole mobility vs. doping concentration at 300 K: Comparison between the model and experimental data

parameters μ_1, μ_2, C_1, C_2, α, and β is modeled by simple power laws.

$$\mu_n^{\mathrm{maj}} = \frac{\mu_n^{\mathrm{L}} - \mu_1 - \mu_2}{1 + \left(\frac{N_\mathrm{D}}{C_1}\right)^\alpha} + \frac{\mu_1}{1 + \left(\frac{N_\mathrm{D}}{C_2}\right)^\beta} + \mu_2 \tag{3.104}$$

$$\mu_1 = \mu_{1,300}^{\mathrm{maj}} \cdot \left(\frac{T_\mathrm{L}}{300\ \mathrm{K}}\right)^{\gamma_1} \tag{3.105}$$

$$\mu_2 = \mu_{2,300}^{\mathrm{maj}} \cdot \left(\frac{T_\mathrm{L}}{300\ \mathrm{K}}\right)^{\gamma_2} \tag{3.106}$$

$$\alpha = \alpha_{300} \cdot \left(\frac{T_\mathrm{L}}{300\ \mathrm{K}}\right)^{\gamma_3} \tag{3.107}$$

$$\beta = \beta_{300}^{\mathrm{maj}} \cdot \left(\frac{T_\mathrm{L}}{300\ \mathrm{K}}\right)^{\gamma_4} \tag{3.108}$$

$$C_1 = C_{1,300} \cdot \left(\frac{T_\mathrm{L}}{300\ \mathrm{K}}\right)^{\gamma_5} \tag{3.109}$$

$$C_2 = C_{2,300}^{\mathrm{maj}} \cdot \left(\frac{T_\mathrm{L}}{300\ \mathrm{K}}\right)^{\gamma_6} \tag{3.110}$$

The minority electron mobility μ_n^{min} is modeled as a function of the acceptor concentration N_A and the lattice temperature. The parameters C_1 and α preserve the values from (3.108) and (3.110), respectively. The new parameters μ_1, μ_2, C_2, and β, used in the calculation of
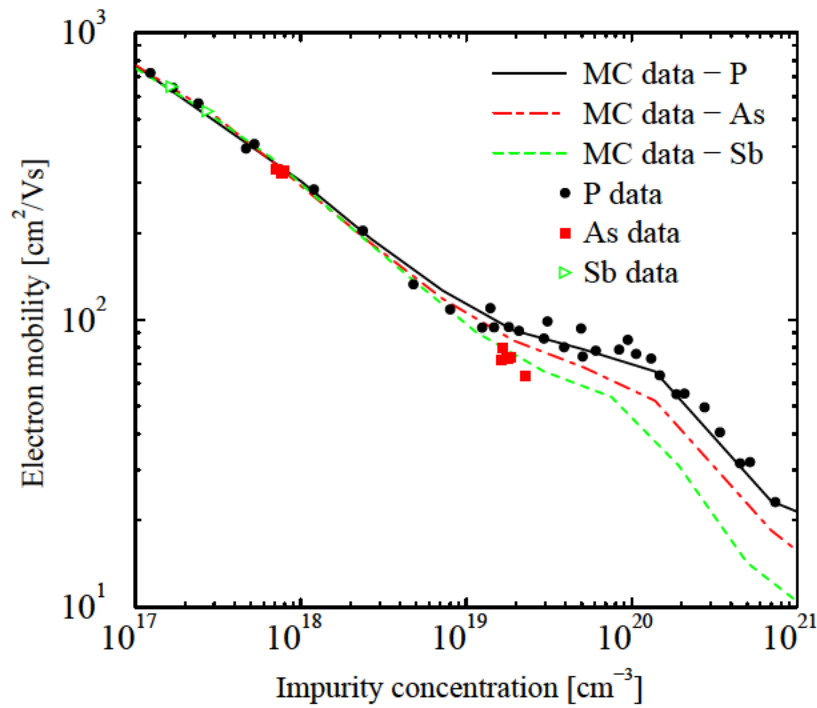
Fig. 3.34: Majority mobility in P-, As- and Sb-doped silicon at 300 K: Comparison between MC simulation data and experimental data
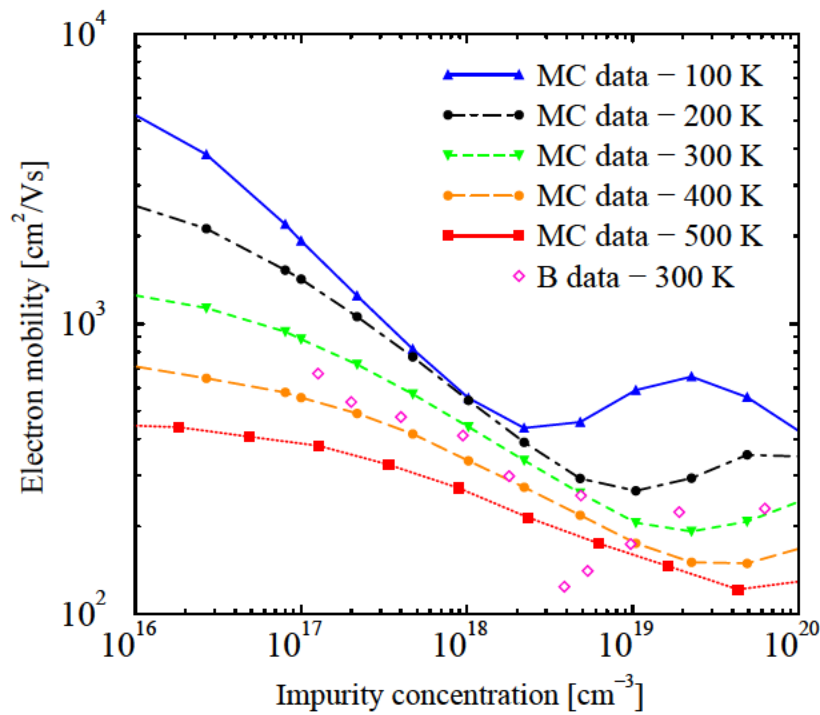
Fig. 3.35: Minority mobility in B-doped silicon as a function of concentration: MC simulation data at different temperatures
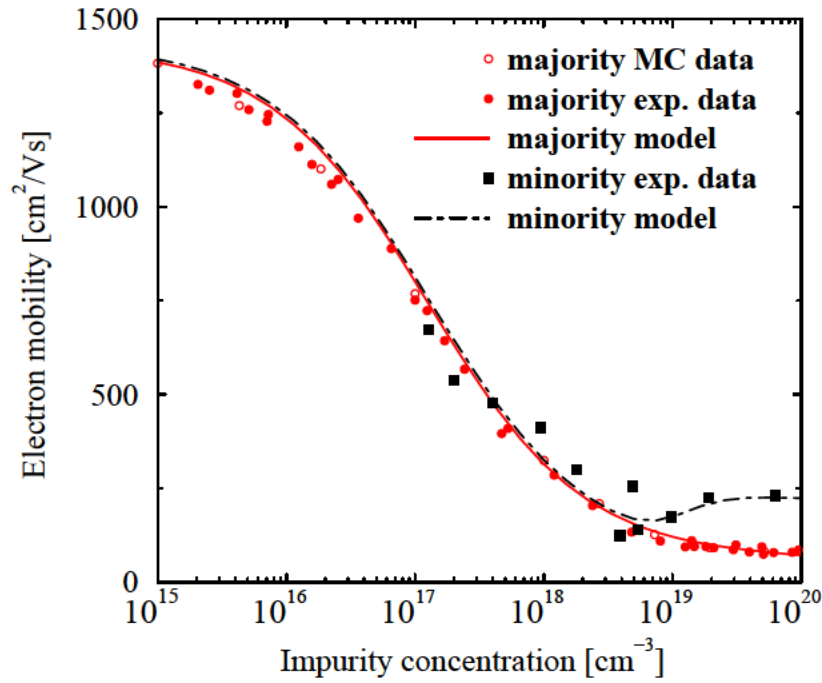
Fig. 3.36: Comparison of the analytical model and MC data for electron mobility in Si at 300 K
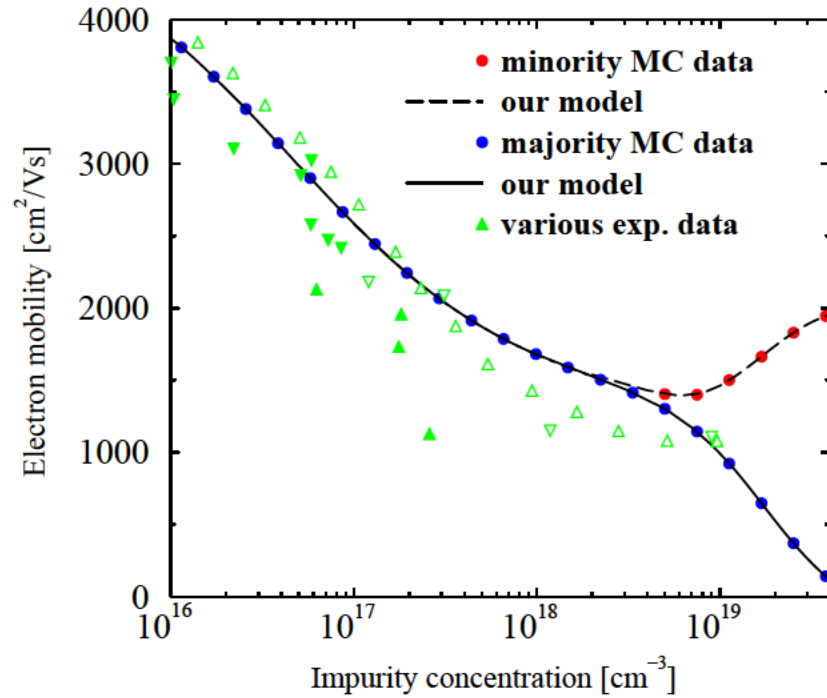
Fig. 3.37: Comparison of the analytical model and MC data for electron mobility in InP at 300 K
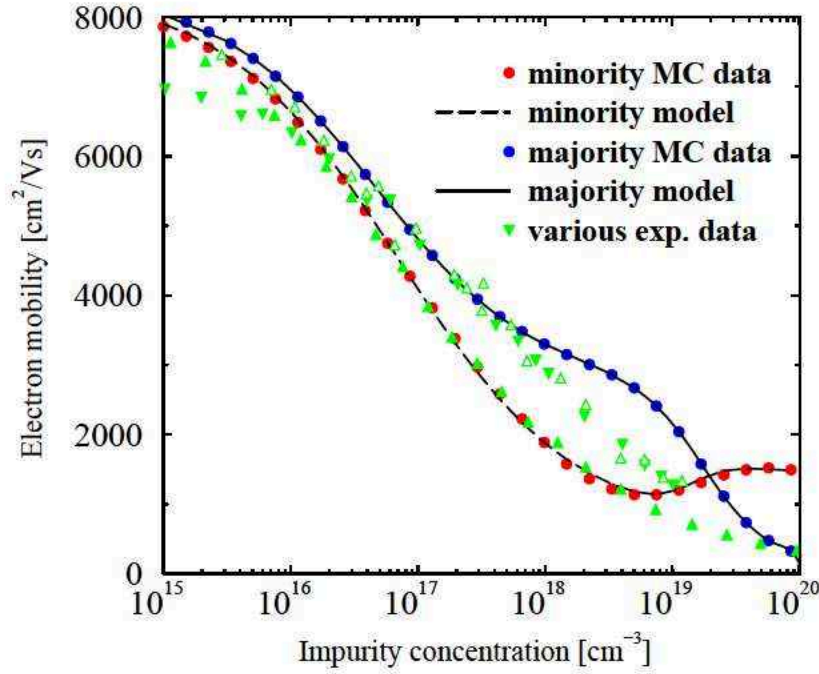
Fig. 3.38: Comparison of the analytical model and MC data for electron mobility in GaAs at 300 K

$\mu_n^{\min}$, again follow simple power laws as a function of temperature.

$$\mu_n^{\min} = \frac{\mu_n^{\mathrm{L}} - \mu_1 - \mu_2}{1 + \left(\dfrac{N_{\mathrm{A}}}{C_1}\right)^{\alpha}} + \frac{\mu_1}{1 + \left(\dfrac{N_{\mathrm{A}}}{C_2}\right)^{\beta}} + \mu_2 \tag{3.111}$$

$$\mu_1 = \mu_{1,300}^{\min} \cdot \left(\frac{T_{\mathrm{L}}}{300 \text{ K}}\right)^{\gamma_7} \tag{3.112}$$

$$\mu_2 = \mu_{2,300}^{\min} \cdot \left(\frac{T_{\mathrm{L}}}{300 \text{ K}}\right)^{\gamma_8} \tag{3.113}$$

$$\beta = \beta_{300}^{\min} \cdot \left(\frac{T_{\mathrm{L}}}{300 \text{ K}}\right)^{\gamma_9} \tag{3.114}$$

$$C_2 = C_{2,300}^{\min} \cdot \left(\frac{T_{\mathrm{L}}}{300 \text{ K}}\right)^{\gamma_{10}} \tag{3.115}$$

To account for a superposition of doping profiles a harmonic mean is used [168].

$$\mu_n^{\mathrm{LI}} = \left(\frac{1}{\mu_n^{\mathrm{maj}}} + \frac{1}{\mu_n^{\min}} - \frac{1}{\mu_n^{\mathrm{L}}}\right)^{-1} \tag{3.116}$$

The model parameters used for Si in the range 70-500 K and for GaAs and InP at 300 K are summarized in Table 3.23.

Parameter	Si	GaAs	InP	Unit
$\mu_{1,300}^{maj}$	52	2590	1140	cm^2/Vs
γ_1	-0.18	–	–	
$\mu_{2,300}^{maj}$	8	133	20	cm^2/Vs
γ_2	-1.49	–	–	
$\mu_{1,300}^{min}$	-200	-750	-742	cm^2/Vs
γ_7	-0.58	–	–	
$\mu_{2,300}^{min}$	230	1400	1920	cm^2/Vs
γ_8	-1.02	–	–	
α_{300}	0.7	0.7	0.6	
γ_3	0.02	–	–	
β_{300}^{maj}	5.33	1.7	2.5	
γ_4	-9.5	–	–	
β_{300}^{min}	2.0	2.8	3.2	
γ_9	-1.2	–	–	
$C_{1,300}$	1.17e17	0.5e17	4e16	cm^{-3}
γ_5	3.55	–	–	
$C_{2,300}^{maj}$	5.8e20	1.8e19	1.6e19	cm^{-3}
γ_6	0.134	–	–	
$C_{2,300}^{min}$	1.0e19	1.4e19	1.6e19	cm^{-3}
γ_{10}	0.12	–	–	

Table 3.23: Parameter values for the majority/minority impurity mobility

Masetti Mobility Model

The *Masetti* bulk mobility model [173] is a default mobility model in several device simulators, e.g. [40, 41]. It can be treated as a simple case of (3.97), only valid at 300 K.

$$\mu_\nu^{LI} = \mu_{min1} \cdot \exp\left(\frac{-P_c}{C_I}\right) + \frac{\mu_{300}^L - \mu_{min2}}{1 + \left(\frac{C_I}{C_r}\right)^\alpha} - \frac{\mu_1}{1 + \left(\frac{C_s}{C_I}\right)^\beta} \tag{3.117}$$

It can be useful to compare some of the parameters from the majority mobility model at 300 K to the default values of the *Masetti* model (without $P_c = 0$) as it is shown in Table 3.24.

Parameter	Si	Parameter	Masetti	Unit
$\mu_{1,300}^{maj}$	52	$-\mu_1$	-56.1	cm^2/Vs
$\mu_{2,300}^{maj}$	8	μ_{min1}	68.5	cm^2/Vs
$\mu_{1,300}^{maj} + \mu_{2,300}^{maj}$	60	μ_{min2}	68.5	cm^2/Vs
$C_{1,300}$	1.17e17	C_r	9.2e16	cm^{-3}
$C_{2,300}^{maj}$	5.8e20	C_s	3.4e20	cm^{-3}
α	0.7	α	0.711	
β	5.33	$-\beta$	-1.98	

Table 3.24: Comparison between model parameters for majority electrons in Si at 300 K and the parameter values for the Masetti impurity mobility model

3.4.3 Surface scattering

Mobility Model of MINIMOS 6
Surface scattering is modeled by the following empirical expression [160]

$$\mu_\nu^{\mathrm{LIS}} = \frac{\mu_\nu^{\mathrm{ref}} + (\mu_\nu^{\mathrm{LI}} - \mu_\nu^{\mathrm{ref}}) \cdot (1 - F(y))}{1 + F(y) \cdot \left(\frac{S_\nu}{S_\nu^{\mathrm{ref}}}\right)^{\gamma_{6,\nu}}}, \tag{3.118}$$

$$\mu_\nu^{\mathrm{ref}} = \mu_{\nu,300}^{\mathrm{ref}} \cdot \left(\frac{T_{\mathrm{L}}}{300\ \mathrm{K}}\right)^{-\gamma_{5,\nu}}, \tag{3.119}$$

The function $F(y)$ depending on the surface distance y describes a smooth transition between the surface and bulk mobility [174, 175]. The parameter y^{ref} describes a critical length.

$$F(y) = \frac{2 \cdot \exp\left(-\left(\frac{y}{y^{\mathrm{ref}}}\right)^2\right)}{1 + \exp\left(-2 \cdot \left(\frac{y}{y^{\mathrm{ref}}}\right)^2\right)} \tag{3.120}$$

The pressing forces S_n and S_p in (3.118) are equal to the magnitude of the normal field strength at the interface if the carriers are attracted by the interface, otherwise zero.

Parameter	electrons	holes	Unit
$\mu_{\nu,300}^{\mathrm{ref}}$	638	240	cm^2/Vs
$\gamma_{5,\nu}$	-1.19	-1.09	
y^{ref}	10	10	nm
S_ν^{ref}	7e7	2.7e7	V/m
$\gamma_{6,\nu}$	1.69	1.0	

Table 3.25: Parameter values for surface mobility reduction in Si - MINIMOS 6 model

Lombardi Mobility Model
Lombardi et al. [176] suggested another surface mobility degradation model. There are two surface scattering contributions due to acoustic phonons, μ_{ac}, and surface roughness, μ_{sr}. They are functions of total doping concentration C_I and the pressing forces S_n and S_p.

$$\mu_\nu^{\mathrm{ac}} = \frac{B_{\nu,300}}{S_\nu} + \frac{C_{\nu,300} \cdot C_I^{L_{\nu,300}}}{S_\nu^{1/3} \cdot T_L} \qquad \nu = n, p \tag{3.121}$$

$$\mu_\nu^{\mathrm{sr}} = \frac{D_{\nu,300}}{S_\nu^2} \tag{3.122}$$

The total mobility is expressed by a *Mathiessen* rule:

$$\frac{1}{\mu_\nu^{\mathrm{LIS}}} = \frac{1}{\mu_\nu^{\mathrm{LI}}} + \frac{1}{\mu_\nu^{\mathrm{ac}}} + \frac{1}{\mu_\nu^{\mathrm{sr}}} \tag{3.123}$$

Parameter	electrons	holes	Unit
$B_{\nu,300}$	4.75e7	9.925e6	cm/s
$C_{\nu,300}$	580	294.7	$cm^{5/3}/V^{2/3}s$
$L_{\nu,300}$	0.125	0.0317	
$D_{\nu,300}$	5.82e14	2.05e14	V/s

Table 3.26: Parameter values for surface mobility reduction in Si - *Lombardi* model

3.4.4 High-Field Mobility for DD Equations

In the case of Si the mobility reduction due to a high field is modeled by

$$\mu_\nu^{\text{LISF}} = \frac{2 \cdot \mu_\nu^{\text{LIS}}}{1 + \left(1 + \left(\frac{2 \cdot \mu_\nu^{\text{LIS}} \cdot F_\nu}{v_\nu^{\text{sat}}}\right)^{\beta_\nu}\right)^{1/\beta_\nu}} \tag{3.124}$$

$$F_\nu = \left| \operatorname{grad} \psi + \frac{s_\nu}{\nu} \cdot \operatorname{grad}\left(U_{T\nu} \cdot \nu\right) \right| \tag{3.125}$$

$$s_n = -1, \ s_p = +1 \tag{3.126}$$

Here F_ν represents the driving forces for carrier ν, and $U_{T\nu}$ are the carrier temperature voltages. The saturation velocities v_ν^{sat} are calculated in a separate model by (3.134). A more detailed discussion on mobility models for III-V compounds can be found in [177, 178]. For III-V materials two models are available, one giving a monotonic velocity versus field curve, while the other one includes an area with negative differential mobility [179].

$$\mu_\nu^{\text{LIF}}\left(F_\nu\right) = \frac{\mu_\nu^{\text{LI}}}{\left(1 + \left(\frac{\mu_\nu^{\text{LI}} \cdot F_\nu}{v_\nu^{\text{sat}}}\right)^{\beta_\nu}\right)^{1/\beta_\nu}}, \quad \nu = n,p \tag{3.127}$$

$$\mu_n^{\text{LIF}}\left(F_n\right) = \frac{\mu_n^{\text{LI}} + v_n^{\text{sat}} \cdot \dfrac{F_n^{\beta_n-1}}{F_0^{\beta_n}}}{1 + \dfrac{F_n^{\beta_n}}{F_0^{\beta_n}}} \tag{3.128}$$

F_ν represents the driving force and v_ν^{sat} the saturation velocities according to (3.125) and (3.134), respectively. The default parameter values used in (3.124) and (3.127) are summarized in Table 3.27. (3.128) is taken for the electron mobility in III-V materials. It includes

Material	β_n	β_p
Si	2.0	1.0
III-Vs	2.0	1.0

Table 3.27: Parameter values for DD high-field mobility model

an additional model parameter, F_0, which is the critical driving force approximately at which the overshoot in the velocity-field characteristics appear. The default parameter values are summarized in Table 3.28.

Material	β_n	$F_0[\text{V/cm}]$
GaAs	4.0	4e3
AlAs	4.0	4e3
InAs	4.0	2.2e3
InP	3.0	10e3
GaP	2.0	10e3

Table 3.28: Parameter values for DD high-field mobility model

3.4.5 High-Field Mobility for HD Equations

The deviation from the ohmic low-field mobility is modeled as a function of the carrier temperature, T_ν, after *Hänsch* [180].

$$\mu_\nu^{\text{LIST}} = \frac{\mu_\nu^{\text{LIS}}}{1 + \alpha_\nu \cdot (T_\nu - T_{\text{L}})} \tag{3.129}$$

$$\alpha_\nu = \frac{3 \cdot k_B \cdot \mu_\nu^{\text{LIS}}}{2 \cdot q \cdot \tau_\epsilon \cdot (v_\nu^{\text{sat}})^2} \tag{3.130}$$

τ_ϵ denotes the energy relaxation times and v_ν^{sat} are the saturation velocities calculated respectively in (3.138) and in (3.134).

For some III-V semiconductor materials a multi-valley mobility model can be used. In the following model a weighted mean is calculated from the low-field mobilities of the Γ- and L-electrons [181].

$$\mu_n^{\text{LIT}} = \frac{\mu_{n,\Gamma}^{\text{LI}} + \mu_{n,\text{L}}^{\text{LI}} \cdot P_{\text{L}}}{1 + P_{\text{L}}} \tag{3.131}$$

$$P_{\text{L}} = 4 \cdot \left(\frac{m_{\text{L}}}{m_\Gamma}\right)^{3/2} \cdot \exp\left(-\frac{E_{C,\text{L}} - E_{C,\Gamma}}{k_B \cdot T_n}\right) \tag{3.132}$$

P_{L} denotes the ratio of the Γ and L-valley populations [86]. The valley mobilities $\mu_{n,\Gamma}^{\text{LI}}$ and $\mu_{n,\text{L}}^{\text{LI}}$ account for impurity scattering after (3.97), and are constant with respect to the lattice temperature.

Parameter	GaAs	Unit
$\mu_{n,\Gamma}^{\text{L}}$	8000	cm^2/Vs
$\mu_{n,\text{L}}^{\text{L}}$	400	cm^2/Vs
μ_n^{min}	1500	cm^2/Vs
C_n^{ref}	1.426e+17	cm^{-3}
α_n	0.5385	
$\tau_{n,\Gamma}$	1.2	ps
$\tau_{n,\text{L}}$	0.6	ps
$v_{n,\Gamma}^{\text{sat}}$	2.5e5	m/s
$v_{n,\text{L}}^{\text{sat}}$	0.9e5	m/s

Table 3.29: Parameter values for the two-valley HD mobility model

Semiconductor Alloys

In the case of *alloy materials* the model employs the low-field mobilities μ^{LI} of the basic materials (A and B) and combines them by a harmonic mean.

$$\frac{1}{\mu^{\text{AB}}} = \frac{1-x}{\mu^{\text{A}}} + \frac{x}{\mu^{\text{B}}} + \frac{(1-x) \cdot x}{C_\mu} \tag{3.133}$$

C_μ is referred to as nonlinear or bowing parameter.

Material	$C_{\mu,n}$ [cm²/Vs]	$C_{\mu,p}$ [cm²/Vs]
SiGe	1e6	-100
AlGaAs	180	1e6
InGaAs	1e6	1e6
InAlAs	1e6	1e6
InAsP	1e6	1e6
GaAsP	1e6	1e6
InGaP	1e6	1e6

Table 3.30: Parameter values for mobility model for alloy materials

For calculation of the high field mobilities no additional parameters need to be specified for the model. The respective interpolations between the *basic materials* are carried out in the models for the saturation velocities and, in the case of HD simulation, of the energy relaxation times.

3.5 Velocity Saturation

The temperature dependence of the saturation velocities of electrons and holes in *basic materials* is calculated by

$$v_\nu^{\text{sat}} = \frac{v_{\nu,300}^{\text{sat}}}{1 - A\nu + A\nu \cdot \left(\dfrac{T_{\text{L}}}{300 \text{ K}}\right)} \tag{3.134}$$

The following model parameters from [182] are used.

Material	$v_{n,300}^{\text{sat}}$ [m/s]	A_n	$v_{p,300}^{\text{sat}}$ [m/s]	A_p
Si	1.0	0.26	0.704	0.63
Ge	0.7	0.55	0.63	0.61
GaAs	0.72	0.56	0.9	0.41
AlAs	0.85	0.55	0.8	0.3
InAs	0.9	0.57	0.5	0.3
InP	0.67	0.68	0.5	0.3
GaP	0.88	0.30	0.5	0.3

Table 3.31: Parameter values for velocity saturation model

In the case of *alloy materials* the temperature dependent saturation velocities are calculated first using (3.134). For an alloy $A_{1-x}B_x$ the model suggests a quadratic interpolation between the saturation velocities for electrons of the basic materials (A and B) depending on the material composition x. In case of holes a linear interpolation is assumed.

$$v_\nu^{AB} = v_\nu^A \cdot (1-x) + v_\nu^B \cdot x + C_{v,\nu} \cdot (1-x) \cdot x \tag{3.135}$$

The bowing parameters $C_{v,n}$ and $C_{v,p}$ are summarized in the following table.

Material	$C_{v,n}$[m/s]	$C_{v,p}$[m/s]
SiGe	-2.28	0.0
AlGaAs	-0.0512	0.0
InGaAs	-0.196	0.0
InAlAs	-2.13	0.0
InAsP	0.0	0.0
GaAsP	0.0	0.0
InGaP	-0.3	0.0

Table 3.32: Parameter values for velocity saturation model for alloy materials

3.6 Energy Relaxation Time

In this section the models for the energy relaxation times of electrons and holes, in Si, Ge, SiGe, and III-V materials are presented. The energy relaxation times are used in the HD mobility models, in the energy balance equations of the hydrodynamic transport model, and in the lattice heat flow equation.

A constant energy relaxation time ($\tau_{\epsilon,n}$), or a quadratic dependence on the electron temperature [183, 184], are usually assumed. A precise simulation needs to include the dependence of $\tau_{\epsilon,n}$ on the lattice and carrier temperatures.

An empirical model for the electron energy relaxation time has been suggested in [185]. It is based on Monte-Carlo simulation results [94], and is applicable to all relevant diamond and zinc-blende structure semiconductors. The energy relaxation times are expressed as functions of the carrier and lattice temperatures, and in the case of semiconductor alloys of the material composition. The influence of doping concentration is not taken into account.

3.6.1 Methodology

Depending on the semiconductor material under investigation, different results are available from Monte-Carlo simulation. Two methods - direct and indirect - are used to obtain $\tau_{\epsilon,n}$.

The Direct Method

For Si, Ge and GaAs, the dependence of the electron energy relaxation time and the average electron energy, w, on the electric field are available in [94]. The average energy is approximated by the thermal energy, with the kinetic term being neglected:

$$w = \frac{1}{2} \cdot m_n \cdot v_n{}^2 + \frac{3}{2} \cdot k_B \cdot T_n \approx \frac{3}{2} \cdot k_B \cdot T_n \qquad (3.136)$$

where m_n, v_n, and T_n are the electron mass, velocity and temperature, respectively. This approximation, together with the interpolation of the Monte-Carlo simulation results for different electric fields allows to obtain directly $\tau_{\epsilon,n}$ as a function of the electron temperature at different lattice temperatures. This procedure is called direct method.

The Indirect Method

In the case of binary and ternary III-V compounds, such as InAs, AlAs, $In_x Ga_{1-x}As$, and $Al_x Ga_{1-x}As$, the dependence of $\tau_{\epsilon,n}$ on the electric field is not available. In this case $\tau_{\epsilon,n}$ is calculated in an indirect way, using the dependence of the electron velocity on the electric field from [94]. The local energy balance equation [86] is obtained by neglecting the energy flux:

$$\tau_{\epsilon,n} = \frac{3 \cdot k_B}{2 \cdot q} \cdot \frac{T_n - T_L}{v_n \cdot E} \qquad (3.137)$$

where q is the electron charge, T_L the lattice temperature, and E is the electric field. Using (3.136) and the dependences of the average electron energy and the electron velocity on the electric field, $\tau_{\epsilon,n}$ is extracted. This procedure is called indirect method.

Fig. 3.39 shows $\tau_{\epsilon,n}$ for GaAs as a function of the electron temperature at T_L=300 K, as it results from both the direct and indirect methods. The correct values are extracted by the direct method as it is based on less approximations. It turns out that $\tau_{\epsilon,n}$ is overestimated by using (3.137) in the indirect method. Nevertheless, the saturation value of $\tau_{\epsilon,n}$ at high electron temperatures, $\tau_{\epsilon,\text{sat}}$, and the location of the peak, $T_{n,\text{peak}}$, are independent of the methodology used. This criteria are used for correct estimation of $\tau_{\epsilon,n}$ in materials where only the indirect method can be applied.

3.6.2 The Relaxation Time Model

The following expression is used to model the electron relaxation time as a function of the carrier and lattice temperatures:

$$\tau_{\epsilon,n} = \tau_{\epsilon,0} + \tau_{\epsilon,1} \exp\left(C_1 \cdot \left(\frac{T_n}{300 \text{ K}} + C_0 \right)^2 + C_2 \cdot \left(\frac{T_n}{300 \text{ K}} + C_0 \right) + C_3 \cdot \left(\frac{T_L}{300 \text{ K}} \right) \right) (3.138)$$

In case of holes a constant energy relaxation time is assumed.

$$\tau_{\epsilon,p} = \tau_{\epsilon,2} \qquad (3.139)$$

The flexibility of this function allows its easy adaption to all considered materials. For Si, Ge, and III-V binary materials, all parameters in (3.138) are summarized in Table 3.33. In the case of III-V semiconductor alloys the dependence of $\tau_{\epsilon,n}$ on the material composition x is included. $\tau_{\epsilon,0}$ and C_0 are modeled as a quadratic function of x. The parameters are summarized in Table 3.34.
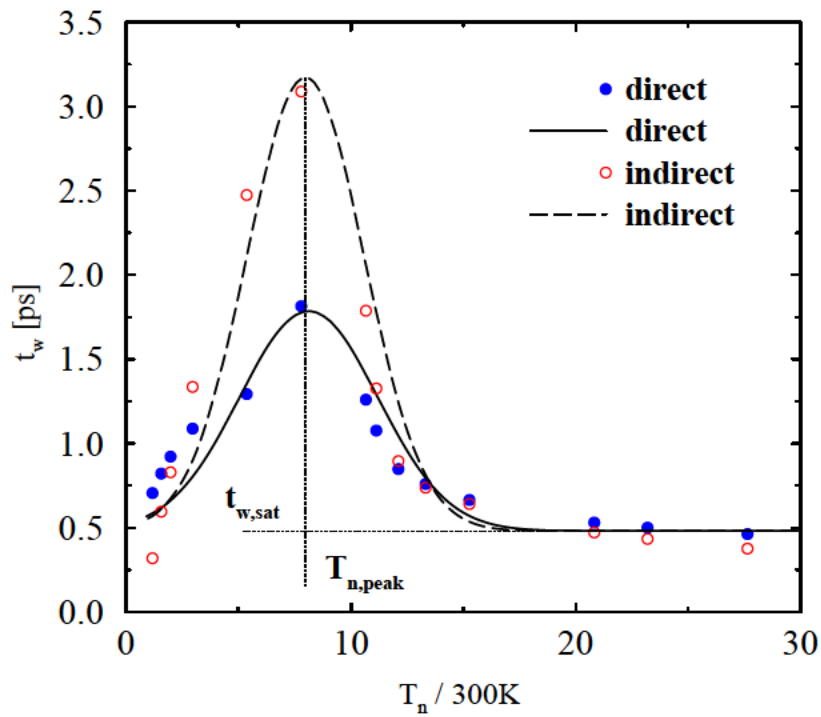
Fig. 3.39: Energy relaxation time as a function of electron temperature: Results from the direct and indirect method for GaAs
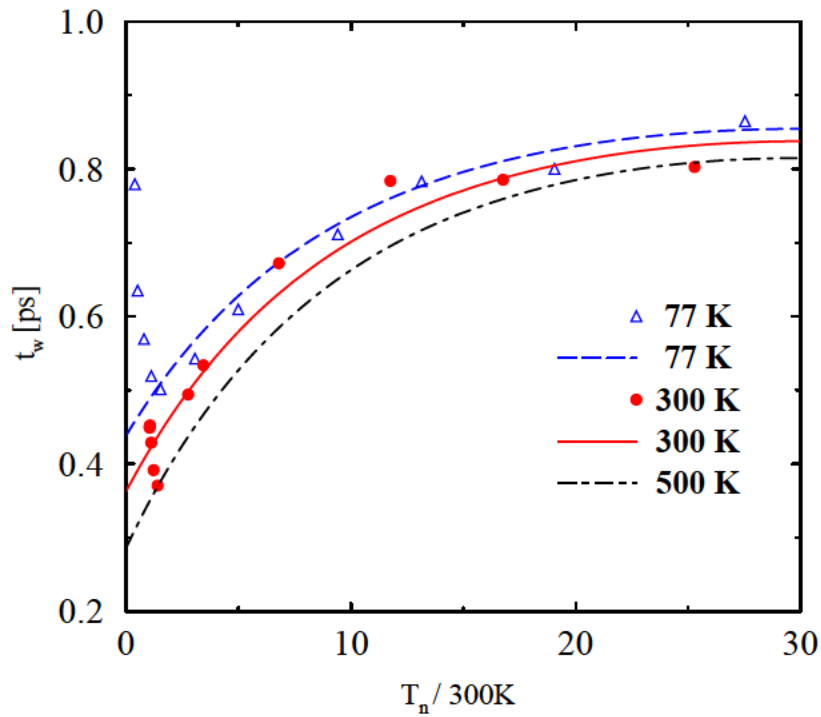

Fig. 3.40: Energy relaxation time as a function of electron temperature: Comparison of the model and MC data for Si at several lattice temperatures

Material	$\tau_{\epsilon,0}$ [ps]	$\tau_{\epsilon,1}$ [ps]	C_0	C_1	C_2	C_3	$\tau_{\epsilon,2}$ [ps]
Si	1.0	-0.538	0	0.0015	-0.09	0.17	0.4
Ge	0.26	1.49	0	-0.434	1.322	0	0.4
GaAs	0.48	0.025	0	-0.053	0.853	0.5	1.0
AlAs	0.17	0.025	61	-0.053	0.853	0.5	1.0
InAs	0.08	0.025	3	-0.053	0.853	0.5	1.0
InP	0.5	0.21	-18	-0.04	0	0	1.0
GaP	0.04	0.21	10	-0.04	0	0	1.0

Table 3.33: Parameter values for the energy relaxation time model for *basic materials*

Elementary and Binary Semiconductors

The direct method is used for Si, Ge and GaAs, and the indirect one for AlAs and InAs, depending on the MC data available. Fig. 3.40 shows the values for $\tau_{\epsilon,n}$ in Si obtained from the model (lines) and Monte-Carlo results (circles and triangles) at different lattice temperatures. The energy relaxation time slightly decreases with increasing lattice temperature. It is also observed that for high electron temperatures, $\tau_{\epsilon,n}$ tends to saturate.

At very low electron temperature $\tau_{\epsilon,n}$ starts to increase. This effect is not reproduced by the model. When the electron temperature is close to the lattice temperature, the term $(T_n - T_L)/\tau_{\epsilon,n}$ appearing in the energy balance tends to zero [183], thus the influence of $\tau_{\epsilon,n}$ is negligible, and therefore its increase can be neglected.

In GaAs and Ge similar behavior was observed at very low electron temperature, and the same assumptions as for Si are made. In the case of Ge Fig. 3.41 shows that $\tau_{\epsilon,n}$ is nearly independent of the lattice temperature, except for very low electron temperature. Therefore, any lattice temperature dependence is neglected ($C_3 = 0$ in (3.138)). The sharp initial fall is attributed to the increase of optical and inter valley scattering as the electrons are heated by the field [186].

The results for GaAs are shown in Fig. 3.42. At high electron temperatures $\tau_{\epsilon,n}$ tends to some saturated value and becomes independent of the lattice temperature. For low and intermediate electron temperatures, the behavior can be attributed to the transition of electrons from the Γ to the L valleys. The electron temperature for which $\tau_{\epsilon,n}$ reaches the peak value is independent of the lattice temperature. The associated average energy, 0.31 eV, is close to the energy difference between the two valleys, 0.27 eV.

Semiconductor Alloys

The similar behavior of the energy relaxation time $\tau_{\epsilon,n}$ in $In_xGa_{1-x}As$ and $Al_xGa_{1-x}As$ to that in GaAs can be seen in Fig. 3.43 and Fig. 3.44. Thus, $\tau_{\epsilon,n}$ of *alloy materials* is modeled by preserving the standard deviation and the amplitude of the function obtained for GaAs with the direct method and by adjusting then the position with the material composition dependence of $\tau_{\epsilon,0}$ ($\tau_{\epsilon,\text{sat}}$) and C_0 ($T_{n,\text{peak}}$).
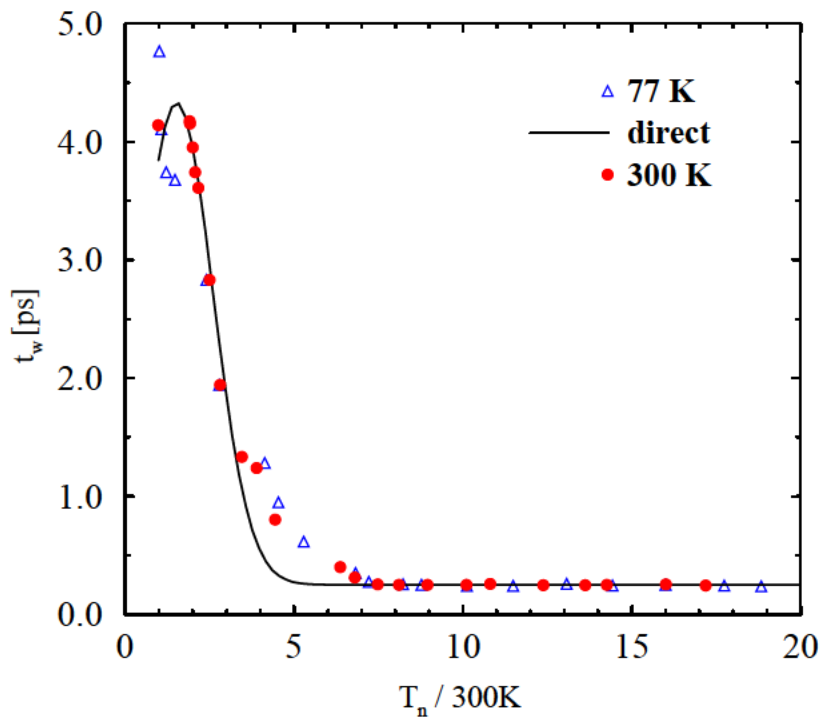
Fig. 3.41: Energy relaxation time as a function of electron temperature: Comparison of the model and MC data for Ge
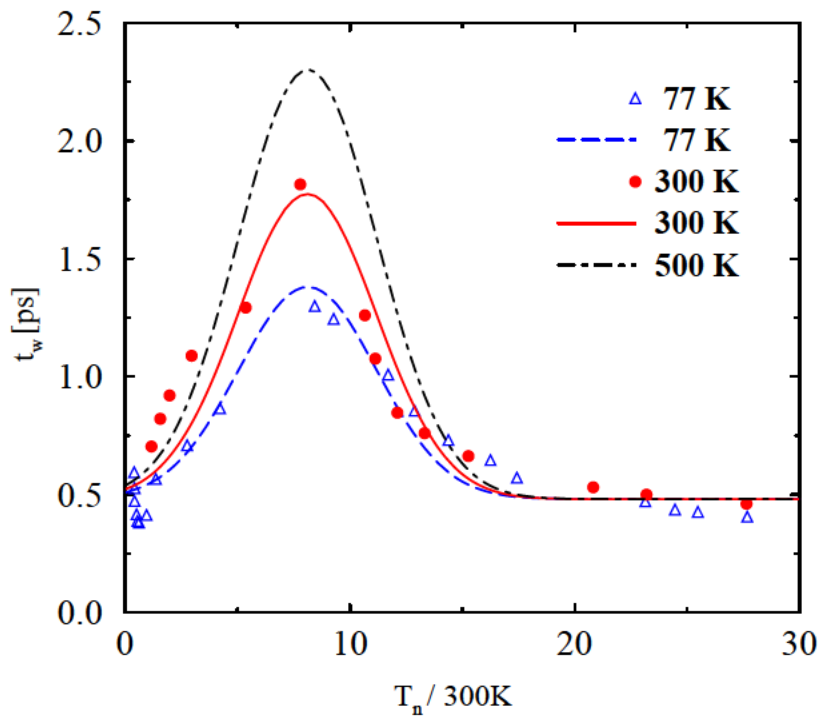

Fig. 3.42: Energy relaxation time as a function of electron temperature: Comparison of the model and MC data GaAs at several lattice temperatures

For $\tau_{\epsilon,0}$ and C_0 of *alloy materials* $(A_{1-x}B_x)$ the model suggests a quadratic interpolation between the the values from Table 3.33 for the *basic materials* (A and B) depending on the material composition x.

$$\tau_{\epsilon,0}^{AB} = \tau_{\epsilon,0}^{A} \cdot (1-x) + \tau_{\epsilon,0}^{B} \cdot x + \tau_C \cdot (1-x) \cdot x \tag{3.140}$$

$$C_0^{AB} = C_0^{A} \cdot (1-x) + C_0^{B} \cdot x + C \cdot (1-x) \cdot x \tag{3.141}$$

τ_C and C are referred to as bowing parameters. The values used in this model are summarized in Table 3.34. The indirect method is applicable for all semiconductor alloys as explained

Material	τ_C [ps]	$\tau_{\epsilon,1}$ [ps]	C	C_1	C_2	C_3	$\tau_{\epsilon,2}$ [ps]
AlGaAs	-0.35	0.025	-61	-0.053	0.853	0.5	1.0
InGaAs	1.8	0.025	-34	-0.053	0.853	0.5	1.0
InGaP	-0.4	0.21	-5.2	-0.04	0	0	1.0

Table 3.34: Parameter values for energy relaxation times in *alloy materials*

in Section 2.2. The lattice temperature dependence of $\tau_{\epsilon,n}$ of GaAs is preserved for both semiconductor alloys considered, $Al_xGa_{1-x}As$ and $In_xGa_{1-x}As$. This approximation is more accurate for low material composition, which is more frequently used ($x < 0.3$).

In Fig. 3.43 the results of the model for $Al_xGa_{1-x}As$ at 300 K for different material compositions x are shown. Note the shift of the electron temperature, at which $\tau_{\epsilon,n}$ reaches its maximum to lower values with the increase of x. For high values ($x > 0.4$) no peak value of $\tau_{\epsilon,n}$ is observed. This behavior can be attributed to the composition dependence of the Γ, L and X valley minima. When the Al fraction changes from 0 to 0.3, the energy difference between the Γ and L valleys varies between 0.27 and 0.1 eV. The corresponding change of the electron energy associated to the peak of $\tau_{\epsilon,n}$, varies between 0.31 to 0.1 eV. Furthermore, for Al contents $x > 0.4$ the X valleys are the lowest ones, and the bandgap becomes indirect. This explains the absence of a peak of $\tau_{\epsilon,n}$ for $x > 0.4$.

For $In_xGa_{1-x}As$ similar results are obtained in Fig. 3.44. There is a shift of the maximum $\tau_{\epsilon,n}$ to higher values with increasing Indium composition up to $x = 0.53$. This can be explained with the electron population change due to $\Gamma - L$ transitions. For InAs a quick shift to lower values is observed, not explained by the dependence of the energy valleys on x. Monte-Carlo simulation results show that at very high Indium contents the average electron energy decreases and the saturation drift velocity increases very much, but no clear results are available in this case.

Model Application

The energy relaxation times are used in the HD mobility model (3.129) and in the relaxation terms of the energy balance equations (3.8) and (3.9). Additionally, if self-heating is included, the energy relaxation times are used in the relaxation terms of the lattice heat flow equation (3.17).
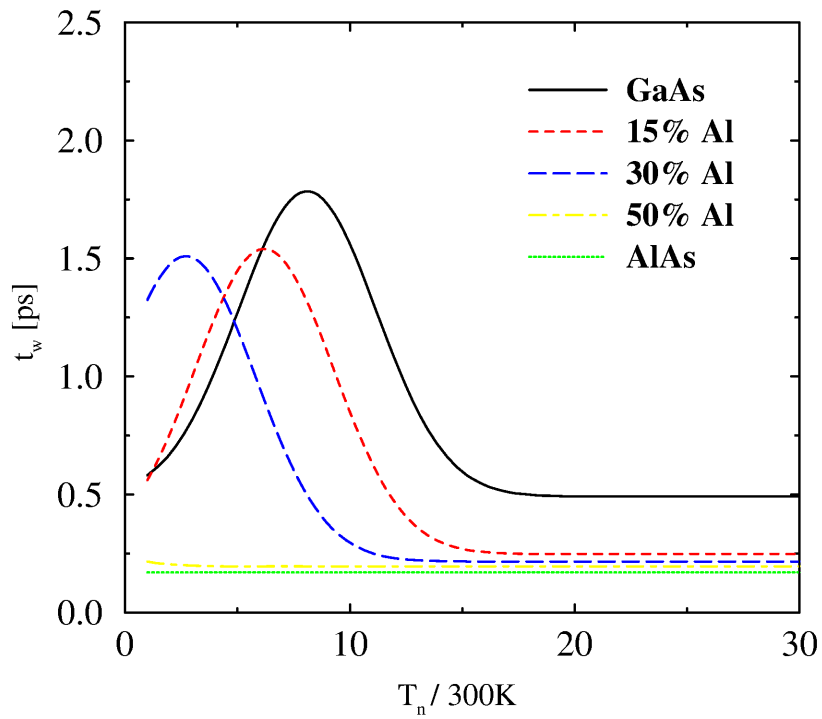
Fig. 3.43: Energy relaxation time as a function of electron temperature for different Al contents in AlGaAs at room temperature
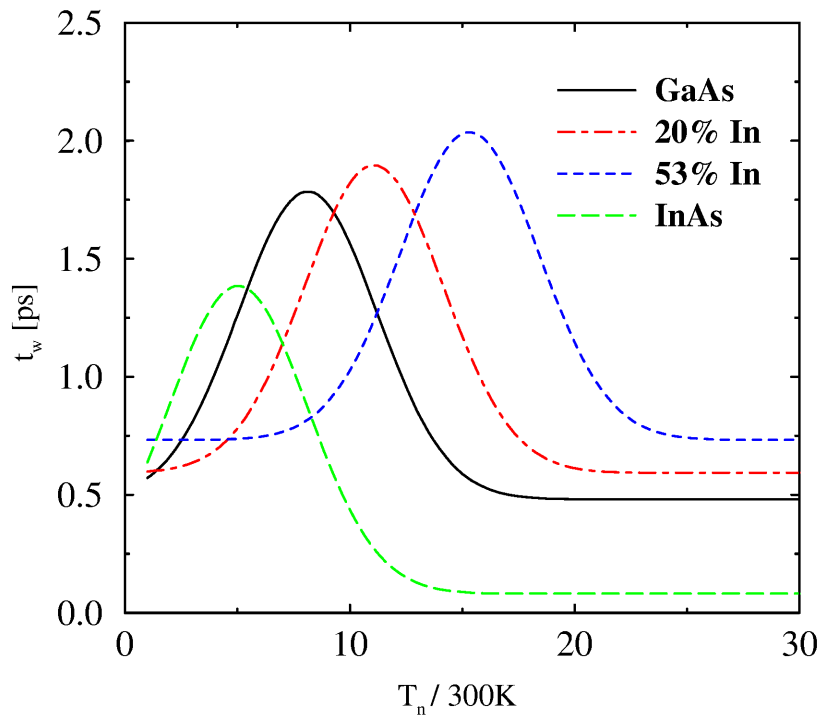

Fig. 3.44: Energy relaxation time as a function of electron temperature for different In contents in InGaAs at room temperature

Using non-constant electron energy relaxation times in (3.129) allows proper modeling of the velocity overshoot in the velocity-field characteristics for III-V materials. In addition, it helps better accuracy for the bias dependence of small-signal parameters to be achieved. Good agreement with the MC simulation results and its simple analytical structure make it attractive for device simulation.

3.7   Generation and Recombination

All described models in the next subsections evaluate a specific carrier recombination rate R. The sum of the calculated rates gives the overall recombination rate for the corresponding carrier type. This overall rate denotes the inhomogeneity of the corresponding continuity equations (3.2) and (3.3).

3.7.1   *Shockley-Read-Hall* and Surface Recombination

Carrier generation in space charge regions and recombination in e.g. high injection regions is modeled using the well known *Shockley-Read-Hall* (SRH) equation

$$R^{\mathrm{SRH}} = \frac{n \cdot p - n_i^2}{\tau_p \cdot (n + n_1) + \tau_n \cdot (p + p_1)}, \qquad n_i^2 = n_1 \cdot p_1. \tag{3.142}$$

The auxiliary variables n_1 and p_1 are defined by

$$n_1 = N_C(T_{\mathrm{L}}) \cdot \exp\left(\frac{-E_C + E_{\mathrm{T}}}{\mathrm{k_B} \cdot T_{\mathrm{L}}}\right), \tag{3.143}$$

$$p_1 = N_V(T_{\mathrm{L}}) \cdot \exp\left(\frac{-E_{\mathrm{T}} + E_V}{\mathrm{k_B} \cdot T_{\mathrm{L}}}\right). \tag{3.144}$$

For trap energy level E_{T} located in the mid gap $n_1 = p_1 = n_i$ and the recombination rate has its maximum. The variables N_C and N_V are the carrier effective densities of states (see Section 3.3). The dependence on the lattice temperature T_{L} is given by the variables $n_1(T_{\mathrm{L}})$ and $p_1(T_{\mathrm{L}})$ and the recombination lifetimes for electrons and holes, $\tau_n(T_{\mathrm{L}})$ and $\tau_p(T_{\mathrm{L}})$. The thermal carrier velocities at 300 K are calculated using

$$v_{n,p} = \sqrt{\frac{3 \cdot \mathrm{k_B} \cdot T_{\mathrm{L}}}{m_{n,p}}} \tag{3.145}$$

to obtain the recombination times at 300 K

$$\tau_{n,300} = \frac{1}{\sigma_{\mathrm{T},n} \cdot N_{\mathrm{T}} \cdot v_{n,300} + S_n/y}, \tag{3.146}$$

$$\tau_{p,300} = \frac{1}{\sigma_{\mathrm{T},p} \cdot N_{\mathrm{T}} \cdot v_{p,300} + S_p/y}. \tag{3.147}$$

The recombination times are modeled using traps of donor, acceptor, or neutral type, respectively, of trap density N_{T}, and the trap capture cross sections for electrons and holes, $\sigma_{\mathrm{T},n}$ and $\sigma_{\mathrm{T},p}$. The effect of surface recombination is included by using non-zero surface recombination velocities for electrons S_n and holes S_p, respectively. The effect is stronger with decreasing distance to the surface y.

Finally, the temperature dependence is included. The effect of trap assisted band to band tunneling (TBB) in Si is accounted for by a field enhancement factors Γ_n and Γ_p, which are modeled after [187]. As TBB is of importance only for materials with indirect bandgap this effect is neglected in literature for technologically important III-V materials, which have a direct bandgap (see Section 3.3.1).

$$\tau_n(T_{\mathrm{L}}) \quad = \quad \left(\frac{300K}{T_{\mathrm{L}}}\right)^{3/2} \cdot \frac{\tau_{n,300}}{1 + \Gamma_n}, \tag{3.148}$$

$$\tau_p(T_{\mathrm{L}}) \quad = \quad \left(\frac{300K}{T_{\mathrm{L}}}\right)^{3/2} \cdot \frac{\tau_{p,300}}{1 + \Gamma_p}, \tag{3.149}$$

The default values recommended for the SRH recombination model are summarized in the following table:

Material	N_{T} [cm^{-3}]	E_{T} [eV]	$\sigma_{T,n}$ [m^2]	$\sigma_{T,p}$ [m^2]	S_n [m/s]	S_p [m/s]
Si, Ge	1e13	0.0	1e-15	1e-15	0.0	0.0
III-Vs	2e16	0.4	1e-14	1e-13	0.0	0.0

Table 3.35: Parameter values for SRH recombination model

3.7.2 Auger Recombination

Auger-processes are modeled using a triple concentration product using the following equation

$$R^{\mathrm{AU}} = \left(C_n^{\mathrm{AU}} \cdot n + C_p^{\mathrm{AU}} \cdot p\right) \cdot \left(n \cdot p - n_i^2\right). \tag{3.150}$$

The default values recommended for the Auger model are summarized in the following table:

Material	C_n^{AU} [cm^6/s]	C_p^{AU} [cm^6/s]
Si&Ge	2.8e-31	9.9e-32
III-Vs	5.0e-30	3.0e-30

Table 3.36: Parameter values for *Auger* recombination model

3.7.3 Direct Recombination

The direct (radiative) recombination is of importance for direct bandgap semiconductors. In Si, Ge, and GaP it is of no significance for all possible conditions [188]. The recombination rate is proportional to the carrier concentrations and is modeled using the following equation

$$R^{\mathrm{DIR}} = C^{\mathrm{DIR}} \cdot \left(n \cdot p - n_i^2\right). \tag{3.151}$$

The coefficients C^{DIR} have constant values from Table 3.37.

Material	C^{DIR} [m^3/s]
GaAs	1.0e-10
AlAs	7.5e-11
InAs	2.1e-11
InP	6.0e-11
GaP	3.0e-15

Table 3.37: Parameter values for the radiative recombination model

3.7.4 Band-to-Band Tunneling

The direct band-to-band tunneling model (BB) describes the carrier generation in the high field region without any influence of local traps. The BB tunneling process describes the field emission of valence electrons leaving back holes. In case the magnitude of the electric field increases the trap assisted band to band tunneling process is replaced by the BB process. Two models are used in MINIMOS-NT. The *Schenk* model [187] is a complex physically-based model applicable to Si. Another simpler model [189] is applicable to all materials.

3.7.5 Impact Ionization

The impact ionization (II) models support both the drift-diffusion (DD) and the hydrodynamic (HD) transport models, therefore, electric field dependent DD II models and carrier temperature dependent HD II models are used in MINIMOS-NT.

Drift-Diffusion Impact Ionization

In DD simulation the model from [33] is used to calculate the II generation rates for electrons and holes, respectively. The overall generation rate is the sum of these two generation rates and can be expressed as a negative recombination rate.

$$-R^{\mathrm{II}} = G_n^{\mathrm{II}} + G_p^{\mathrm{II}} = \alpha_{n,\mathrm{bulk}} \cdot \frac{|\mathbf{J}_n|}{\mathrm{q}} + \alpha_{p,\mathrm{bulk}} \cdot \frac{|\mathbf{J}_p|}{\mathrm{q}}. \tag{3.152}$$

The ionization coefficients $\alpha_{n,\mathrm{bulk}}$ and $\alpha_{p,\mathrm{bulk}}$ are expressed by *Chynoweth*'s law

$$\alpha_{n,\mathrm{bulk}} = \alpha_{n,\mathrm{bulk}}^{\infty} \cdot \exp\left(-\left(\frac{E_{n,\mathrm{bulk}}^{\mathrm{crit}} \cdot |\mathbf{J}_n|}{\mathbf{E} \cdot \mathbf{J}_n}\right)^{\beta_n}\right) \tag{3.153}$$

$$\alpha_{p,\mathrm{bulk}} = \alpha_{p,\mathrm{bulk}}^{\infty} \cdot \exp\left(-\left(\frac{E_{p,\mathrm{bulk}}^{\mathrm{crit}} \cdot |\mathbf{J}_p|}{\mathbf{E} \cdot \mathbf{J}_p}\right)^{\beta_p}\right) \tag{3.154}$$

The default values are summarized in Table 3.38.

To account for surface effects, the surface ionization rates $\alpha_{n,\mathrm{surf}}$ and $\alpha_{p,\mathrm{surf}}$ can deviate from the bulk rates. The electron surface ionization rate is calculated in a similar way (analog for holes)

$$\alpha_{n,\mathrm{surf}} = \alpha_{n,\mathrm{surf}}^{\infty} \cdot \exp\left(-\left(\frac{E_{n,\mathrm{surf}}^{\mathrm{crit}} \cdot |\mathbf{J}_n|}{\mathbf{E} \cdot \mathbf{J}_n}\right)^{\beta_n}\right). \tag{3.155}$$

Material	$\alpha_{n,\text{bulk}}[\text{m}^{-1}]$	$E_{n,\text{bulk}}^{\text{crit}}[\text{V/m}]$	β_n	$\alpha_{p,\text{bulk}}[\text{m}^{-1}]$	$E_{p,\text{bulk}}^{\text{crit}}[\text{V/m}]$	β_p	Reference
Si	7.03e7	1.231e8	1.0	1.528e8	2.036e8	1.0	
Ge	1.55e9	1.560e8	1.0	1e9	1.28e8	1.0	[33]
GaAs	3.5e7	6.85e7	2.0	3.5e7	6.85e7	2.0	[190]
GaP	4.0e7	1.18e8	2.0	4.0e7	1.18e8	2.0	[190]

Table 3.38: Parameter values for DD impact ionization model

$F(y)$ is given by (3.120) and depending on the surface distance y describes a smooth transition between the surface and bulk generation rates. The parameter y^{ref} denotes a critical length. The final surface dependent ionization rate reads

$$\alpha_{n,\text{eff}} = F(y) \cdot \alpha_{n,\text{surf}} + (1 - F(y)) \cdot \alpha_{n,\text{bulk}}. \tag{3.156}$$

The effect is considered only for Si and the following values are used:

Material	$\alpha_{n,\text{surf}}\ [\text{m}^{-1}]$	$E_{n,\text{surf}}^{\text{crit}}\ [\text{V/m}]$	$\alpha_{p,\text{surf}}\ [\text{m}^{-1}]$	$E_{p,\text{surf}}^{\text{crit}}\ [\text{V/m}]$	$y^{\text{ref}}\ [\text{nm}]$
Si	1.03e7	1.50e8	4.0e8	3.0e8	10

Table 3.39: Parameter values for surface DD impact ionization model

Hydrodynamic Impact Ionization

In a HD simulation, the carrier temperatures are used as parameters in the hydrodynamic impact ionization model. The implemented equation for the electron generation rate depending on the concentration n and the bandgap energy E_g [191, 192] reads (analog for holes)

$$G_n\left(T_n, n\right) = n \cdot A \cdot \left(\left(1 + \frac{u}{2}\right) \cdot \text{erfc}\left(\frac{1}{\sqrt{u}}\right) - \frac{1}{2} \cdot \sqrt{u} \cdot \exp\left(\frac{-1}{u}\right)\right), \tag{3.157}$$

$$u = \frac{\text{k}_\text{B} \cdot T_n}{E_\text{g}}. \tag{3.158}$$

The prefactor A depends on the carrier and lattice temperatures and the local bandgap

$$A(T_\text{L}, T_n, E_\text{g}) = \frac{1}{C_1} \cdot \exp\left(C_2 \cdot \frac{T_\text{L}}{T_0} + \frac{E_0 \cdot u}{\text{k}_\text{B} \cdot T_0} \cdot \left(C_3 - C_4 \cdot \frac{T_\text{L} - T_0}{T_0}\right)\right). \tag{3.159}$$

The variables T_0 and E_0 correspond to 300 K and $E_\text{g}(300\ \text{K})$, respectively.

Material	$C_1\ [\text{s}]$	C_2	C_3	C_4
Si	9.531e-9	3.823	0.346333	0.0922

Table 3.40: Parameter values for HD impact ionization model

The overall generation rate is the sum of the electron and hole generation rates, and is equal to a negative recombination rate

$$R^{\text{II}} = -G_n^{\text{II}} - G_p^{\text{II}}. \tag{3.160}$$

Another simple, but very practical model is available for modeling the impact ionization rate in all semiconductors. It reads for electrons

$$G_n\left(T_n, T_{\mathrm{L}}, n\right) = n \cdot A \cdot \exp\left(\frac{-B \cdot E_{\mathrm{g}}}{k_{\mathrm{B}} \cdot T_n}\right) \tag{3.161}$$

and, respectively, for holes

$$G_p\left(T_p, T_{\mathrm{L}}, p\right) = p \cdot A \cdot \exp\left(\frac{-B \cdot E_{\mathrm{g}}}{k_{\mathrm{B}} \cdot T_p}\right). \tag{3.162}$$

The default values recommended for the simple HD II model are summarized in the following table:

Material	$A\ [\mathrm{s}^{-1}]$	B
Si&Ge	1e13	0.92
III-Vs	1e13	1.0

Table 3.41: Parameter values for HD impact ionization model

This model has been already successfully applied in simulation of GaAs-based and InP-based HEMTs [193, 194]. However, it has not been applied in simulation of III-V HBTs yet.

Chapter 4

Simulation Application

IN this chapter simulation results for several different types of bipolar transistors are presented. The examples are selected to demonstrate a variety of applications which can be covered by MINIMOS-NT.

4.1 GaAs versus SiGe HBTs

In addition to devices based on III-V semiconductor materials several simulations of SiGe HBTs are performed as well. Simplified device structures are used in the early development of MINIMOS-NT for testing the graded material composition and temperature dependent models of the simulator.

4.1.1 The Test Device

A device with a conservative design is shown in Fig. 4.1. This structure was used as a reference device in [158]. It was initially used to tune simulations of AlGaAs/GaAs HBTs with MINIMOS-NT and was later adopted for testing of SiGe HBTs.

The electrical behavior at room temperature of a Si BJT, a Si HBT with SiGe narrow-bandgap base, and a GaAs HBT with AlGaAs wide-bandgap emitter was studied in a comparative way using the same geometry and HBT typical doping profiles with high base doping concentration of 10^{19} cm^{-3}. The possibility to perform such simulations was presented in [195].

Later on in [124] a material composition optimization was shown. The optimization is automatically run using the VISTA framework [196] with ten operating points distributed at equal distances of 11 nm over the 100 nm thick SiGe base starting from constant 20% Ge content constrained to 25%. The possibility to increase the maximum current gain and cutoff frequency by material optimization can be seen in Fig. 4.2 and Fig. 4.3.
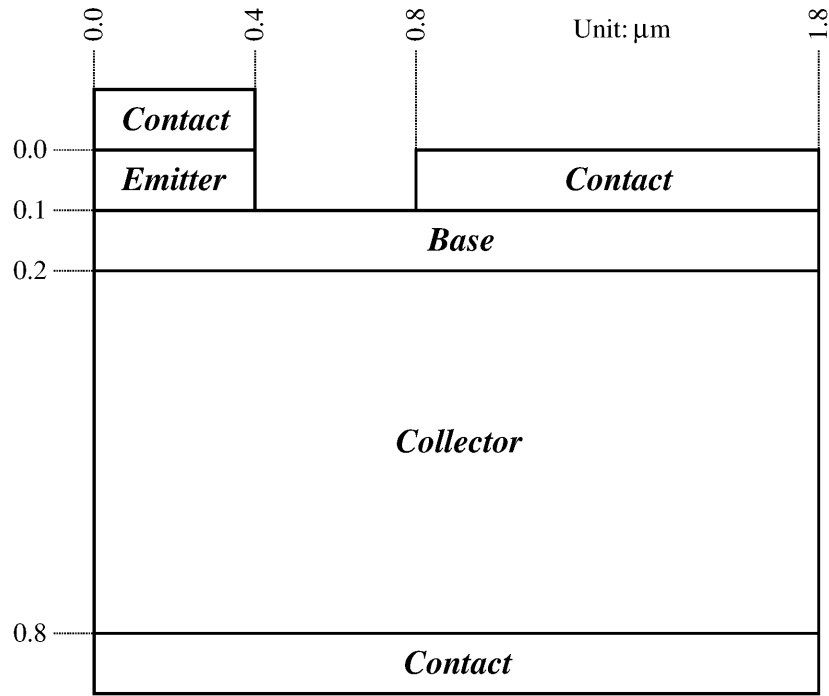
Fig. 4.1: Simulated HBT test structure

The cutoff frequency f_T is determined using the quasi-static approximation, which can give results close to those from a small-signal analysis, as shown in [158]

$$f_T \quad = \quad \frac{g_m}{2 \cdot \pi \cdot C_{in}} \tag{4.1}$$

$$g_m \quad = \quad \frac{\Delta J_C}{\Delta V_{BE}} \tag{4.2}$$

$$C_{in} \quad = \quad \frac{\Delta Q_s}{\Delta V_{BE}} \tag{4.3}$$

Thus, by applying small steps of V_{BE}, f_T can be calculated by

$$f_T \quad = \quad \frac{\Delta J_C}{2 \cdot \pi \cdot \Delta Q_s} \tag{4.4}$$

where ΔQ_s is the change of the total charge in the device.

Furthermore, the impact of new mobility and bandgap narrowing models of MINIMOS-NT is studied at different temperatures and for different dopant concentrations [66]. In Fig. 4.4 the Gummel plots for SiGe HBT at 77 K and at 300 K obtained with the model of Slotboom et al. [133] (Mod.1) and with our new model (Mod.2) are compared. The significant difference in the current density values at 77 K, resulting in a higher current gain obtained by the new model (Fig. 4.5), is experimentally confirmed.
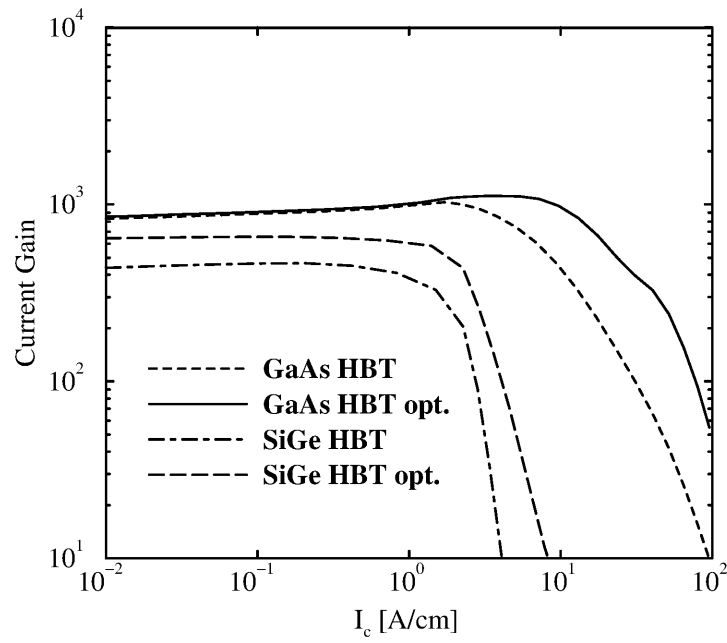
Fig. 4.2: Current gain vs. collector current
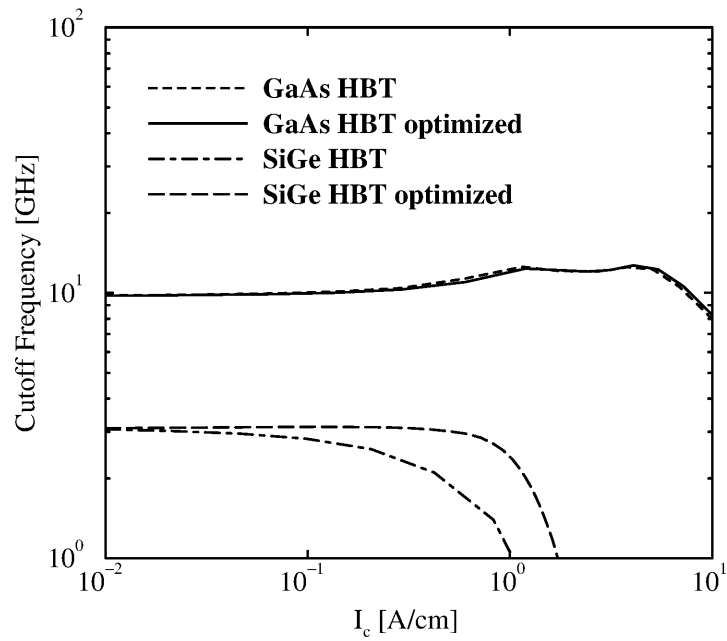
Fig. 4.3: Cutoff frequency vs. collector current
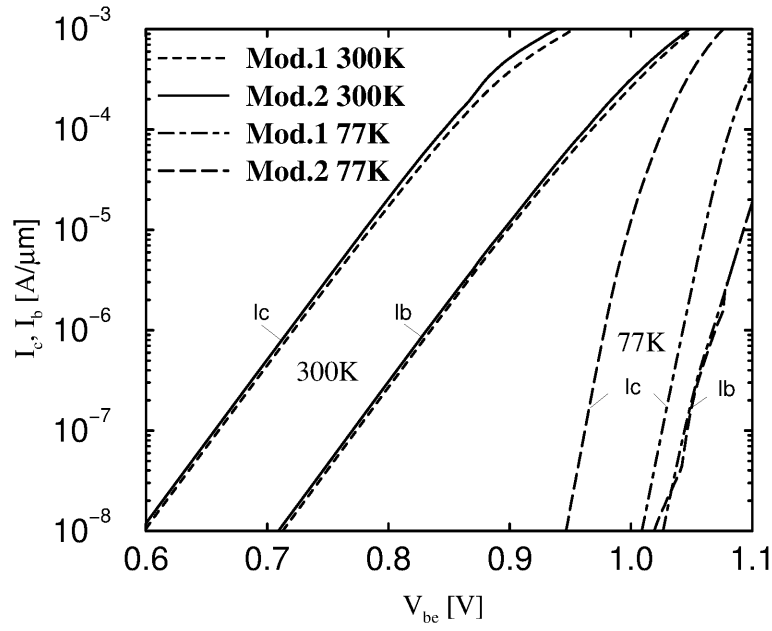
Fig. 4.4: Gummel plots at $V_{CE} = 2$ V for Mod. 1 and Mod. 2
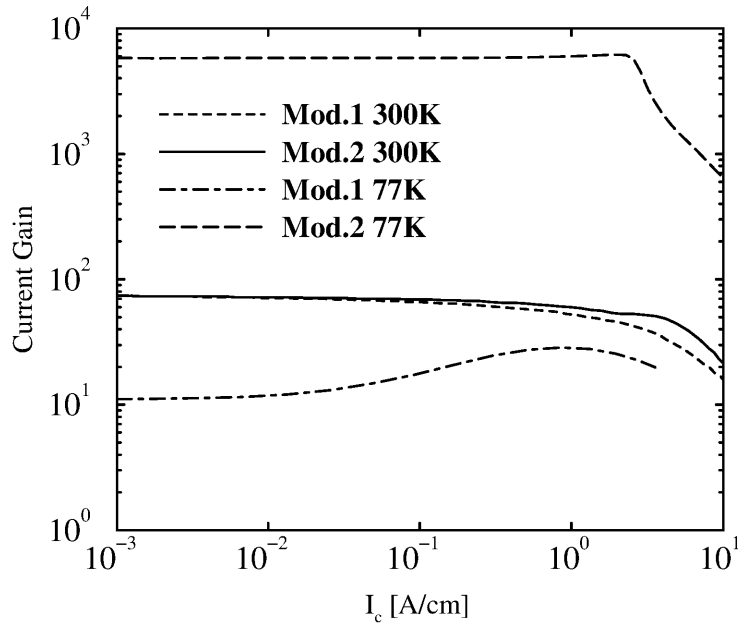
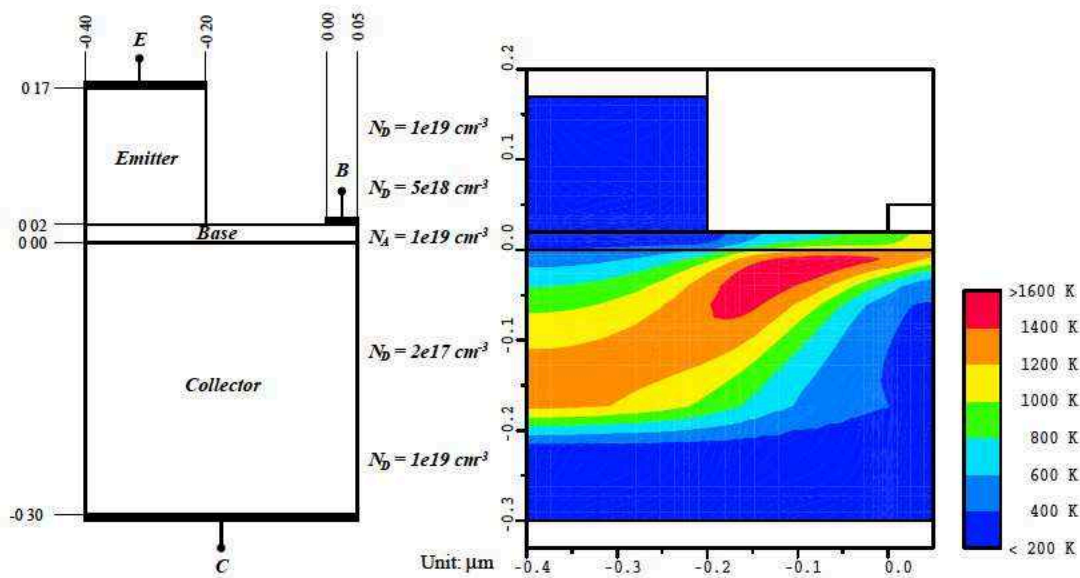**Fig. 4.5:** Current gain versus collector current for Mod. 1 and Mod. 2

Fig. 4.6: The HBT structure and electron temperature distribution in the device: Simulation results at $V_{BE} = 0.87$ V and $V_{CE} = 1$ V

4.1.2 The Realistic Device

A $Si_{0.8}Ge_{0.2}$ HBT with a realistic device structure (see Fig. 4.6, left) from [67] and the Monte Carlo simulation results there was employed for further tuning of MINIMOS-NT models which are used in HD simulations. A comparison, similar to the one presented in [67] was performed. The MC simulation results were compared to DD and HD results obtained with MINIMOS-NT for the electron concentration, the electrostatic potential, the electron velocity, and the electron temperature distribution in the device (see Fig. 4.6). Such comparisons are useful not only to verify the validity of the models for SiGe and the HD transport model, but also to gain an insight why and where the HD model should be used having in mind the higher computational effort.

In [62] the capabilities of MINIMOS-NT were demonstrated by a HD mixed-mode device-circuit simulation of a 5-stage Current-Mode Logic (CML) ring oscillator containing 10 SiGe HBTs (Fig. 4.7). The DD simulation shows a much lower inverter delay time compared to the HD simulation (see Fig. 4.8). This is due to the velocity overshoot in the base-collector space charge region which cannot be modeled using a DD simulation [67]. Furthermore, since the current is higher in the case of HD simulation, the overall speed of the circuit increases. The error of the DD simulation in the inverter delay is in the range of 60% compared to the HD simulation, thus proving the necessity of a HD model.

This example, together with the example presented in the following section, not only confirms the capabilities of MINIMOS-NT to handle complex device structures (such as HBT structures), but also confirms the correct modeling so far of the properties of SiGe in the simulator. The results are quite promising taking into consideration that the emphasis of the work was put on III-V materials and devices.
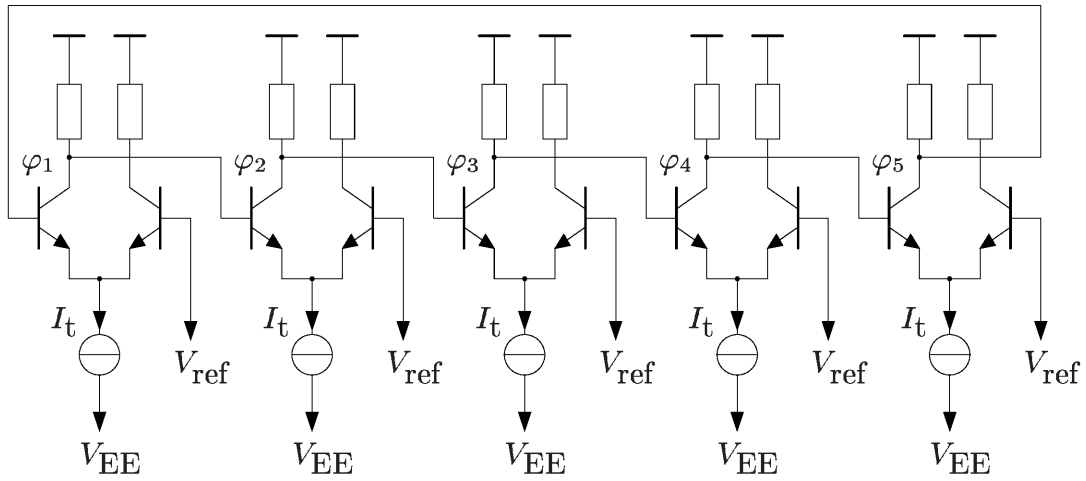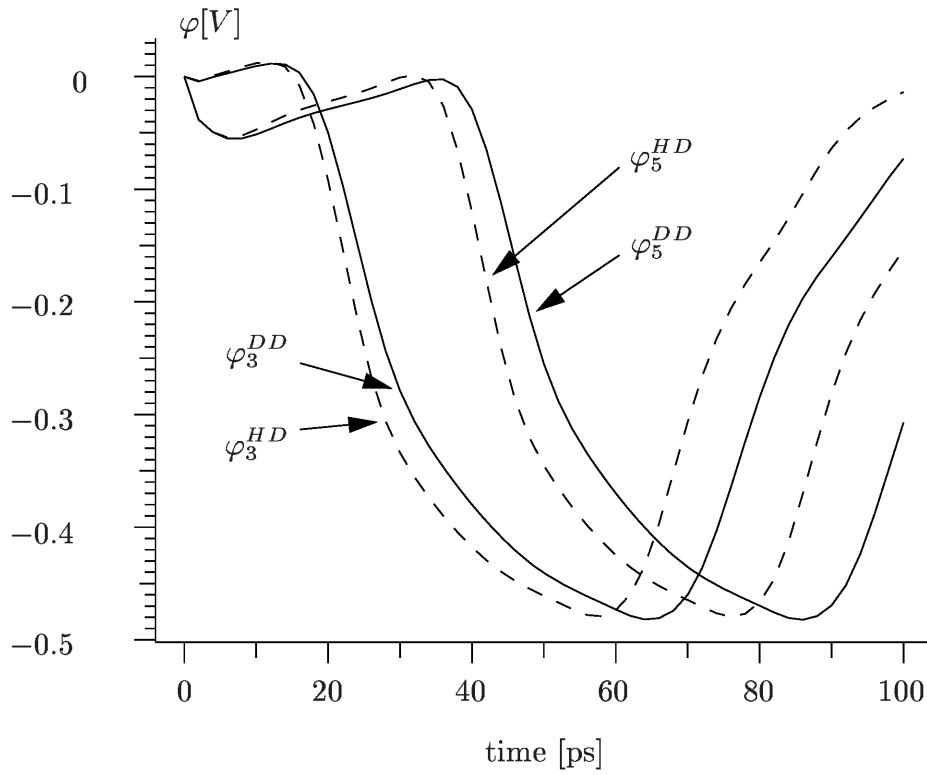
Fig. 4.7: CML ring oscillator circuit

Fig. 4.8: Comparison of DD vs. HD transient response

4.1.3 The Real Device

Five 400x400 μm^2 Si$_{1-x}$Ge$_x$ HBTs have been fabricated with the same geometry and layer specification as shown in Fig. 4.9. The only difference is the Ge content x in the base, which is constant for a given device and varies between 16% and 28% for the respective devices. The following layer sequence applies for all devices: The emitter consists of an antimony doped n$^+$=2.10^{20} cm^{-3} contact region and n=10^{18} cm^{-3} region. The base is boron doped (p$^+$ = 5.10^{19} cm^{-3}) and has thin undoped spacers on the top and beneath of it, respectively. The collector is antimony doped (n$^-$ = 2.10^{16} cm^{-3}) and is followed by an intrinsic buffer and the substrate.

The device with the lowest Ge fraction in the base $x = 16\%$ is analyzed first. In Fig. 4.10 results of several simulations are presented in their consecutive order compared to measured data at V$_{BC}$ =0 V (red symbols). They are presented as an example of calibration of forward Gummel plot characteristics. The first simulation is performed with the default models and the device is defined according to the specification (green dashed lines). Thus, important effects, such as BGN and SRH recombination are still not taken into account. Note the significant disagreement between simulation and measurement, especially in the high-field region. However, the slope in the collector current density at low and middle voltages is correct, which shows that the conduction band discontinuity at base-to-emitter junction is modeled correctly. In the next simulation the BGN is switched on (black dot-dashed lines) and comparatively good agreement can be observed for I$_C$. In the high-field region still a different behavior is observed. This can be explained by the complete depletion of the two spacers in the simulation which is not the case for the real device. As stated in [197] the spacers are used to prevent outdiffusion of boron from the base to the emitter in the following thermal processing. In the final device the SiGe spacers contain boron and are parts of real the base layer. In the next simulation already gradual boron doping profiles varying from 5.10^{13} cm^{-3} at the spacer-to-emitter and spacer-to-collector interfaces, respectively, to 5.10^{19} cm^{-3} at the base-to spacer interfaces are included. The only remaining step is to include SRH recombination in order to match the base current. Finally, good agreement for the complete bias range is achieved (solid red lines).

The next simulations are performed with the remaining four devices, which have higher Ge content in the base. In Fig. 4.11 a comparison between the simulated and measured Gummel plots for the devices with $x = 16\%$, 22%, and 28% Ge are shown. All simulations are performed with the same set of models and no adjusting of model parameters is performed. The only exception is done for the concentration of traps in the base, because with the high Ge content also more traps are introduced. Thus, quite good agreement is finally achieved.

Finally, the assumption for the doping is confirmed to some extend by SIMS measurements, which were not initially available. As can be seen in Fig. 4.12 it is true that in the real device outdiffusion of boron has taken place. However, the effect appears to be even more pronounced than initially assumed.
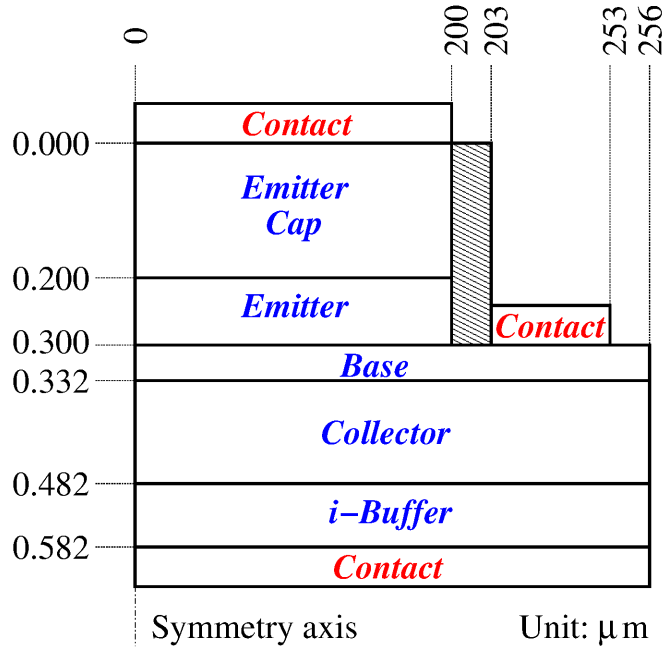
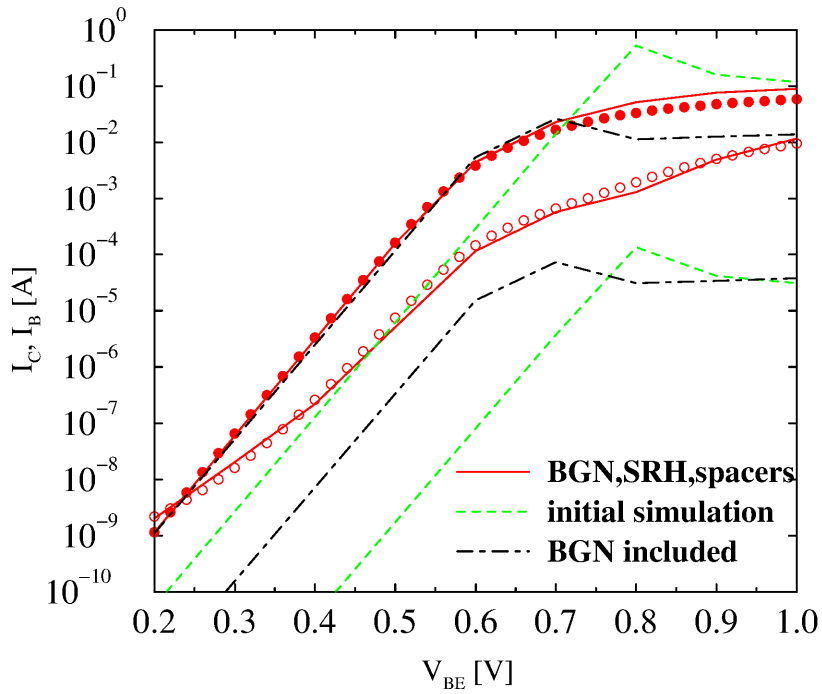**Fig. 4.9:** Simulated device structure of five SiGe HBTs

Fig. 4.10: Forward Gummel plots at $V_{BC} = 0$ V: Study of different effects in a $Si_{0.84}Ge_{0.16}$ HBT
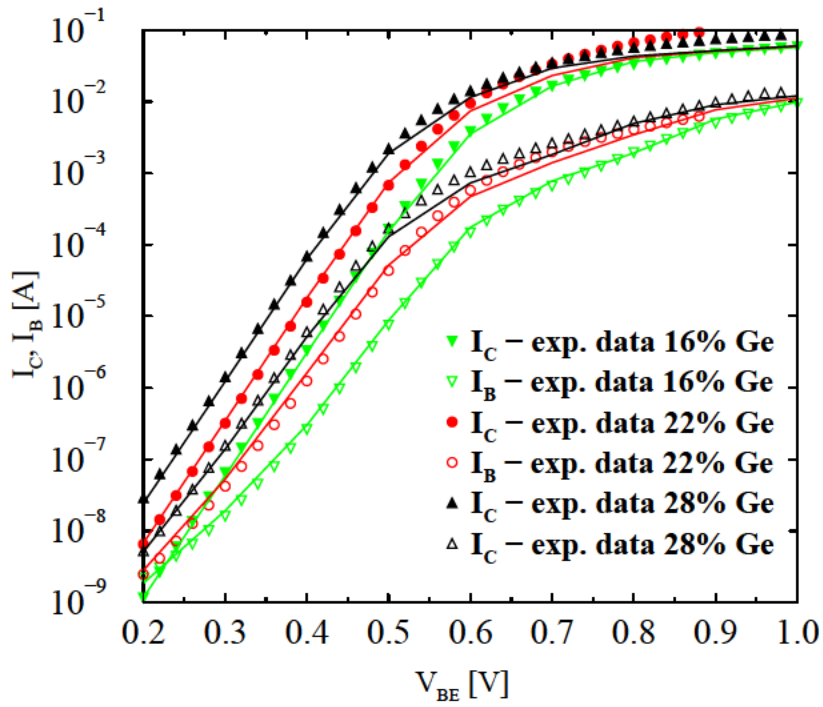
Fig. 4.11: Forward Gummel plots at $V_{BC} = 0$ V: Comparison between simulation and measurement for different material contents
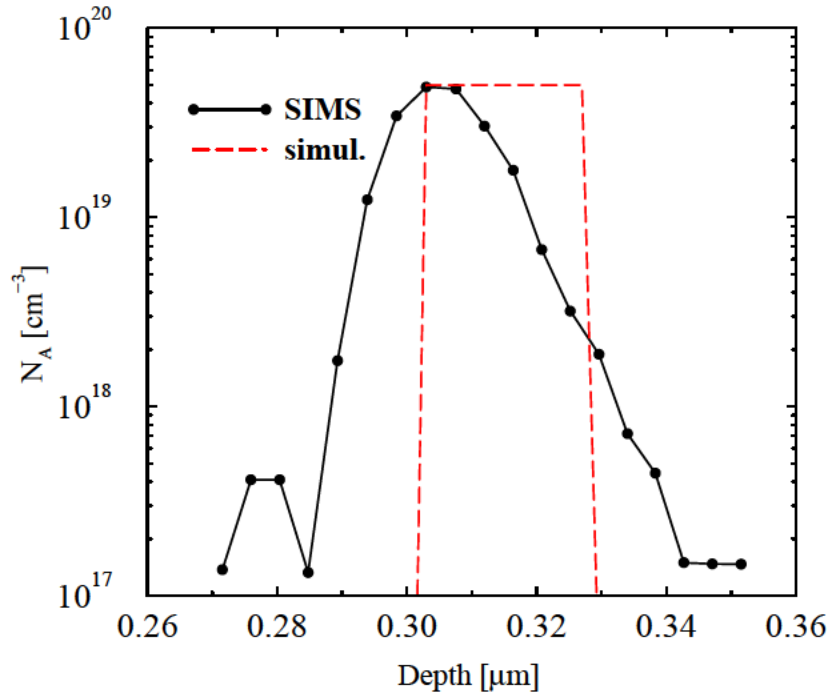

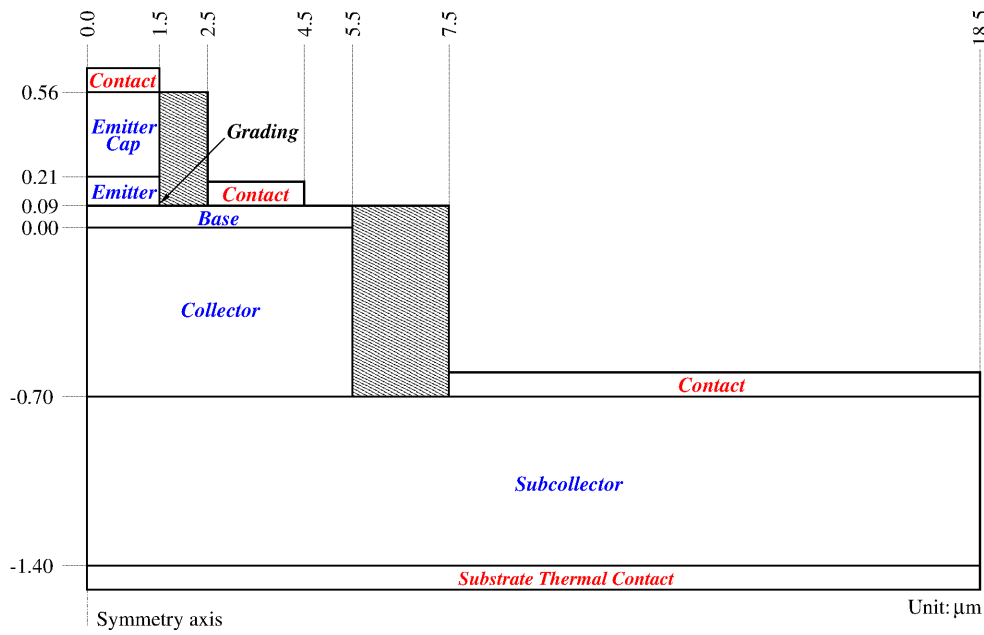**Fig. 4.12:** Boron profile in the base region: Comparison between specification and SIMS data

Fig. 4.13: Simulated device structure of AlGaAs/GaAs HBT

4.2 High Power GaAs HBTs

In this section the results of two-dimensional hydrodynamic simulations of one-finger high power Heterojunction Bipolar Transistors (HBTs) on GaAs substrate are demonstrated. An overview of the physical models used and comparisons with experimental data are presented.

In particular the electrical behavior of AlGaAs/GaAs and AlGaAs/InGaP/GaAs one-finger high power HBTs with emitter areas of 90 μm^2 are studied at several ambient temperatures. Typical values for the devices under consideration range from 300 K up to 380 K [198].

4.2.1 Fabrication of the Simulated Devices

All four HBT structures are MOCVD epitaxially grown on GaAs substrates. The first device, later on referred to as Dev. 1, has the following layer sequence: The cap is formed by an n^+-InGaAs/n-GaAs layer. The emitter consists of 80 nm Si-doped n-Al$_{0.28}$Ga$_{0.72}$As with 20 nm graded layers on its top and bottom, respectively. The 120 nm GaAs base is carbon doped ($p^+ = 3.10^{19}$ cm^{-3}), followed by a 700 nm GaAs collector ($n^- = 2.10^{16}$ cm^{-3}) and a 700 nm GaAs subcollector ($n^+ = 5.10^{18}$ cm^{-3}). The simulated device structure is shown in Fig. 4.13.

In two devices (Dev. 2 and Dev. 3) the graded AlGaAs layer next to the base-to-emitter junction is replaced by a 20 nm InGaP ledge layer ($n = 4.10^{17}$ cm^{-3} and 3.10^{17} cm^{-3}, respectively). Both devices differ in base carbon doping ($p^+ = 3.10^{19}$ cm^{-3} vs. 4.10^{19} cm^{-3}) and layer thickness (80 nm vs. 120 nm). A 40 nm InGaP emitter ($n = 4.10^{19}$ cm^{-3}) HBT with 120 nm base thickness is the last considered device type (Dev. 4). All HBTs are processed
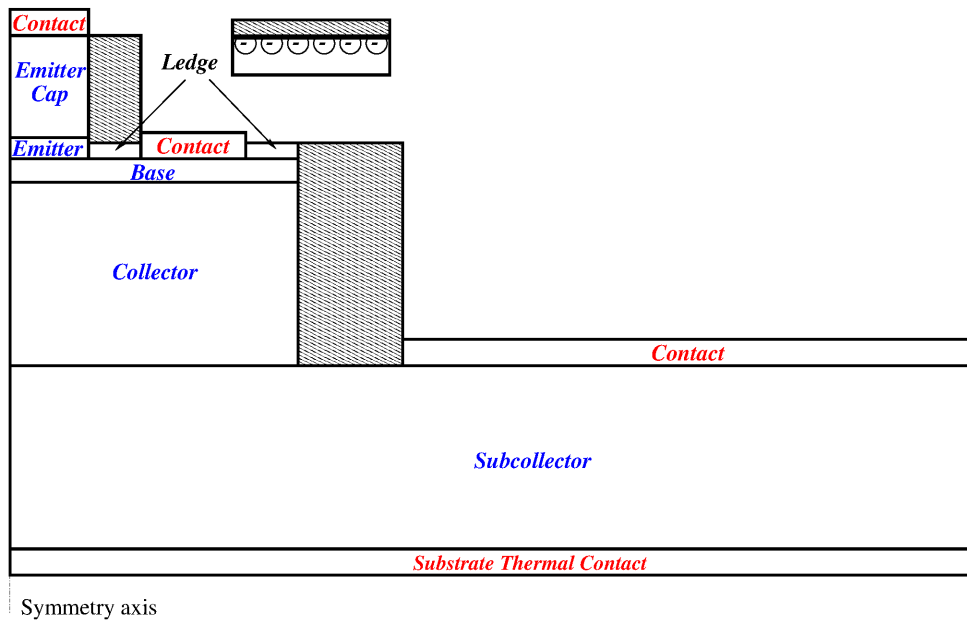
Fig. 4.14: Simulated device structure of InGaP/GaAs HBT

by etching a double mesa structure and passivated by Si_3N_4. The simulated device structure is shown in Fig. 4.14.

4.2.2 Simulation Results

One concise set of model parameters is used in all simulations. The extrinsic parasitics, e.g. the emitter interconnect resistance, are accounted for in the simulation by adding lumped resistances of 1 Ω to all electric contacts.

Forward and Reverse Gummel Plots

In Fig. 4.15 the simulated forward Gummel plot for Dev. 1 at 293 K is shown and compared to experimental data. Note the good agreement at moderate and high voltages, typical for operation of this kind of devices. The measured leakage currents at $V_{BE} \leq 1$ V cannot be reproduced by simulation, despite of the fact that several generation/recombination mechanisms, such as SRH recombination, surface recombination, and BB are taken into account.

Encouraging results are also achieved for Dev. 2. In Fig. 4.16 the simulated Gummel plot at 373 K is included to demonstrate the ability of MINIMOS-NT to reproduce the thermal device behavior correctly. Comparisons with measured data for Dev. 4 are shown in Fig. 4.17 and Fig. 4.18. Note that very good agreement for the reverse Gummel plots is achieved also at higher temperatures. These results verify our models and therefore are a good prerequisite for simulation of self-heating effects.
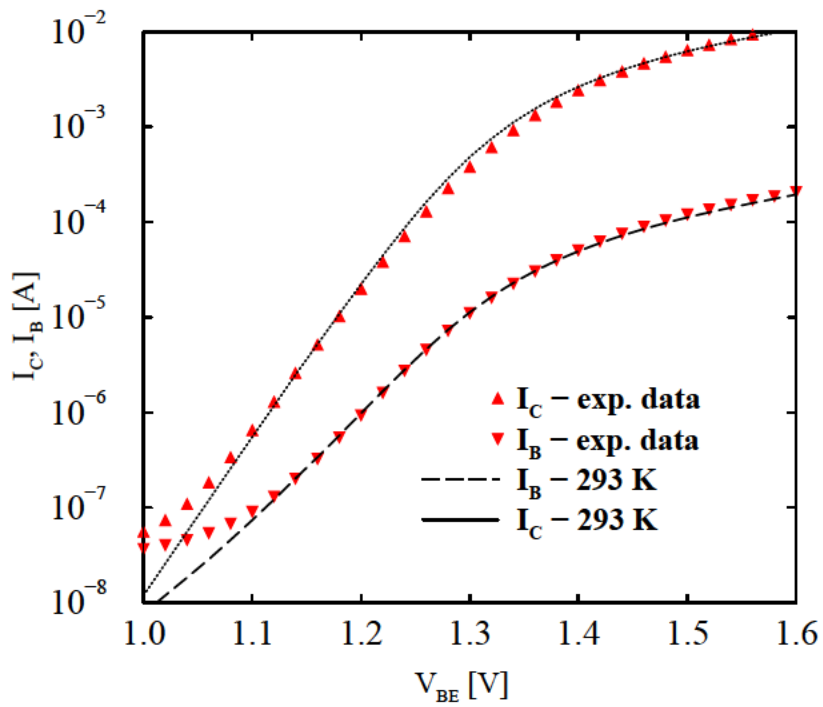
Fig. 4.15: Forward Gummel plots at $V_{CB} = 0$ V for Dev. 1: Comparison with measurement data at 296 K
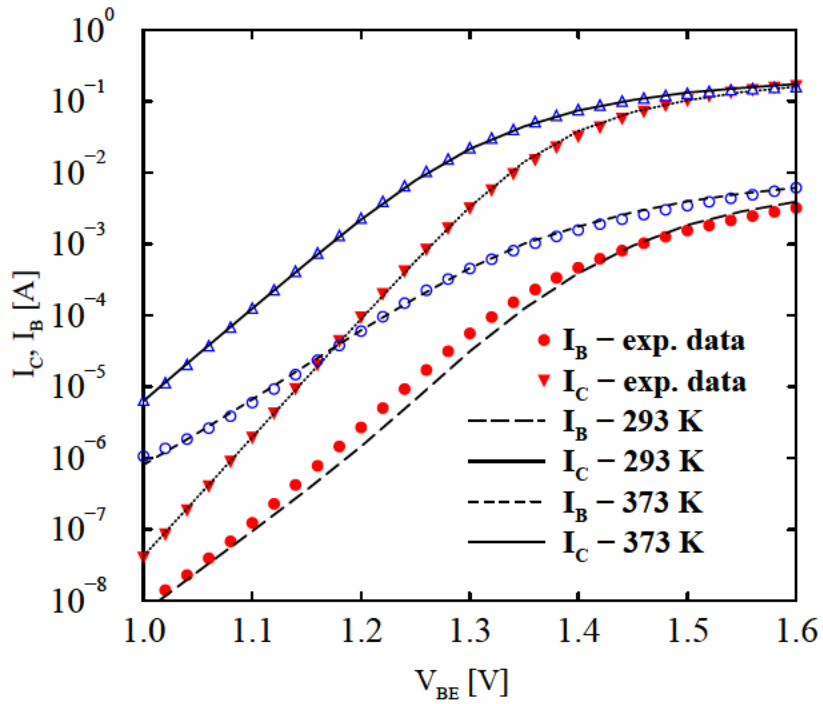
Fig. 4.16: Forward Gummel plots at $V_{CB} = 0$ V for Dev. 2: Comparison with measurement data at 296 K and 376 K
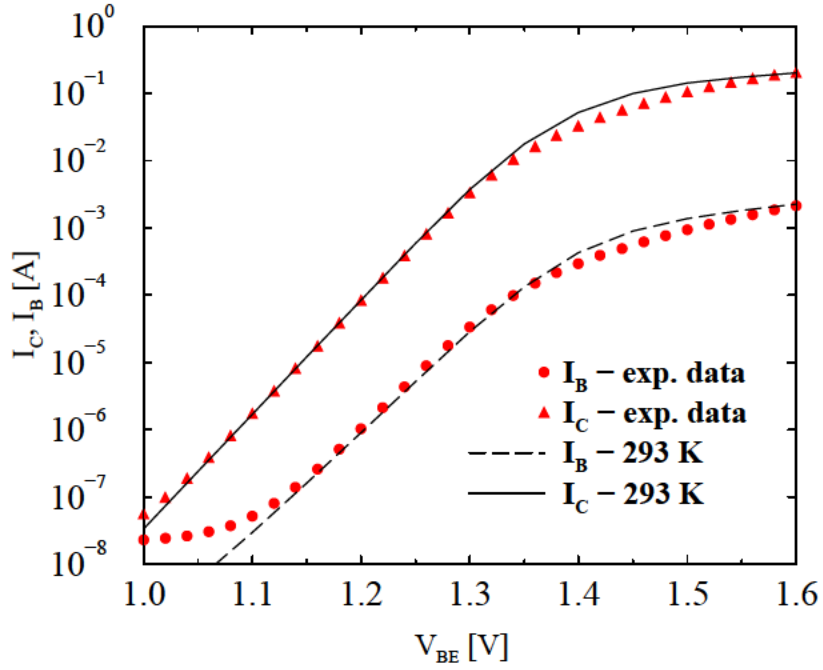
Fig. 4.17: Forward Gummel plots at $V_{CB} = 0$ V for Dev. 4: Comparison with measurement data
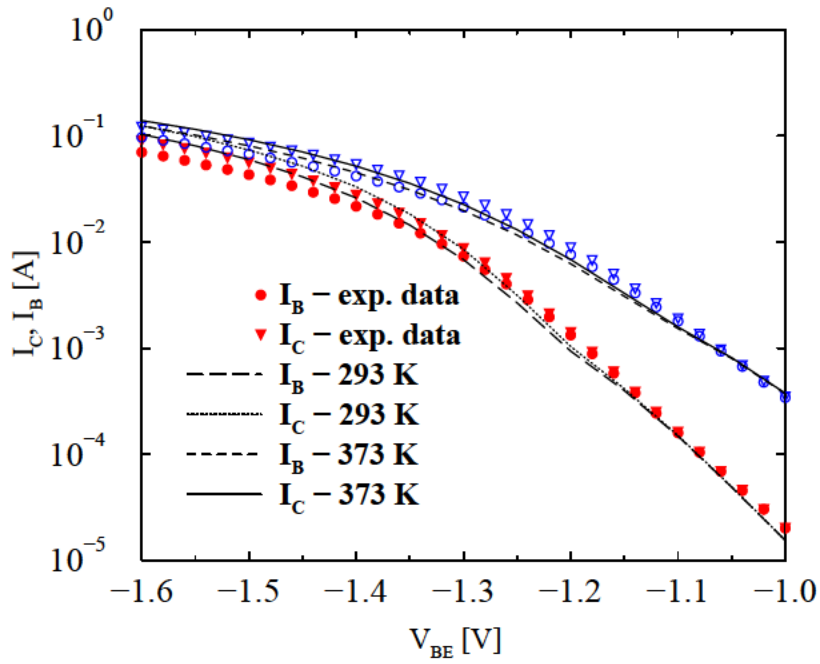
Fig. 4.18: Reverse Gummel plots at $V_{CB} = 0$ V for Dev. 4: Comparison with measurement data at 293 K and 373 K

Simulation with Self-Heating

In order to account for self-heating effects the lattice heat flow equation (3.14) is solved self-consistently with the energy transport equations (3.6) and (3.7), which results in a system of six partial differential equations. An additional, substrate thermal contact is introduced. The thermal heat flow density is calculated by (3.28) using a thermal contact resistance R_T with a measured value of about 400 K/W [27, 199]. The thermal dissipation through the emitter and base contacts is neglected, therefore a Neumann boundary condition is assumed.

Simulation of Output Characteristics

It is a severe problem to achieve realistic results in simulation of output HBT characteristics. This is especially true for power devices which are considered in this work. As stated in [71] the power dissipation increases with collector-to-emitter voltage V_{CE}, gradually elevating the junction temperature above the ambient temperature. This leads to gradually decreasing collector currents I_C at constant applied base current I_B or, respectively, gradually increasing I_C at constant base-to-emitter voltage V_{BE}. The simulated output device characteristics compared to measurements for constant $V_{BE} = 1.4$ V to 1.45 V using a 0.01 V step are shown in Fig. 4.19. A good agreement is achieved by simulation including self-heating effects. In Fig. 4.20 the intrinsic temperature T_j in the device depending on the V_{CE} is presented. For Dev. 3 the temperature reaches as much as 400 K for the specified thermal resistance. As already stated in [63] such lattice temperatures significantly change the material properties of the device and, consequently, its electrical characteristics. This confirms the necessity of exact DC-simulations at several high ambient temperatures before including self-heating effects.

Hydrodynamic simulation is needed to account for non-local effects. For example, the electron temperature (see Fig. 4.21) is used as an input to the hydrodynamic mobility model and therefore allows to simulate the electron velocity overshoot in the collector space charge region. The carrier temperature also influences the current flux across the heterointerfaces – the higher it is the more carriers are able to surmount the energy barrier. This effect is referred to as real-space transfer [70]. Considering the nature of the simulated devices (including graded and abrupt heterojunctions) and the high electron temperatures observed at maximum bias (above 2500 K - see Fig. 4.21) a thermionic-field emission interface model (3.48) is used in conjunction with the hydrodynamic transport model.

The resulting lattice temperature distribution in the device at $V_{CE} = 6.0$ V and $V_{BE} = 1.45$ V is shown in Fig. 4.22. The heat generated at the heterojunctions flows out of the device in the direction of the substrate heat sink. In the opposite direction the heat cannot leave the device and therefore the emitter finger is heated up significantly up to 400 K. The simulation shown is of practical interest and demonstrates the necessity of a thermal shunt at the emitter contact rather than reducing the substrate thickness.
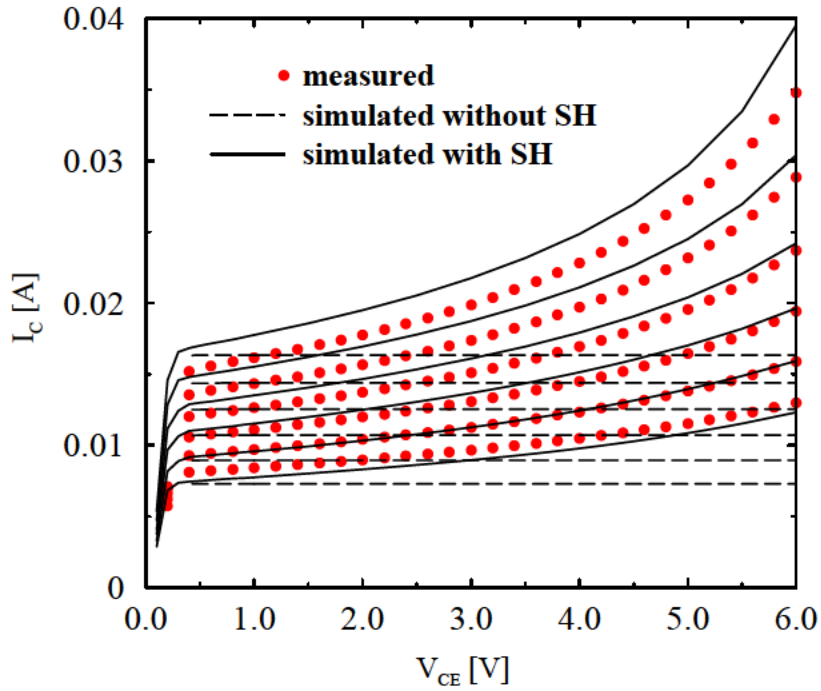
Fig. 4.19: Output characteristics for Dev. 3: Simulation with and without self-heating compared to measurement data
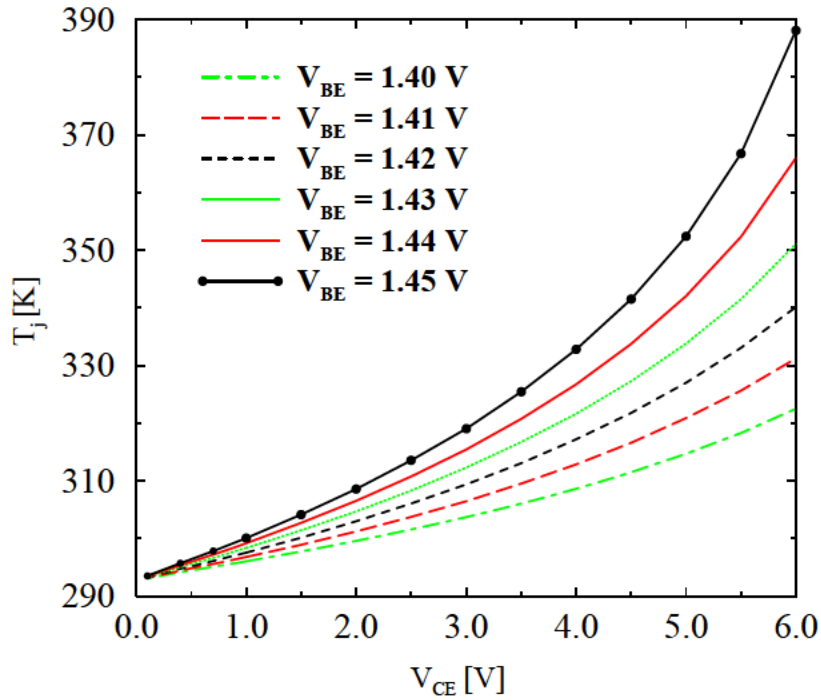
Fig. 4.20: Intrinsic device temperature vs. V_{CE} for Dev. 3
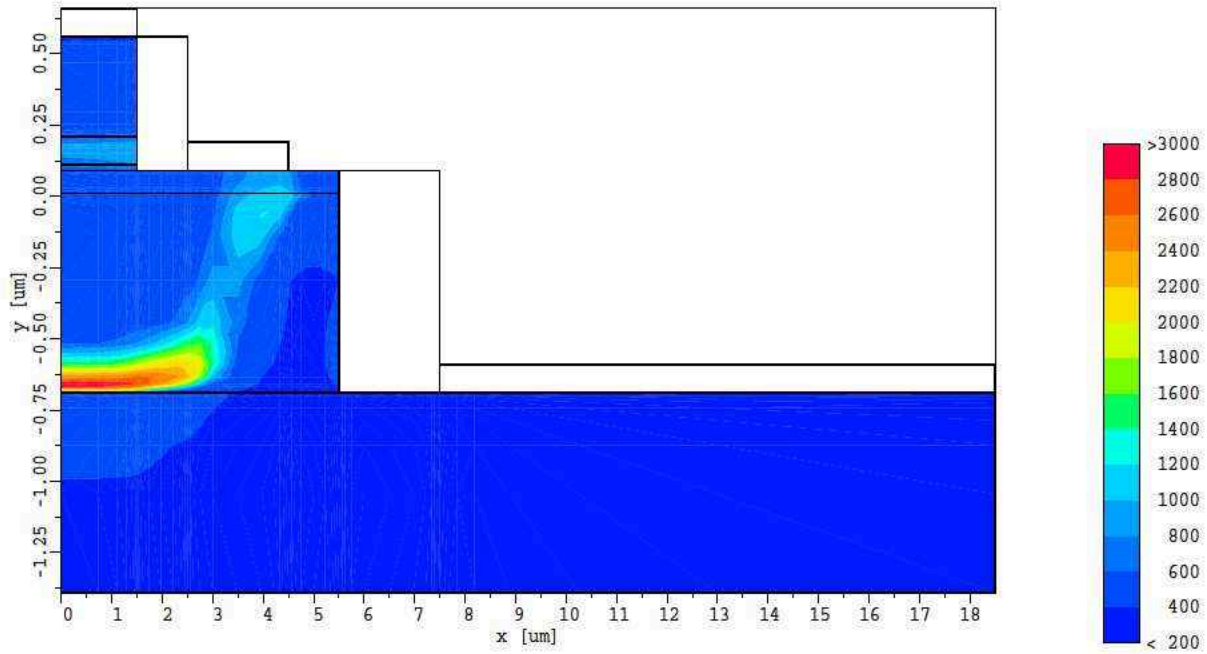
Fig. 4.21: Electron temperature distribution [K] at $V_{CE} = V_{BE} = 1.6$ V
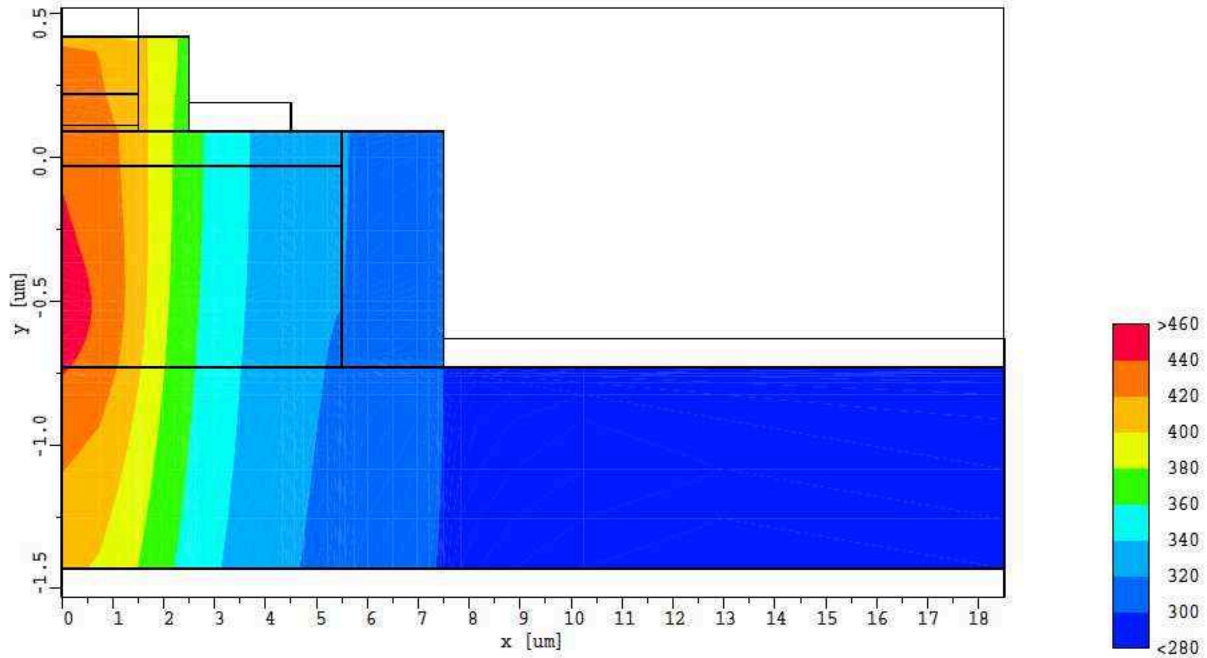

Fig. 4.22: Lattice temperature distribution [K] at $V_{CE} = 6.0$ V and $V_{BE} = 1.45$ V: A substrate thermal contact with $R_T = 400$ K/W is added.
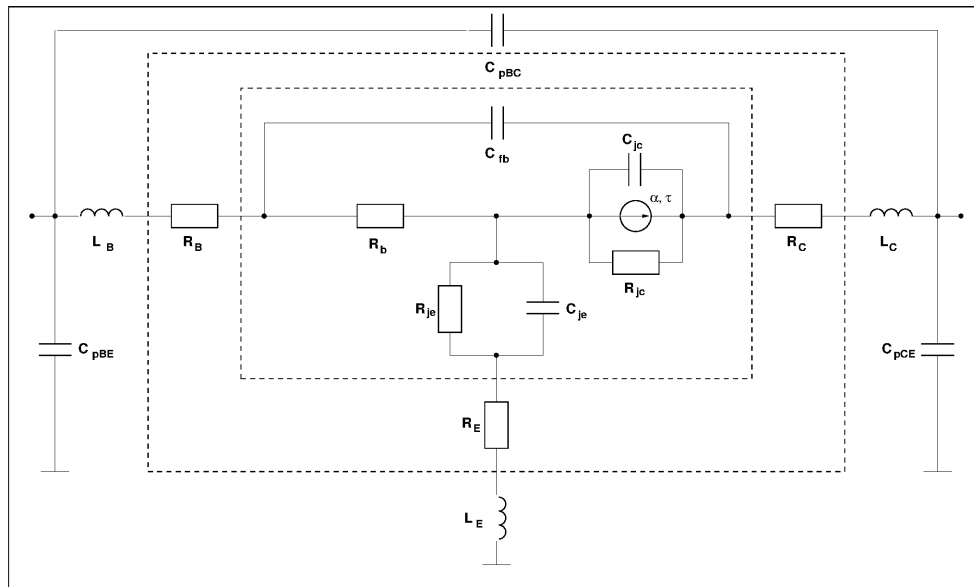
Fig. 4.23: T-like eight-element small-signal HBT equivalent circuit used for S-parameter calculation

4.3 S-Parameter Simulation

In the previous section two-dimensional simulations of one-finger power HBTs on GaAs are presented. A good agreement of simulations of four different types of devices with measured data in a wide temperature range is demonstrated. In addition, it is possible by accounting properly for self-heating to simulate correctly the output device characteristics. Considering the ability to reproduce correctly the DC-device behavior including thermal aspects the work is extended with transient simulation of small-signal parameters to connect DC- and RF-device operation. In the following subsections a comparison of simulated and measured S-parameters and the dependence of f_T on some device parameters are presented.

4.3.1 Simulation Approach

The simulation approach is similar to the one used in [61] for High Electron Mobility Transistors (HEMTs). In two independent simulations with MINIMOS-NT small-signal voltages are applied to the device terminals. The intrinsic Y-parameters are extracted from the results as shown in [200]. A frequency of 5 GHz at which the measured data was extracted is chosen for the simulation to avoid dispersion effects in a lower frequency range. The intrinsic Y-parameters are converted to Z-parameters and from those the intrinsic small-signal elements are calculated. A T-like eight-element small-signal equivalent circuit model [201] as shown in Fig. 4.23 is used. The Ohmic resistances are completely accounted for in the simulation. The S-parameter calculation uses the same typical values for the extrinsic parasitic elements (inductances and capacities) as extracted from the underlying technology [202] for compact modeling. From this set of parameters extrinsic S-parameters are calculated for the frequency range of 0 to 20 GHz suitable for comparison to the measurements in the same frequency range.

4.3.2   Simulation Results

The combined Smith/polar charts in Fig. 4.24 and Fig. 4.25 show comparisons of the simulated and measured S-parameters of a 90 μm^2 AlGaAs/GaAs HBT with InGaP ledge at $V_{CE} = 3$ V and $I_C = 22$ mA in frequency range between 0 and 20 GHz. Due to the large emitter area, the limitations of the eight-element intrinsic circuit, and the fact that the physical extraction procedure includes no fitting perfect agreement cannot be expected. As shown in Fig. 4.24 the deviations of measured and simulated S-parameters are more pronounced than for unipolar devices given the bias point is in a typical operation regime of a high power device. However, the small-signal extraction supplies valuable information about the modeling and the device itself.
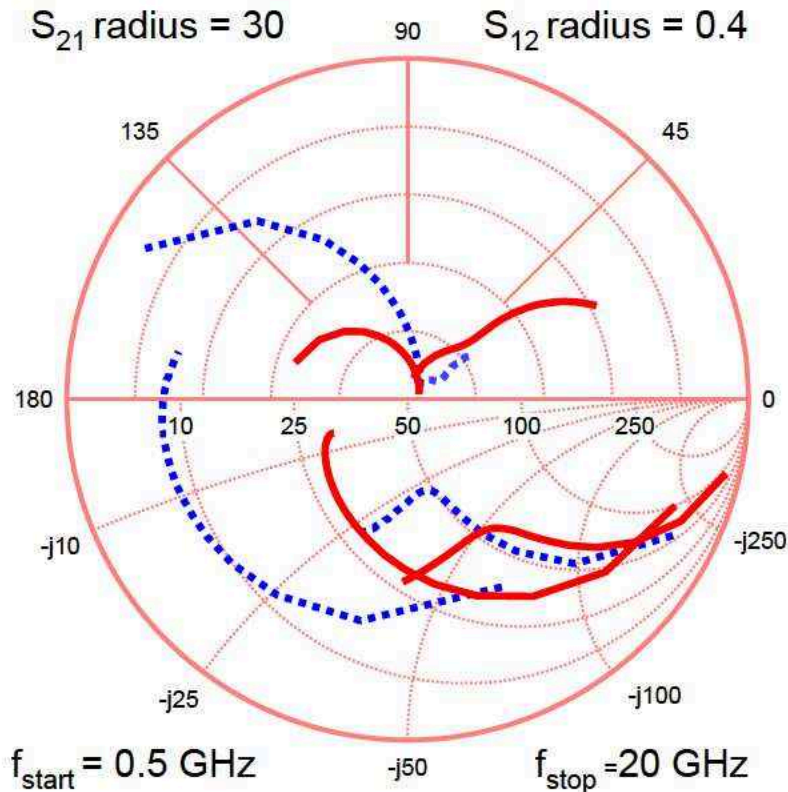

Fig. 4.24: S-parameters in a combined Smith chart (S_{11} and S_{22}) and a polar graph (S_{21} and S_{12}) from 0 to 20 GHz at $V_{CE} = 3$ V, $I_C = 22$ mA: Simulation (solid lines) vs. experiment (dashed lines)

Using the extraction above it is found that the physical background of some crucial elements can be improved. These are the small-signal elements base resistance R_b and the emitter junction capacity C_{je}, which show significant deviations on first approach. It is found that neglecting the difference between majority and minority electron mobilities results in underestimation of the electron mobility in the GaAs base of the HBT (see Section 3.4). This results in a significant overestimation of the extracted base resistance, as can be seen in Fig. 4.24. Including the respective mobility model much better agreement is achieved (see Fig. 4.25).
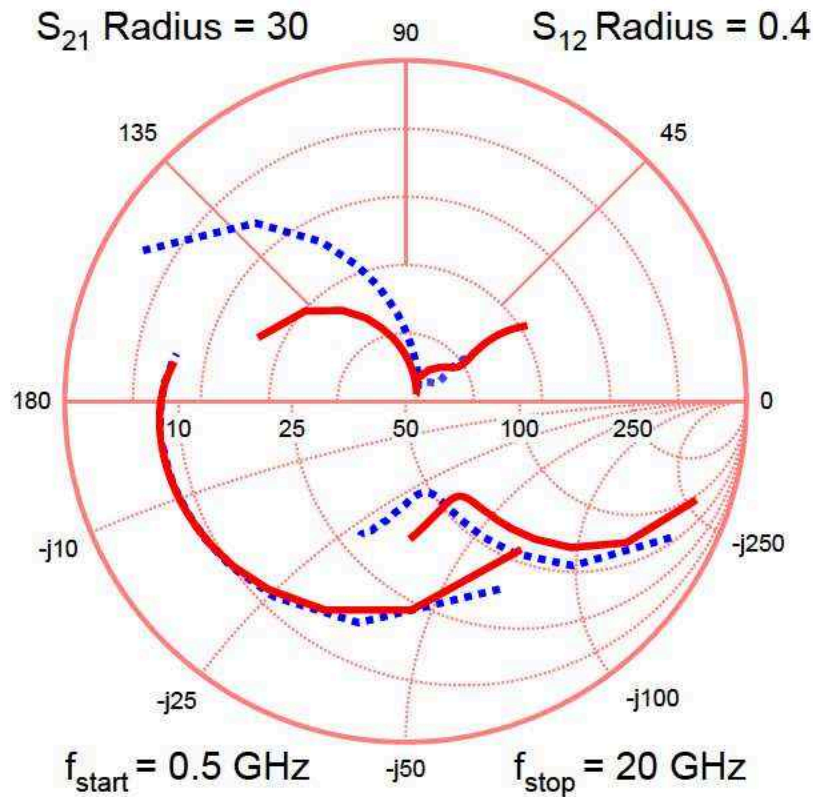
Fig. 4.25: S-parameters in a combined Smith chart (S_{11} and S_{22}) and a polar graph (S_{21} and S_{12}) from 0 to 20 GHz at $V_{CE} = 3$ V, $I_C = 22$ mA: Simulation (solid lines) vs. experiment (dashed lines)

For S_{11} and S_{22} good agreement with the measurements is obtained. The remaining underestimation of the magnitude of S_{21} is partly due to the fact that no HD simulation is performed. Further, R_b and C_{je} are still overestimated including the improved mobility model. For S_{12} very good agreement is achieved, given the the uncertainties of the measurement process of the feedback.

The simulated S-parameter are converted to h-parameters at 5 GHz. The current gain cutoff frequency f_T is obtained by extrapolation of the element $\|h21\|$ by 20 dB/decade frequency dependence. In addition, the dependence of f_T on important parameters, such as base width and ambient temperature, is investigated by simulation. The results are shown in Fig. 4.26 and Fig. 4.27, respectively. The contribution of the base delay time to the total delay can be estimated from the decrease of f_T with the base width, shown in Fig. 4.26. The degradation of f_T at high temperatures, shown in Fig. 4.27, is experimentally observed. The simulated f_T is in good agreement with the measured value at ambient temperature of 293 K.

This section shows, that given the constraints mentioned due to the compact modeling of HBT S-parameters, the RF extraction is available and suitable for predictive simulations, especially for quantitative estimations of dependence on not experimentally available degrees of freedom during device design.
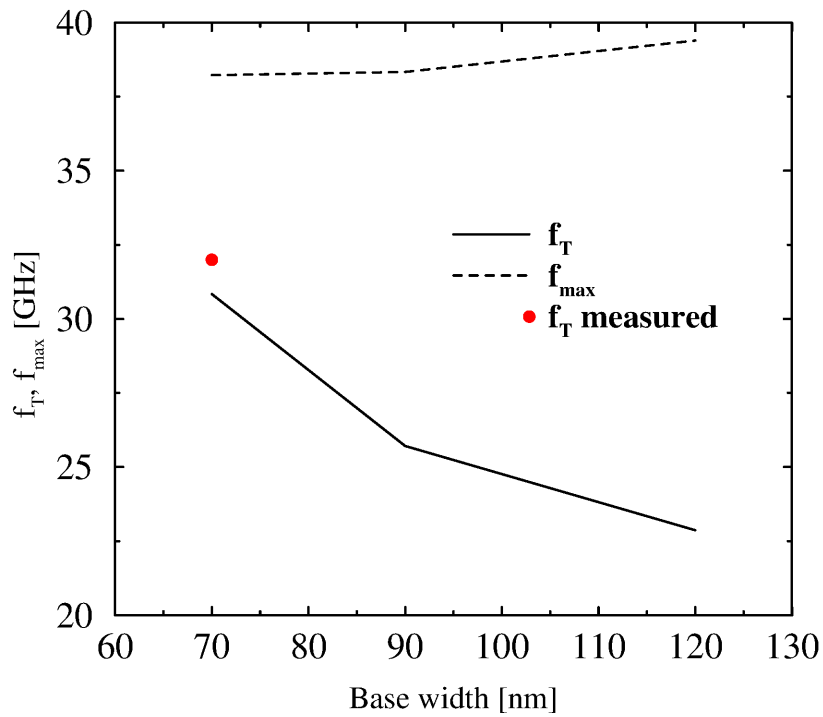
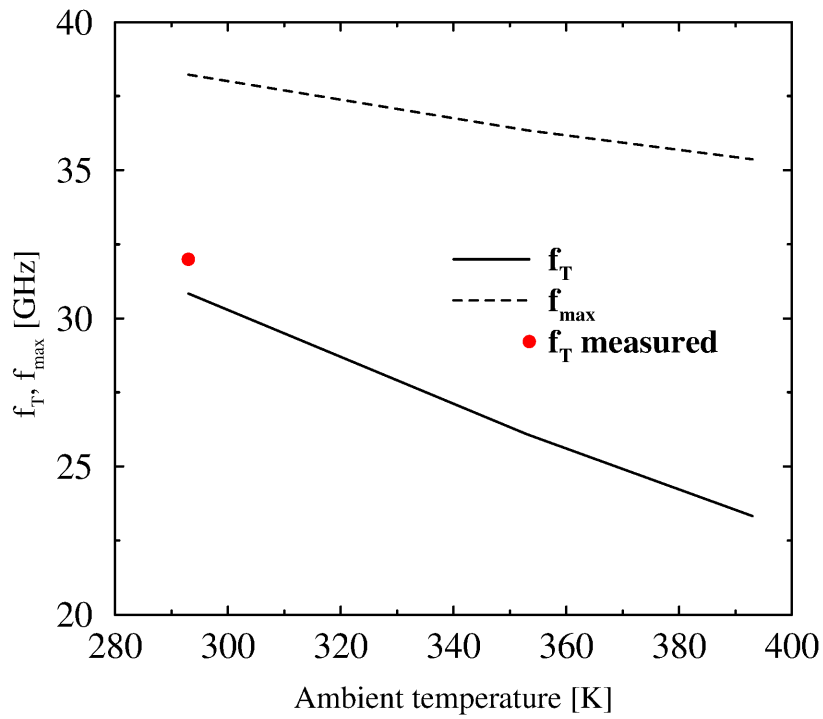**Fig. 4.26:** Cutoff frequencies vs. base width

Fig. 4.27: Cutoff frequencies vs. ambient temperature

4.4   Analysis of HBT Behavior After Electrothermal Stress

In this section simulations of one-finger power InGaP/GaAs HBTs before and after both electrical and thermal stress aging are presented. The influence of the ledge thickness and of the surface charges on the device performance and its impact on reliability is analyzed. Possible explanations of device degradation mechanisms, e.g. the effect of vanishing negative surface charges on the ledge/SiN interface, are proposed.

4.4.1   Importance of the InGaP Ledge

It is well known that GaAs-HBTs with an InGaP ledge have an improved reliability [203]. The emitter material covers the complete p-doped base layer, thus forming the so-called ledge. The impact of the ledge thickness d and negative surface charges, which exist at the ledge/nitride interface, on the device performance is investigated using MINIMOS-NT. The surface charges have large impact on the Fermi-level pinning at the InGaP/SiN interface. A schematic drawing of the simulated device structure is shown in Fig. 4.14. In order to save computational effort, the simulation domain covers only one half of the real symmetric device structure.
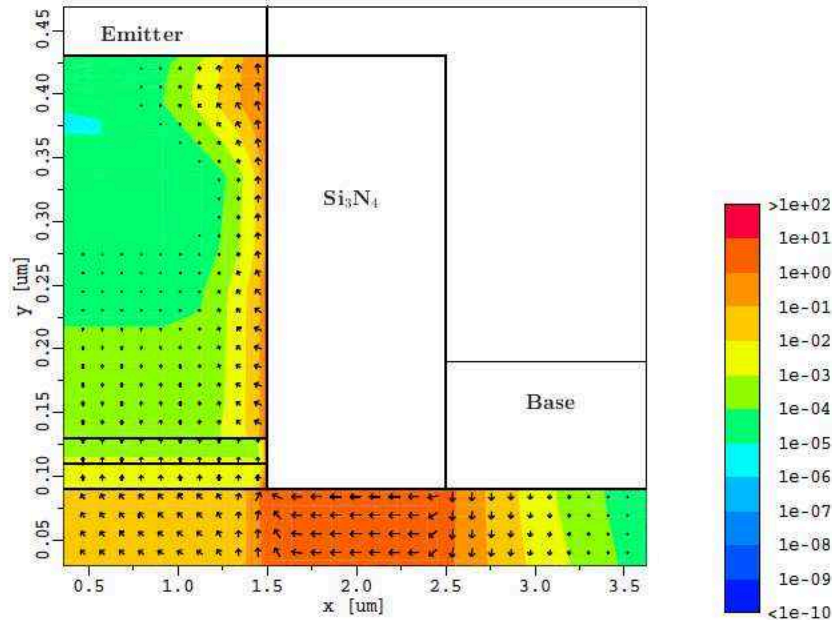
Fig. 4.28: Hole current density [A/cm^2]: Leakage path near the Si$_3$N$_4$ interface occurring in the presence of negative charges

Degradation Mechanisms in Devices without Ledge

In case of devices where no ledge is present (see Fig. 4.28), the simulation results suppose that during stress some of the electrons flowing in the emitter are injected in the insulator and get trapped there. The negative charge at the semiconductor/insulator interface can lead to a hole leakage path in the vicinity of the interface, and therefore, to undesirably high base currents.

Fig. 4.29: Dependence of I_B on the InGaP ledge thickness compared to measurement

InGaP Ledge Thickness

In Fig. 4.29 measured and simulated collector and base currents of one-finger InGaP/GaAs HBTs with different ledge thickness operating under forward Gummel plot conditions with $V_{BC} = 0$ V are shown. Measurement refers to a device with 40 nm ledge thickness. Surface charges at any of the device interfaces are not yet considered in the simulation. Note the strong increase in the base current at low bias 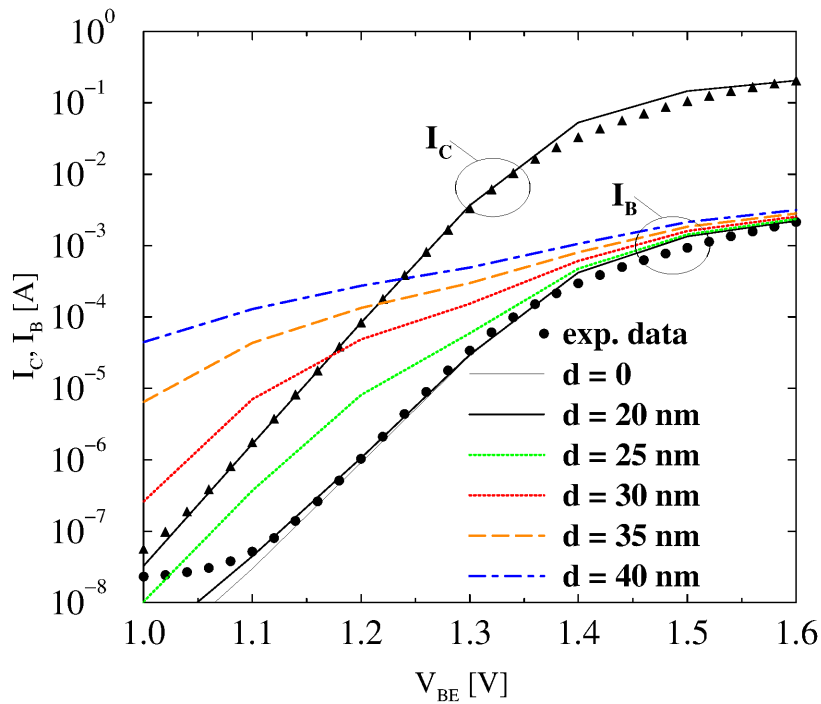with increasing ledge thickness. As can be seen from Fig. 4.29 simulated and measured base currents differ significantly in the case of 40 nm ledge thickness. Only simulation with a ledge thickness of less than 20 nm delivers a good match. The reason is that insulator surface Fermi-level pinning is not taken into account if surface charges are not considered in the simulation. Therefore, a non-physical electron current path occurs in the upper part of the ledge, as shown in Fig. 4.30. However, this leakage path can be overcome by means of electrically isolated base contacts. The corresponding electron distribution in the ledge using vertical cross-sections at x = 1.6 μm, 2.0 μm, and 2.4 μm is shown in Fig. 4.31. The hole distribution in the middle of the ledge (x = 2.0 μm) is also included. These concentrations shall be compared to the ones in the case of surface charges in the next subsection.

Negative Surface Charges

As can be seen from Fig. 4.32, where symbols represent experimental data for the collector current I_C and the base current I_B and simulation refers to a device with 40 nm ledge, the base current decreases if more negative surface charges are introduced. The upper part of the ledge
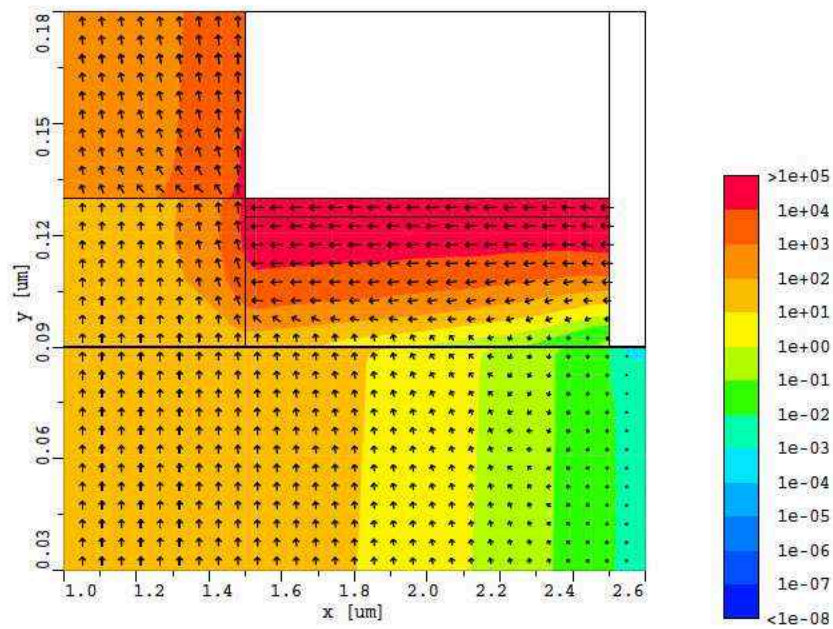
Fig. 4.30: Electron current density [A/cm^2] at V$_{BE}$=1.2V: Simulation without surface charges
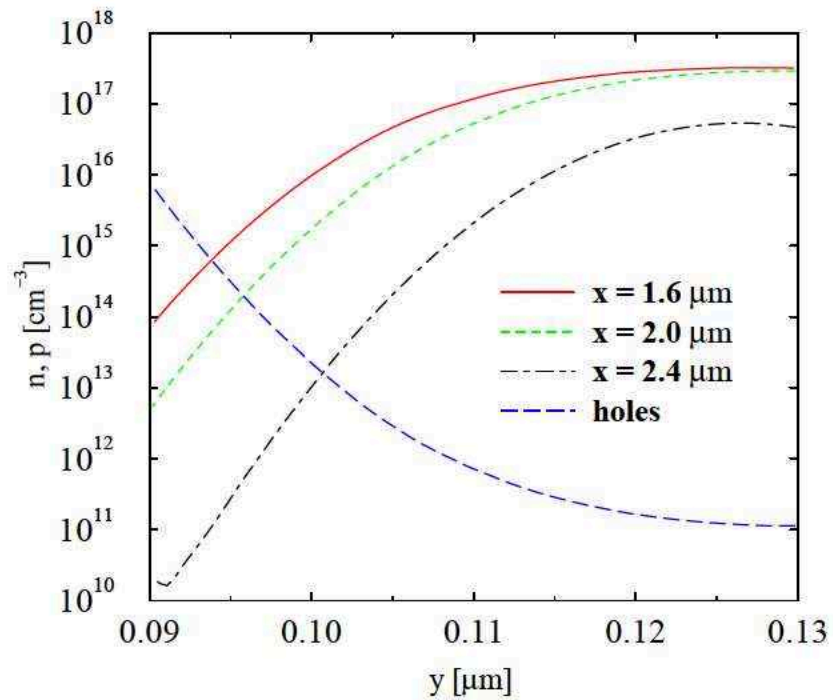

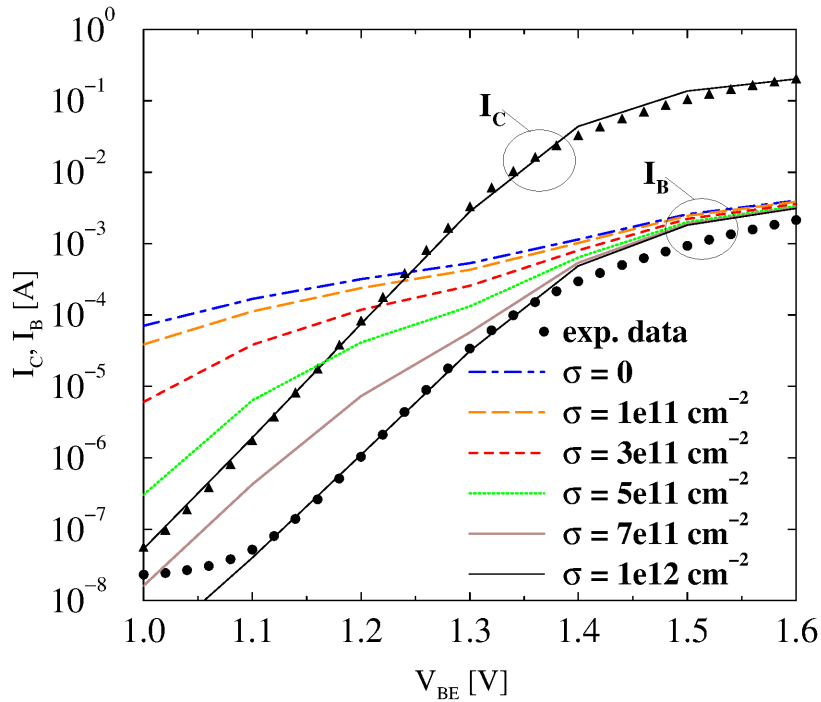**Fig. 4.31:** Electron and hole distribution in the ledge: Simulation without surface charges

Fig. 4.32: Dependence of I_B on the negative charge density at the ledge/nitride interface with d = 40 nm: A charge density of 10^{12} cm^{-2} is sufficient to get good fit to the measurements

is depleted as well [204] and the leakage is reduced (Fig. 4.33). The corresponding electron distribution in the ledge at x = 1.6 μm, 2.0 μm, and 2.4 μm, and the hole distribution at x = 2.0 μm are presented in Fig. 4.34. Note that even in this case the ledge is not completely depleted. However, the electron concentrations near the InGaP/SiN interface are significantly lower in comparison to the ones shown in Fig. 4.31. Thus, with a surface charge density of 10^{12} cm^{-2} the measured base current can be simulated very well. Note that in the case of negative surface charges the hole concentration in the ledge increases and at higher values gives the opportunity a hole current path to occur.

4.4.2   Device Reliability

Based on these investigations it is now possible to explain the base current degradation of an InGaP/GaAs HBT which is strongly stressed under conditions far from normal operating conditions. In this case the base current degradation in the middle voltage range can be explained by a decreasing surface charge density along the interface between ledge and passivation from 10^{12} cm^{-2} to 4.10^{11} cm^{-2}. This might be due to compensation of the negative surface charges by H+ ions which are known to be present in the device due to the epitaxial manufacturing processes [205, 206]. In Fig. 4.35 a comparison of measured and simulated forward Gummel plots at V_{CB} = 0 V is shown. Filled and open symbols denote measured characteristics of the non-degraded and degraded device, respectively. The lines show the corresponding simulation results. The good agreement also for stressed devices demonstrates

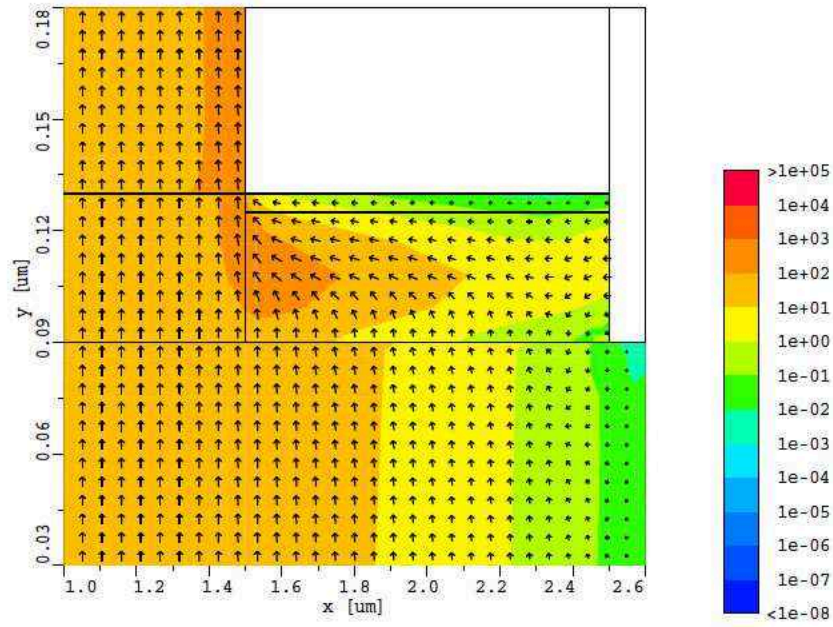**Fig. 4.33:** Electron current density [A/cm^2] at V_{BE}=1.2V: Simulation with a surface charge density of 10^{12} cm^{-2}
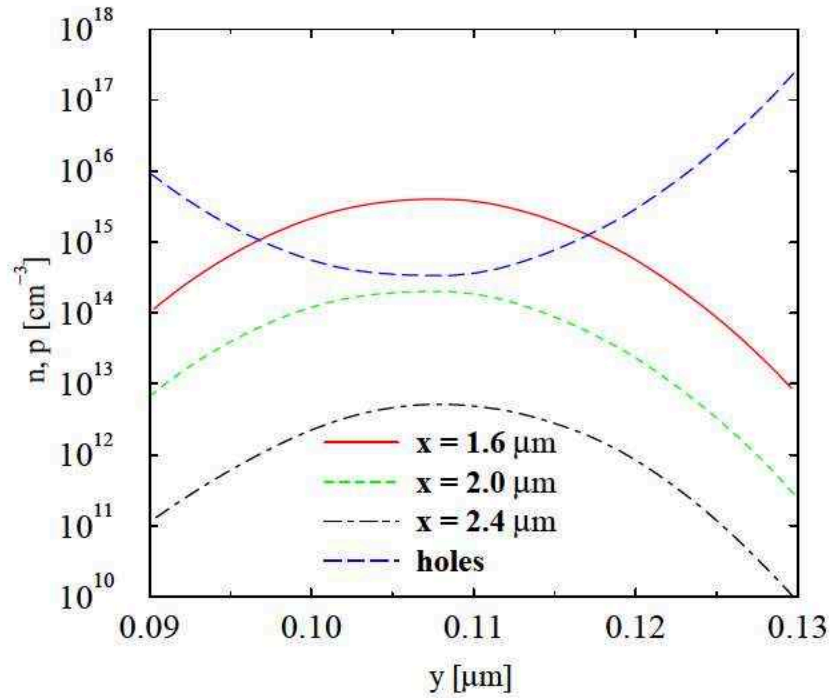

Fig. 4.34: Electron and hole distribution in the ledge: Simulation with a surface charge density of 10^{12} cm^{-2}
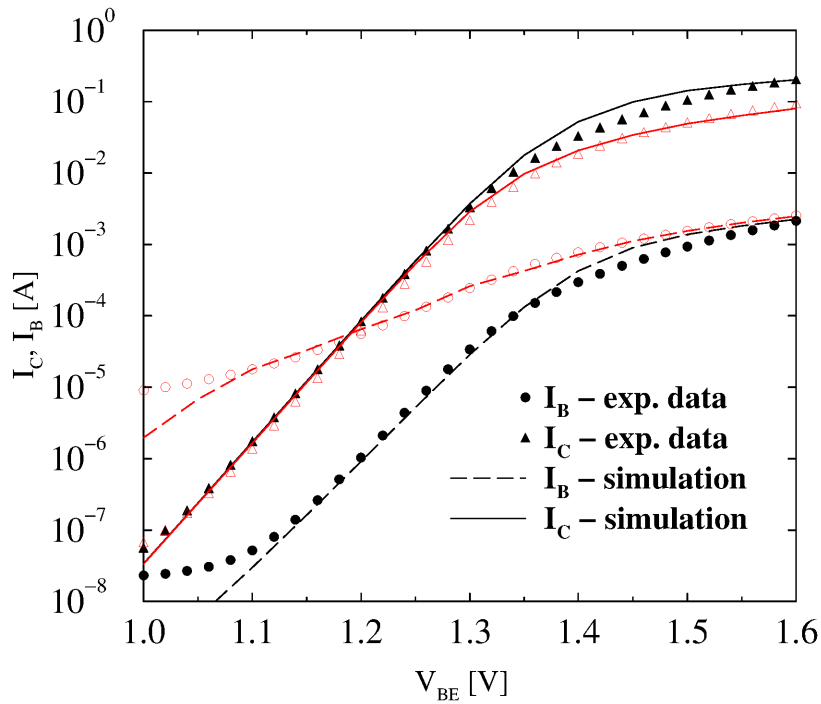
Fig. 4.35: Forward Gummel plots at $V_{CB} = 0$ V: Comparison between measurement (symbols) and simulation (lines) before (filled) and after (open) HBT aging.

the applicability of physically-based device simulation to device reliability issues. The electron current density corresponding to a surface charge density of 4.10^{11} cm^{-2} is presented in Fig. 4.36. Fig. 4.37 shows the corresponding electron distribution in the ledge at x = 1.6 μm, 2.0 μm, and 2.4 μm, and the hole distribution at x = 2.0 μm. Note that the upper part of the ledge is now not completely depleted, thus allowing a base leakage current.

Several other effects supposed to lead to a strong increase in the base leakage current, e.g. spreading out of the base contact at the metal/GaAs interface, increased recombination-generation in the InGaP layer, degradation of the SiN/GaAs interface (see e.g. [207], [208] and references therein) are also analyzed. The simulation results show that such effects cannot be the dominant reason for degradation of the current gain. The decrease in the collector current at high level injection is suggested to be due to increased emitter resistance which could occur due to emitter contact detachment, indium segregation in the metal layer, or dislocations at the InGaAs/GaAs interface (see e.g. [208]). Our simulations show, that contact detachment leads to an electron current crowding in the remaining contact area which leads to insignificant changes. Only an emitter contact detachment of more than 80%, which is slightly probable, can explain the measured values (see Fig. 4.38). Indium segregation in the metal is found to be a possible reason, as the emitter contact resistance increases, while the decrease of the indium content in the cap has no significant influence on the emitter resistance.

Fig. 4.36: Electron current density [A/cm^2] at V_{BE}=1.2V: Simulation with a surface charge density of 4.10^{11} cm^{-2}
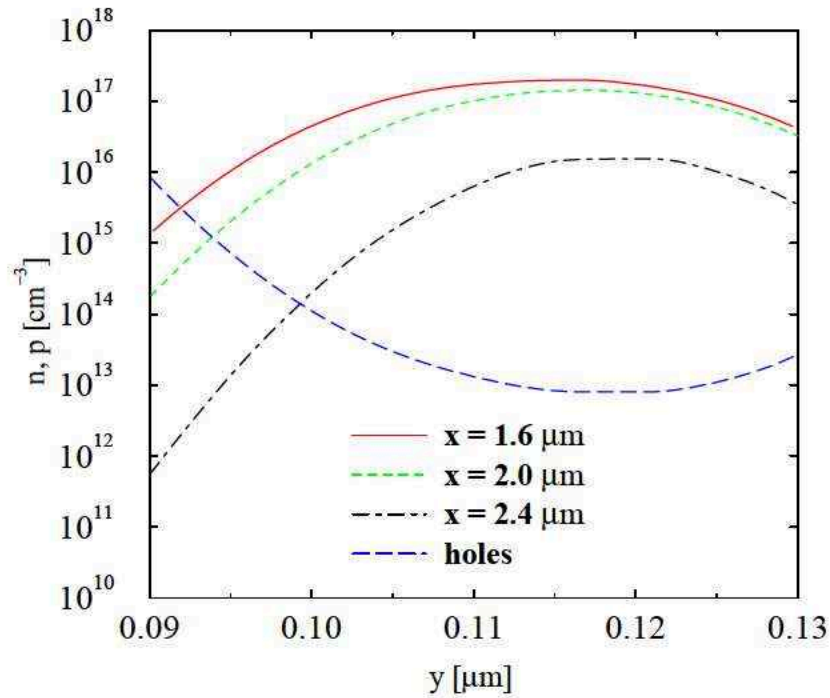
Fig. 4.37: Electron and hole distribution in the ledge: Simulation with a surface charge density of 4.10^{11} cm^{-2}
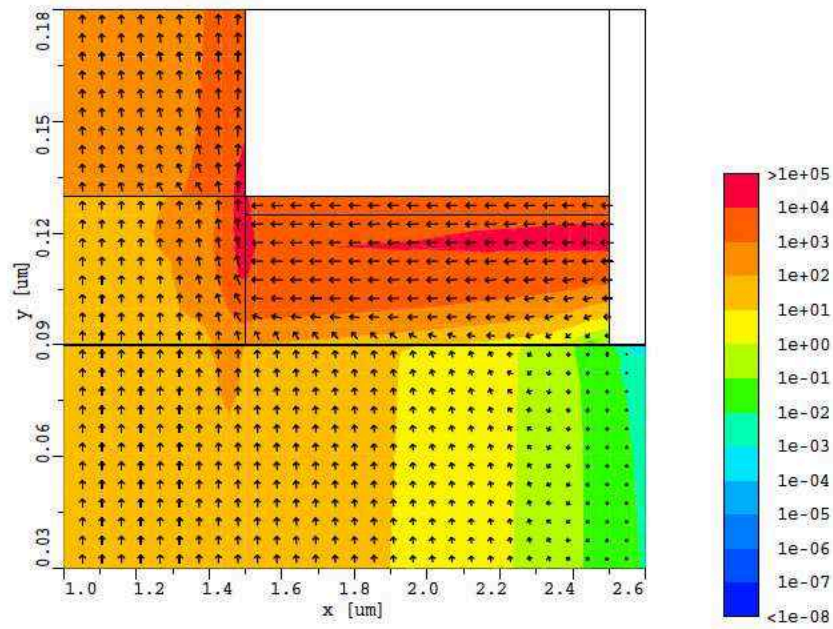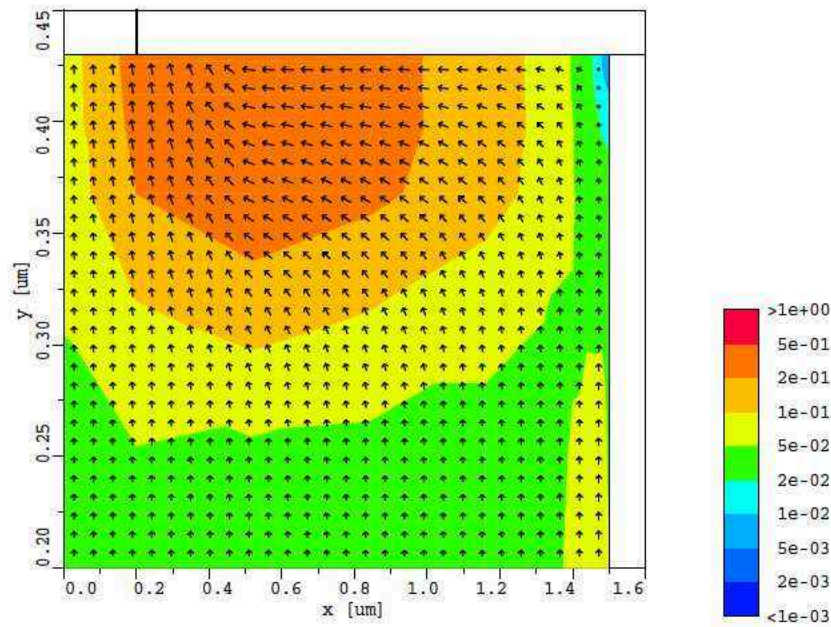
Fig. 4.38: Electron current density [A/cm^2]: Simulation of emitter contact detachment

4.4.3   Effectiveness of Silicon Nitride Passivation

The quality of Si$_3$N$_4$ thin film passivation is of importance for the reliability of III-V based HBTs. Both theoretical and experimental studies have been conducted in order to minimize base leakage currents as a major source of degradation. The effectiveness of the passivation of devices before and after electrothermal stress aging is investigated by the means of two-dimensional numerical simulations. For that purpose proper electrical and thermal models are implemented in MINIMOS-NT allowing simulation of silicon nitride as a wide bandgap semiconductor material.

Silicon Nitride as a Wide Bandgap Semiconductor

The non-ideal properties of the passivation are accounted by considering it as a semiconductor material. A bandgap energy of 5 eV, relative dielectric constant of 7, and constant carrier mobilities based on resistivity of 10^{16} Ω-cm are used. Thus, previous results assuming an ideal insulator material are verified. However, it has to be noted that the transport properties in the insulator, being treated as a semiconductor, strongly depend on the bandgap alignment on the insulator/semiconductor interface which can be altered in the presence of surface charges.

The impact of the surface charge density is illustrated in Fig. 4.39 where simulation results for the electron current density at $V_{BE} = 1.2$ V without and with a surface charge density of 10^{12} cm^{-2}, respectively, are shown. *Shockley-Read-Hall* recombination is taken into account also in the SiN with a trap density of 10^{8} cm^{-3}. Note, the decrease in the electron current density also in the insulator in the presence of negative charges (Fig. 4.40).

Fig. 4.39: Electron current density $[\text{A/cm}^2]$ at $V_{BE}=1.2$ V: Simulation without surface charges

Fig. 4.40: Electron current density $[\text{A/cm}^2]$ at $V_{BE}=1.2$ V: Simulation with surface charge density of 10^{12} cm^{-2}

4.5 Simulation of Polysilicon Emitter Bipolar Transistors

Polysilicon emitter silicon based Bipolar Junction Transistors (BJTs) are attractive semiconductor devices with their high performance-to-cost ratio and power application in modern mobile telecommunication systems.
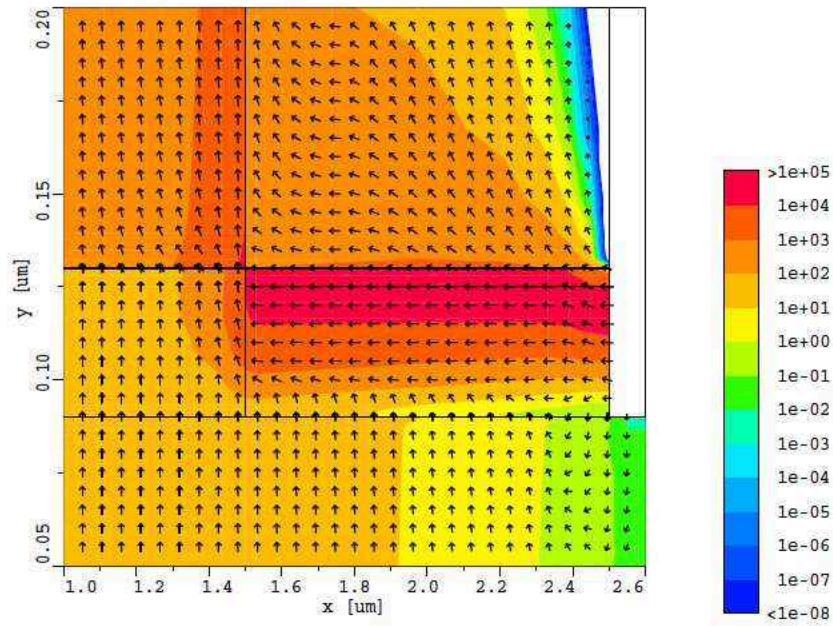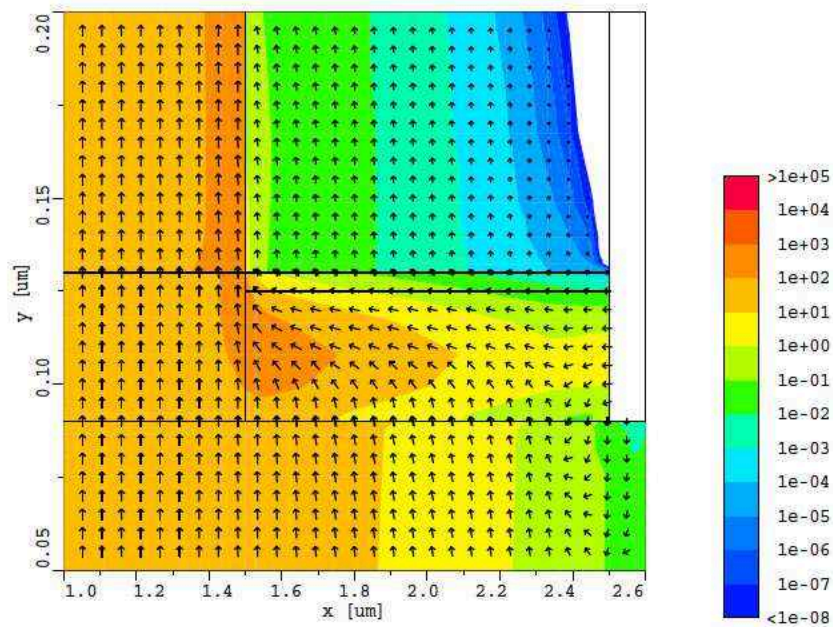
In this section results of two-dimensional simulations of polysilicon emitter BJTs are presented. For that purpose proper polysilicon contact models have been implemented in MINIMOS-NT.

4.5.1 Device Fabrication

The device under investigation is a Double Base Silicon Bipolar Junction Transistor epitaxially grown by a Chemical Vapor Deposition (CVD) process. An n-well (Arsenic), similar to the implanted one used in the standard CMOS technology, is grown during the epitaxial process. The buried layer (Antimony) is connected to a sinker (Phosphorus) to conduct the electron current from the buried layer to the collector contact.
The base consists of an intrinsic base (below the emitter window, Boron-doped) and the extrinsic base (highly Boron-doped under the base contact).
The emitter-base junction is formed by a diffusion process of a polysilicon layer which is placed on the p-doped base under the emitter window. After implantation of Arsenic, a diffusion process pushes the Arsenic into the p-doped base, thus forming the emitter-base junction.

4.5.2 Process Simulation

In order obtain results of practical use appropriate process simulation followed by device simulation and device optimization need to be performed. The process simulation is straightforward and good results can be obtained using e.g. TSUPREM [209] or DIOS [210]. The device structure and net doping profile are shown in Fig. 4.41. The simulation domain covers only one half of the real device, because of the symmetric device structure.

4.5.3 Device Simulation Results and Comparison with Measurements

As shown in previous example (see Section 4.1.3) proper modeling of bandgap narrowing (BGN) and recombination have particular importance. In addition, the polysilicon contact model (see Section 3.1.6) is used. The contribution of BGN to the conduction band $\Delta E_C / \Delta E_g$, the trap charge density N_T from the SRH model, and the velocity recombination for holes at the emitter contact S_p are the only fitting parameters used.

The result for the electron current density at $V_{BE} = 1.5$ V (V_{CE}) is shown in Fig. 4.42. Note, the comparatively high electron current portion of the base current. The simulation gives an explanation of the experimentally observed decrease in the current gain at high bias. Comparisons between the measured and simulated forward Gummel plot (Fig. 4.43) and current gain (Fig. 4.44) show good agreement.
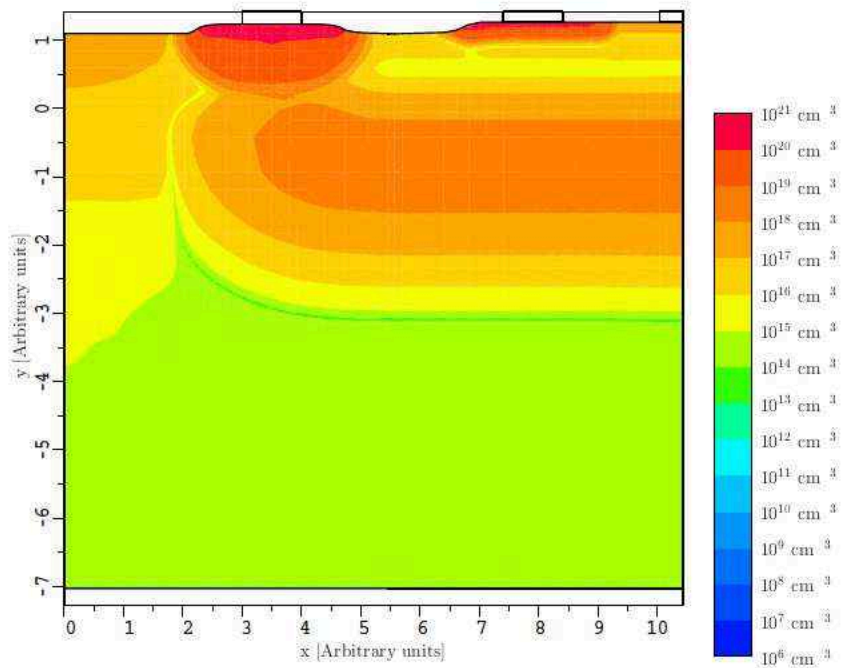
Fig. 4.41: Device structure and net doping profile (absolute value)
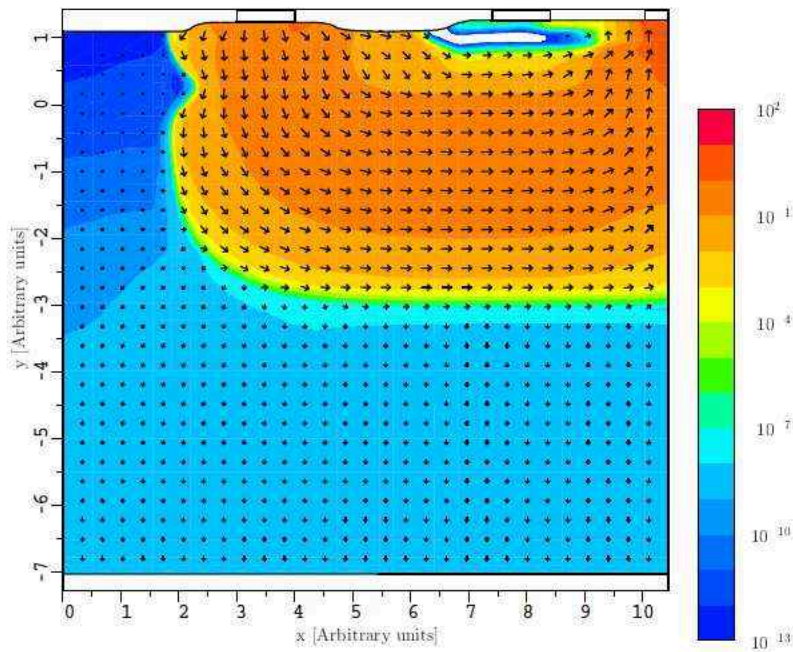
Fig. 4.42: Electron current density at $V_{BE} = 1.5$ V
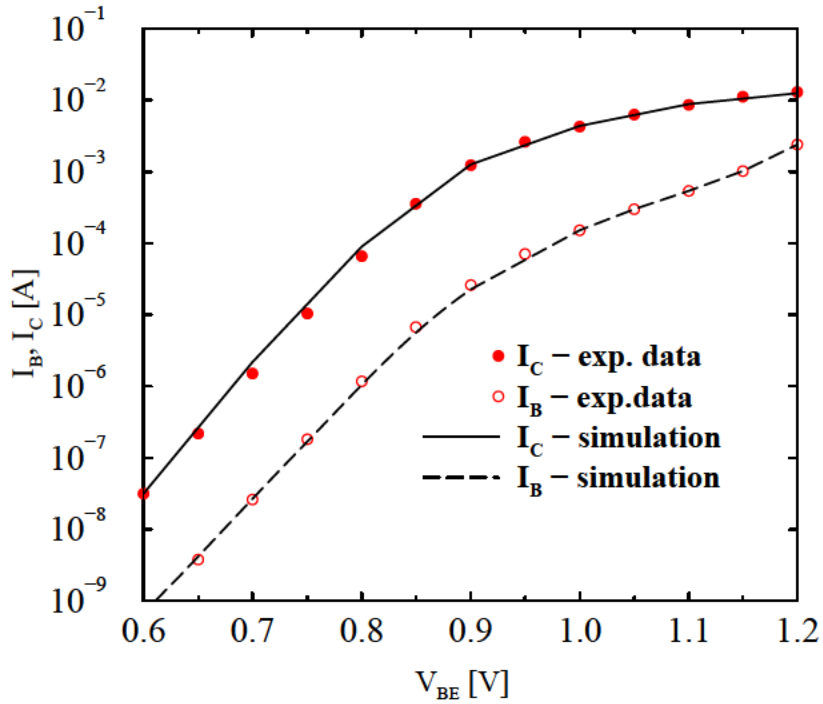
Fig. 4.43: Measured and simulated forward Gummel plot at $V_{BC} = 0$ V at 300 K
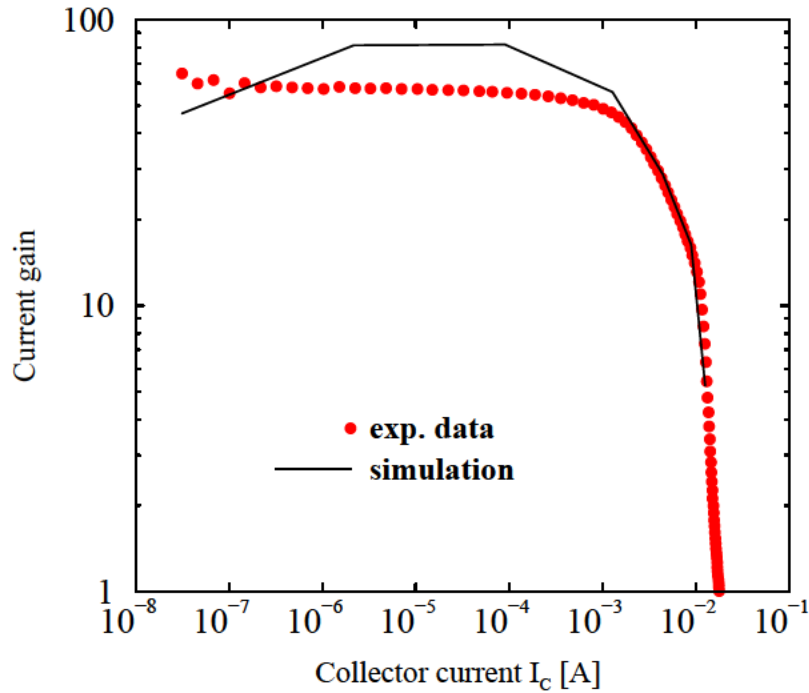
Fig. 4.44: Current gain vs. collector current
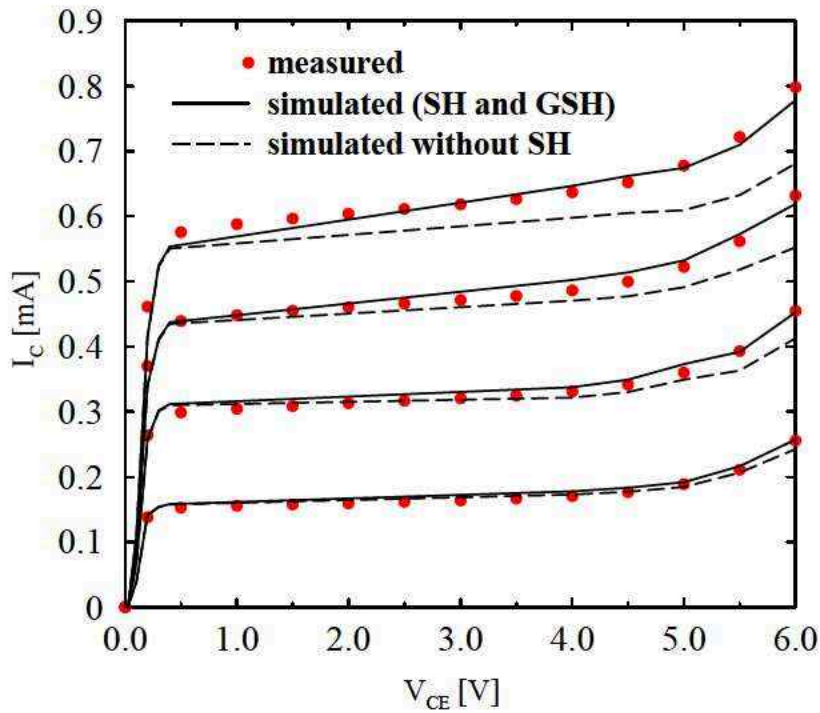
Fig. 4.45: Simulation with SH (solid lines) and without SH (dashed lines) compared to measurement data (symbols)

In the case of simulation of the output characteristics one meets severe problems to achieve realistic results, especially in the case of power devices. Therefore, self-heating (SH) effects have to be accounted for by solving the lattice heat flow equation self-consistently with the energy transport equations. An alternative Global SH model (GSH) has been offered in [211]. The model calculates a spatially constant (global) lattice temperature T_L in the device from the dissipated power as

$$T_L = T_C + R_g \cdot \sum_C I_C \cdot V_C \tag{4.5}$$

with I_C and V_C being the contact currents and voltages, T_C being contact temperature, and R_g being the global thermal resistance.

In Fig. 4.45 the simulated output device characteristics compared to measurements for base currents of 2, 4, 6, and 8 μA are shown. The GSH model with $R_g = 800$ K/W delivers the same results (within 2%) as the SH model, but for 40% less CPU time. Both models deliver results in very good agreement with the measured output device characteristics. In contrast to that, simulation without including of SH effects cannot reproduce the experimental data, especially at high power levels. Similar and even stronger observation were already done in the case of GaAs power HBTs (see Section 4.2.2).

Chapter 5

Conclusion and Outlook

THE basic purpose of this thesis was to find or develop physical models in order to allow simulation of advanced heterostructure devices, such as HBTs or HEMTs, with the two-dimensional device/circuit simulator MINIMOS-NT. For that purpose, the state-of-the-art in device technology and device simulation, was analyzed.

5.1   Conclusion

Considerable effort was spent on MINIMOS-NT to get it ready for simulation of devices with high complexity in respect to materials, geometries, etc. Many of the existing physical models (bandgap, mobility, thermal conductivity, energy relaxation times, specific heat, etc.) were refined, some of them were replaced by promising new ones, and many new models were added as well. Critical issues concerning simulation of heterostructures were analyzed, such as interface modeling at heterojunctions and insulator surfaces, band structure and bandgap narrowing, the modeling of self-heating and high-field effects. Being an ancestor of the well-known MOS device simulator MINIMOS, its experience with silicon devices was inherited. Thereby, MINIMOS-NT became a generic device simulator accounting for a variety of micro-materials, including group IV semiconductors, III-V compound semiconductors and their alloys, and non-ideal dielectrics.

Several applications of industrial interest employ devices operating in a wide temperature range. Therefore, our models have been designed to meet this challenge in addition to the conventional Silicon applications. MINIMOS-NT has been successfully used for simulation of heterostructure devices, such as HEMTs and HBTs. Physics-based DC-simulations, mixed-mode device/circuit simulations, small-signal RF-parameter simulations, and device reliability investigations of high practical value were performed.

In the thesis, simulation results for several different types of GaAs-based and Si-based HBTs demonstrating the extended capabilities of MINIMOS-NT are shown, most of them in comparison with experimental data. Special emphasis is put on the simulation of high-power AlGaAs/GaAs and InGaP/GaAs HBTs. Two-dimensional DC-simulations of four different types of one-finger devices in very good agreement with measured data in a wide temperature range are demonstrated. Self-heating effects are accounted for the output device character-

istics. The work is extended with transient simulation of small-signal parameters to connect DC- and RF-operation. A comparison between simulated and measured S-parameters is presented. Device reliability investigations which confirm the usefulness of device simulation for practical applications are also offered. In particular, the influence of the InGaP ledge on the device performance of InGaP/GaAs-HBTs is analyzed. Examples of SiGe HBTs and polysilicon emitter BJT conclude the work presented in the thesis.

5.2 Future Directions

One possible direction is to continue expanding the material database of MINIMOS-NT with multinary III-V materials of relevance, such as III-Nitrides and III-Antimonides. Including group II-VI semiconductors is also feasible. As for group IV materials, SiC or SiGeC need still to be included in MINIMOS-NT, and a more rigorous approach to SiGe has to be applied.

New models for physical properties with respect to material composition and strain conditions due to lattice mismatch have to be developed. The models must be valid for the whole composition range in the temperature range between 70 K and 500 K. Anisotropic effective carrier masses, density of states, and carrier mobilities should be considered. A built-in feature for automatic estimation of the strain condition based on empirical relation for the growth-condition dependent critical layer thickness (see e.g. [127, 128]) can also be developed. The materials used in two consecutive layers can be checked if they cannot be grown without a lattice mismatch. It is imaginable to apply the algorithm for estimation of the strain condition of arbitrary relevant material structures. The convergence behavior must be optimized and the complexity of the models should be cross-checked with the computational effort in order to ensure the effectiveness of the new models.

Possible simulation applications in the future could be the simulation of leakage currents at low bias in GaAs-based HBTs, breakdown simulation in III-V devices, thermal investigations not only in the device, but also in the interconnects. The accuracy of the device simulation for all devices has to be verified not only against DC-, but also against RF-measurements. Simulations will aid reliability investigations also in the future, as they offer practical solutions.

Bibliography

[1] S. Iyer, G. Patton, S. Delage, S. Tiwari, and J. Stork, "Silicon-Germanium Base Heterojunction Bipolar Transistors by Molecular Beam Epitaxy," in *Proc. Si-MBE Symp.*, pp. 114–125, 1987.

[2] T. Kamins, K. Nauka, L. Camnitz, J. Kruger, J. Turner, S. Rosner, M. Scott, J. Hoyt, C. King, D. Noble, and J. Gibbons, "High Frequency Si/Si$_{1-x}$Ge$_x$ Heterojunction Bipolar Transistors," in *Intl.Electron Devices Meeting*, pp. 647–650, 1989.

[3] J. Cressler, J. Comfort, E. Crabbe, G. Patton, J. Stork, J.-C. Sun, and B. Meyerson, "On the Profile Design and Optimization of Epitaxial Si- and SiGe-Base Bipolar Technology for 77 K Applications - Part I: Transistor DC Design Considerations," *IEEE Trans.Electron Devices*, vol. 40, no. 3, pp. 525–541, 1993.

[4] P. Narozny, H. Dämbkes, H. Kibbel, and E. Kasper, "Si/SiGe Heterojunction Bipolar Transistor Made by Molecular-Beam Epitaxy," *IEEE Trans.Electron Devices*, vol. 36, no. 10, pp. 2363–2366, 1989.

[5] A. Schüppen, A. Gruhle, H. Kibbel, U. Erben, and U. König, "SiGe HBTs with High f_T at Moderate Current Densities," *Electron.Lett.*, vol. 30, no. 14, pp. 1187–1188, 1994.

[6] K. Oda, E. Ohue, M. Tanabe, H. Shimamoto, T. Onai, and K. Washio, "130-GHz f_T SiGe HBT Technology," in *Intl.Electron Devices Meeting*, pp. 791–794, 1997.

[7] A. Schüppen, U. Erben, A. Gruhle, H. Kibbel, H. Schumacher, and U. König, "Enhanced SiGe Heterojunction Bipolar Transistors with 160-GHz f_{max}," in *Intl.Electron Devices Meeting*, pp. 743–746, 1995.

[8] K. Oda, E. Ohue, M. Tanabe, H. Shimamoto, and K. Washio, "DC and AC Performances in Selectively Grown SiGe-Base HBTs," *IEICE Trans.Electron.*, vol. E82-C, no. 11, pp. 2013–2020, 1999.

[9] G. Freeman, D. Ahlgren, D. Greenberg, R. Groves, F. Huang, G. Hugo, B. Jagannathan, S. Jeng, K. Schonenberg, K. Stein, R. Volant, and S. Subbanna, "A 0.18 μm 90 GHz f_T SiGe HBT BiCMOS, ASIC-Compatible, Copper Interconnect Technology for RF and Microwave Applications," in *Intl.Electron Devices Meeting*, pp. 569–572, 1999.

[10] W. Klein and B.-U. Klepser, "75-GHz Bipolar Production Technology for the 21st Century," in *29th European Solid-State Device Research Conference* (H. Maes, R. Mertens, G. Declerck, and H. Grünbacher, eds.), (Leuven, Belgium), pp. 88–94, Editions Frontiers, 1999.

[11] S. Subbanna, G. Freeman, D. Ahlgren, B. Jagannathan, D. Greenberg, J. Johnson, P. Bacon, R. Najarian, D. Herman, and B. Meyerson, "Review of Silicon-Germanium BICMOS Technology after 4 Years of Production and Future Directions," in *Tech.Dig. GaAs IC Symp.*, (Seattle, USA), pp. 7–10, 2000.

[12] A. Schüppen, "SiGe-HBTs for Mobile Communications," *Solid-State Electron.*, vol. 43, pp. 1373–1381, 1999.

[13] K. Washio, E. Ohue, K. Oda, R. Hayami, M. Tanabe, H. Shimamoto, T. Masuda, K. Ohhata, and M. Kondo, "Self-Aligned Selective-Epitaxial-Growth SiGe HBTs: Process, Device, and ICs," *Thin Solid Films*, vol. 369, no. 1-2, pp. 352–357, 2000.

[14] T. Niwa, Y. Amamiya, M. Mamada, and H. Shimawaki, "High-f_T AlGaAs/InGaAs HBTs with Reduced Emitter Resistance for Low-Power-Consumption, High-Speed ICs," in *Proc. Intl. Symp. on Compound Semiconductors*, (Bristol, UK), pp. 309–312, IOP, 1999.

[15] T. Oka, K. Hirata, K. Ouchi, H. Uchiyama, T. Taniguchi, K. Mochizuki, and T. Nakamura, "Advanced Performance of Small-Scaled InGaP/GaAs HBTs with f_T over 150 GHz and f_{max} over 250 GHz," in *Intl.Electron Devices Meeting*, pp. 653–656, 1998.

[16] D. Mensa, Q. Lee, J. Guthrie, S. Jaganathan, and M. Rodwell, "Transferred-Substrate HBTs with 250 GHz Current-Gain Cutoff Frequency," in *Intl.Electron Devices Meeting*, pp. 657–660, 1998.

[17] Q. Lee, S. Martin, D. Mensa, R. Smith, J. Guthrie, and M. Rodwell, "Submicron Transferred-Substrate Heterojunction Bipolar Transistors," *IEEE Electron Device Lett.*, vol. 20, no. 8, pp. 396–398, 1999.

[18] M. Yanagihara, H. Sakai, Y. Ota, M. Tanabe, K. Inoue, and A. Tamura, "253-GHz f_{max} AlGaAs/GaAs HBT with Ni/Ti/Pt/Ti/Pt-Contact and L-Shaped Electrode," in *Intl.Electron Devices Meeting*, pp. 807–810, 1995.

[19] C. Bolognesi, M. Dvorak, O. Pitts, and S. Watkins, "200 GHz InP/GaAs$_x$Sb$_{1-x}$ Double Heterojunction Bipolar Transistors," in *Tech.Dig. GaAs IC Symp.*, (Seattle, USA), pp. 233–236, 2000.

[20] K. Oda, E. Ohue, M. Tanabe, H. Shimamoto, and K. Washio, "Si$_{1-x}$Ge$_x$ Selective Epitaxial Growth for Ultra-High-Speed Self-Aligned HBTs," *Thin Solid Films*, vol. 369, no. 1-2, pp. 358–361, 2000.

[21] K. Washio, E. Ohue, K. Oda, R. Hayami, M. Tanabe, H. Shimamoto, T. Harada, and M. Kondo, "82 GHz Dynamic Frequency Divider in 5.5 ps ECL SiGe HBTs," in *Dig. Intl. Solid-State Circuits Conference*, (San Francisco, USA), pp. 210–211, 2000.

[22] T. Suemitsu, T. Ishii, H. Yokoyama, Y. Umeda, T. Enoki, and T. Tamamura, "30-nm-gate InAlAs/InGaAs HEMTs Lattice-Matched to InP Substrates," in *Intl.Electron Devices Meeting*, pp. 223–226, 1998.

[23] L. Nguyen, A. Brown, M. Thompson, and L. Jelloian, "50-nm Self-Aligned-Gate Pseudomorphic AlInAs/GaInAs High Electron Mobility Transistors," *IEEE Trans. Electron Devices*, vol. 39, no. 9, pp. 2007–2014, 1992.

[24] M. Wojtowicz, R. Lai, D. Streit, G. Ng, T. Block, K. Tan, P. Liu, A. Freudenthal, and R. Dia, "0.10 μm Graded InGaAs Channel InP HEMT with 305 GHz f_T and 340 GHz f_{max}," *IEEE Electron Device Lett.*, vol. 15, no. 11, pp. 477–479, 1994.

[25] H. Nakajima, T. Ishibashi, E. Sano, M. Ida, S. Yamahata, and Y. Ishii, "InP-Based High-Speed Electronics," in *Intl. Electron Devices Meeting*, pp. 771–774, 1999.

[26] C. Gässler, V. Ziegler, C. Wölk, R. Deufel, F.-J. Berlec, N. Käb, and E. Kohn, "Metamorphic HFETs on GaAs with InP-Sub-Channels for Device Performance Improvements," in *Intl. Electron Devices Meeting*, (in print), 2000.

[27] J.-E. Müller, P. Baureis, O. Berger, T. Boettner, N. Bovolon, R. Schultheis, G. Packeiser, and P. Zwicknagl, "A Small Chip Size 2 W, 62% Efficient HBT MMIC for 3 V PCN Applications," *IEEE J. Solid-State Circuits*, vol. 33, no. 9, pp. 1277–1283, 1998.

[28] K. Yamamoto, S. Suzuki, K. Mori, T. Asada, T. Okuda, A. Inoue, T. Miura, K. Chomei, R. Hattori, M. Yamanouchi, and T. Shimura, "A 3.2-V Operation Single-Chip Dual-Band AlGaAs/GaAs HBT MMIC Power Amplifier with Active Feedback Circuit Technique," *IEEE J. Solid-State Circuits*, vol. 35, no. 8, pp. 1109–1120, 2000.

[29] W. Okamura, L. Yang, A. Gutierrez-Aitken, E. Kaneshiro, J. Lester, D. Sawdai, P. Grossman, K. Kobayashi, H. Yen, A. Oki, P. Chin, and T. Block, "K-Band 76% PAE InP Double Heterojunction Bipolar Power Transistors and a 23 GHz Compact Linear Power Amplifier MMIC," in *Tech. Dig. GaAs IC Symp.*, (Seattle, USA), pp. 219–222, 2000.

[30] C. Rheinfelder, H. Kuhnert, J. Luy, W. Heinrich, and A. Schuppen, "SiGe MMIC's Beyond 20 GHz on a Commercial Technology," in *Dig. MTT-S Intl. Microwave Symp.*, (Denver, USA), vol. 2, pp. 727–730, 1997.

[31] G. Raghavan, M. Sokolich, and W. Stanchina, "Indium Phosphide ICs Unleash the High-Frequency Spectrum," *IEEE Spectrum*, pp. 47–52, Oct. 2000.

[32] D. Pavlidis, "HBT vs. PHEMT vs. MESFET: What's Best and Why," *Compound Semiconductor*, vol. 5, no. 5, pp. 56–59, 1999.

[33] S. Selberherr, *Analysis and Simulation of Semiconductor Devices.* Wien, New York: Springer, 1984.

[34] W. Hänsch, *The Drift Diffusion Equation and its Application in MOSFET Modeling.* Wien, New York: Springer, 1991.

[35] C. Jacoboni and P. Lugli, *The Monte Carlo Method for Semiconductor Device Simulation.* Wien, New York: Springer, 1989.

[36] K. Hess, ed., *Monte Carlo Device Simulation: Full Band and Beyond.* Boston, Dordrecht, London: Kluwer, 1991.

[37] H. Kosina and S. Selberherr, "A Hybrid Device Simulator that Combines Monte Carlo and Drift-Diffusion Analysis," *IEEE Trans. Computer-Aided Design*, vol. 13, no. 2, pp. 201–210, 1994.

[38] W. Engl, A. Emunds, B. Meinerzhagen, H. Peifer, and T. Thoma, "Bridging the Gap between the Hydrodynamic and the Monte Carlo Model – An Attempt –," in *Proc. VLSI Process/Device Modeling Workshop*, (Osaka, Japan), pp. 32–33, 1989.

[39] S. Laux and M. Fischetti, "The DAMOCLES Monte Carlo Device Simulation Program," in *Computational Electronics* (K. Hess, J. Leburton, and U. Ravaioli, eds.), pp. 87–92, Kluwer, 1991.

[40] ISE Integrated Systems Engineering AG, Zürich, Switzerland, *DESSIS-ISE, ISE TCAD Release 6.0*, 1999.

[41] Technology Modeling Associates, Inc., Sunnyvale, CA, *TMA Medici, Two-Dimensional Device Simulation Program, Version 4.0 User's Manual*, 1997.

[42] S. Beebe, F. Rotella, Z. Sahul, D. Yergeau, G. McKenna, L. So, Z. Yu, K. Wu, E. Kan, J. McVittie, and R. Dutton, "Next Generation Stanford TCAD—PISCES 2ET and SUPREM 007," in *Intl. Electron Devices Meeting*, pp. 213–216, 1994.

[43] C. Fischer, P. Habaš, O. Heinreichsberger, H. Kosina, P. Lindorfer, P. Pichler, H. Pötzl, C. Sala, A. Schütz, S. Selberherr, M. Stiftinger, and M. Thurner, *MINIMOS 6 User's Guide*. Institut für Mikroelektronik, Technische Universität Wien, 1994.

[44] R. Anholt, *Electrical and Thermal Characterization of MESFETs, HEMTs, and HBTs*. Boston: Artech House, 1995.

[45] Avant! Corporation, Fremont, CA, *Medici, Two-Dimensional Device Simulation Program, Version 1999.2*, 1999.

[46] J.J. Liou, *Principles&Analysis of AlGaAs/GaAs Heterojunction Bipolar Transistors*, Boston: Artech House, 1996.

[47] E. Lyumkis, R. Mickevicius, O. Penzin, B. Polsky, and K. E. Sayed, "Numerical Analysis of Electron Tunneling through Hetero-Interfaces and Schottky Barriers in Heterostructure Devices," in *Tech. Dig. GaAs IC Symp.*, (Seattle, USA), pp. 129–132, 2000.

[48] C. Morton, J. Atherton, C. Snowden, R. Polard, and M. Howes, "A Large-Signal Physical HEMT Model," in *Dig. MTT-S Intl. Microwave Symp.*, (San Francisco, USA), pp. 1759–1763, 1996.

[49] C. Morton and C. Snowden, "Comparison of Quasi-2D and Ensemble Monte Carlo Simulations for Deep Submicron HEMTs," in *Dig. MTT-S Intl. Microwave Symp.*, (Boston, USA), pp. 153–156, 2000.

[50] Silvaco International, Santa Clara, CA, *ATLAS User's Manual, Ed. 6*, 1998.

[51] J. Geßner, F. Schwierz, H. Mau, D. Nuernbergk, M. Roßberg, and D. Schipanski, "Simulation of the Frequency Limits of SiGe HBTs," in *Proc. Intl. Conf. on Modeling and Simulation of Microsystems*, (San Juan, Puerto Rico, USA), pp. 407–410, 1999.

[52] G. Formicone, D. Vasileska, and D. Ferry, "2D Monte Carlo Simulation of Hole and Electron Transport in Strained Si," *VLSI Design*, vol. 6, no. 1-4, pp. 167–171, 1998.

[53] Y. Apanovich, R. Cottle, E. Lyumkis, B. Polsky, A. Shur, and P. Blakey, "2D Simulation of Heterojunction Devices Including Energy Balance and Lattice Heating," in *24th European Solid State Device Research Conference* (C. Hill and P. Ashburn, eds.), (Edinburgh, Scottland), pp. 463–466, Editions Frontiers, 1994.

[54] J. Kuo-JB, H. Chen, B. Chen, and T. Lu, "DC and Transient Analysis of a SiGe-Base Heterojunction Bipolar Device in an ECL Buffer Using a Modified PISCES Program," *Solid-State Electron.*, vol. 36, pp. 1273–1276, 1993.

[55] D. Richey, J. Cressler, and A. Joseph, "Scaling Issues and Ge Profile Optimization in Advanced UHV/CVD SiGe HBT's," *IEEE Trans.Electron Devices*, vol. 44, no. 3, pp. 431–440, 1997.

[56] T. Binder, K. Dragosits, T. Grasser, R. Klima, M. Knaipp, H. Kosina, R. Mlekus, V. Palankovski, M. Rottinger, G. Schrom, S. Selberherr, and M. Stockinger, *MINIMOS-NT User's Guide*. Institut für Mikroelektronik, Technische Universität Wien, 1998.

[57] S. Selberherr, A. Schütz, and H. Pötzl, "MINIMOS—A Two-Dimensional MOS Transistor Analyzer," *IEEE Trans.Electron Devices*, vol. ED-27, no. 8, pp. 1540–1550, 1980.

[58] M. Stockinger and S. Selberherr, "Closed-Loop CMOS Gate Delay Time Optimization," in *29th European Solid-State Device Research Conference* (H. Maes, R. Mertens, G. Declerck, and H. Grünbacher, eds.), (Leuven, Belgium), pp. 504–507, Editions Frontiers, 1999.

[59] T. Simlinger, H. Brech, T. Grave, and S. Selberherr, "Simulation of Submicron Double-Heterojunction High Electron Mobility Transistors with MINIMOS-NT," *IEEE Trans.Electron Devices*, vol. 44, no. 5, pp. 700–707, 1997.

[60] H. Brech, T. Grave, T. Simlinger, and S. Selberherr, "Optimization of Pseudomorphic HEMT's Supported by Numerical Simulations," *IEEE Trans.Electron Devices*, vol. 44, no. 11, pp. 1822–1828, 1997.

[61] R. Quay, R. Reuter, V. Palankovski, and S. Selberherr, "S-Parameter Simulation of RF-HEMTs," in *Proc. High Performance Electron Devices for Microwave and Optoelectronic Applications EDMO*, (Manchester, UK), pp. 13–18, 1998.

[62] T. Grasser, V. Palankovski, G. Schrom, and S. Selberherr, "Hydrodynamic Mixed-Mode Simulation," in *Simulation of Semiconductor Processes and Devices* (K. De Meyer and S. Biesemans, eds.), (Leuven, Belgium), pp. 247–250, Springer, 1998.

[63] V. Palankovski, S. Selberherr, and R. Schultheis, "Simulation of Heterojunction Bipolar Transistors on Gallium-Arsenide," in *Simulation of Semiconductor Processes and Devices*, (Kyoto, Japan), pp. 227–230, 1999.

[64] V. Palankovski, R. Quay, S. Selberherr, and R. Schultheis, "S-Parameter Simulation of HBTs on Gallium-Arsenide," in *Proc. High Performance Electron Devices for Microwave and Optoelectronic Applications EDMO*, (London, UK), pp. 15–19, 1999.

[65] V. Palankovski, G. Kaiblinger-Grujin, H. Kosina, and S. Selberherr, "A Dopant-Dependent Band Gap Narrowing Model Application for Bipolar Device Simulation," in *Simulation of Semiconductor Processes and Devices* (K. De Meyer and S. Biesemans, eds.), (Leuven, Belgium), pp. 105–108, Springer, 1998.

[66] V. Palankovski, G. Kaiblinger-Grujin, and S. Selberherr, "Implications of Dopant-Dependent Low-Field Mobility and Band Gap Narrowing on the Bipolar Device Performance," *J.Phys.IV*, vol. 8, pp. 91–94, EDP Sciences, 1998.

[67] B. Neinhüs, P. Graf, S. Decker, and B. Meinerzhagen, "Examination of Transient Drift-Diffusion and Hydrodynamic Modeling Accuracy for SiGe HBTs by 2D Monte-Carlo Device Simulation," in *27th European Solid-State Device Research Conference* (H. Grünbacher, ed.), (Stuttgart, Germany), pp. 188–191, Editions Frontiers, 1997.

[68] T. Kumar, M. Cahay, and K. Roenker, "Ensemble Monte Carlo Analysis of Self-Heating Effects in Graded Heterojunction Bipolar Transistors," *J.Appl.Phys.*, vol. 83, no. 4, pp. 1869–1877, 1998.

[69] V. Palankovski, B. Gonzales, H. Kosina, A. Hernandez, and S. Selberherr, "A New Analytical Energy Relaxation Time Model for Device Simulation," in *Proc. Intl. Conf. on Modeling and Simulation of Microsystems*, (San Juan, Puerto Rico, USA), pp. 395–398, 1999.

[70] D. Schroeder, *Modelling of Interface Carrier Transport for Device Simulation*. Springer, 1994.

[71] W. Liu, *Fundamentals of III-V Devices: HBTs, MESFETs, and HFETs/HEMTs*. New York: Wiley, 1999.

[72] T. Grasser, K. Tsuneno, H. Masuda, and S. Selberherr, "Mobility Parameter Tuning for Device Simulation," in *28th European Solid-State Device Research Conference* (A. Touboul, Y. Danto, J.-P. Klein, and H. Grünbacher, eds.), (Bordeaux, France), pp. 336–339, Editions Frontiers, 1998.

[73] S. Adachi, "Material Parameters of $In_{1-x}Ga_xAs_yP_{1-y}$ and Related Binaries," *J.Appl.Phys.*, vol. 53, no. 12, pp. 8775–8792, 1982.

[74] B. Bouhafs, H. Aourag, M. Ferhat, A. Zaoui, and M. Certier, "Theoretical Analysis of Disorder Effects on Electronic and Optical Properties in InGaAsP Quaternary Alloy," *J.Appl.Phys.*, vol. 82, no. 10, pp. 4923–4930, 1997.

[75] H. Brand, *Thermoelektrizität und Hydrodynamik*. Dissertation, Technische Universität Wien, 1994.

[76] C. Fischer, *Bauelementsimulation in einer computergestützten Entwurfsumgebung*. Dissertation, Technische Universität Wien, 1994.

[77] Z. Yu, B. Ricco, and R. Dutton, "A Comprehensive Analytical and Numerical Model of Polysilicon Emitter Contacts in Bipolar Transistors," *IEEE Trans.Electron Devices*, vol. 31, no. 6, pp. 773–784, 1984.

[78] T. Simlinger, *Simulation von Heterostruktur-Feldeffekttransistoren*. Dissertation, Technische Universität Wien, 1996.

[79] M. Grupen, K. Hess, and G. Song, "Simulation of Transport over Heterojunctions," in *Simulation of Semiconductor Devices and Processes* (W. Fichtner and D. Aemmer, eds.), (Konstanz, Switzerland), vol. 4, pp. 303–310, Hartung-Gorre, 1991.

[80] S. Mottet and J. Viallet, "Thermionic Emission in Heterojunctions," in *Simulation of Semiconductor Devices and Processes* (G. Baccarani and M. Rudan, eds.), (Bologna, Italy), vol. 3, pp. 97–108, Tecnoprint, 1988.

[81] C. Wu and E. Yang, "Carrier Transport Across Heterojunction Interfaces," *Solid-State Electron.*, vol. 22, pp. 241–248, 1979.

[82] K. Yang, J. East, and G. Haddad, "Numerical Modeling of Abrupt Heterojunctions Using a Thermionic-Field Emission Boundary Condition," *Solid-State Electron.*, vol. 36, no. 3, pp. 321–330, 1993.

[83] T. Simlinger, M. Rottinger, and S. Selberherr, "A Method for Unified Treatment of Interface Conditions Suitable for Device Simulation," in *Simulation of Semiconductor Processes and Devices*, (Cambridge, USA), pp. 173–176, 1997.

[84] M. Fischetti, "Monte Carlo Simulation of Transport in Technologically Significant Semiconductors of the Diamond and Zinc-Blende Structures–Part I: Homogeneous Transport," *IEEE Trans.Electron Devices*, vol. 38, no. 3, pp. 634–649, 1991.

[85] K. Ng, *Complete Guide to Semiconductor Devices*. McGraw-Hill, 1995.

[86] S. Sze, *Physics of Semiconductor Devices*. New York: Wiley, second ed., 1981.

[87] T. González Sánchez, J. Velázques Pérez, P. Gutiérrez Conde, and D. Pardo Collantes, "Five-Valley Model for the Study of Electron Transport Properties at Very High Electric Fields in GaAs," *Semicond.Sci.Technol.*, vol. 6, pp. 862–871, 1991.

[88] K. Brennan and K. Hess, "High Field Transport in GaAs, InP and InAs," *Solid-State Electron.*, vol. 27, no. 4, pp. 347–357, 1984.

[89] J. Blakemore, *Gallium Arsenide*. American Institute of Physics, 1987.

[90] J. Singh, *Physics of Semiconductors and their Heterostructures*. McGraw Hill, 1993.

[91] M. Landolt and J. Börnstein, *Zahlenwerte und Funktionen aus Naturwissenschaften und Technik*, vol. 17/A of *Neue Serie, Gruppe III*. Berlin: Springer, 1982.

[92] S. Tiwari, *Compound Semiconductor Device Physics*. Academic Press, 1992.

[93] E. Schubert, *Doping in III-V Semiconductors*. Cambridge University Press, 1993.

[94] M. Fischetti and S. Laux, "Monte Carlo Simulation of Transport in Technologically Significant Semiconductors of the Diamond and Zinc-Blende Structures–Part II: Submicrometer MOSFET's," *IEEE Trans.Electron Devices*, vol. 38, no. 3, pp. 650–660, 1991.

[95] D. Bose and B. Nag, "Electron Velocity in Indium Phosphide Single-Heterojunction Quantum Wells," *Semicond.Sci.Technol.*, vol. 6, pp. 1135–1140, 1991.

[96] T. González Sánchez, J. Velázques Pérez, P. Gutiérrez Conde, and D. Pardo Collantes, "Electron Transport in InP Under High Electric Field Conditions," *Semicond.Sci.Technol.*, vol. 7, pp. 31–36, 1992.

[97] M. Gospodinova-Daltcheva, R. Arnaudov, and P. Philippov, "Energy Propagation Properties of Al-Lossy Lines in High-Speed Circuits on Silicon Substrate," in *Proc. High Performance Electron Devices for Microwave and Optoelectronic Applications EDMO*, (London, UK), pp. 295–300, 1999.

[98] Ferro-Ceramic Grinding Inc., "Ceramic Materials Physical, Mechanical, Thermal and Electrical Properties Reference Chart," *http://ferroceramic.com/tables/*, 2000.

[99] B. Cheng, M. Cao, R. Rao, A. Inani, P. Voorde, W. Greene, J. Stork, Z. Yu, P. Zeitzoff, and J. Woo, "The Impact of High-k Gate Dielectrics and Metal Gate Electrodes on Sub-100 nm MOSFET's," *IEEE Trans.Electron Devices*, vol. 46, no. 7, pp. 1537–1544, 1999.

[100] S. Krishnan, G. Yeap, B. Yu, Q. Xiang, and M. Lin, "High-k Scaling of Gate Insulators: an Insightful Study," in *Proc. Conf. on Microelectronic Device Technology*, vol. 3506, (Santa Clara, USA), pp. 65–72, SPIE, 1998.

[101] G. Bai, "High k Gate Stack for Sub-0.1 um CMOS Technology," in *Advances in Rapid Thermal Processing*, (Pennington, USA), pp. 39–44, Electrochem. Soc., 1999.

[102] M. Littlejohn, K. Kim, and H. Tian, "High-Field Transport in InGaAs and Related Heterostructures," in Bhattacharya [111], section 4.2, pp. 107–116.

[103] C. Besikci and M. Razeghi, "Electron Transport Properties of $Ga_{0.51}In_{0.49}P$ for Device Applications," *IEEE Trans.Electron Devices*, vol. 41, no. 6, pp. 1066–1069, 1994.

[104] S. Adachi, "GaAs, AlAs, and $Al_xGa_{1-x}As$: Material Parameters for Use in Research and Device Applications," *J.Appl.Phys.*, vol. 58, pp. R1–R29, 1985.

[105] J. King, ed., *Material Handbook for Hybrid Microelectronics*. Artech House, 1988.

[106] P. Maycock, "Thermal Conductivity of Silicon, Germanium, III-V Compounds and III-V Alloys," *Solid-State Electron.*, vol. 10, pp. 161–168, 1967.

[107] M. Landolt and J. Börnstein, *Numerical Data and Functional Relationships in Science and Techology*, vol. 22/A of *New Series, Group III*. Berlin: Springer, 1987.

[108] A. Katz, *Indium Phosphide and Related Materials*. Boston: Artech House, 1992.

[109] S. Adachi, *Physical Properties of III-V Semiconductor Compounds*. Wiley, 1992.

[110] S. Adachi, ed., *Properties of Aluminium Gallium Arsenide*. No. 7 in EMIS Datareviews Series, IEE INSPEC, 1993.

[111] P. Bhattacharya, ed., *Properties of Lattice-Matched and Strained Indium Gallium Arsenide*. No. 8 in EMIS Datareviews Series, IEE INSPEC, 1993.

[112] Y. Varshni, "Temperature Dependence of the Energy Gap in Semiconductors," *Physica*, vol. 34, pp. 149–154, 1967.

[113] V. Wilkinson and A. Adams, "The Effect of Temperature and Pressure on InGaAs Band Structure," in Bhattacharya [111], section 3.2, pp. 70–75.

[114] P. Wang, S. Holmes, T. Le, R. Stradling, I. Ferguson, and A. de Oliveira, "Electrical and Magneto-Optical Studies of MBE InAs on GaAs," *Semicond.Sci.Technol.*, vol. 7, pp. 767–786, 1992.

[115] B. Nag, *Electron Transport in Compound Semiconductors*, vol. 11 of *Springer Series in Solid-State Sciences*. Springer, 1980.

[116] M. Krijn, "Heterojunction Band Offsets and Effective Masses in III-V Quaternary Alloys," *Semicond.Sci.Technol.*, vol. 6, pp. 27–31, 1991.

[117] B. Jalali and S. Pearton, eds., *InP HBTs: Growth,Processing,and Applications*. Boston: Artech House, 1995.

[118] F. Gaensslen, R. Jaeger, and J. Walker, "Low-Temperature Threshold Behavior of Depletion Mode Devices - Characterization and Simulation," in *Intl.Electron Devices Meeting*, pp. 520–524, 1976.

[119] F. Gaensslen and R. Jaeger, "Temperature Dependent Threshold Behavior of Depletion Mode MOSFET's," *Solid-State Electron.*, vol. 22, pp. 423–430, 1979.

[120] M. Green, "Intrinsic Concentration, Effective Densities of States, and Effective Mass in Silicon," *J.Appl.Phys.*, vol. 67, no. 6, pp. 2944–2954, 1990.

[121] K. Shim and H. Rabitz, "Electronic and Structural Properties of the Pentanary Alloy $Ga_xIn_{1-x}P_ySb_zAs_{1-y-z}$," *J.Appl.Phys.*, vol. 85, no. 11, pp. 7705–7715, 1999.

[122] K. Kim, M. Lee, J. Bahng, K. Shim, and B. Choe, "Optical Constants and Electronic Interband Transitions of Disordered $GaAs_{1-x}P_x$ Alloys," *J.Appl.Phys.*, vol. 84, no. 7, pp. 3696–3699, 1998.

[123] M. Shur, *GaAs Devices and Circuits*. Plenum Press, 1987.

[124] V. Palankovski, M. Knaipp, and S. Selberherr, "Influence of the Material Composition and Doping Profiles on HBTs Device Performance," in *Proc. Intl. Conf. on Modelling and Simulation*, (Pittsburgh, USA), pp. 7–10, 1998.

[125] H. Casey and M. Panish, *Heterostructure Lasers, Part B: Materials and Operating Characteristics*. Academic Press, 1978.

[126] M. Bugajski, A. Kontkiewicz, and H. Mariette, "Energy Bands of Ternary Alloy Semiconductors: Coherent-Potential-Approximation Calculations," *Physical Review B*, vol. 28, no. 12, pp. 7105–7114, 1983.

[127] S. Jain, *Germanium-Silicon Strained Layers and Heterostructures*, vol. 24 of *Advances in Electronics and Electron Physics*. Academic Press, 1994.

[128] C. Köpf, H. Kosina, and S. Selberherr, "Physical Models for Strained and Relaxed GaInAs Alloys: Band Structure and Low-Field Transport," *Solid-State Electron.*, vol. 41, no. 8, pp. 1139–1152, 1997.

[129] F. Capasso and G. Margaritondo, eds., *Heterojunction Band Discontinuities*. Elsevier, 1987.

[130] C. Van de Walle, "Band Lineups and Deformation Potentials in the Model-Solid Theory," *Physical Review B*, vol. 39, no. 3, pp. 1871–1883, 1989.

[131] C. Van de Walle and R. Martin, "Theoretical Study of Band Offsets at Semiconductor Interfaces," *Physical Review B*, vol. 35, no. 15, pp. 8154–8165, 1987.

[132] A. Lindell, M. Pessa, A. Salokatve, F. Bernardini, R. Nieminen, and M. Paalanen, "Band Offsets at the GaInP/GaAs Heterojunction," *J.Appl.Phys.*, vol. 82, no. 7, pp. 3374–3380, 1997.

[133] J. Slotboom and H. de Graaff, "Measurements of Bandgap Narrowing in Si Bipolar Transistors," *Solid-State Electron.*, vol. 19, pp. 857–862, 1976.

[134] V. Palankovski, G. Kaiblinger-Grujin, and S. Selberherr, "Study of Dopant-Dependent Band Gap Narrowing in Compound Semiconductor Devices," *Materials Science & Engineering*, vol. B66, pp. 46–49, 1999.

[135] D. Klaassen, J. Slotboom, and H. de Graaff, "Unified Apparent Bandgap Narrowing in n- and p-Type Silicon," *Solid-State Electron.*, vol. 35, no. 2, pp. 125–129, 1992.

[136] J. DelAlamo, E. Swirhun, and R. Swanson, "Simultaneous Measuring of Hole Lifetime, Hole Mobility and Bandgap Narrowing in Heavily Doped n-type Silicon," in *Intl.Electron Devices Meeting*, pp. 290–293, 1985.

[137] H. Bennet and C.L.Wilson, "Statistical Comparisons of Data on Band-Gap Narrowing in Heavily Doped Silicon: Electrical and Optical Measurements," *J.Appl.Phys.*, vol. 55, no. 10, pp. 3582–3587, 1984.

[138] Y. Mamontov and M. Willander, "Simulation of Bandgap Narrowing and Incomplete Ionization in Strained $Si_{1-x}Ge_x$ Alloys on (001) Si Substrate (for Temperatures from 40K up to 400K)," *Solid-State Electron.*, vol. 38, no. 3, pp. 599–607, 1995.

[139] D. Ferry, *Semiconductors*. New York: Macmillan, 1991.

[140] G. Kaiblinger-Grujin, H. Kosina, and S. Selberherr, "Influence of the Doping Element on the Electron Mobility in n-Silicon," *J.Appl.Phys.*, vol. 83, no. 6, pp. 3096–3101, 1998.

[141] J.-S. Park, A. Neugroschel, and F. Lindholm, "Comments on Determination of Bandgap Narrowing from Activation Plots," *IEEE Trans.Electron Devices*, vol. 33, no. 7, pp. 1077–1078, 1986.

[142] Z.H.Lu, M.C.Hanna, and A.Majerfeld, "Determination of Band Gap Narrowing and Hole Density for Heavily C-doped GaAs by Photoluminescence Spectroscopy," *Appl.Phys.Lett.*, vol. 64, no. 1, pp. 88–90, 1994.

[143] B.P.Yan, J.S.Luo, and Q.L.Zhang, "Study of Band-Gap Narrowing Effect and Nonradiative Recombination Centers for Heavily C-doped GaAs by Photoluminescence Spectroscopy," *J.Appl.Phys.*, vol. 77, no. 9, pp. 4822–4824, 1995.

[144] S. Jain and D. Roulston, "A Simple Expression for Band Gap Narrowing (BGN) in Heavily Doped Si, Ge, GaAs and Ge_xSi_{1-x} Strained Layers," *Solid-State Electron.*, vol. 34, no. 5, pp. 453–465, 1991.

[145] Z. Matutinovic-Krstelj, V. Venkataraman, E. Prinz, J. Sturm, and C.W.Magee, "A Comprehensive Study of Lateral and Vertical Current Transport in $Si/Si_{1-x}Ge_x/Si$ HBT's," in *Intl.Electron Devices Meeting*, pp. 87–90, 1993.

[146] M.Libezny, S.C.Jain, J.Poortmans, M.Caymax, J.Nijs, R.Mertens, K.Werner, and P.Balk, "Photoluminescence Determination of the Fermi Energy in Heavily Doped Strained $Si_{1-x}Ge_x$ Layers," *Appl.Phys.Lett.*, vol. 64, no. 15, pp. 1953–1955, 1994.

[147] E.S.Harmon, M.R.Melloch, and M.S.Lundstrom, "Effective Band-Gap Shrinkage in GaAs," *Appl.Phys.Lett.*, vol. 64, no. 4, pp. 502–504, 1994.

[148] H.Yao and A.Compaan, "Plasmons, Photoluminescence, and Band-Gap Narrowing in Very Heavily Doped n-GaAs," *Appl.Phys.Lett.*, vol. 57, no. 2, pp. 147–149, 1990.

[149] R.M.Sieg and S.A.Ringel, "Reabsorption, Band Gap Narrowing, and the Reconciliation of Photoluminescence Spectra with Electrical Measurements for Epitaxial n-InP," *J.Appl.Phys.*, vol. 80, no. 1, pp. 448–458, 1996.

[150] C.-H. Wang and A. Neugroschel, "Minority-Carrier Transport Parameters in Degenerate n-Type Silicon," *IEEE Electron Device Lett.*, vol. 11, no. 12, pp. 576–578, 1990.

[151] C. Köpf, *Modellierung des Elektronentransports in Verbindungshalbleiterlegierungen.* Dissertation, Technische Universität Wien, 1997.

[152] M. Ilegems, "InP-Based Lattice-Matched Heterostructures," in Bhattacharya [111], section 1.3, pp. 16–25.

[153] R. Dittrich and W. Schroeder, "Empirical Pseudopotential Band Structure of $In_{0.53}Ga_{0.47}As$ and $In_{0.52}Al_{0.48}As$," *Solid-State Electron.*, vol. 43, pp. 403–407, 1999.

[154] K. Brennan and P. Chiang, "Calculated Electron and Hole Steady-State Drift Velocities in Lattice Matched GaInP and AlGaInP," *J.Appl.Phys.*, vol. 71, no. 2, pp. 1055–1057, 1992.

[155] B. Nag and M. Das, "Electron Mobility in $In_{0.5}Ga_{0.5}P$," *J.Appl.Phys.*, vol. 83, no. 11, pp. 5862–5864, 1998.

[156] I. Yoon, T. Ji, S. Oh, J. Choi, and H. Park, "Concentration Dependent Photoluminescence of Te-doped $In_{0.5}Ga_{0.5}P$ Layers Grown by Liquid Phase Epitaxy," *J.Appl.Phys.*, vol. 82, no. 8, pp. 4024–4027, 1997.

[157] J. Sutherland and J. Hauser, "A Computer Analysis of Heterojunction and Graded Composition Solar Cells," *IEEE Trans.Electron Devices*, vol. ED-24, no. 4, pp. 363–372, 1977.

[158] B. Pejčinović, L. Kay, T.-W. Tang, and D. Navon, "Numerical Simulation and Comparison of Si BJTs and $Si_{1-x}Ge_x$ HBTs," *IEEE Trans.Electron Devices*, vol. 36, no. 10, pp. 2129–2137, 1989.

[159] S. Selberherr, "MOS Device Modeling at 77K," *IEEE Trans.Electron Devices*, vol. 36, no. 8, pp. 1464–1474, 1989.

[160] S. Selberherr, W. Hänsch, M. Seavey, and J. Slotboom, "The Evolution of the MINI-MOS Mobility Model," *Solid-State Electron.*, vol. 33, no. 11, pp. 1425–1436, 1990.

[161] M. Fischetti and S. Laux, "Band Structure, Deformation Potentials, and Carrier Mobility in Strained Si, Ge, and SiGe Alloys," *J.Appl.Phys.*, vol. 80, no. 4, pp. 2234–2252, 1996.

[162] M. Sotoodeh, A. Khalid, and A. Rezazadeh, "Empirical Low-Field Mobility Model for III-V Compounds Applicable in Device Simulation Codes," *J.Appl.Phys.*, vol. 87, no. 6, pp. 2890–2900, 2000.

[163] D. Caughey and R. Thomas, "Carrier Mobilities in Silicon Empirically Related to Doping and Field," *Proc.IEEE*, vol. 52, pp. 2192–2193, 1967.

[164] J. Lowney and H. Bennett, "Majority and Minority Electron and Hole Mobilities in Heavily Doped GaAs," *J.Appl.Phys.*, vol. 69, no. 10, pp. 7102–7110, 1991.

[165] E. Harmon, M. Lovejoy, M. Melloch, M. Lundstrom, T. de Lyon, , and J. Woodall, "Experimental Observation of a Minority Electron Mobility Enhancement in Degenerately Doped p-Type GaAs," *Appl.Phys.Lett.*, vol. 63, no. 4, pp. 5597–5602, 1993.

[166] H. Ito and T. Ishibashi, "Minority-Electron Mobility in p-Type GaAs," *J.Appl.Phys.*, vol. 65, no. 12, pp. 5197–5199, 1989.

[167] G. Kaiblinger-Grujin, H. Kosina, and S. Selberherr, "Monte Carlo Simulation of Electron Transport in Doped Silicon," in *High Performance Computing on the Information Superhighway – HPC Asia '97*, (Seoul, Korea), pp. 444–449, IEEE Computer Society Press, 1997.

[168] G. Kaiblinger-Grujin, T. Grasser, and S. Selberherr, "A Physically-Based Electron Mobility Model for Silicon Device Simulation," in *Simulation of Semiconductor Processes and Devices* (K. De Meyer and S. Biesemans, eds.), (Leuven, Belgium), pp. 312–315, Springer, 1998.

[169] V. Palankovski, R. Strasser, H. Kosina, and S. Selberherr, "A Systematic Approach for Model Extraction for Device Simulation Application," in *Proc. Intl. Conf. Applied Modelling and Simulation*, (Cairns, Australia), pp. 463–466, 1999.

[170] T. Grasser, R. Strasser, M. Knaipp, K. Tsuneno, H. Masuda, and S. Selberherr, "Device Simulator Calibration for Quartermicron CMOS Devices," in *Simulation of Semiconductor Processes and Devices* (K. De Meyer and S. Biesemans, eds.), (Leuven, Belgium), pp. 93–96, Springer, 1998.

[171] C. Köpf, G. Kaiblinger-Grujin, H. Kosina, and S. Selberherr, "Influence of Dopant Species on Electron Mobility in InP," in *Proc. Intl. Conf. on Indium Phosphide and Related Materials*, (Hyannis, USA), pp. 280–283, 1997.

[172] C. Köpf, G. Kaiblinger-Grujin, H. Kosina, and S. Selberherr, "Reexamination of Electron Mobility Dependence on Dopants in GaAs," in *27th European Solid-State Device Research Conference* (H. Grünbacher, ed.), (Stuttgart, Germany), pp. 304–307, Editions Frontiers, 1997.

[173] G. Masetti, M. Severi, and S. Solmi, "Modeling of Carrier Mobility Against Carrier Concentration in Arsenic-, Phosphorus- and Boron-Doped Silicon," *IEEE Trans.Electron Devices*, vol. ED-30, no. 7, pp. 764–769, 1983.

[174] J. Slotboom, G. Streutker, M. v. Dort, P. Woerlee, A. Pruijmboom, and D. Gravesteijn, "Non-Local Impact Ionization in Silicon Devices," in *Intl.Electron Devices Meeting*, pp. 127–130, 1991.

[175] M. van Dort, J. Slotboom, G. Streutker, and P. Woerlee, "Lifetime Calculations of MOSFET's Using Depth-Dependent Non-Local Impact Ionization," in *Simulation of Semiconductor Devices and Processes* (S. Selberherr, H. Stippel, and E. Strasser, eds.), (Vienna, Austria), vol. 5, pp. 469–472, Springer, 1993.

[176] C. Lombardi, S. Manzini, A. Saporito, and M. Vanzi, "A Physically Based Mobility Model for Numerical Simulation of Nonplanar Devices," *IEEE Trans.Computer-Aided Design*, vol. 7, no. 11, pp. 1164–1171, 1988.

[177] J. Xu and M. Shur, "Velocity-Field Dependence in GaAs," *IEEE Trans.Electron Devices*, vol. ED-34, no. 8, pp. 1831–1832, 1987.

[178] M. Hirose, J. Yoshida, and N. Toyoda, "An Improved Two-Dimensional Simulation Model (MEGA) for GaAs MESFET Applicable to LSI Design," *IEEE Trans.Computer-Aided Design*, vol. 7, no. 2, pp. 225–230, 1988.

[179] K. Kramer and W. Hitchon, *Semiconductor Devices – A Simulation Approach.* Prentice Hall, 1997.

[180] W. Hänsch, M. Orlowski, and W. Weber, "The Hot-Electron Problem in Submicron MOSFET," in *18th European Solid State Device Research Conference* (J.-P. Nougier and D. Gasquet, eds.), (Montpellier, France), *J.Phys.*, vol. 49, pp. 597–606, les éditions de physique, 1988.

[181] R. Deutschmann, *Entwicklung eines physikalischen HFET-Modells: Parameterextraktion und Verifikation.* Dissertation, Technische Universität Wien, 1995.

[182] R. Quay, C. Moglestue, V. Palankovski, and S. Selberherr, "A Temperature Dependent Model for the Saturation Velocity in Semiconductor Materials," *Materials Science in Semiconductor Processing*, vol. 3, no. 1-2, pp. 149–155, 2000.

[183] H. Brech, *Optimization of GaAs Based High Electron Mobility Transistors by Numerical Simulation*. Dissertation, Technische Universität Wien, 1998.

[184] V. Agostinelli, T. Bordelon, X. Wang, C. Yeap, C. Maziar, and A. Tasch, "An Energy-Dependent Two-Dimensional Substrate Current Model for the Simulation of Submicrometer MOSFETs," *IEEE Electron Device Lett.*, vol. 13, no. 11, pp. 554–556, 1992.

[185] B. Gonzales, V. Palankovski, H. Kosina, A. Hernandez, and S. Selberherr, "An Energy Relaxation Time Model for Device Simulation," *Solid-State Electron.*, vol. 43, pp. 1791–1795, 1999.

[186] C. Jacoboni, F. Nava, C. Canali, and G. Ottaviani, "Electron Drift Velocity and Diffusivity in Germanium," *Physical Review B*, vol. 24, no. 2, pp. 1014–1026, 1981.

[187] A. Schenk, "A Model for the Field and Temperature Dependence of Shockley-Read-Hall Lifetimes in Silicon," *Solid-State Electron.*, vol. 35, no. 11, pp. 1585–1596, 1992.

[188] S. Sze, ed., *Semiconductor Sensors*. Wiley, 1994.

[189] G. Hurkx, D. Klaassen, and M. Knuvers, "A New Recombination Model for Device Simulation Including Tunneling," *IEEE Trans. Electron Devices*, vol. 39, no. 2, pp. 331–338, 1992.

[190] S. Sze and G. Gibbons, "Avalanche Breakdown Voltages of Abrupt and Linearly Graded p-n Junctions in Ge, Si, GaAs, and GaP," *Appl. Phys. Lett.*, vol. 8, pp. 111–113, 1966.

[191] W. Quade, M. Rudan, and E. Schöll, "Hydrodynamic Simulation of Impact-Ionization Effects in P-N Junctions," *IEEE Trans. Computer-Aided Design*, vol. 10, no. 10, pp. 1287–1294, 1991.

[192] W. Quade, E. Schöll, and M. Rudan, "Impact Ionization within the Hydrodynamic Approach to Semiconductor Transport," *Solid-State Electron.*, vol. 36, no. 10, pp. 1493–1505, 1993.

[193] R. Quay, H. Massler, W. Kellner, V. Palankovski, and S. Selberherr, "Simulation of Gallium-Arsenide Based High Electron Mobility Transistors," in *Simulation of Semiconductor Processes and Devices*, (Seattle, USA), pp. 74–77, 2000.

[194] R. Quay, V. Palankovski, M. Chertouk, A. Leuther, and S. Selberherr, "Simulation of InAlAs/InGaAs High Electron Mobility Transistors with a Single Set of Physical Parameters," in *Intl. Electron Devices Meeting*, (in print), 2000.

[195] V. Palankovski, M. Rottinger, T. Simlinger, and S. Selberherr, "Two-Dimensional Simulation and Comparison of Si-based and GaAs-based HBTs," in *Viewgraphs III-V Semiconductor Device Simulation Workshop*, (Turin, Italy), 1997.

[196] C. Pichler, R. Plasun, R. Strasser, and S. Selberherr, "High-Level TCAD Task Representation and Automation," *IEEE J.Technology Computer Aided Design*, May 1997. `http://www.ieee.org/journal/tcad/accepted/pichler-may97/`.

[197] E. Prinz, P. Garone, P. Schwartz, X. Xiao, and J. Sturm, "The Effect of Base-Emitter Spacers and Strain-Dependent Densities of States in $Si/Si_{1-x}Ge_x/Si$ Heterojunction Bipolar Transistors," in *Intl.Electron Devices Meeting*, pp. 639–642, 1989.

[198] R. Schultheis, N. Bovolon, J.-E. Müller, and P. Zwicknagl, "Electrothermal Modelling of Heterojunction Bipolar Transistors (HBTs)," in *Viewgraphs III-V Semiconductor Device Simulation Workshop*, (Lille, France), 1999.

[199] N. Bovolon, P. Baureis, J.-E. Müller, P. Zwicknagl, R. Schultheis, and E. Zanoni, "A Simple Method for the Thermal Resistance Measurement of AlGaAs/GaAs Heterojunction Bipolar Transistors," *IEEE Trans.Electron Devices*, vol. 45, no. 8, pp. 1846–1848, 1998.

[200] S. Laux, "Techniques for Small-Signal Analysis of Semiconductor Devices," *IEEE Trans.Electron Devices*, vol. ED-32, no. 10, pp. 2028–2037, 1986.

[201] D. Peters, W. Daumann, W. Brockerhoff, R. Reuter, E. Koenig, and F. Tegude, "Direct Calculation of the HBT Small-Signal Equivalent Circuit with Special Emphasis to the Feedback Capacitance," in *Proc. European Microwave Conference*, (Bologna, Italy), pp. 1032–1036, 1995.

[202] R. Schultheis, N. Bovolon, J.-E. Müller, and P. Zwicknagl, "Modelling of Heterojunction Bipolar Transistors (HBTs) Based on Gallium Arsenide (GaAs)," *Intl.J. of RF and Microwave Computer-Aided Engineering*, vol. 10, no. 1, pp. 33–42, 2000.

[203] T. Low, C. Hutchison, P. Canfield, T. Shirley, R. Yeats, J. Chang, G. Essilfie, W. Whiteley, D. D'Avanzo, N. Pan, J. Elliot, and C. Lutz, "Migration from an AlGaAs to an InGaP emitter HBT IC process for improved reliability," in *Tech.Dig. GaAs IC Symp.*, (Atlanta, USA), pp. 153–157, 1998.

[204] P. Ma, P. Zampardi, L. Zhang, and M. Chang, "Determining the Effectiveness of HBT Emitter Ledge Passivation by Using an On-Ledge Schottky Diode Potentiometer," *IEEE Electron Device Lett.*, vol. 20, no. 9, pp. 460–462, 1999.

[205] N. Bovolon, R. Schultheis, J.-E. Müller, P. Zwicknagl, and E. Zanoni, "A Short-Term High-Current-Density Reliability Investigation of AlGaAs/GaAs Heterojunction Bipolar Transistors," *Electron.Lett.*, vol. 19, no. 12, pp. 469–471, 1998.

[206] M. Borgarino, R. Plana, S. Delage, F. Fantini, and J. Graffeuil, "Influence of Surface Recombination on the Burn-In Effect in Microwave GaInP/GaAs HBT's," *IEEE Trans.Electron Devices*, vol. 46, no. 1, pp. 10–16, 1999.

[207] K. Christianson, "Reliability of III–V Based Heterojunction Bipolar Transistors," *Microelectron.Reliab.*, vol. 38, no. 1, pp. 153–161, 1997.

[208] K. Mochizuki, T. Oka, K. Ouchi, and T. Tanoue, "Reliability Investigation of Heavily C-doped InGaP/GaAs HBTs Operated under a Very High Current-Density Condition," *Solid-State Electron.*, vol. 43, pp. 1425–1428, 1999.

[209] Technology Modeling Associates, Inc., Sunnyvale, California, *TMA TSUPREM-4, Two-Dimensional Process Simulation Program, Version 6.5 User's Manual*, 1997.

[210] ISE Integrated Systems Engineering AG, Zürich, Switzerland, *DIOS-ISE, ISE TCAD Release 6.0*, 1999.

[211] T. Grasser, R. Quay, V. Palankovski, and S. Selberherr, "A Global Self-Heating Model for Device Simulation," in *30th European Solid-State Device Research Conference* (W.A. Lane, G.M. Crean, F.A. McCabe, and H. Grünbacher, eds.), (Cork, Ireland), pp. 324–327, Frontier Group, 2000.

List of Publications

[P1] V. Palankovski, M. Rottinger, T. Simlinger, and S. Selberherr, "Two-Dimensional Simulation and Comparison of Si-based and GaAs-based HBTs," in *Viewgraphs III-V Semiconductor Device Simulation Workshop*, (Turin, Italy), Oct. 1997.

[P2] V. Palankovski, M. Knaipp, and S. Selberherr, "Influence of the Material Composition and Doping Profiles on HBTs Device Performance," in *Proc. IASTED Intl. Conf. on Modelling and Simulation*, (Pittsburgh, Pennsylvania, USA), pp. 7–10, May 1998.

[P3] V. Palankovski, T. Grasser, and S. Selberherr, "SiGe HBT in Mixed-Mode Device and Circuit Simulation," in *Proc. Workshop on Compound Semiconductor Devices and Integrated Circuits*, (Zeuthen, Germany), pp. 145–146, May 1998.

[P4] V. Palankovski, G. Kaiblinger-Grujin, and S. Selberherr, "Study of Dopant-Dependent Band Gap Narrowing in Compound Semiconductor Devices," in *Abstracts Intl. Workshop on Expert Evaluation & Control of Compound Semiconductor Materials & Technologies*, (Cardiff, Wales, UK), PSA p. 15, June 1998.

[P5] V. Palankovski, G. Kaiblinger-Grujin, and S. Selberherr, "Implications of Dopant-Dependent Low-Field Mobility and Band Gap Narrowing on the Bipolar Device Performance," in *Proc. European Workshop on Low Temperature Electronics*, (San Miniato, Italy), June 1998; in L. Brogiato, D.V. Camin, and G. Pessina, editors, *J.Phys.IV*, vol. 8, pp. 91–94, EDP Sciences, 1998.

[P6] V. Palankovski, G. Kaiblinger-Grujin, H. Kosina, and S. Selberherr, "A Dopant-Dependent Band Gap Narrowing Model Application for Bipolar Device Simulation," in K. De Meyer and S. Biesemans, editors, *Simulation of Semiconductor Processes and Devices*, pp. 105–108, Springer, 1998. (Leuven, Belgium), Sept. 1998.

[P7] T. Grasser, V. Palankovski, G. Schrom, and S. Selberherr, "Hydrodynamic Mixed-Mode Simulation," in K. De Meyer and S. Biesemans, editors, *Simulation of Semiconductor Processes and Devices*, pp. 247–250, Springer, 1998. (Leuven, Belgium), Sept. 1998.

[P8] R. Quay, R. Reuter, V. Palankovski, and S. Selberherr, "S-Parameter Simulation of RF-HEMTs," in *Proc. High Performance Electron Devices for Microwave and Optoelectronic Applications EDMO*, pp. 13–18, (Manchester, UK), Nov. 1998.

[P9] V. Palankovski, B. Gonzales, H. Kosina, A. Hernandez, and S. Selberherr, "A New Analytical Energy Relaxation Time Model for Device Simulation," in *Proc. Intl. Conf. on Modeling and Simulation of Microsystems, Semiconductors, Sensors, and Actuators,* (San Juan, Puerto Rico, USA), pp. 395–398, April 1999.

[P10] B. Gonzales, V. Palankovski, H. Kosina, A. Hernandez, and S. Selberherr, "An Energy Relaxation Time Model for Device Simulation," in *Proc. IASTED Intl. Conf. on Modelling and Simulation,* (Philadelphia, Pennsylvania, USA), pp. 367–370, May 1999.

[P11] R. Quay, C. Moglestue, V. Palankovski, and S. Selberherr, "A Temperature Dependent Model for the Saturation Velocity in Semiconductor Materials," in *Abstracts E-MRS Spring Meeting,* (Strasbourg, France), p. L-7, June 1999.

[P12] B. Gonzales, V. Palankovski, H. Kosina, A. Hernandez, and S. Selberherr, "An Analytical Model for the Electron Energy Relaxation Time," in *Proc. Electron Devices Conference CDE,* (Madrid, Spain), pp. 263–266, June 1999.

[P13] V. Palankovski and S. Selberherr, "Thermal Models for Semiconductor Device Simulation," in *IEEE Proc. European Conference on High Temperature Electronics,* (Berlin, Germany), pp. 25–28, July 1999.

[P14] R. Quay, V. Palankovski, R. Reuter, M. Schlechtweg, W. Kellner, and S. Selberherr, "III/V Device Optimization by Physics-Based S-Parameter Simulation," in *Proc. Intl. Symp. on Compound Semiconductors,* (Berlin, Germany), pp. 325–328, Aug. 1999.

[P15] V. Palankovski, R. Strasser, H. Kosina, and S. Selberherr, "A Systematic Approach for Model Extraction for Device Simulation Application," in *Proc. IASTED Intl. Conf. on Applied Modelling and Simulation,* (Cairns, Australia), pp. 463–466, Sept. 1999.

[P16] V. Palankovski, S. Selberherr, and R. Schultheis, "Simulation of Heterojunction Bipolar Transistors on Gallium-Arsenide," in *Proc. Intl. Conf. on Simulation of Semiconductor Processes and Devices,* (Kyoto, Japan), pp. 227–230, Sept. 1999.

[P17] V. Palankovski, R. Quay, S. Selberherr, and R. Schultheis, "S-Parameter Simulation of HBTs on Gallium-Arsenide," in *Proc. High Performance Electron Devices for Microwave and Optoelectronic Applications EDMO,* (London, UK), pp. 15–19, Nov. 1999.

[P18] B. Gonzales, V. Palankovski, H. Kosina, A. Hernandez, and S. Selberherr, "An Energy Relaxation Time Model for Device Simulation," *Solid-State Electronics,* vol. 43, pp. 1791–1795, Nov. 1999.

[P19] V. Palankovski, G. Kaiblinger-Grujin, and S. Selberherr, "Study of Dopant-Dependent Band Gap Narrowing in Compound Semiconductor Devices," *Materials Science & Engineering,* vol. B66, pp. 46–49, Dec. 1999.

[P20] V. Palankovski, R. Schultheis, A. Bonacina, and S. Selberherr, "Effectiveness of Silicon Nitride Passivation in III-V Based HBTs," in *Abstracts Intl. Conf. on Defects in Insulating Materials,* (Johannesburg, South Africa), p. 188, April 2000.

[P21] V. Palankovski and S. Selberherr, "State-of-the-Art Micro Materials Models in MINIMOS-NT," in *Abstracts Intl. Conf. on Micro Materials MicroMat*, (Berlin, Germany), pp. 290–291, April 2000, and in *Proc. Intl. Conf. Micro Materials MicroMat*, in print.

[P22] V. Palankovski and S. Selberherr, "III-V Semiconductor Materials in MINIMOS-NT," in *Abstracts MRS Spring 2000 Meeting*, (San Francisco, California, USA), p. 249, April 2000.

[P23] V. Palankovski, R. Schultheis, A. Bonacina, and S. Selberherr, "Investigations on the Impact of the InGaP Ledge on HBT-Performance," in *Proc. Workshop on Compound Semiconductor Devices and Integrated Circuits*, (Egean See, Greece), pp. (VII-) 5–6, May 2000.

[P24] R. Quay, C. Moglestue, V. Palankovski, and S. Selberherr, "A Temperature Dependent Model for the Saturation Velocity in Semiconductor Materials," *Materials Science in Semiconductor Processing*, vol. 3(1-2), pp. 149–155, May 2000.

[P25] R. Quay, H. Massler, W. Kellner, T. Grasser, V. Palankovski, and S. Selberherr, "Simulation of Gallium-Arsenide Based High Electron Mobility Transistors," in *Proc. Intl. Conf. on Simulation of Semiconductor Processes and Devices*, (Seattle, Washington, USA), pp. 74–77, Sept. 2000.

[P26] V. Palankovski, S. Selberherr, R. Quay, and R. Schultheis, "Analysis of HBT Degradation After Electrothermal Stress," in *Proc. Intl. Conf. on Simulation of Semiconductor Processes and Devices*, (Seattle, Washington, USA), pp. 245–248, Sept. 2000.

[P27] T. Grasser, R. Quay, V. Palankovski, and S. Selberherr, "A Global Self-Heating Model for Device Simulation," in W.A. Lane, G.M. Crean, F.A. McCabe, and H. Grünbacher, editors, *Proc. 30th European Solid-State Device Research Conference*, (Cork, Ireland), pp. 324–327, Frontier Group, Sept. 2000.

[P28] V. Palankovski, T. Grasser, M. Knaipp, and S. Selberherr, "Simulation of Poly-silicon Emitter Bipolar Transistors," in W.A. Lane, G.M. Crean, F.A. McCabe, and H. Grünbacher, editors, *Proc. 30th European Solid-State Device Research Conference*, (Cork, Ireland), pp. 608–611, Frontier Group, Sept. 2000.

[P29] V. Palankovski, R. Quay, and S. Selberherr, "Industrial Application of Heterostructure Device Simulation," in *Tech.Dig. GaAs IC Symposium*, (Seattle, Washington, USA), pp. 117–120, (invited), Nov. 2000.

[P30] R. Quay, V. Palankovski, M. Chertouk, A. Leuther, and S. Selberherr, "Simulation of InAlAs/InGaAs High Electron Mobility Transistors with a Single Set of Physical Parameters," in *Intl. Electron Devices Meeting*, (Washington D.C., USA), Dec. 2000, in print.

[P31] V. Palankovski, R. Schultheis, A. Bonacina, and S. Selberherr, "Effectiveness of Silicon Nitride Passivation in III-V Based Heterojunction Bipolar Transistors," in *Radiation Effects and Defects in Solids*, accepted Sept. 2000, in print.

[P32] R. Quay, K. Hess, R. Reuter, M. Schlechtweg, T. Grave, V. Palankovski, and S. Selberherr, "Nonlinear Electronic Transport and Device Performance of HEMTs," *IEEE Trans.Electron Devices*, accepted Sept. 2000, in print.

[P33] V. Palankovski, S. Selberherr, and R. Schultheis, "Simulation of Power Heterojunction Bipolar Transistors on Gallium Arsenide," *IEEE Trans.Electron Devices*, submitted Nov. 1999, revised Oct. 2000.

[P34] V. Palankovski, N. Belova, T. Grasser, H. Puchner, S. Aronowitz, and S. Selberherr, "A Methodology for Deep Sub-Quartermicron CMOS Technology Characterization," *IEEE Trans.Electron Devices*, submitted Nov. 2000.

Curriculum Vitae

February 9th, 1969	Born in Sofia, Bulgaria
09/1976 – 07/1983	Primary School Education
09/1983 – 07/1988	High School Education at the English Language School, Sofia
09/1988 – 07/1993	University Education at the Technical University, Sofia. Specialization in Microelectronics and Technology of the Microelectronics Production
05/1989	Ranked second in the National Students Mathematical Olympiad
07/1993	Final exam and master's thesis on "Design of Silicon HBTs with SiGe Base". Received diploma degree in Electrical Engineering.
09/1993 – 01/1994	Compulsory military service in reduced time (4 months instead of 24) as one of the top-twenty specialists (per year) of national importance
03/1994 – 03/1997	Industrial experience at the Siemens Joint-Venture Digicom Ltd, Sofia
03/1997	Entered doctoral program at the Institute for Microelectronics, TU Wien
07/1997 – 12/2000	Free researcher of Siemens, Munich, Germany (since 1999 Infineon Technologies)
06/2000 – 09/2000	Visiting researcher at LSI Logic, Milpitas, CA, USA